博士論文

Search for the $N\Delta$ resonance in the $\gamma d \to d\pi^+\pi^-$ reaction

($\gamma d \to d\pi^+\pi^-$反応における $N\Delta$共鳴の探索)

東北大学大学院理学研究科

物理学専攻

外山　裕一

令和 3 年

Tohoku University

Doctoral Thesis

Search for the $N\Delta$ resonance in the $\gamma d \to d\pi^+\pi^-$ reaction

Author:
Yuichi Toyama

Supervisor:
Prof. Dr. Satoshi N. Nakamura

TOHOKU
UNIVERSITY

A thesis submitted in fulfillment of the requirements
for the degree of Doctor of Philosophy

2022

TOHOKU UNIVERSITY

Abstract

Graduate school of Science
Department of Physics

Doctor of Philosophy

Search for the $N\Delta$ resonance in the $\gamma d \to d\pi^+\pi^-$ reaction

by Yuichi Toyama

A dibaryon which is an object with baryon number $B = 2$ has been studied for a long time. Dyson and Xuong classified non-strangeness dibaryon states based on SU(6) symmetries in 1960's. In the framework, the deuteron is classified as one of the sextet states of dibaryons. Although dibaryon have been an interesting subject of research for a long time, most of the experimental studies up to the early 2000's were unsuccessful.

The CELCIUS/WASA collaboration reported this state via the double-pionic fusion reaction ($pn \to d\pi^0\pi^0$) in 2009. Thereafter, the WASA-at-COSY collaboration revealed properties of the isoscaler resonance state via the $pn \to d\pi^0\pi^0$ reaction in 2011. The dibaryon resonance state with isospin $I = 0$ and spin $S = 3$ thought to be a D_{03} which was predicted by Dyson and Xuong at 2.35 GeV/c^2 with a configuration of $\Delta\Delta$. The reported mass and width of that state were 2.37 GeV/c^2 and 0.07 GeV/c^2, respectively. The mass was ~0.08 GeV/c^2 smaller than that of 2Δ, the width was narrower than that of single Δ. This surprising result made dibaryon study come back into the limelight.

D_{12} is one of the dibaryon states classified by Dyson and Xuong with isospin $I = 1$, spin $S = 2$. This state can be regarded as an s-wave $N\Delta$ resonance. D_{12} is an interesting state from the point of view of the possibilities of existence as an internal structure of D_{03} and contribution to many-body effects in nuclei. Though there were some experimental clues and theoretical studies of this state, it was unclear whether the obtained experimental results represented a real resonance or not due to the difficulty of separation from kinematical effects. Very recently, the FOREST group at Tohoku University reported a photoproduced isovector dibaryon state at mass of 2.14 GeV/c^2 in the $d\pi^0$ invariant mass spectra of the $\gamma d \to d\pi^0\pi^0$ reaction. The most probable J^P configuration was 2^+ although they didn't exclude the possibility of $J^P = 1^+$ or 3^-. They separated the dibaryon production process from conventional pion production process for the first time using angular distribution of deuteron.

We investigated the $\gamma d \to d\pi^+\pi^-$ reaction for study of a possible $N\Delta$ dibaryon state using a deuterium target at the Research Center for Electron Photon Science, Tohoku University, Japan. In the experiment, ~3×10^12 tagged photon beam at energies ranging from 0.8 to 1.1 GeV was impinged to the liquid deuterium target (~520 mg/cm^2) and the charged particles in the final state: deuteron, π^+, and π^-, were detected by a magnetic spectrometer with a large solid angle named NKS2. NKS2 had capabilities of reconstructing momentum of charged particles, multi-track analysis, and p/π separation. We performed two different analyses named 2-track analysis and 3-track analysis. The 2-track (3-track) analysis was for events in which two (three) particles of $d\pi^+\pi^-$ in the final state, including deuteron, were detected by NKS2. In the 3-track and 2-track analysis, ~2000, ~15000 events were identified as the $\gamma d \to d\pi^+\pi^-$ reaction events, respectively. The 2-track analysis with higher statistics was mainly used to derive the cross sections, and the 3-track analysis was used to check the consistency of the 2-track analysis.

In this thesis, we have shown the total cross section, the differential cross sections of the $\gamma d \to d\pi^+\pi^-$ reaction in the region of $|t| > 0.15$ GeV^2. This is the world's first measurement of this reaction in this energy region. Dibaryon resonance structures were observed below the $N\Delta$ threshold in the differential cross section of the invariant mass of $d\pi^\pm$. The mass and width of the structure were consistent with these of D_{12} measured by the $\gamma d \to d\pi^0\pi^0$ reaction. The mechanism of the production process was discussed based on the angular distribution of emitted deuteron.

Acknowledgements

First and foremost, I would like to express my utmost gratitude to my supervisor, Prof. Dr. Satoshi Nue Nakamura for his warm advice for the past 8 years since I joined the strangeness nuclear physics group of Tohoku University in 2014. Not only in our weekly meetings, he always welcomed my questions and discussions despite his very busy schedule no matter how my question was inexperienced or stupid. His sincere attitude toward physics and his enjoyment of physics have been an ideal model and a guideline for me. I also thank him for giving me opportunities to participate in various domestic and international conferences and experiments. Without these experiences, I would not have been able to overcome the challenges of writing and presenting my thesis. I am proud to say that I have grown a lot not only as a scientist but also as a person through the research under his supervise.

I would also like to appreciate Prof. Dr. Kazushige Maeda, who has been leading the NKS2 project for many years. Thanks to his many years of contributions, I was able to conduct analyses on the interesting topic. At the analysis meeting, he pointed out various sharp points, which made me realize many things.

I am also deeply grateful to Prof. Hiroki Kanda. This research was originally based on his idea, and he continuously gave me advice on analysis even after leaving Tohoku University. He always encouraged me warmly, and I looked forward to reporting my progress to him.

I would like to express deep appreciation to Dr. Takatsugu Ishikawa. He taught me hadron and dibaryon physics from the basics, which I did not understand very well at first. I was able to proceed with my study thanks to his advise backed by a wealth of data analysis experience.

I owe special thanks to Dr. Masashi Kaneta for his concrete advice on various aspects about the NKS2 analysis and simulation programs. His advice and experience were very reassuring to me, as I did not join data taking of this study. I also would like to express my sincere gratitude to Dr. Sho Nagao for being my substantial research supervisor for a long time since I was an undergraduate student. It is no exaggeration to say that I learned everything important as an experimentalist from him. Thanks to the research skills that I developed while working with him, I was able to tackle the new challenges in this research smoothly. I thank Dr. Toshiyuki Gogami and Prof. Dr. Yu Fujii for discussion and advise in the weekly meetings. They also helped me a lot in daily life and experiments in the United States.

I appreciate all staffs of the strangeness nuclear physics group in Tohoku University, Prof. Dr. Hirokazu Tamura, Prof. Takeshi Koike, Prof. Koji Miwa, Prof. Mifuyu Ukai, Dr. Shuhei Hayakawa and Dr. Junya Yoshida, and senior scientists who graduated from our group, Prof. Ryotaro Honda, Prof. Takeshi Yamamoto, Dr. Yuya Akazawa, and Dr. Manami Fujita. As forerunners, they gave me advice and helped me in various situations of the analysis.

I also wish to acknowledge secretaries and a technician of the lab, Ms. Ayumi Takahashi, Ms. Yukie Sasaki, Ms. Yoko Wada, and Mr. Hiroo Umetsu, for their wonderful support. Thanks to their support, I was able to concentrate on my thesis.

I also thank staffs of the Graduate Program on Physics for the Universe, Tohoku University (GP-PU), Dr. Yusuke Tanimura, Dr. Hideyoshi Ozaki, and Ms. Hiroko Lane Miwa. Through the GP-PU program, I was able to deepen my knowledge of other fields related to the physics for the universe.

I appreciate juniors of ELS group, Mr. Genki Aida, Mr. Hiroki Takeuchi, Mr. Yuta Muroi, Mr. Yoshihiro Konishi, Dr. Kosuke Itabashi, Mr. Takeru Akiyama, Mr. Kazuki Okuyama, Mr. Keita Uehara, Mr. Tomomasa Fujiwara, Mr. Masaya Mizuno, Mr. Yuki R. Nakamura, Ms. Ryoko Kino, Mr. Koga Tachibana, Mr. Shintaro Nagano, and Mr. Tatsuhiro Ishige, for their support and encouragement. Especially, the preliminary analysis of the $\gamma d \to d\pi^+\pi^-$ reaction by Mr. Y. Muroi helped me a lot. I also thank students in the strangeness nuclear physics group, Ms. H. Kanauchi, Mr. Y. Ishikawa, Ms. A. Rogers, Mr. S. Kajikawa, and Ms. T. Sakao,

for giving me opportunities of fruitful discussion. I appreciate colleagues in Mainz University, Prof. Dr. J. Pochodzalla, Prof. Dr. P. Achenbach, Dr. W. Lauth, Dr. P. Herrmann, Mr. P. Klag, and Mr. P. Eckert, for kindful support during my stay in Mainz and participating an experiment performed at ELPH in 2018. I also thank all colleagues in the Jefferson Lab, especially, Prof. Dr. L. Tang, Prof. Dr. J. Reinhold, and Dr. B. Pandey for great helps during my stay in the United States and discussion about my analysis.

I am indebted to members of my thesis committee, Prof. Dr. S.N. Nakamura, Prof. Dr. H. Tamura, Prof. Dr. H. Ohnishi, Prof. T. Sanuki, and Prof. K. Miwa. The discussions in the pre-defense meeting helped me to improve the quality of my thesis and myself as a scientist.

I would like to express my gratitude and respect to members of the NKS2 collaboration in Oct. 2010, Prof. Dr. K. Maeda, Prof. H. Kanda, Dr. M. Kaneta, Dr. B.O. Beckford, Prof. K. Tsukada, Dr. S. Nagao, Ms. C. Kimura, Mr. F. Yamamoto, Mr. T. Fujii, and Mr. A. Okuyama. Their tireless efforts to acquire worthful data for one month allowed me to conduct this research. I also thank the accelerator group of ELPH, Tohoku University for providing stable electron beams.

Last but not least, I would like to express my gratitude to my family for their warmful support.

Contents

List of Figures

List of Tables

1 Introduction

In this chapter, physics motivation of this research will be described. General introduction of hadron physics, the status of dibaryon study including its historical overview, and specific motivations of this study will be given.

1.1 Hadron Physics

Hadron is a composite particle consisting of strongly interacting quarks (q), antiquarks ($\bar{q}$), and gluons (g). Hadron is generally classified into baryon, which consists of three quarks (qqq), and meson, which consists of quark-antiquark pairs ($q\bar{q}$). Baryon is a fermion represented by nucleons, which are the constituent particles of a nucleus such as proton and neutron, and meson is a boson with integer spin represented by pion, which was predicted by H. Yukawa in 1935. At the time of their discovery, these hadrons were thought to be elementary particles, but the quark model which describes hadrons as composite states of quarks was proposed by M. Gell-Mann and G. Zweig in 1964. Experimentally, the internal structure of hadrons was confirmed by deep inelastic scattering of high-energy electrons and hadrons in the late 1960s, and the view that hadrons are composite particles of quarks was established.

Nowadays, quantum chromodynamics (QCD), the fundamental theory of strong interaction, is established. According to QCD, hadrons are made of quarks and gluons which are gauge bosons, and the strong interaction is described by the gauge interaction between quarks and gluons with color charge. However, the description of hadrons in the low energy region by QCD, which is a non-perturbative theory, is still insufficient, and various theoretical studies have been carried out on the properties and interactions of hadrons, such as lattice QCD, which treats QCD as a numerical simulation, and analysis by effective field theory based on symmetries. Although each method has its own limitations, the goal of hadron physics is to give a comprehensive picture by combining them. In order to construct and verify these theoretical models, various high-quality experimental data are necessary.

Exotic hadrons are hadrons that are not classified as conventional mesons or baryons. QCD states that hadrons must be white for color confinement. In addition to the conventional mesons and baryons, there are other quark and gluon states that satisfy this requirement, such as glueballs consisting of multiple gluons, hadrons consisting of two quarks and two antiquarks, and hadrons consisting of six quarks and so on, but such states have not been discovered until recently. In 2003, a pentaquark state was reported by LEPS [Nak+03][1], followed by several tetraquark state candidates from the KEK B-factory [Cho+03]. After that, a number of candidates for exotic hadrons containing particularly heavy quarks were discovered at the LHC at CERN and elsewhere. More than 30 candidates of the exotic hadrons are now listed in PDG [Gro+20]. However, the internal structure and other properties of these exotic hadrons remain unresolved. Since the structure of exotic hadrons is closely related to the quark confinement problem, it is expected that the understanding of QCD will be further enhanced by clarifying the properties of exotic hadrons. Diabaryon with a configuration of hexaquark structure is one of the exotic hadrons to be studied for this purpose.

[1]The existence of this Θ pentaquark is still controversial because a higher statistics experiment at JLab failed to find the signal [McK+06].

1.2 Dibaryon

A dibaryon is an object with baryon number $B = 2$ [Cle17]. The dibaryon, a oppositeness of six constituent quark states, has long been an interesting subject of study, since its existence has not been ruled out by QCD. In this section, we briefly describe properties of nucleon-nucleon systems, the history of the study of the dibaryon and introduce previous experimental and theoretical studies on D_{12}, the subject of our study. Though experimental and theoretical studies on the dibaryons in the strange sectors are also interesting topics, the introduction of them are not treated as they are not so related with this study.

1.2.1 Deuteron

The deuteron is the first established dibaryon, which is defined as an object with $B = 2$. Since its discovery in 1932 by observing the atomic spectrum of hydrogen gas in a discharge tube [UBM32], its properties have been studied through various experiments.

As a result, it is known that deuteron belongs to the spin triplet and isospin singlet as $I(J^P) = 0(1^+)$. The mass, dipole moment, quadrupole moment, and form factors have also been measured with high precision.

Deuteron can be understood as a very loosely bound state of a proton and a neutron with a binding energy of 2.2 MeV (=1.1 MeV/A). This binding energy is much smaller than the typical binding energy of a nucleon in normal nuclei ~8 MeV/A. As a result, deuteron has a charge radius of 2.1 fm, which is larger than the typical range of pion exchange, $r \sim \frac{\hbar c}{M_\pi c^2} \sim 1.4$ fm. Therefore, the wave function of deuteron is relatively well reproduced as the molecular state of a proton and a neutron. It is still an open question, how much of a hexaquark configuration within a compact six-quark bag exists in deuteron.

1.2.2 Dineutron and Diproton

Dineutron and diproton, i.e., the two-nucleon isospin triplet systems, are known as virtual states. If the scattering length between the two particles is negative, the interaction is attractive, but not strong enough to form a bound state. If the scattering length is positive and larger than the effective range of the interaction, a bound state can be formed.

The isoscalar $^3S_1$ channel S-wave, the np spin singlet, has a scattering length of about +5 fm [Mac01] and forms a bound state (deuteron). The scattering length of the isovector $^1S_0$ partial wave is −18 fm for nn [Sch+87][Gab+84] and pp [Noy72], and −24 fm for np [Mac01]. These differences are due to the charge independence breaking. Therefore, there are no bound states in the pp or nn systems and np system with $I = 1$.

The NN interaction is too weak to form a bound state in the isovector $^1S_0$ channel, but strong enough to form a virtual state at only 57 keV [FW07] above the bound state threshold. This effect appears in nuclear reaction experiments as an enhancement near the threshold of the invariant mass distribution of the NN as a final state interaction between two emitted nucleons.

1.2.3 Historical Overview

Although dibaryon have been an interesting subject of research for a long time, most of the experimental studies up to the early 2000s were unsuccessful. Recently, they have come back into the limelight. In this section, we will briefly introduce the history of non-strangeness dibaryon research, which is roughly divided into the following four periods.

1. 1960s: Prediction based on SU(6) Group Theory
2. 1970s–1980s: Dibaryon rush era

TABLE 1.1: Classification of dibaryon state without strangeness by Dyson Xuong mass formula (Eq. 1.2).

D_{IS}	D_{01}	D_{10}	D_{12}	D_{21}	D_{03}	D_{30}
BB config.	NN	NN	$N\Delta$	$N\Delta$	$\Delta\Delta$	$\Delta\Delta$
Mass formula	A	A	A+6B	A+6B	A+10B	A+10B
Approximate mass [MeV/c^2]	1878	1878	2160	2160	2348	2348

3. 1990s and early 2000s: $d'(2065)$ in the double charge exchange reactions
4. Later 2000s and beyond: $d^*(2380)$ found by WASA collaboration and later

A more detailed historical overview of the dibaryon before 2017 is well summarized in [Cle17].

Prediction Based on SU(6) Group Theory

In 1960's, F.J. Dyson and N.H. Xuong classified s-wave dibaryons state of $S = 0$ by their spin and isospin based on SU(6) symmetry[DX64] [DX65]. A baryon which belongs to baryon decuplet with spin 3/2 or baryon octet with spin 1/2 belongs to 56 multiplet in terms of SU(6). Thus, two-baryon states are represented as direct product of 56 multiplets as,

$$56 \otimes 56 = 462 \oplus 1050 \oplus 1134 \oplus 490. \tag{1.1}$$

From the fact that baryons are fermions, the two antisymmetric representations, 1050 and 490, are allowed. They discussed low-lying state of all two-baryon resonances only appear in 490 multiplet of SU(6). Then, they predicted 6 dibaryon states in non strangeness sector. They also predicted masses of the each states using a simple mass formula,

$$M = A + B(I(I+1) + S(S+1) - 2), \tag{1.2}$$

where I and S represent isospin and spin, respectively. They represented a dibaryon with spin S and isospin I as D_{IS}, where D mean dibaryon. Parameter $A = 1878$ MeV and $B = 47$ MeV were tuned to reproduce masses of deuteron and D_{12}, although D_{12} was not confirmed as a true resonance state at that time. The predicted dibaryons and their mass, spin, isospin, and baryon-baryon configuration are summarized in Tab. 1.1.

Later, M. Oka and K. Yazaki performed a calculation of non-relativistic quark cluster model [OY80]. In their study, while the interaction of $(I,\ S) = (1,\ 0)$ and $(0,\ 1)$ states (correspond to D_{01} and D_{10}) is a strongly repulsive at short distance, that of $(I,\ S) = (3,\ 0)$ and $(0,\ 3)$ states (correspond to D_{03} and D_{30}) is attractive. It also should be noted that they did not necessarily predict the bound state for the D_{12} and D_{21} states.

The Dibaryon Rush Era

Starting with the prediction of the so-called H-dibaryon, a bound state of $\Lambda\Lambda$, by R.L. Jaffe in 1977 [Jaf77], the dibaryon rush era had begun. Jaffe's prediction led up a number of theoretical predictions of bound or unbound baryon-baryon systems. Many experiments to search bound or resonant dibaryon states have been performed, particularly interested in narrow dibaryon states. The narrow width structures were attractive for the following reasons. First, that narrow resonant states are experimentally easy to separate from the background events of conventional hadronic processes. Second, the existence of narrow dibaryon state means that it is an exotic dibaryon which has no structure that can be explained by the

asymptotic configuration of conventional hadrons. Specifically, the state must either (i) have an exotic internal structure that does not overlap significantly with the asymptotic hadronic configuration of the decay particles, (ii) be prohibited from decaying into the hadronic channel of the presentation by a specific quantum number, or (iii) have a mass below the threshold of the emitting particle.

As a result, a number of narrow dibaryon states were experimentally claimed, but even one has not survived critical inspections. A major reason for this failure was due to poor quality of experimental data collected by not optimal instruments. In addition, the reactions and energy regions for these experiments might not be optimal. K.K. Seth concluded that "Nobody, anywhere, has seen a genuine, bona-fide, gold-(silver, nickel-, or even un-)plated dibaryon, yet!" in 1988 [Set88]. Seth also commented that "We should concentrate on exclusive experiments." This is one of the insights obtained from discussions of this period. The only survived dibaryon candidate in this period is a broad resonance structure around the $N\Delta$ threshold. Detail discussion of this state will be described in Sec. 1.2.5.

$d'(2065)$ in the Double Charge Exchange Reactions

Another dibaryon state candidate was proposed as an intermediate state in nuclei in the double charge exchange reactions (DCX). In the double charge exchange reactions, $A(\pi^+,\pi^-)B$, or $A(\pi^-,\pi^+)B$, where A, B represent target and reacted nuclei, two protons are converted to two neutrons or vice versa. This reaction depends on the correlation of reacted two nucleons because it is a genuine two-nucleon process. Thus, this reaction is considered to be suited for the dibaryon search. Peak structures were observed in the π^- forward cross sections in low energy region of the $A(\pi^+,\pi^-)B$ reaction for various nucleus targets as shown in Fig. 1.1. A dibaryon state, $d'(2065)$, was introduced at the mass of ~2065 MeV with a width of ~0.5 MeV to explain the peak structures. It seemed to work well, however, the predicted state has not been observed in free space. The obtained upper limit of the $d'(2065)$ production cross section in the $pp \to pp\pi^+\pi^-$ reaction was $\sigma < 20$ nb (95% C.L.) [Bro+02]. Conclusion of this state in [Bro+02] was as follows,

- either d' does not exist at all, or
- d' production cross section in pp collisions is smaller than expected from theoretical estimates, or
- the mass of free d' is outside the range of investigated here, or
- it exist only in the nuclear medium

After all, $d'(2065)$ state has not been established.

$d^*(2380)$ Found by the WASA Collaboration and Later

After many failure of experiments, finally a "genuine dibaryon[2]" resonance was found in 2010's.

In 2009, the CELSIUS/WASA Collaboration carried out the exclusive and kinematically complete measurement of the most basic double-pionic fusion reaction $pn \to d\pi^0\pi^0$ for the first time [Bas+09]. They reported the s-channel resonance like structure in energy dependence of the total cross section. Later, the WASA detector was moved to COSY in J$\acute{\text{u}}$lich and the measurement of the $pn \to d\pi^0\pi^0$ reaction with higher statics was carried out [Adl+11]. Energy dependence of total cross section is shown in Fig 1.2. This channel had not been measured before due to experimental difficulty despite the fact that it has only

[2]This statement was used in [Cle17]

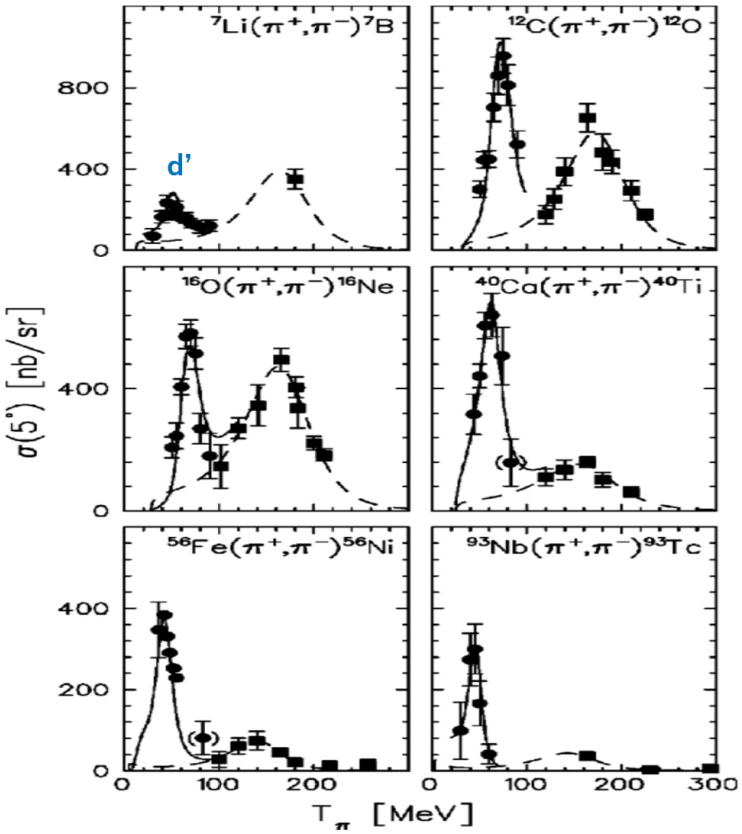

FIGURE 1.1: Energy dependence of the forward angle cross section for nonanalog DCX groundstate transitions [Dra+00]. Solid lines show the calculation result with assuming $d'(2065)$ state.

the isoscalar component and is an interesting channel with a very small conventional process background. Since free neutrons could not be used either as a beam or as a target, the use of neutrons inside the deuteron as quasi-free neutrons in $pd \rightarrow d\pi^0\pi^0 + p_{spectator}$ reactions was the only way to carry out the experiment. In addition, it was necessary to use detectors such as the WASA detector to capture charged and uncharged particles at essentially full solid angles. Following experiments and theoretical calculations tried to reveal the properties of this resonance. Since it is an isoscalar dibaryon resonance state, it was named $d^*(2380)$ by analogy with the excited state of deuteron. The quantum numbers of this state were consistent with D_{03}. A more detail explanation about properties of $d^*(2380)$ will be described in Sec. 1.2.4.

The success of the WASA collaboration spurred interest in the dibaryon issue again. Photoproduced dibaryon states were reported from the FOREST group at Tohoku University [Ish+19], see Sec. 1.2.5 for detail. An experiment in order to search for D_{30} is also planned at the high-p beam line of J-PARC [Ish+20].

1.2.4 Properties of the Isoscaler Dibaryon: $d^*(2380)$

As mentioned in the previous section, d^* was observed in the $pn \rightarrow d\pi^0\pi^0$ reaction by WASA collaboration [Bas+09] [Adl+11]. The follow-up experiments were carried out to reveal properties of $d^*(2380)$ via the various reactions. The isospin of this state was understood by measurements of the $pn \rightarrow d\pi^0\pi^0$ reaction, which is a pure isoscalar reaction, followed by different two fusion processes, the $pp \rightarrow d\pi + \pi^0$ reaction, which is a pure isovector reaction, and the $pn \rightarrow d\pi^+\pi^-$ reaction, which contains both isovector and isoscalar components.

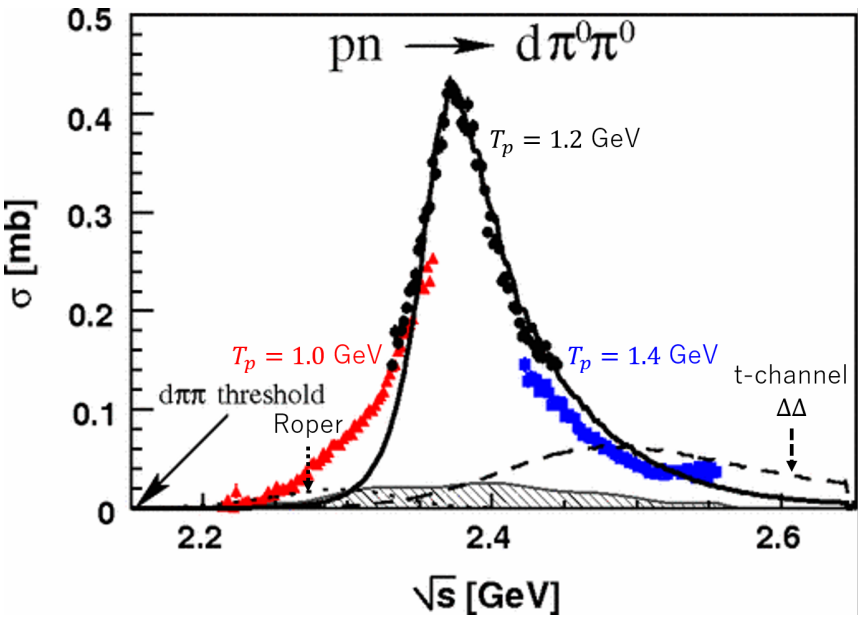

FIGURE 1.2: Total cross section of the $pn \to d\pi^0\pi^0$ reaction derived from the measurement of the $pd \to d\pi^0\pi^0 + p_{spectator}$ reaction [Adl+11]. Red triangles, black dots, and blue squares show the cross section measured in different proton beam energy, T_p = 1.0, 1.2, and 1.4 GeV, respectively. The hatched area indicates systematic uncertainties. The solid line shows the expected cross section for a $s-$channel resonance with m = 2.37 GeV and Γ = 68 MeV. The dotted and dashed lines show the expected cross sections for conventional processes, Roper excitation process and $t-$channel $\Delta\Delta$ process, respectively. The conventional processes clearly under estimate the obtained cross section.

The obtained cross sections are in good agreement with the following equation derived from isospin symmetry, which confirms that $d^*(2380)$ is a pure isoscalar state [Adl+13a],

$$\sigma(pn \to d\pi^+\pi^-) = 2\sigma(pn \to d\pi^0\pi^0) + \frac{1}{2}\sigma(pp \to d\pi^+\pi^-). \tag{1.3}$$

From the measurement of the decay angular distribution by the WASA collaboration [Adl+11], the spin parity is estimated to be 3^+, which is consistent with the partial wave analysis of np scattering [Adl+14] as described later.

The $d^*(2380)$ contribution was measured from the 2π production reaction with an isoscalar component in the non-fusion process by the WASA-at-COSY collaboration [Adl+13b] [CBS15] [Adl+15] and HADES at GSI [Aga+15]. The phase space of the non-fusion process with a four-body final state is much larger than that of the fusion process with a three-body final state, and the contribution of the conventional t-channel reaction process increases rapidly with increasing energy. In addition, since it is not possible to select a pure isoscalar process, $d^*(2380)$ contribution does not appear as a clear peak structure on the total cross section as in the fusion process, but as a shoulder-like structure on the steep slope of the total cross section. As a result, for all the 2π production processes, the cross sections were consistent with the assumption of a $d^*(2380)$ which is dibaryon resonance with $I(J^P) = 0(3^+)$.

If $d^*(2380)$ is a true s-channel resonance, it must also be observed in np scattering. We need to show that the pole is generated by a ${}^3D_3 - {}^3G_3$ coupled partial wave corresponding to $I(J^P) = 0(3^+)$. The contribution of $d^*(2380)$ to the total np elastic scattering cross section of 40 mb was estimated to be about 0.170 mb. Thus, the analyzing power was measured to see the small contribution. Figure 1.3 shows the analyzing power at around 90 degrees,

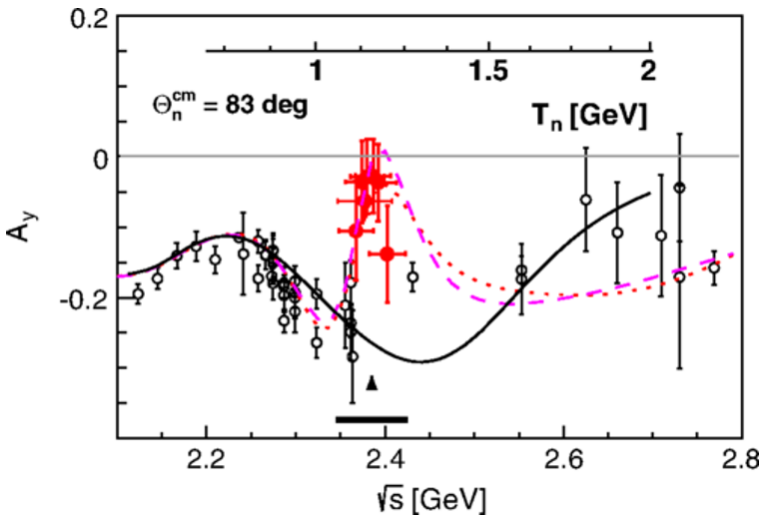

FIGURE 1.3: Energy dependence of the np analyzing power at $\Theta_n^{\rm cm}$ = 83 degree [Adl+14]. The solid symbols denote the results from WASA-at-COSY, the open symbols, those from farmer studies [Bal+93] [Les+99] [Mak+80] [New+89] [Arn+00] [Bal+87] [McN+93] [Gla+93]. Vertical arrow and horizontal bar indicate mass and width of the resonance. The black solid line show the SAID SP07 phase shift prediction without including new data from WASA-at-COSY. The magenta dashed line, and red dotted line show the result of the new weighted and unweighted SAID partial-wave solution with including new data from WASA-at-COSY, respectively.

where the contribution of the resonance becomes large. The signal was observed at the point corresponding to $d^*(2380)$.

There are two thresholds that can appear in this mass region, $NN\eta$ and $NN^*(1440)$, but they cannot make the d^* signal in this case because both of them also have isovector components. From the above discussion, it is reasonable to consider $d^*(2380)$ as an s-channel resonance.

Decay and Configuration of $d^*(2380)$

F.J. Dyson and N.H. Xuong predicted D_{03} to be a configuration of $\Delta\Delta$. On the other hand, the obtained mass is $M_{d^*} \sim 2370$ MeV, which corresponds binding energy $\epsilon_{d^*} \sim 80$ MeV using the formula for estimating the radius of two quark clusters based on the uncertainty principle as,

$$r_{d^*} \sim \frac{\hbar c}{\sqrt{2M_\Delta \epsilon_{d^*}}} \sim 0.5 \text{ fm}, \tag{1.4}$$

where M_Δ is a mass of the Δ resonance. This estimated radius is smaller than the typical size of a nucleon, suggesting a large overlap between the wave functions of the two Δ. The quark model calculation also yields a radius of $r \sim 0.8$ fm [Hua+15]. From these values, $d^*(2380)$ seems to exist as a compact hexaquark system.

However, it is natural to think that $d^*(2380)$ has an asymptotic configuration of $\Delta\Delta$ in order to explain the ABC effect, which is a feature of the isoscalar 2π invariant mass distribution in the fusion process with enhancement in lower mass region. The ABC effect was originally discovered when a peculiar peak structure appeared in the 2π isoscalar state of $pd \to {}^3\text{He}(\pi\pi)$ as shown in Fig. 1.4, and was an unsolved problem for a long time [ABC60] [BAC61]. This enhancement of the 2π-invariant mass distribution has also been observed in the $pn \to d\pi^0\pi^0$ reaction by WASA collaboration, and this effect was successfully reproduced

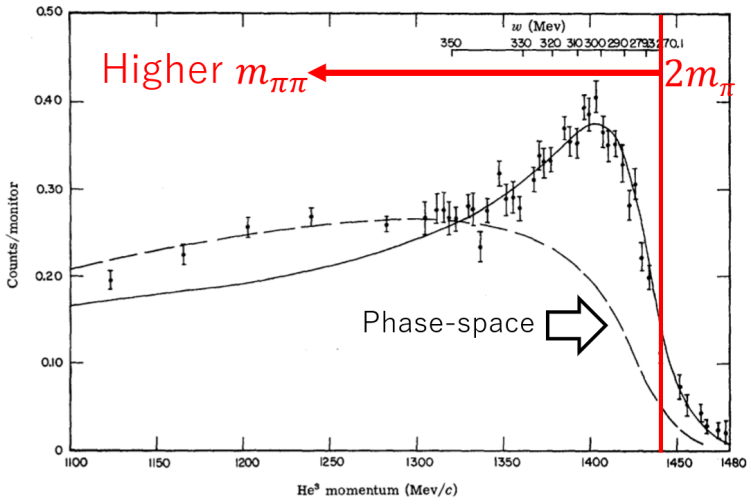

FIGURE 1.4: A momentum spectra of ^{3}He in the $pd \to {}^3\mathrm{He}\pi\pi$ reaction with $I = 0$ configuration of $\pi\pi$ system [BAC61]. The dashed curve is the phase-space volume fitted to the points below 1300 MeV/c. The solid curve is the phase-space volume multiplied by the pion-pion enhancement factor. The w scale shown in right upper region gives the invariant mass of two-pion.

by introducing a vertex function for $d^* \to \Delta\Delta$ in [Adl+11]. This is consistent with the fact that the ABC effect has been observed only in the fusion process.

M.N. Platonove and V.I. Kukulin proposed an idea that $d^* \to D_{12}\pi$ (p wave) is occurred instead of $d^* \to \Delta\Delta$. In order to reproduce the ABC effect, $d* \to d\sigma$ (d wave) was assumed to occur at a branching ratio of 5% [PK16] [PK13]. If $d^*(2380)$ is a compact hexaquark state, it seems quite natural that it would decay into other dibaryons rather than immediately into the two-baryon system $\Delta\Delta$. However, since D_{12} has a decay channel to NN as described later (Sec. 1.2.5), the decay of $d* \to D_{12}\pi \to NN\pi$ should also occur, the corresponding signal is not observed in the preliminary results of the $np \to pp\pi^-$ reaction and the $pp \to pp\pi^0$ analysis by the WASA collaboration.

1.2.5 Isovector Dibaryon: D_{12}

D_{12} is one of the dibaryon states classified by F.J. Dyson and N.H. Xuong with isospin $I = 1$, spin $S = 2$ [DX64]. They considered this state was an s-wave $N\Delta$ resonance. The experimental clue of this state was already obtained in 1950s . However, the interpolation of the experimental result was not straightforward. The former experimental and theoretical studies about D_{12}, and roles of D_{12} in hadron physics are shown in this section.

Previous Studies of D_{12} Before 2010

The first clue of the state was obtained by the pion induced reaction on a deuterium target in 1950's [NP19]. Resonant behavior in the $\pi^+ d \to pp$ reaction which corresponded to a resonance with a mass of ~2.16 GeV, and a width of ~0.12 GeV as shown in Fig. 1.5. The angular distribution of proton agreed with the assignment $J = 2$. The parameter B of Dyson-Xuong mass formula (Eq. 1.2) was determined to reproduce the peak position of Fig. 1.5.

Later, SAID group showed that $^1D_2$ partial wave shows a remarkable loop structure with s-channel resonance in Argand diagram based on the $\pi d \to pp$, and $\pi d \to \pi d$ reaction cross section and polarization data [Arn+93][ASW94]. Figure 1.6 shows Argand plot obtained from the $\pi^+ d \to pp$ reaction [Arn+93]. NN partial waves of $^3P_2 - {}^3F_2$, $^3F_3$, $^1G_4$, and

$^3F_4 - {}^3H_4$ show loop structure too, though the effects are small compared to that of $^1D_2$ partial wave.

Based on these experimental observations, several theoretical models performed calculations on the configuration of D_{12}. Bag model [MAS80] and bag model + pion cloud [MT83] predicted a dibaryon state with $I(J^2) = 1(2^+)$ as 6-quark state although the predicted mass was a little bit larger (2.36 GeV/c^2). More recently, A. Gal and H. Garcilazo studied πNN by Faddeev calculations with hadronic interactions [GG14]. They found a resonance pole at $(2147 - i60)$ MeV for the $I(J^2) = 1(2^+)$ state. M.N. Platonove and V.I. Kukulin approached this state by very different way. They argued that the use of a soft meson-baryon form factor consistent with πN elastic scattering, especially in the $pp \to d\pi$ reaction, leads to too small π production cross sections in conventional t-channel meson exchange calculations [PK16]. The experimental data are reproduced by assuming a dibaryon resonance corresponding to D_{12} in the intermediate reaction process in their calculation.

However, the problem was that the observed structure cannot be kinematically distinguished between the dibaryon resonance state and the quasi-free Δ excitation because the observed mass was close to the $N\Delta$ threshold and the width was compatible with that of single Δ. There were both theoretical calculations that supported [Hos93] and rejected [Nis82] the dibaryon resonance state. Therefore, existence of D_{12} as a resonance state was still questionable at that time.

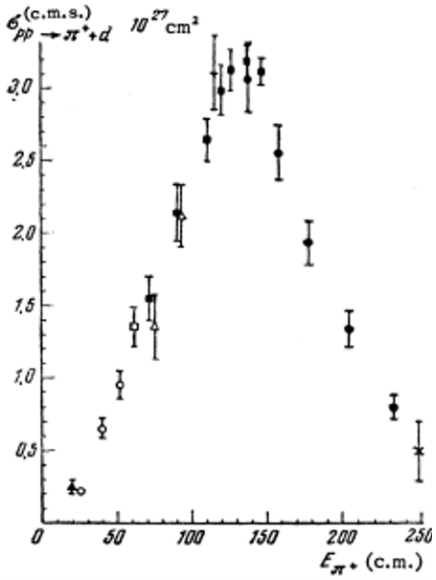

FIGURE 1.5: Total cross section of $pp \to \pi^+ d$[NP19]. $E_{\pi+} = 130$ MeV corresponds to $\sqrt{s} \sim 2160$ MeV

Recent Measurement of D_{12} via the $\gamma d \to d\pi^0\pi^0$ Reaction

In 2019, D_{12} state was reported via the $\gamma d \to d\pi^0\pi^0$ reaction from the FOREST group at ELPH, Tohoku University[Ish+19]. They reported 3 isoscalar dibaryons and 1 isovector dibaryon. They suggested sequential decay of an isoscalar dibaryon to an isovector dibaryon, as $\gamma d \to R_{IS} \to R_{IV}\pi^0 \to d\pi^0\pi^0$, where R_{IS} and R_{IV} represent isoscaler dibaryon and isovector dibaryon, respectively. The advantage of the photoproduction is that quasi-free pion production is kinematically separable because quasi-free pion production process shows a very backward peak in deuteron emission angle in the γd center of mass frame. Since the observed deuteron emission angle distribution was almost flat, they concluded that the

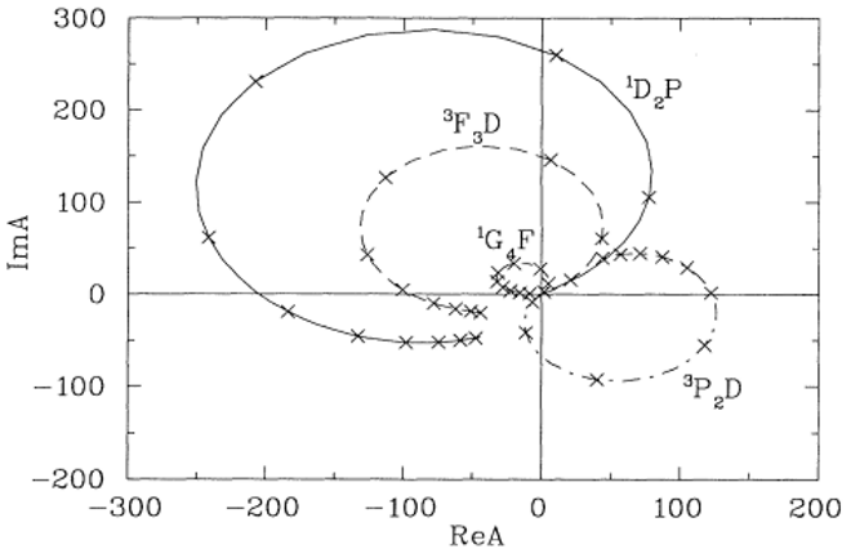

FIGURE 1.6: Argand plot of dominant partioal-wave amplitudes obtained form the $\pi^+ d \to pp$ reaction data [Arn+93]. The points shown as crosses donate 50 MeV steps.

process was dominated by dibaryon production processes. The correlation deuteron angular distribution and reaction process will be discussed in Sec. 5.2 in detail.

They reported a resonance structure in $d\pi^0$ invariant mass with a mass of 2.140 ± 0.011 GeV/c^2 and a width of 0.091 ± 0.011 GeV/c^2. The most probable spin parity was 2^+ although they could not exclude the possibility of 1^+ or 3^- state. Figure 1.7 shows the $d\pi^0$ invariant mass spectra for two different total energy region. The red solid curves show the fitted functions, expressed as a sum of a Breit–Wigner (BW) peak (dotted curves in red), its reflection[3] (dotted curves in red), and phase-space (dash-dotted curves in magenta) contributions, to the data. Contributions of a BW peak and its reflection are summed up at an amplitude level. The dashed green curves correspond to the FA calculations [FA05] with arbitrary normalization.

This is the first time that D_{12} signal was observed in the condition of kinematically separated from quasi-free pion production. The obtained mass of D_{12} was smaller than that of $N\Delta \sim 2.17$ GeV/c^2 and the obtained width of D_{12} was narrower than that of single $\Delta \sim 0.12$ GeV/c^2. However, there is a theoretical studies that attempt to explain the experimental data without assuming any dibaryon resonance, especially for the angular distribution of deuteron [Ego20], and further investigation is necessary.

Importance of D_{12}

D_{12} may be obtained as a decay particle of $d^*(2380)$, as claimed in [PK16], or it may be obtained as a decay particle of an unknown dibaryonic state of even higher mass, as claimed in [Ish+19]. This may be because the original dibaryon state is an exotic six-quark state, and it is more natural to transition to another dibaryon state than to decay to a two-baryon system. Alternatively, the molecular states of D_{12} and π might be interpreted as forming a higher-mass dibaryon state. In any case, D_{12} plays an important role in understanding the internal structure of the heavier dibaryon states.

[3] Invariant mass distribution of $d\pi^0_2$ when $d\pi^0_1$ makes a resonant state.

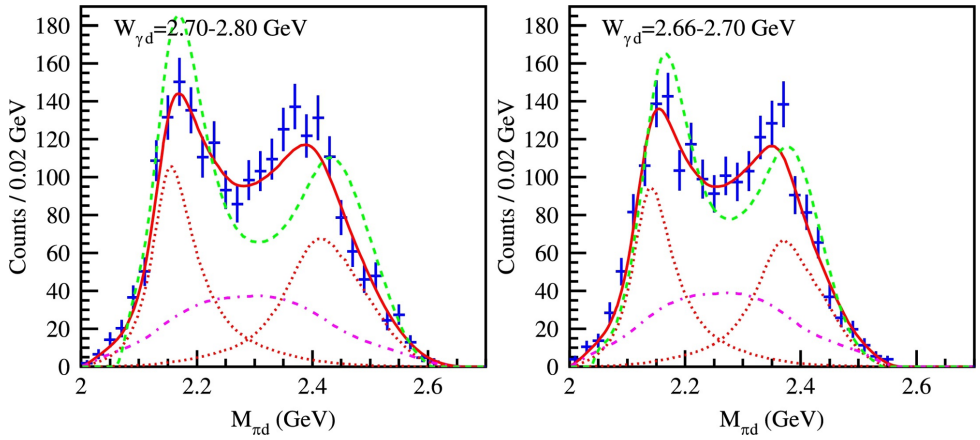

FIGURE 1.7: $d\pi^0$ invariant mass of the $\gamma d \to d\pi^0\pi^0$ reaction for two different total energy region [Ish+19]. Left panel shows higher energy region. The red solid curves show the fitted functions, expressed as a sum of a Breit–Wigner (BW) peak (dotted curves in red), its reflection (dotted curves in red), and phase-space (dash-dotted curves in magenta) contributions, to the data. Contributions of a BW peak and its reflection are summed up at an amplitude level. The dashed curves (green) correspond to the FA calculations [FA05] with arbitrary normalization.

When considering nucleon-nucleon interactions in nuclei, the 2π exchange picture, which is currently introduced as a three-body force, may include contributions from the $N\Delta$ dibaryon resonance including D_{12}.

From these things, D_{12} is the key state to understand hadron interaction and few body baryon systems.

1.3 Motivation of This Research

In this thesis, a possible dibaryon state, especially $N\Delta$ dibaryon, is studied via the $\gamma d \to d\pi^+\pi^-$ reaction.

The width and mass of D_{12} can be measured by analyzing the momentum of charged particles using a magnetic spectrometer. Since the γd system has an isovector component in this reaction, D_{12} might be produced by a different process than the $\gamma d \to d\pi^0\pi^0$.

It should be noticed that there is an only one cross section measurement of the $\gamma d \to d\pi^+\pi^-$ reaction with the old bubble chamber, which measured the cross section in a limited deuteron kinematic region (the backward emission region of d in the γd center of mass system) [Ben+74]. The measurement of the angular distribution and cross section of deuteron in the forward region is important.

2 Experiment

Experimental principle and apparatus will be described in this chapter. First, experimental principle will be shown. Next, experimental facility including photon beam apparatus will be explained. Finally, apparatus of a magnetic spectrometer, Neutral Kaon Spectrometer 2 (NKS2), including data acquisition system will be introduced.

2.1 Experimental Principle

The experiment was originally designed to measure a cross section of strangeness photoproduction on a deuterium target. Especially, the reaction,

$$\gamma n_{QF} \rightarrow \Lambda K_s^0 \tag{2.1}$$
$$\rightarrow p\pi^-\pi^+\pi^-, \tag{2.2}$$

where n_{QF} means a quasi-free neutron in a deuteron, was interested and focused. Branching ratio of $\Lambda \rightarrow p\pi^-$ and $K_s^0 \rightarrow \pi^+\pi^-$ are about 68% and 40%, respectively. Since the experiment was performed as an inclusive measurement, the reaction,

$$\gamma p_{QF} \rightarrow \Lambda K^+ \tag{2.3}$$
$$\rightarrow p\pi^- K^+, \tag{2.4}$$

was also measured simultaneously. Λ and K_s^0 were identified by invariant mass spectra of $p\pi^-$ and $\pi^+\pi^-$, respectively.

In the experiment, we measured trajectories of charged particles with a large solid angle (~25% for a single charged particle) magnetic spectrometer, Neutral Kaon Spectrometer 2 (NKS2), including the forward region, and derived momenta and a position of a decay point. Fig. 2.1 shows a top view sketch around the target with trajectories of charged particles. NKS2 has capabilities of particle identification for p/π separation and a invariant mass resolution of a few MeV/c^2 for Λ and K_s^0. Apparatus and a specification of NKS are shown in Sec. 2.4.

In addition the incident photon energy region was 0.8–1.1 GeV, which covered threshold of strangeness production (~0.9 GeV) and was enough to produce 2 pions in the final state. The energy of the incident photon was tagged by a photon tagging system (tagger) with a resolution of several MeV. Detail description of the tagger is shown in Sec. 2.3.2.

Since no discrimination other than e^+e^- rejection was performed in the data acquisition trigger, and only the measurement of two charged particles was required as the triggering condition, events including $d\pi^+\pi^-$ in the final state were collected in the same data set. The $\gamma d \rightarrow d\pi^+\pi^-$ reaction was selected by particle identification and selection of kinematic conditions, and the production cross section was derived. The measurement with the large solid angle spectrometer was an advantage for obtaining information on the decay angular distribution, which is important for understanding the formation mechanism of dibaryon. The invariant mass resolution was also sufficiently good to search for the resonant states with such a broad width (>10 MeV).

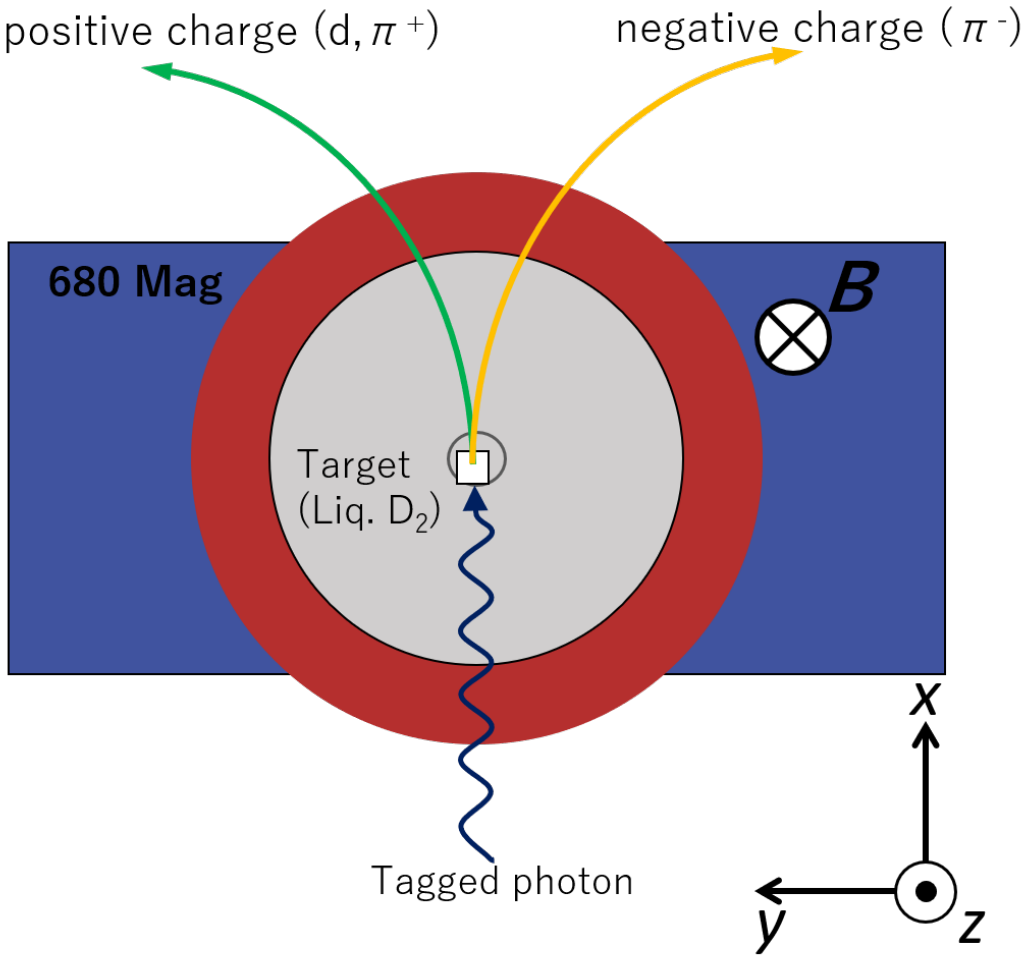

FIGURE 2.1: A rough sketch of the experimental setup around the target. This is sliced along horizontal direction at the beam height. $\boldsymbol{B}$ means a vector of the magnetic field of NKS2. Blue box and red circle represent a yoke and a coil of the magnet respectively. Scale is not exactly correct. A detailed sketch of the apparatus can be found in Fig. 2.10.

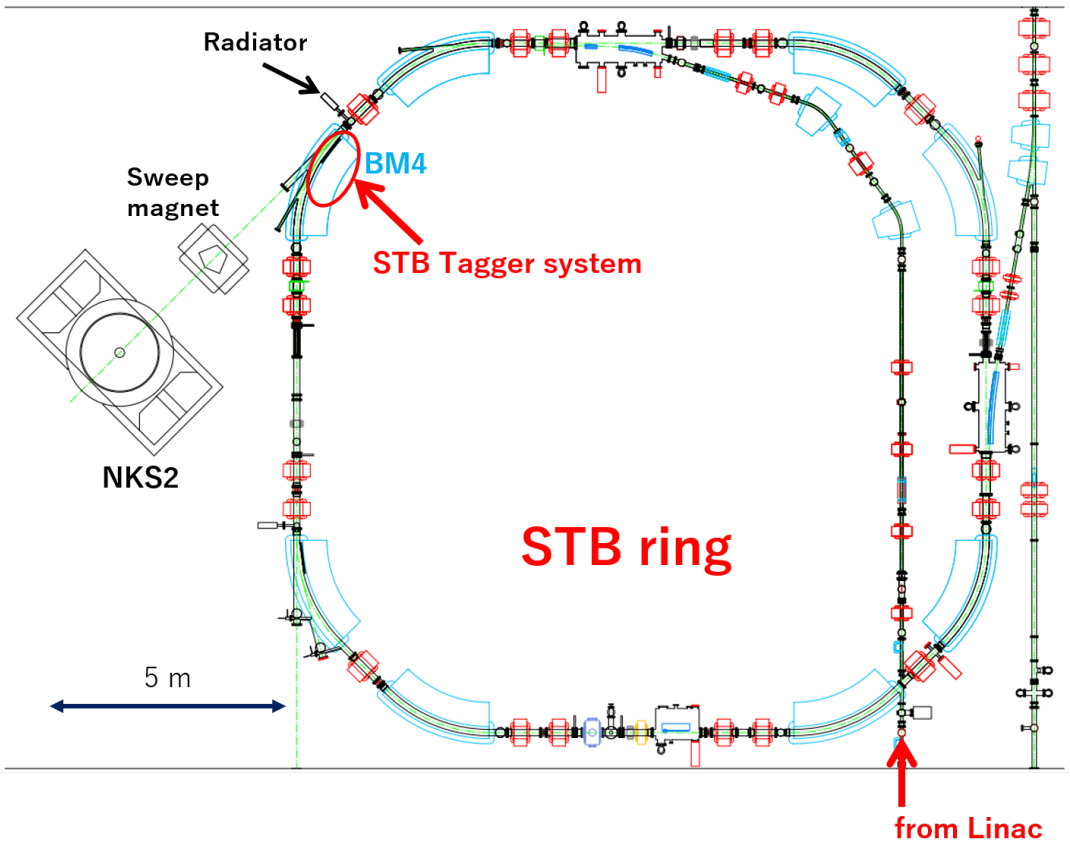

FIGURE 2.2: Floor map of the 2nd experimental hall at ELPH. A synchrotron (STB ring), a photon tagging system (STB Tagger system), a sweep magnet, and NKS2 are shown.

2.2 Research Center for ELectron PHoton Science (ELPH), Tohoku University

The experiment was performed at Research center for ELectron PHoton Science (ELPH), Tohoku University in October 2010.

2.2.1 Stretcher Booster Ring (STB ring)

Fig. 2.2 shows floor map of the 2nd experimental hall of ELPH. Electrons were injected from a linac to the synchrotron with an energy of 200 MeV and accelerated up to 1.2 GeV by the STretcher-Booster (STB) ring in about 1.2 seconds. Incident beam to an experimental target (liquid deuterium) were real photons created by bremsstrahlung caused at a radiator.

Accelerator Upgrade in 2011

The accelerators (the linac and the STB ring) were seriously damaged by the Great East Japan Earthquake on March 11, 2011. Therefore, the current situation (2022) of the accelerators is different from what it was in 2010. Although this is not directly related to the result of this study, it would be helpful to describe a brief summary of the current situation as follows. As a part of the recovery work, the linac was replaced new one with a maximum energy of 90 MeV and The STB ring with a top energy of 1.2 GeV was upgraded to Booster Stretcher

Ring (BST ring) with that of 1.3 GeV. This upgrade allowed us to use higher photon energy region upto ~1.2 GeV.

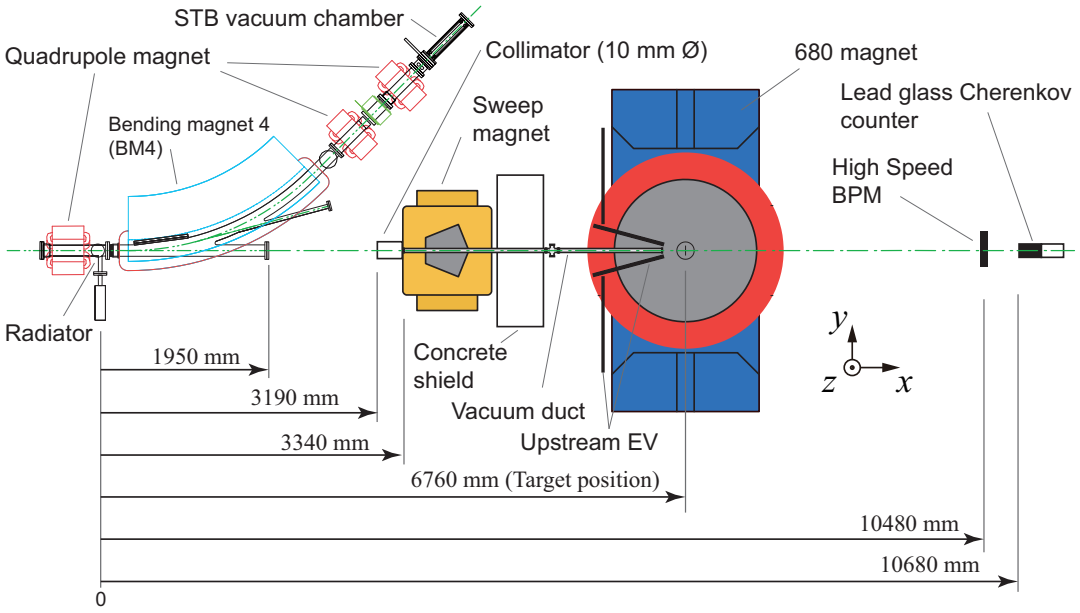

FIGURE 2.3: Top view of the photon beam line setup [Kan+18]. A lead collimator, a sweep magnet, and a vacuum duct were located upstream from the target. A high-speed beam profile monitor (HSBPM) and a lead glass Cherenkov counter were placed downstream from the target.

2.3 Photon Beam Line

The radiator was inserted to the path of the accelerated electrons, and the photons generated by bremsstrahlung are extracted as a beam.
Fig. 2.3 shows schematic top view of the photon beam line. Apparatus of the photon beam line described from upstream to downstream in this section.

2.3.1 Radiator for Bremsstrahlung

There are three methods for generating tagged photons: (1) using inverse Compton scattering by laser light at LEPS [Mur+14], (2) using extracted electron beams at JLab [Sob+00] and Mainz [McG+08] , (3) and an internal target system using a radiator placed inside of a vacuum chamber of an accelerator. An internal target system was adopted in our setup.

The radiator is a carbon fiber (11ϕ µm) mounted on a aluminum frame and remotely controlled by a computer from a counting house which is a separate building from the accelerator building and is about 50 m away from the experimental hall in a straight line. The radiator was kept away from the electron orbit during acceleration and inserted to the electron orbit to cause bremsstrahlung. Minimum step size of a stepping motor is approximately 2 µm. Insertion position and speed of the radiator were optimized to achieve a flat beam intensity in a spill. Figure 2.4 shows a sketch of the radiator. Accelerated electrons pass through perpendicular to the paper.

2.3.2 STB Tagger System

Incident photons have to be measured indirectly otherwise the photon cannot be used as beam. Therefore, photons were tagged by measuring electrons which were scattered by the radiator.

The photon tagging system (STB Tagger I, tagger [Yam+05]) had been placed at inside of the fourth bending magnet (BM4) of the STB ring[1]. Fig. 2.5 shows a schematic view of

[1]3rd generation of STB tagger is under development now (February 10, 2022)

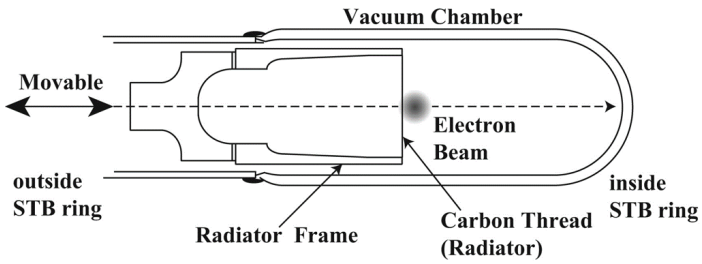

FIGURE 2.4: A sketch of the radiator for bremsstrahlung of BM5 beam line [Ish+10]. The design of the radiator of BM4 beam line is almost same with that of BM5 beam line.

the tagger and trajectories of recoil electrons. The recoil electrons that lose energy due to bremsstrahlung at the radiator were bent inward from their orbits by the magnetic field of BM4 according to the lost energy, and pass through the detector units of the photon tagging system. Since recoil electrons passed through different orbits for each energy as shown in Fig. 2.5, the energy of the photon was identified by the position of its passage. Tagger consisted of position measurement counters named TagF and trigger counters named TagB. TagF and TagB consisted of 48 and 12 segments of plastic scintillation counters, respectively. Segment numbers of TagF and TagB were assigned from 1 to 48 and 1 to 12, respectively, from the upstream of the electron beam. Size of scintillator of TagF was $20^H \times 3\text{–}8^W \times 5^T$ mm^3 (Fig. 2.6). The width of the scintillator of TagF was designed to cover 6 MeV by one segment with a 1.2 GeV mode of the STB ring. That resulted the width was set in six steps from 3 mm to 8 mm depending its position. The width of TagB was arranged so that four TagF segments correspond to one TagB segment. The space inside the BM4 was limited, thus it is not possible to place PMTs. Scintillation light was transported by optical fiber cable (Eska CK-40) to the photocathode of the 1 inchϕ PMT (Hamamatsu H6524-01), which was placed outside of the magnetic field. Fig. 2.7 shows a cross section view of STB Tagger1.

Coincidence of TagF and TagB was required to ensure that the trajectory of recoil electron was reasonable. Energy of incident photon is presented by Eq. (2.5).

$$E_\gamma = E_e - E'_e - E_{recoil}, \tag{2.5}$$

where
E_γ: energy of a tagged photon,
E_e : energy of circulating electron in the STB ring,
E'_e: energy of scattered electron measured by the tagger,
E_{recoil}: energy of recoil carbon nucleus.
Since mass of a carbon nucleus is much larger than mass of an electron, E_{recoil} is extremely small. Therefore, Eq. (2.5) can be approximated with Eq. (2.6).

$$E_\gamma = E_e - E'_e \tag{2.6}$$

Energy calibration was performed via the $\gamma d \to \pi^- pp$ reaction in 2010 [YC+10]. Systematic uncertainty was estimated to be ~10 MeV.

2.3.3 Sweep Magnet

A pentagonal shaped dipole magnet named sweep magnet was placed between a beam pipe flange and a target. The beam pipe flange is 1 mm thickness aluminum plate. A collimator which was composed of five lead blocks (50 mm thickness for each) were placed upstream of the sweep magnet to eliminate the beam halo. The aperture of the collimator was ϕ10 mm. The

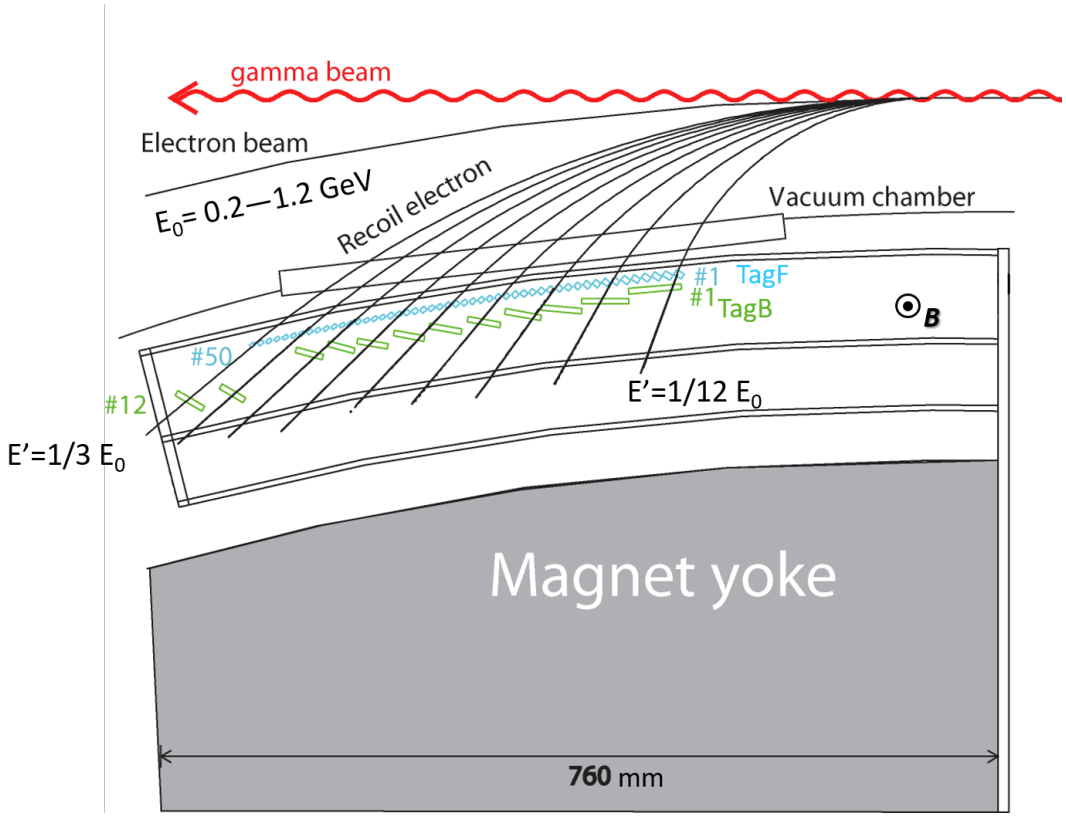

FIGURE 2.5: Schematics of STB Tagger I [Yam+05]. The orbits of the primary electron beam with an energy of E_0 and recoil electrons in BM4 are shown. The orbits of the recoil electrons are displayed with the energies from $1/12E_0$ to $1/3E_0$ with $1/24E_0$ step. The STB ring was operated with $E_0 = 1.2$ GeV mode in this experiment.

sweep magnet was used to remove the e^+e^- background that is produced in large quantities at the collimator or the beam flange. Maximum magnetic field is about 1.1 T at 300 A operation. $\int Bdl$ along the central ray is about 0.5 T·m. Fig. 2.8 shows a schematic top view of the sweep magnet and electron trajectories with several momenta. As shown in Fig. 2.8, higher energy electrons cannot be swept perfectly. Therefore, veto counters were installed to reject such background events (see Sec. 2.4.7 for detail).

2.3.4 Beam Profile Monitor (BPM)

Beam profile monitor is a scintillation fiber counter which provides a two dimensional beam profile. 8 diced scintillation fibers (3×3 mm^2) are lined up in each direction, horizontally and vertically and read out by multi-anode PMT (H6568-10). BPM combined with two trigger counters (Trigger PS1, 2), an aluminum converter, and a veto counter (Charge PS) as shown in Fig. 2.9. When a positron-electron pair was produced by the aluminum converter, a data taking trigger was made. Signals of charged particles that were generated upstream were eliminated by the veto counter since the distributions would be spread wider than the beam diameter . BPM was monitored to check the beam position on the target was proper.

2.3.5 Lead Glass Cherenkov Counter

A lead glass counter is placed at the most downstream of the photon beam line (9.5 m downstream of the target). The lead glass counter was only used on purpose of calibration

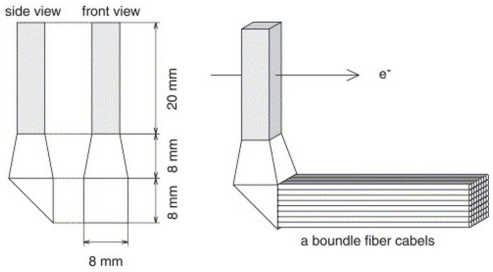

FIGURE 2.6: A schematic view of a scintillator of TagF [Yam+05]. Scintillation photons are transported to a photo-cathode of PMT via the optical fibers.

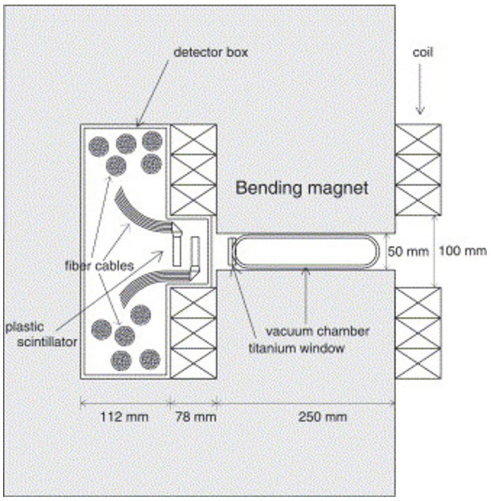

FIGURE 2.7: Cross section view of STB Tagger1 [Yam+05].

of number of incident photons with a faint beam. The crystal is made of an optical glass SF5 with a size of $15 \times 15 \times 30\,\mathrm{cm}^3$. SF5 consists of $PbO : SiO_2$ with a refractive index of 1.67. 5 inch PMT (HAMAMATSU R1250) was used as a photon sensor. The crystal is large enough to cover the beam spread in yz direction, and thick enough to stop showers created highest energy tagged photons (~1.1 GeV). During production runs, the lead glass counter was put at ~0.5 m below the beam center and turned off high voltage because of its poor rate tolerance.

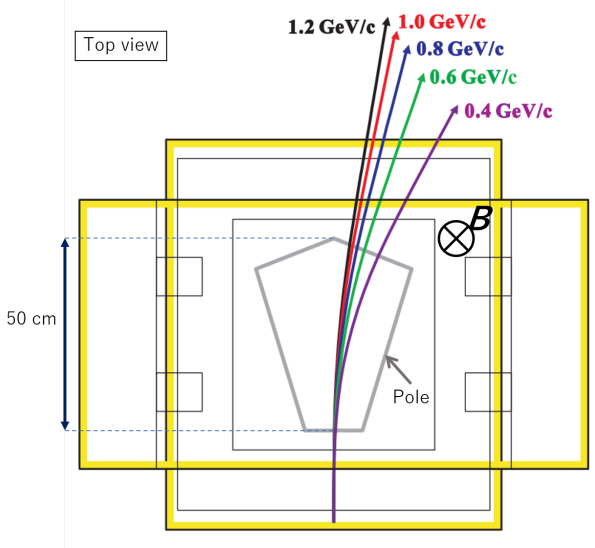

FIGURE 2.8: Schematics of the sweep magnet. Trajectories of electrons with several momentum values are shown.

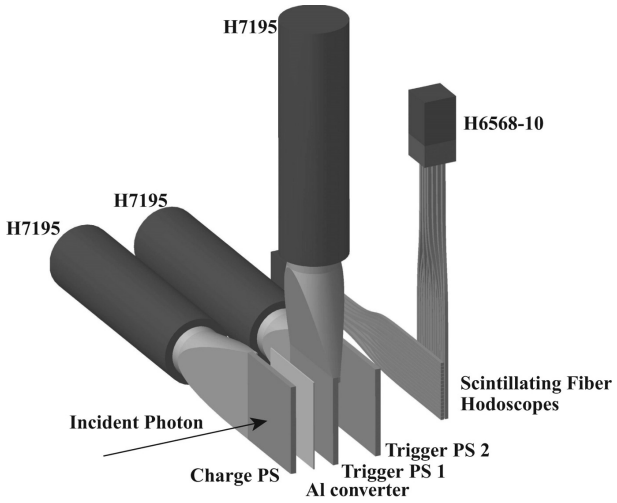

FIGURE 2.9: Schematic of BPM [Ish+10]. 8 diced scintillation fibers ($3 \times 3\,\mathrm{mm}^2$) are lined up in each direction, horizontally and vertically and read out by multi-anode PMT (H6568-10). BPM combined with two trigger counters (Trigger PS1, 2), an aluminum converter,and a veto counter (Charge PS).

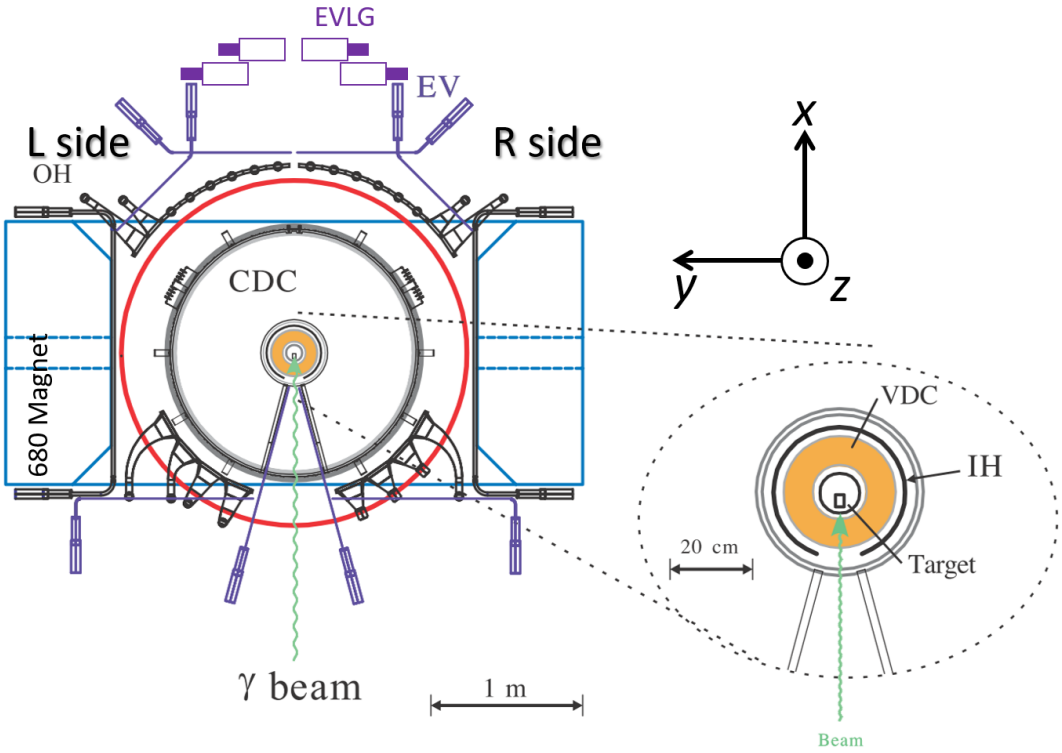

FIGURE 2.10: Schematic view of NKS2. The NKS2 system consists of a dipole magnet, 2 drift chambers (VDC and CDC) for momentum analysis, 2 layers of plastic scintillator hodoscopes (IH and OH) for Time of Flight (ToF) measurement, and additional plastic scintillator bars (EV) to reject background e^+e^- events.

2.4 Neutral Kaon Spectrometer2 (NKS2)

Apparatus of NKS2 system is described in this section. NKS2 is a magnetic spectrometer installed at the second experimental hall at ELPH in 2004. NKS2 has a large solid angle (~25% for a single particle), capability of multi-track analysis.

Originally, a tracking system of NKS2 consisted of straw drift chamber (SDC) and cylindrical drift chamber (CDC). The lack of vertical position information from SDC resulted the poor vertex position resolution. In 2009, a vertex drift chamber (VDC) was installed in stead of SDC. Inner hodoscopes (IH) were also replaced simultaneously. This upgrade improved the resolution of the decay point by about a factor of two. In addition, the detection efficiency of weak decay events of hyperons and K^0 mesons was improved because the position of the ToF start counter (IH) was moved away from the target. In this thesis, the hole setup of a dipole magnet (680 magnet), a tracking system (VDC+CDC), and trigger counters is just called as NKS2[2].

When viewed from upstream of the beam, the left side is called the L side and the right side is called the R side as shown in Fig. 2.10. Apparatus of NKS2 is described in order of inside to outside in this section.

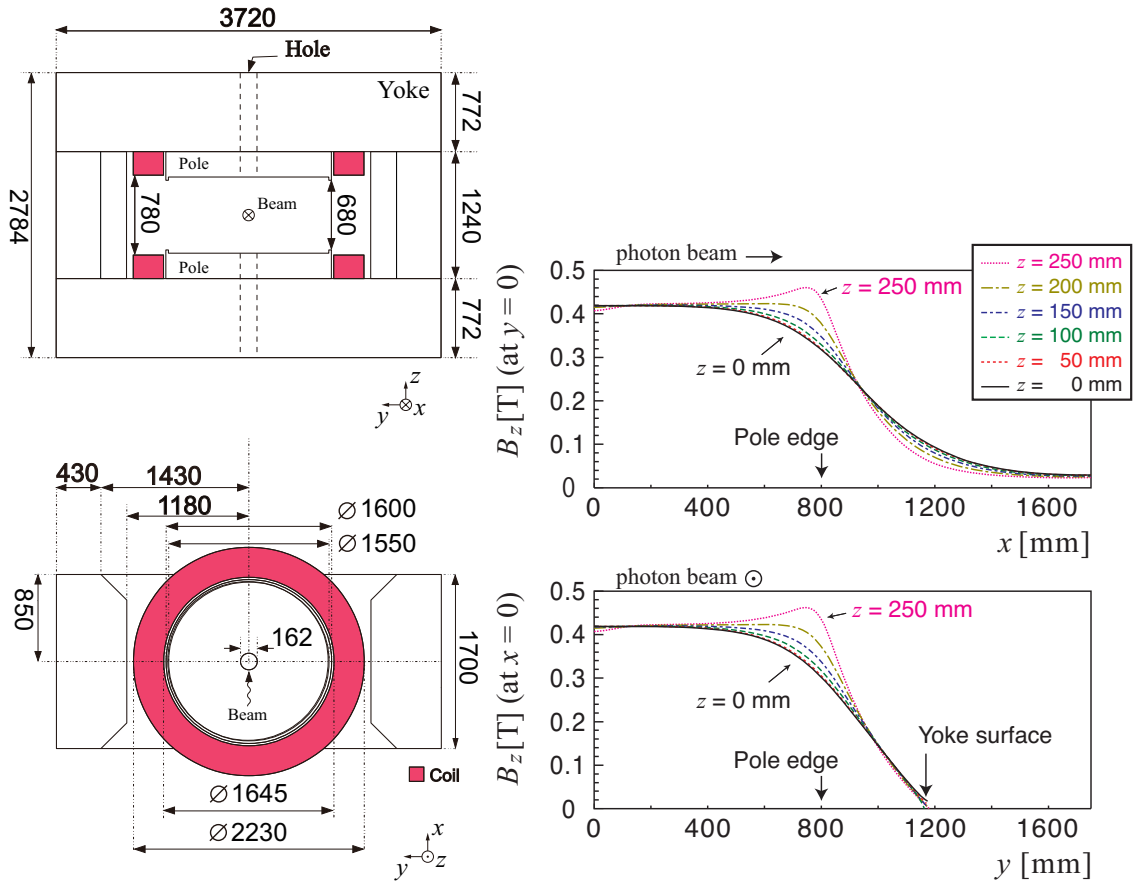

(A) Schematic view of the 680 magnet.

(B) The magnetic field of the 680 magnet.

FIGURE 2.11: Schematic view and a field of the 680 magnet [Kan+18]. (A)Schematic view. The top figure shows a slice along vertical (horizontal) direction. The bottom figure shows a slice along horizontal direction. The unit is mm. (B)Magnetic field calculated by using 3D finite element method (OPERA-3d/TOSCA) [ST80].

2.4.1 680 Magnet

The 680 magnet is a resistive dipole magnet which was originally used as a cyclotron magnet at Cyclotron Radio Isotope Center, Tohoku University. Modifications were made to increase the gap size when it was installed in ELPH. The gap size was determined 680 mm by combining the acceptance as large as possible while keeping strength of the magnetic field to achieve a sufficient momentum resolution. The detail geometrical information is shown in Fig. 2.11(A). The name “680” comes from its gap size.
Its magnetic field map was constructed using 3D finite element method (OPERA-3d/TOSCA) [ST80]. The magnetic field distribution is shown in Fig. 2.11(B). The maximum magnetic field strength is 0.42 T at 1000 A.
There are two holes of 162 mm ϕ at the center of the top and bottom of the yoke in order to insert the target.

[2]This system is defined as "NKS2+" in [Bec13]. The setup with SDC is called "NKS2-".

2.4.2 Target System

A liquid target is preferable to a gaseous target because the available space for a target installation is limited, and a liquid target have higher density and more target nuclei in the same thickness for efficient data collection. The target system of NKS2 was designed to be moved in and out through a hole on the top of the 680 magnet. Schematic view of the target system is shown in Fig. 2.12. The inside of the target cryostat was pumped by a turbo-molecular pump, Leibold Turbovac 151 to keep the pressure $\sim 10^{-5}$ Pa during the experiment. Due to the structure of inserting the target through the hole in the 680 magnet, the diameter of the part less than ~1 m from the target cell must be within 120ϕ mm. Therefore, the target cryostat is composed of a thick part ($300\phi \times 300L$ mm) and a thin part ($100\phi \times 1500L$ mm). Thick part of the target cryostat (300ϕ mm) has a two-staged Gifford–McMahon refrigerator Sumitomo Heavy Industries (SHI) RD-208B inside. An oxygen-free copper rod for electric heating was attached to the second stage of the refrigerator to extend the cooling section to the target cell vicinity. The copper rod is covered with a radiation shield made of aluminum alloy to prevent heat inflow due to thermal radiation. The first stage of the refrigerator was used to cool not only the target but also the thermal shield since cooling power of the first stage was stronger than that of the second stage. The deuterium (hydrogen) was liquefied at the condenser located below the copper rod and dropped into the target cell.

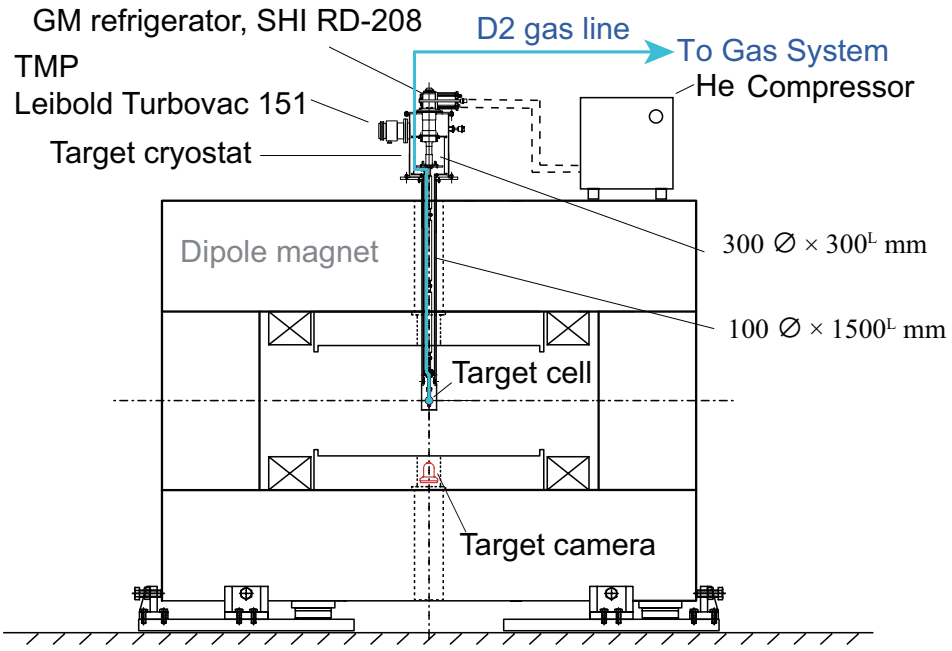

FIGURE 2.12: Schematic view of the target system [Kan+18].

Target Cell

A target cell is placed inside of the cylindrical vacuum chamber which is made of 1.5-mm-thick aluminum.

Shape of a target cell is shown in Fig. 2.13. The shell of the cell is made of 1 mm thickness aluminum except for the beam window. The beam windows are made of 75 μm thickness polymide films (Ube Industries, ltd., UPILEX-S) to reduce the amount of material. The diameter of the beam windows was designed to be 40 mm. The target cell pressure and absolute pressure were remotely monitored to obtain the number of target nuclei during the

experimental term because of the inaccessibility of the experimental hall. The target thickness was designed to be 2.97 cm.

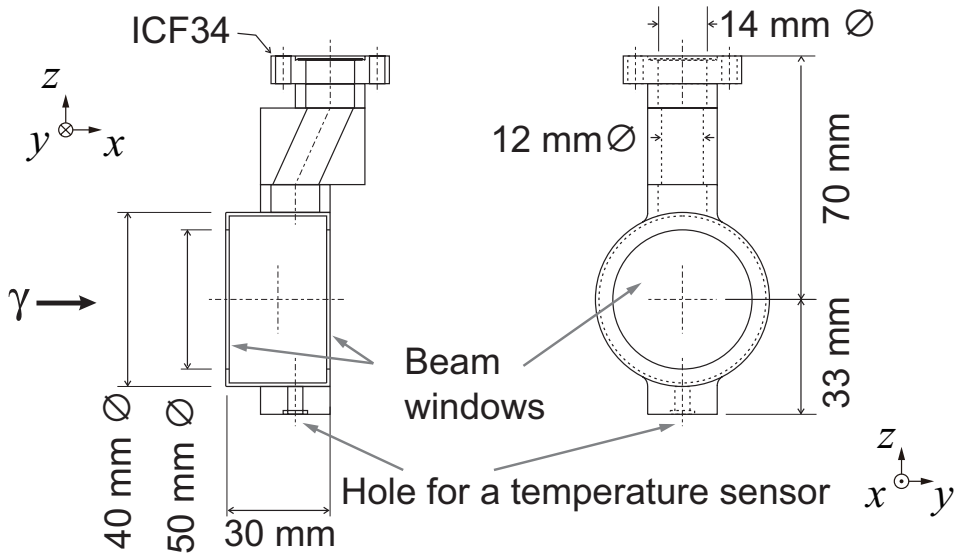

FIGURE 2.13: Schematic view of the target cell [Kan+18].

TABLE 2.1: VDC specification

Drift gas	Ar + C_2H_6 (50:50)
Gas pressure	1 atm
Body material	Aluminum alloy (JIS A5052)
Pillar material	0.5 mm thick CFRP
Body size	110-330 mm $\phi \times 506^H$ mm
Num. of layers	8 (all stereo layers)
Stereo angle of sense wiere	6.18–10.83°
Sense wire	20 μm ϕ Au plated W (Re doped)
Field and shield wire	100 μm ϕ Au plated Cu-Be
Wire tension	0.39 N (sense)
	0.78 N (field and shield)
Cell shape	Trapezoid
Half-cell size	4 mm
Operation voltage	-2.1 kV (field) and -1.4 kV (shield)

TABLE 2.2: VDC wire geometry.

Group number	Layer number	Half-cell size radial [mm]	Half-cell size azimuthal [mm]	Stereo angle [deg]	Radius [mm]	Num. of sense wires
1	1 (U)	4	3.89	6.18	73	59
	2 (U')	4	4.31	6.85	81	59
2	3 (V)	4	3.88	-7.52	89	72
	4 (V')	4	4.23	-8.19	97	72
3	5 (U)	4	3.88	8.85	105	85
	6 (U')	4	4.18	9.52	113	85
4	7 (V)	4	3.92	-10.18	121	97
	8 (V')	4	4.18	-10.83	129	97
					Total	626

2.4.3 Vertex Drift Chamber (VDC)

Vertex drift chamber (VDC) was newly developed and installed in 2009 instead of SDC in order to improve the vertex position resolution. Schematic view of VDC is shown in Fig. 2.14. The outer (inner) diameter of VDC is 330 (110) mm with a height of 506 mm. It consists 626 sense wires, 2072 field wires, and 312 shield wires. All of the wires of VDC are stereo wires. VDC improved vertex position resolution about factor two comparing the analysis with a configuration of CDC only. Its cell shape is trapezoid as shown in Fig. 2.15. General specification of VDC are summarized in Tab. 2.1. Layer configuration of VDC is U, U', V, V', U, U', V, V' (8 layers). Geometry of VDC wire is summarized in Tab. 2.2. Stereo angle is defined as the angle with respect to the gravity direction. Radius is defined at the end cap. Common readout electronics were used for VDC and CDC and explained in Sec. 2.4.5.

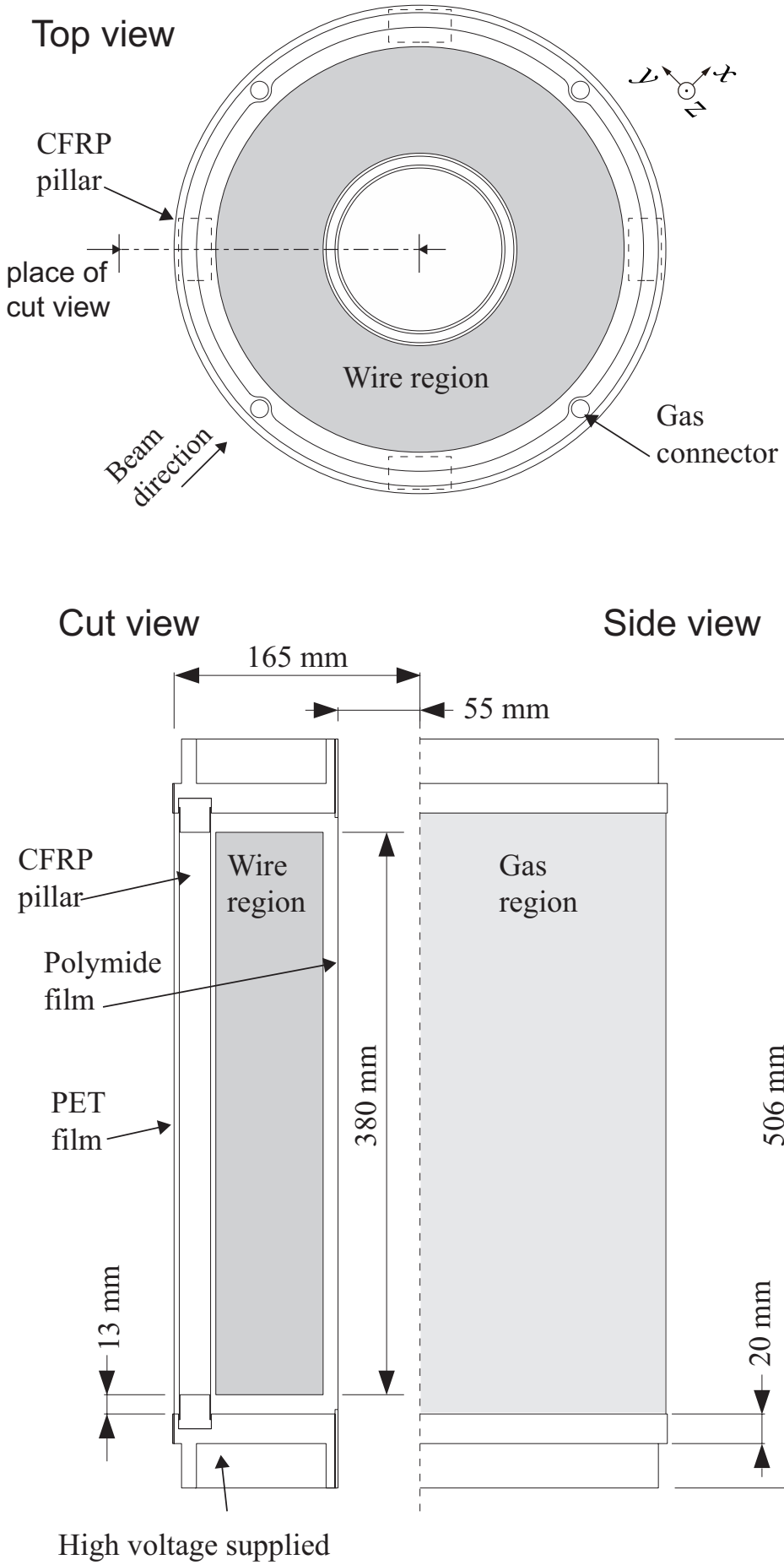

FIGURE 2.14: Schematic view of VDC [Kan+18]. Upper figure shows top view. Bottom figure shows cut view in vertical direction.

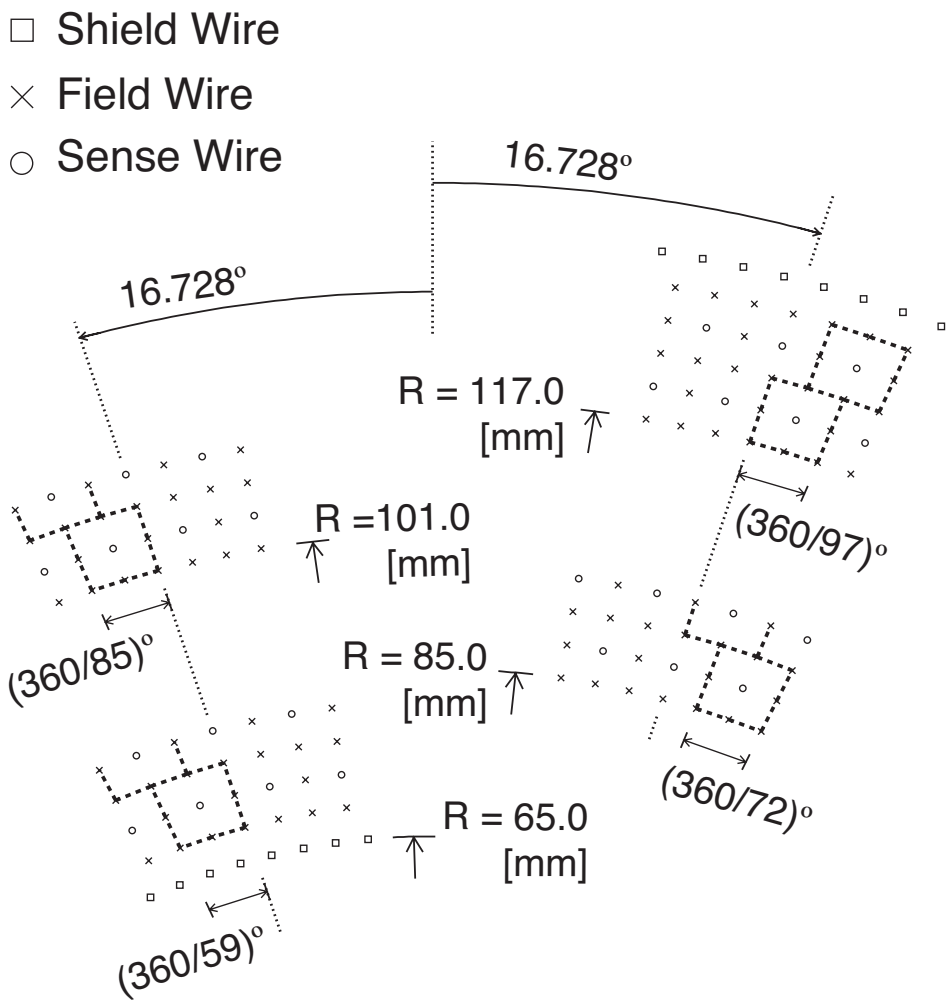

FIGURE 2.15: Cell structure of VDC [Kan+18]. Its cell shape is trapezoid. It consists 626 sense wires, 2072 field wires, and 312 shield wires. Squares, crosses, and circles show shield wires, field wires, and sense wires, respectively. All wires are stereo wires.

TABLE 2.3: IH geometry.

Segment Num.	Angle coverage	Dimensions	Radius
IH	[deg]	[cm]	[cm]
IH1	±(−4–4)	$16.5^H \times 2.54^W \times 0.5^T$	18.3
IH2	±(4–10)	$38.0^H \times 2.47^W \times 0.5^T$	18.3
IH3	±(10–18)	$38.0^H \times 3.74^W \times 0.5^T$	18.3
IH4	±(18–30)	$38.0^H \times 7.53^W \times 0.5^T$	18.3
IH5	±(30–54)	$38.0^H \times 7.53^W \times 0.5^T$	18.3
IH6	±(54–78)	$38.0^H \times 7.53^W \times 0.5^T$	18.3
IH7	±(78–102)	$38.0^H \times 7.53^W \times 0.5^T$	18.3
IH8	±(102–126)	$38.0^H \times 7.53^W \times 0.5^T$	18.3
IH9	±(126–144)	$38.0^H \times 5.64^W \times 0.5^T$	18.3
IH10	±(144–162)	$38.0^H \times 5.64^W \times 0.5^T$	18.3

2.4.4 Inner Hodoscopes (IH)

IH was used as start counters of ToF measurement and time reference of the event trigger. The energy loss information in the scintillators is collected and used for particle identification. Geometrical specification of IH is shown in Tab. 2.3. Each segment of IH was arranged to enclose VDC. Schematic views and a picture of constructed IH are shown in Fig. 2.16. Since it was operated in a magnetic field of 0.42 T, a fine-mesh type PMT (HAMAMATSU H6152-01B) was used. IH2–IH10 at the left and right side were both side readout counters to achieve better time resolution. Since IH1 was located on photon beam line, it was divided into upper and lower sections so that no material is placed ±25 mm from the beam plane. The height of scintillator was designed to cover full acceptance VDC. The width of the scintillators was designed so that the singles rate of each segment would be less than 200 kHz. Therefore, the width of scintillators of forward counters were narrower than backward counters. Aluminized mylar was used as the reflective material for the scintillator part, and 25 μm thick Teflon tape was used for the light guide part. The entire detector was covered with black tape to shade the light.

2.4.5 Cylindrical Drift Chamber (CDC)

CDC is a honeycomb cell structure drift chamber consists 10 layers (X, X', U, U', X, X', V, V', X, X') with 160 cm total diameter and 63 cm height. Schematic top view of CDC is shown in Fig. 2.17. The layer number of CDC was defined by the serial number from VDC. Two layers each make up a layer group consisting of the same type of layers. e.g. layer group1 consists layer9 and layer10 (XX'). The axial wires (X and X') are aligned parallel to the gravity direction. Stereo angle of stereo wires (U, U', V, and V') is defined as the angle with respect to the gravity direction. CDC consists aluminum end-plates, a CFRP cylinder, and an aluminum alloy support frame.

Readout Electronics

Readout electronics were the same for VDC and CDC. A signal from a sense wire was discriminated by a GNA-220 read-out card put a space between CDC (VDC) and a top pole of the 680 magnet. The GNA-220 has 32 channel analog inputs and digital outputs with Amplifier-shaper-discriminator (ASD) cards (SONY CXA3183Q chip)[3]. LVDS signals from

[3]The ASD chip also have analog outputs, but it was not used in our setup.

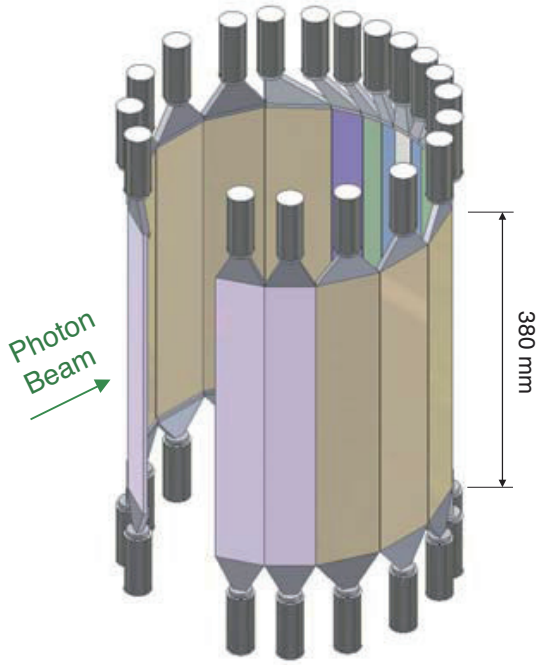

(A) 3D schematic view of IH

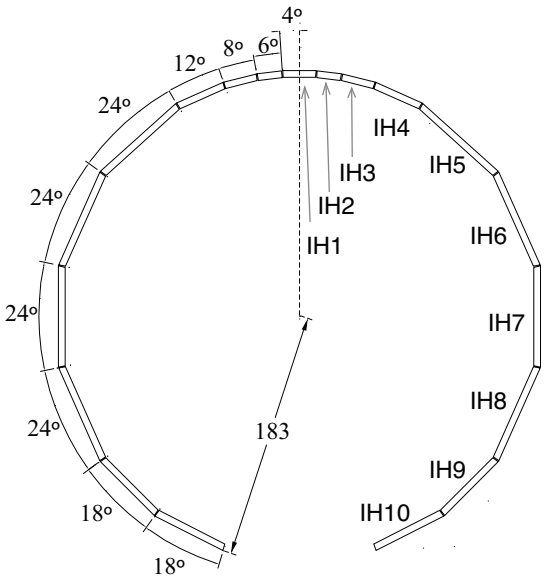

(B) Cross section of the scintillators of IH in xy space

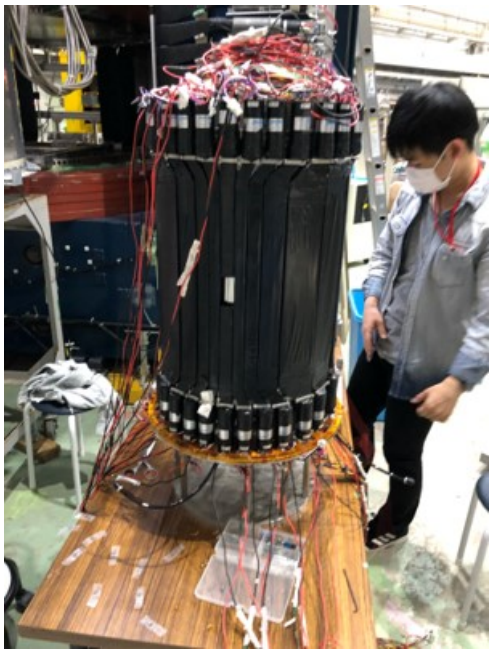

(C) Picture of IH from downstream side.

FIGURE 2.16: Schematic view of IH (A) 3D (B)2D [Kan+18]. (C)A picture of IH combined with VDC taken from the downstream side.

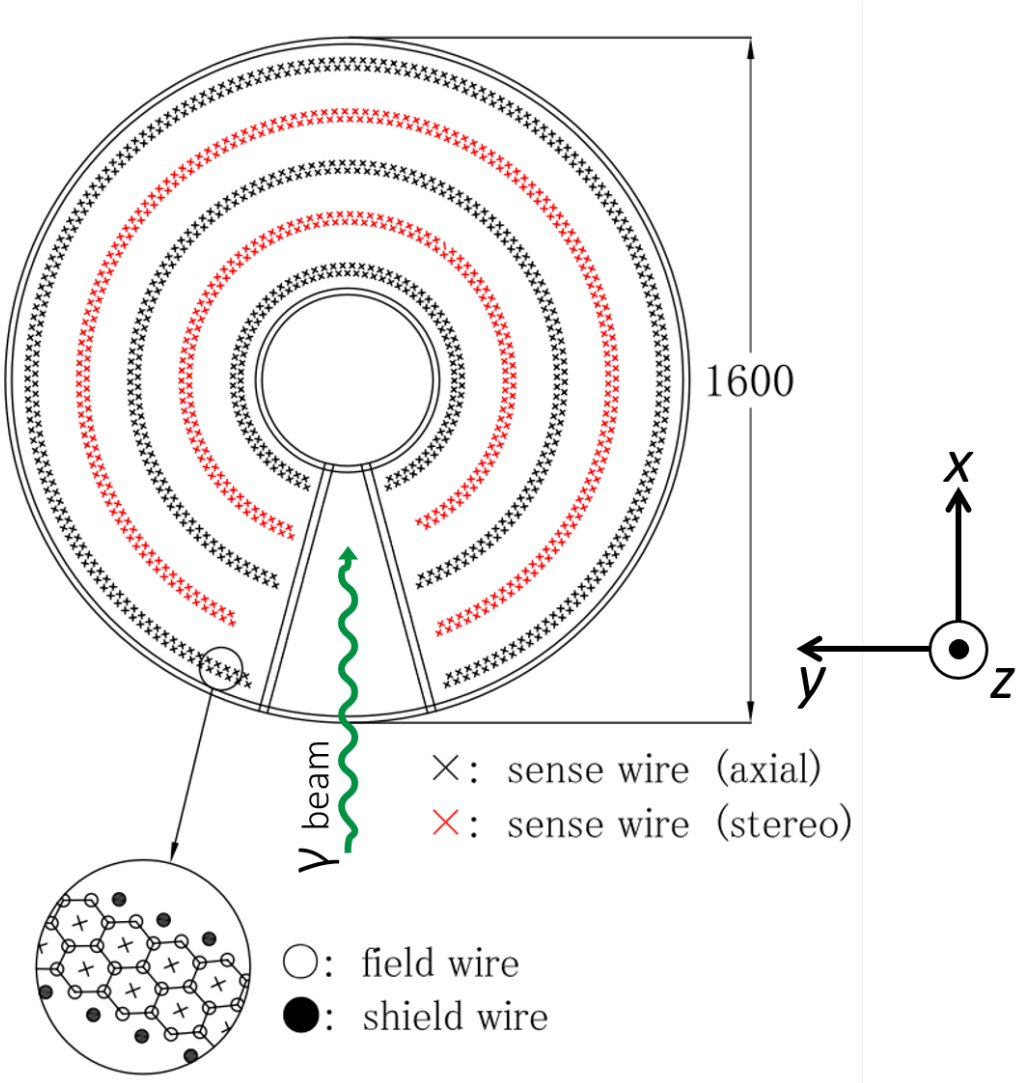

FIGURE 2.17: Schematic view of CDC. CDC consists 10 layers (6 axial wire layers, 4 stereo wire layers). Axial wires and stereo wires are shown as black and red crosses, respectively.

TABLE 2.4: CDC specification

Drift gas	Ar + C_2H_6 (50:50)
Gas pressure	1 atm
Body material	Aluminum alloy (JIS A5052)
Support cylinder material	0.5 mm thick CFRP
Body size	400–1600 mm $\phi \times 630^H$ mm
Num. of layers	10 (6 axial and 4 stereo layers)
Stereo angle	6.44–6.87°
Sense wire	20 μm ϕ Au plated W (Re doped)
Field and shield wire	100 μm ϕ Au plated Cu-Be
Wire tension	0.49 N (sense)
	0.78 N (field and shield)
Cell shape	Hexagon
Half-cell size	12 mm
Operation voltage	-2.8 kV (field) and -1.4 kV (shield)

TABLE 2.5: CDC geometry.

Group number	Layer number	Cell size [mm]	Stereo angle [deg]	Radius [mm]	Num. of sense wires
1	9 (X)	10.36	0	250	68
	10 (X')	11.1	0	268	67
2	11 (U)	10.36	6.216	370	89
	12 (U')	11.1	6.519	388	90
3	13 (X)	10.36	0	490	119
	14 (X')	11.1	0	508	120
4	15 (V)	10.36	-6.442	610	143
	16 (V')	12.05	-6.632	628	144
5	17 (X)	11.78	0	730	175
	18 (X')	12.07	0	748	176
				Total	1191

the ASD cards were transported to multi-hit TDC modules, ATLAS Muon TDC (AMT) module with a resolution of 0.78 ns/ch. The AMT modules placed beside the 680 magnet have 128 ch per modules.

2.4.6 Outer Hodoscopes (OH)

OH is a plastic scintillation counter which is used as a stop counter of ToF measurement. And OH was also used a part of the trigger system (See Sec. 2.5.1 for detail). OH consists of vertically mounted scintillators (OHV) and horizontally mounted scintillators (OHH). OHV, OHH has 12, 9 segment for one side (left or right) respectively.

Orientation of OH is shown in Fig. 2.18. OHV1–8 was placed at downstream (forward direction) of the 680 magnet. Size of the scintillators was $74.8^H \times 7.53^W \times 2.0^T$ cm^3. OHV1–8 was not fixed on 680 magnet because they need to be uninstalled to access CDC, VDC, and IH. Figure 2.19 is a picture of OHV1–8 from upstream side before installation. OHV1–8 was handled by using a hand pallet truck when the installation. The reproducibility of the installation position was ensured by installing OHV1–8 along the aluminum rails on the hall floor. OHV9–12 was placed at upstream (backward direction) of 680 Magnet. Size of the

TABLE 2.6: OH geometry.

Segment Num. OHV	Angle coverage [deg]	Dimensions [cm]	Radius [cm]
OHV1	±(1.4–8.6)	$74.8^H \times 15.0^W \times 2.0^T$	121
OHV2	±(8.6–15.8)	$74.8^H \times 15.0^W \times 2.0^T$	121
OHV3	±(15.8–23.0)	$74.8^H \times 15.0^W \times 2.0^T$	121
OHV4	±(23.0–30.2)	$74.8^H \times 15.0^W \times 2.0^T$	121
OHV5	±(30.2–37.4)	$74.8^H \times 15.0^W \times 2.0^T$	121
OHV6	±(37.4–44.6)	$74.8^H \times 15.0^W \times 2.0^T$	121
OHV7	±(44.6–51.8)	$74.8^H \times 15.0^W \times 2.0^T$	121
OHV8	±(51.8–59.0)	$74.8^H \times 15.0^W \times 2.0^T$	121
OHV9	±(113.8–126.2)	$50.0^H \times 20.0^W \times 2.0^T$	93
OHV10	±(126.2–138.6)	$50.0^H \times 20.0^W \times 2.0^T$	93
OHV11	±(138.6–151.0)	$50.0^H \times 20.0^W \times 2.0^T$	93
OHV12	±(151.0–163.4)	$50.0^H \times 20.0^W \times 2.0^T$	93
OHH	x, y, z [cm]	Size [cm]	[cm]
OHH1	0., ±115.0, 30.25	$160.0^L \times 8.25^W \times 2.0^T$	121
OHH2	0., ±115.0, 22.25	$160.0^L \times 8.0^W \times 2.0^T$	121
OHH3	0., ±115.0, 14.25	$160.0^L \times 8.0^W \times 2.0^T$	121
OHH4	0., ±115.0, 6.25	$160.0^L \times 8.0^W \times 2.0^T$	121
OHH5	0., ±115.0, 0.00	$160.0^L \times 4.5^W \times 2.0^T$	121
OHH6	0., ±115.0, −6.25	$160.0^L \times 8.0^W \times 2.0^T$	121
OHH7	0., ±115.0, −14.25	$160.0^L \times 8.0^W \times 2.0^T$	121
OHH8	0., ±115.0, −22.25	$160.0^L \times 8.0^W \times 2.0^T$	121
OHH9	0., ±115.0, −30.25	$160.0^L \times 8.25^W \times 2.0^T$	121

scintillators was $50.0^H \times 20.0^W \times 2.0^T$ cm^3. OHH is horizontally aligned among the yoke of 680 Magnet. Most of the scintillators are $160.0^L \times 8.0^W \times 2.0^T$ cm^3 except for OHH1,5, and 9. The size of scintillators of OHH1, and 9 is $160.0^L \times 8.25^W \times 2.0^T$ cm^3. The scintillator of OHH5 is narrower than other scintillators ($160.0^L \times 4.5^W \times 2.0^T$ cm^3) because it is placed on the plane of the beam line and has higher counting rate. Geometry and specification of OH are summarized in Tab. 2.6.

Light guides made of acrylic were attached to the scintillators and PMTs to transport scintillation lights to photo-cathodes of PMTs. Two PMTs were attached to each scintillator, and in the OHV (OHH), the one attached to the upper (upstream) side is called Top PMT and the lower (downstream) side is called Bottom PMT. The PMTs except for OHVR10–OHVR12 were on the surface of the magnet yoke to avoid a strong magnetic field region. The PMTs for OHVR10–OHVR12 could not be placed same as others because there were the power supply and cooling water lines for the magnet. These PMTs had to be placed in the magnetic field. Therefore, 2-in. fine mesh dynode type PMT (HAMAMATSU Photonics R5924-700) were used for those segments. For the other segments, 2 in. PMTs (HAMAMATSU Photonics, H1161 or H7195) were used. The method of light shielding of OH was the same as for IH as described in Sec. 2.4.4.

2.4.7 Electron Veto Counters (EV)

The largest background event in this experiment was electron-positron pair production. This was characteristic of experiments using high-energy photon beams. Since e^+e^- pairs were emitted very far forward, many events were concentrated on the beam plane in the NKS2

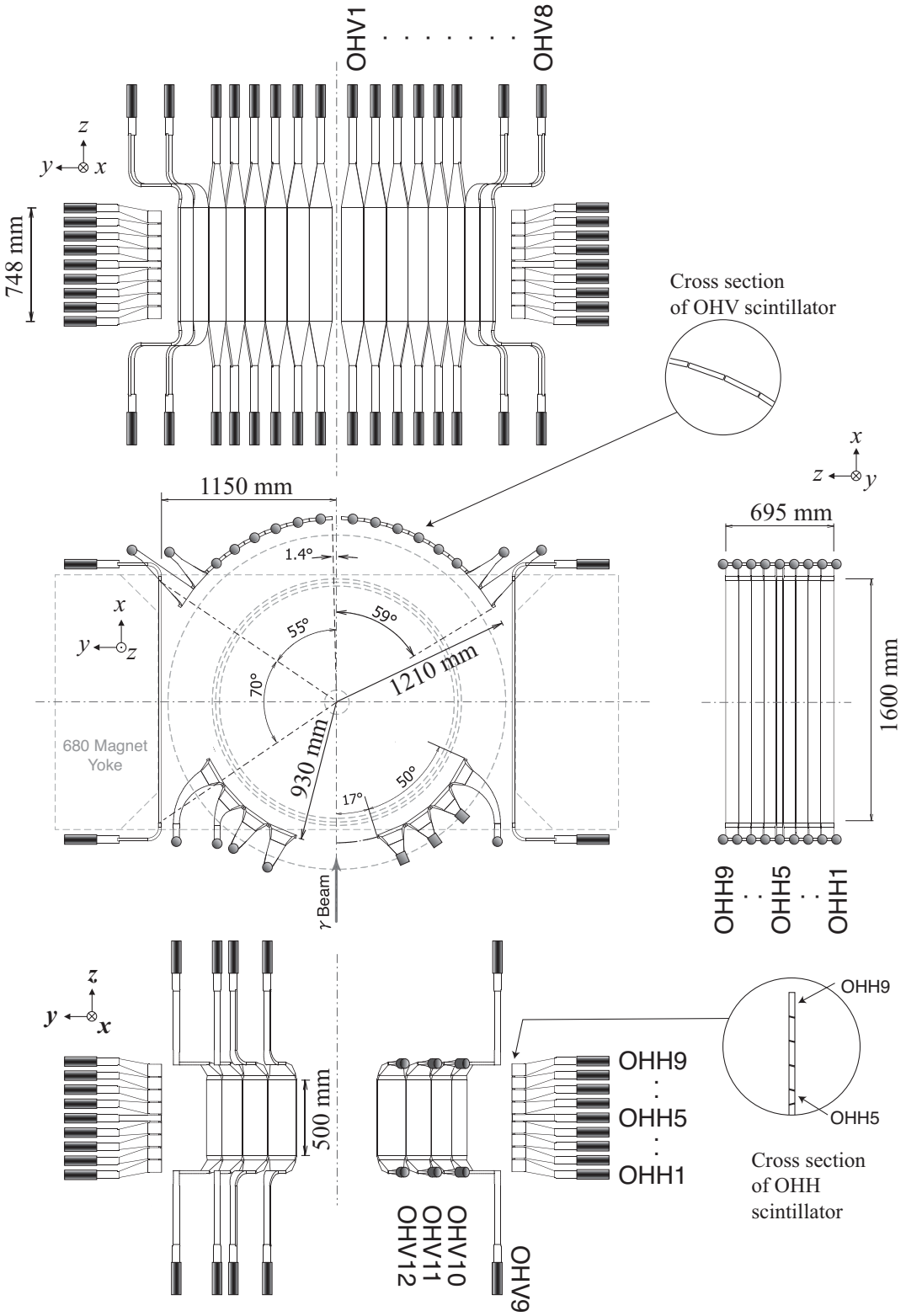

FIGURE 2.18: Schematic view of OH. OH counters were separated left and right arms (left/right was defined as seeing from upstream of the beam line). OHV was arranged vertically (a) in downstream of the target (OHV1–8) and (b) in the upstream (OHV9–12). OHH1–9 was installed at the position of the symmetry to the $y - z$ plane. [Kan+18]

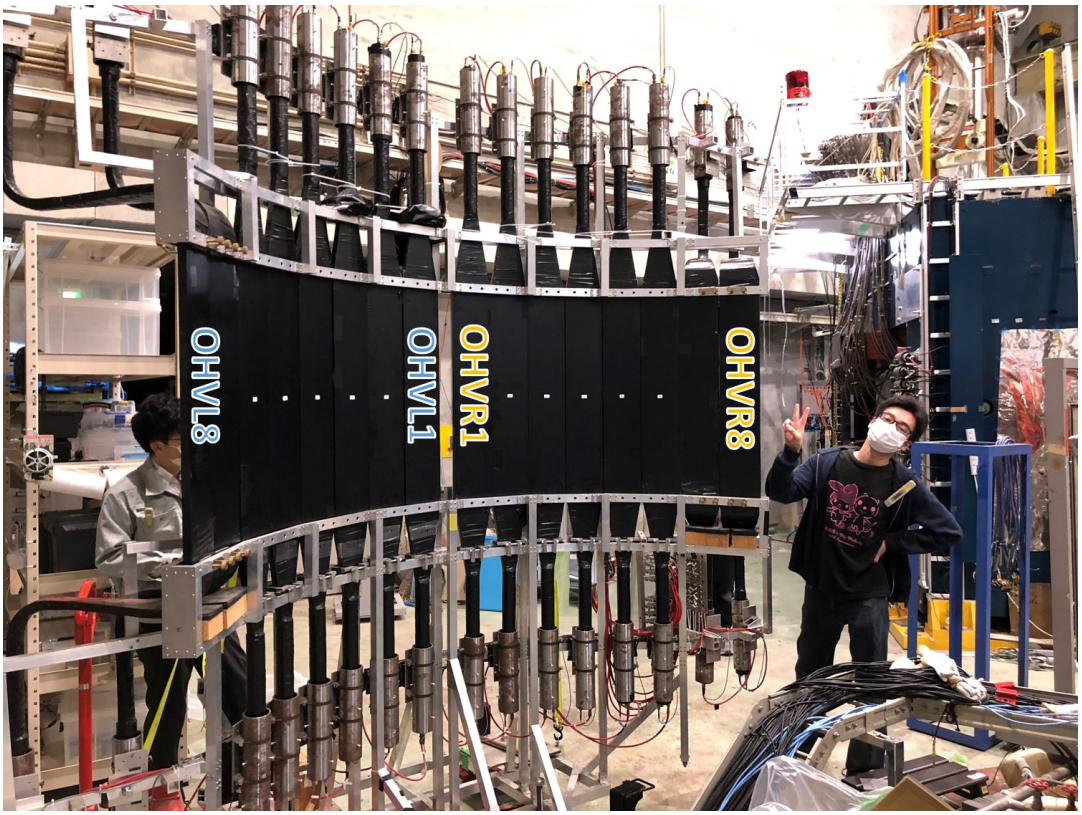

FIGURE 2.19: A picture of OHV1–8 taken from upstream side before installation. OHV1–8 was moved using a hand pallet truck and installed in NKS2 system. The reproducibility of the installation position was ensured by installing OHV1–8 along the aluminum rails on the hall floor.

experiment where a vertical magnetic field was applied. To reduce such background, two types of Electron veto (EV) counters were installed.

Electron Veto Scintillation Counters (EVS)

Plastic scintillator counters named EVS was used. EV1, 2 were placed at downstream of NKS2 to reject e^+e^- that was produced at the target. EV3, 4 were placed at upstream of NKS2 to reject e^+e^- that was produced upstream of NKS2 and was not perfectly swept by the sweep magnet. Only upstream EVS (EV3, 4) joined trigger logic (See Sec. 2.5.1 for detail) because downstream EVS (EV1, 2) might make a bias in kinematics.

Electron Veto Lead Glass Counters (EVLG)

Electron Veto Lead Glass counters were placed downstream at beam plane. Since the incident electron (positron) signal is larger than that of hadrons, the background event of e^+e^- can be eliminated by setting the threshold appropriately. EVLG was placed behind of downstream of OHV1–8 at 15 mm higher than beam height. The size of the clystal is $15^H \times 30^L \times 15^T$ cm^3.

2.5 Trigger Logic and Data Acquisition System (DAQ)

2.5.1 Trigger Logic

For efficient data acquisition, a trigger signal was generated using logic signals of the tagger, IH, OH and EV.
The trigger for production run is shown as Equation 2.7

$$\text{Normal Trigger} = (\text{nIH} \geq 2) \otimes (\text{nOH} \geq 2) \otimes \text{Tag} \otimes \overline{\text{EV}} \tag{2.7}$$

$$\text{Tag} = \text{TagB} \otimes \text{TagF} \tag{2.8}$$

$$\text{EV} = \text{EVS3} \oplus \text{EVS4} \oplus \text{EVLG} \tag{2.9}$$

The tagger trigger signal was the logical sum of the coincidence signals of a TagB and the corresponding TagFs (see Fig. 2.20).
Multiplicity signals of IH and OH were managed by FPGA modules named Tohoku Universal Logic module (TUL-8040). As the name suggests, TUL-8040 was developed by the Tohoku University group to reduce NIM modules and cables in a trigger circuit. TUL-8040 has 80 input (NIM 16 ch + ECL 64 ch) and 40 (NIM 8ch + ECL 32 ch) output channels. Mounted FPGA chip is a ALTERA APEX 20 series (EP20K300E) with 33 MHz internal clock. TUL-8040 was also used to make the mean time signals of a OH hit. Typical trigger rate was 1kHz at a tagger rate of 2.5 MHz[Kan+18]. Fig. 2.21 shows the trigger logic of IH, OH, and EV. Fig. 2.22 shows the trigger logic of NKS2.

2.5.2 DAQ System

Data was taken by 3 Personal Computers (PC). Unidaq on Linux based operating systems [Nom+94] was installed in each PC as DAQ software. Each machine was named K0Daq*i* (*i*=0, 1, 2). K0Daq0 and K0Daq1 managed data from drift chambers. K0Daq2 managed data from hodoscopes, taggers, and CAMAC scalers. Although the data triggers are common, in order to avoid event slips, 4-bit loop counters created in FPGA were recorded and event matched when it was analyzed. Typical DAQ efficiency was about 70% at a trigger rate of 2 kHz.

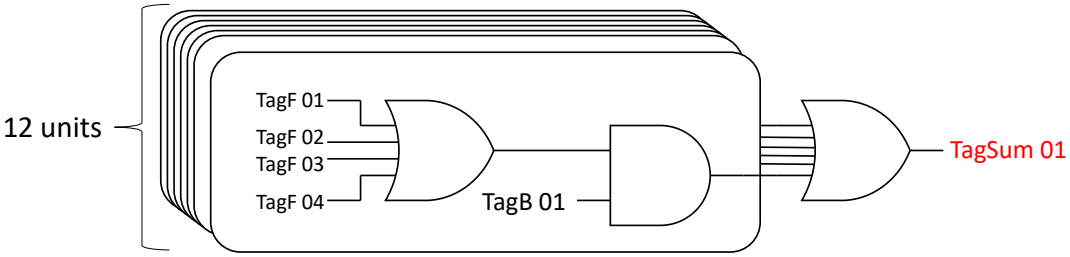

FIGURE 2.20: Trigger logic of Tagger.

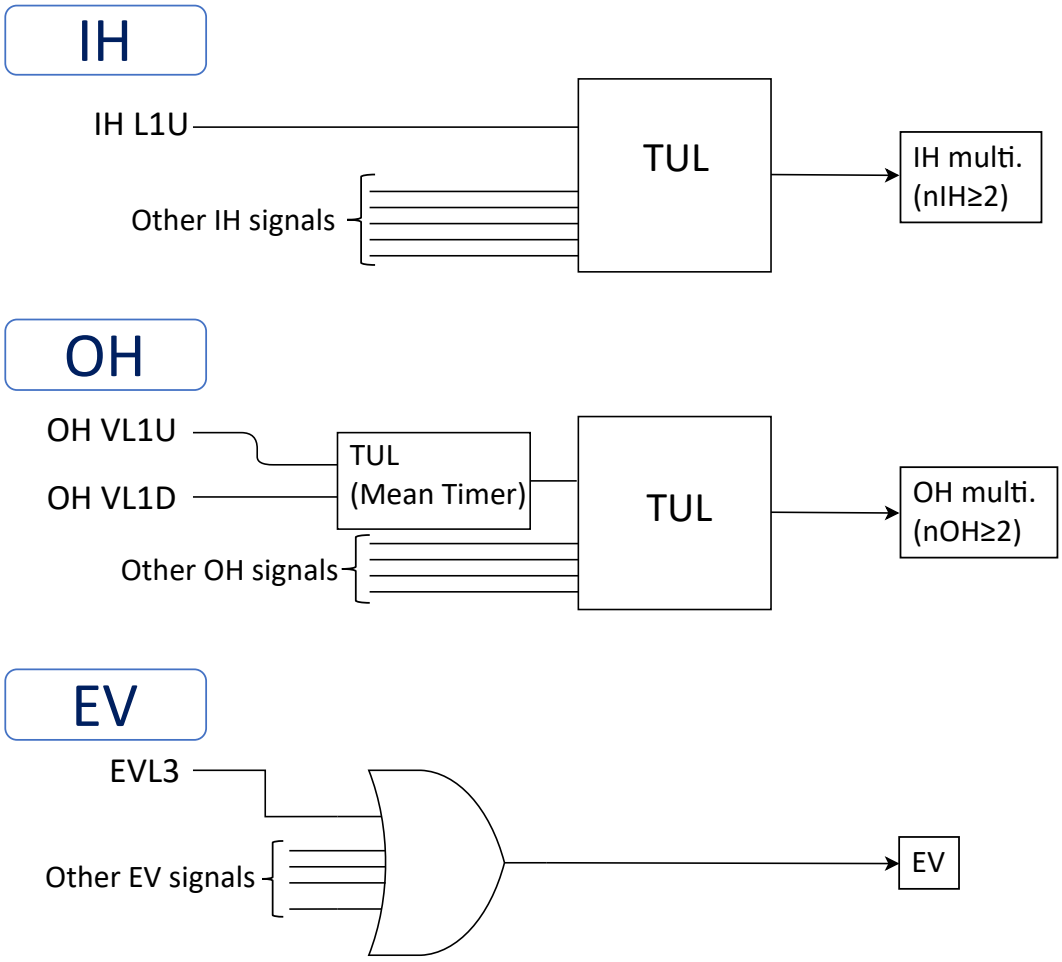

FIGURE 2.21: Trigger logic of IH, OH, and EV.

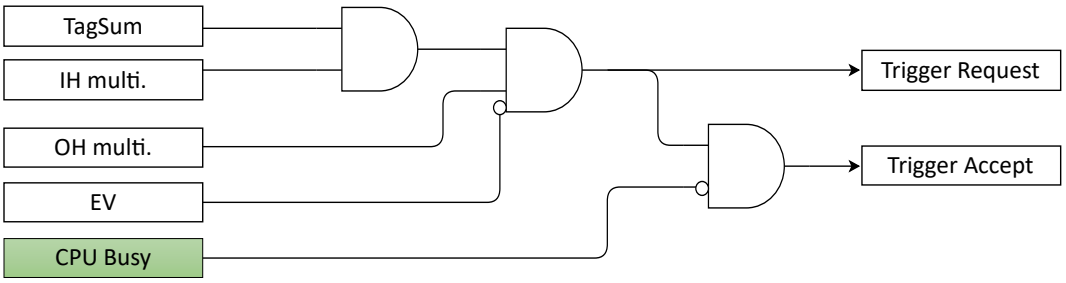

FIGURE 2.22: Trigger logic of NKS2.

3 Analysis

Analysis to obtain differential and total cross section of the $\gamma d \rightarrow d\pi^+\pi^-$ reaction will be described in this chapter. Firstly, overview of the analysis procedure will be introduced. Then, detail of the analysis in order of calibration and performance of detectors, $d\pi^+\pi^-$ event selection, cross section analysis.

3.1 Overview of the Analysis Procedure

The goal of this analysis is deriving the cross section of $\gamma d \rightarrow d\pi^+\pi^-$. In this chapter, the method of data analysis is presented, including the calibration method of the detectors. The general procedure for data analysis is shown in Fig. 3.1. The details of each procedure are as follows.

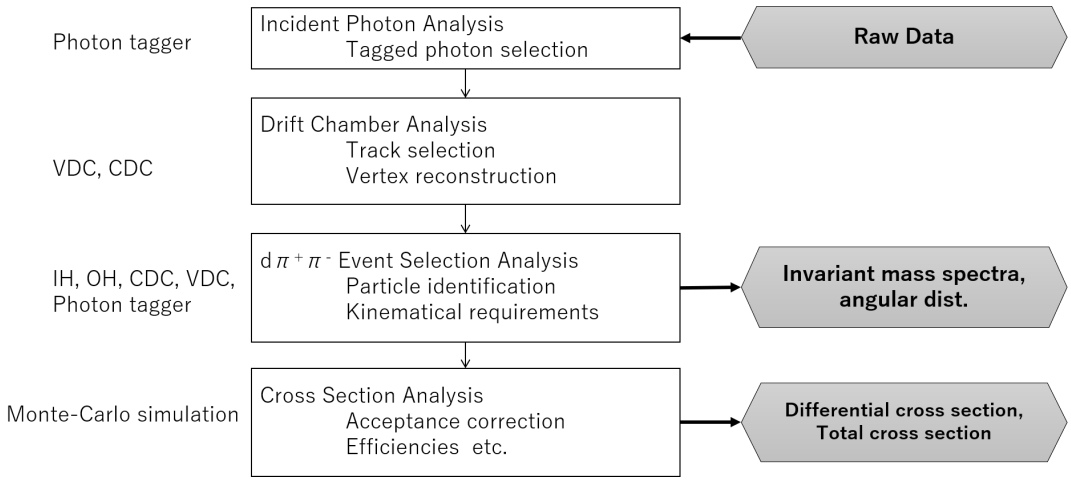

FIGURE 3.1: Analysis procedure. The analysis part is roughly divided into four parts: analysis of incident photons using a tagger, reconstruction of the trajectory using drift chambers, selection of the $d\pi^+\pi^-$ events, and derivation of the cross sections.

Incident Photon Analysis

It was necessary to clarify that the event contained one or more "tagged photons." "Tagged photon" means the real photon which energy and timing were identified. Energy and timing were determined by the combination of TagB and TagF hit patterns and TDC information. Specific event selection conditions are described in Sec. 3.4.1.

Drift Chamber Analysis

Drift chambers (VDC, CDC) were essential detectors for the measurement. Trajectories and vertices of charged particles were derived from wire hit patterns of DCs. See Sec. 3.3 for detail.

$d\pi^+\pi^-$ Event Selection Analysis

In this part, in addition to the event selection by particle identification, the selection by kinetic requirements was also performed.
Momentum, charge, and flight length information of the particle were derived by the DC analysis. Flight time was derived from timing information measured by IH and OH. Mass of the particle was calculated by combining these information. With the obtained mass, species of the charged particle was identified. See Sec. 3.4.2 for detail. Since this measurement was an exclusive measurement, the kinematic constraints of conservation of momentum and conservation of energy had to be met. We performed two different analyses named 2-track analysis and 3-track analysis. The 2-track (3-track) analysis was for events in which two (three) particles of $d\pi^+\pi^-$ in the final state, including deuteron, were detected by NKS2. The kinematical event selection method in this analysis is described in Sec. 3.4.6 and 3.4.7. Then the $\gamma d \rightarrow d\pi^+\pi^-$ events were extracted.

Cross Section Analysis

We derived total cross section of the $\gamma d \rightarrow d\pi^+\pi^-$ reaction and differential cross sections of invariant masses of $d\pi^+$, $d\pi^-$, and $\pi^+\pi^-$ and deuteron emission angle in the γd center of mass system to quantitatively interpret the obtained result. The total cross section is represented as,

$$\sigma_{CS} = \frac{N_{ev}}{N_{\mathrm{Target}} \cdot N_\gamma \cdot \eta_{acpt} \cdot \epsilon_{DAQ} \cdot \epsilon_{Ana}}, \tag{3.1}$$

where N_{ev} is the number of the event which was identified as the $\gamma d \rightarrow d\pi^+\pi^-$ reaction event, N_{Target} is the number of the target nuclei, ϵ_{DAQ} is the data acquisition efficiency, ϵ_{Ana} is the analysis efficiency. N_{Target} was estimated from the measured temperature and pressure of the target cell in Sec. 3.10. ϵ_{DAQ} was estimated from the scaler information in Sec. 3.9. ϵ_{Ana} was estimated in Sec. 3.4. η_{acpt} was estimated by a Monte-Carlo simulation based on GEANT4 frame work as described in Sec. 3.6 for detail.

3.2 Calibration and Performance of Detectors

Calibration methods and performance of detectors are described in this section.

3.2.1 Hodoscopes (IH, OH)

Two layers of hodoscopes which were composed of plastic scintillators and PMTs are mainly used for timing measurement. Time of flight between IH and OH was used to calculate velocity of charged particles. Output signals of IH and OH were discriminated and recored as timing information. Analog signal information was also recorded. It was converted to energy deposit in the plastic scintillators and used for pulse height correction and particle identification. TDC (Time to Digital Converter) and QDC (Charge to Digital Converter) CAEN modules V775 and V792 were used for digital and analog signal measurement, respectively.

Energy Deposit

Energy deposit in plastic scintillators (dE) were obtained from pulse charge information of PMTs of hodoscopes (Q). Firstly, the peak position of the pedestal (represents ground position of the signals) was adjusted to zero by introducing an offset parameter, Q_0. Then, a conversion factor C_Q was adjusted so that the energy loss of the minimum ionized particles (MIP) was

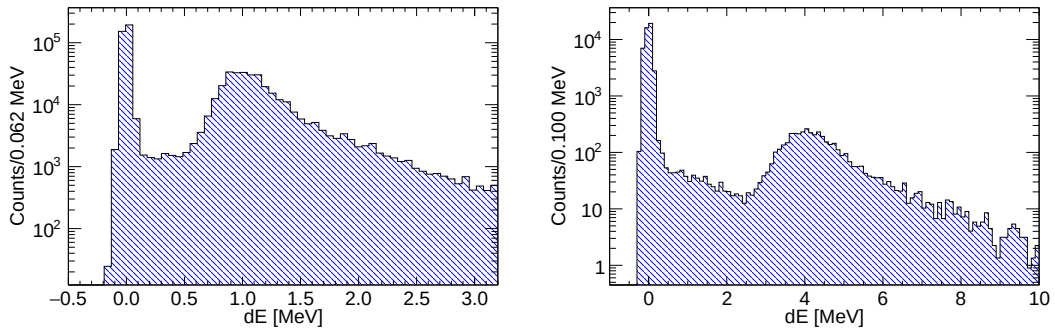

(A) IHL2U (B) OHL3U

FIGURE 3.2: Typical energy deposit distribution of hodoscopes (IHL2 (A), OHL3 (B)). Sharp peak structures show the pedestals.

2 MeV/cm. The mathematical expression for this conversion is

$$dE = C_Q(Q - Q_0), \tag{3.2}$$

where Q is the digitized pulse information of the PMT. The energy loss is defined as the synergetic average of the pulse height of both PMTs because hodoscopes are double-reading type with PMTs on both sides of the scintillator except for IH1. Figure 3.2 shows typical dE distributions of IH and OH after the energy deposit calibration. As IH and OH consist of scintillators of different thickness, the calibration parameters were determined so that the most probable values of the MIP signals were 1 MeV and 4 MeV, respectively. Sharp peaks at $dE = 0$ MeV in Fig. 3.2 show the pedestals of the PMT signals.

Pulse Height Correction

A reading edge type descriptor emits a logic signal when the voltage of the analog signal exceeds a certain threshold value. The timing of the logic signal output differs depending on the size of the analog signal, even if the actual signal produced timing is the same. The correction of this timing shift is called time walk correction, slewing correction, or pulse height correction (PHC). Since the timing deviation is correlated with the size of the analog signal as described above, the timing resolution of the detector can be improved by applying pulse height correction. Upper panels of Fig. 3.3 and 3.4 show correlations of dE and ToF before and after PHC. In Fig. 3.3, the abscissa is not the time of flight of a single particle passing through IHL2 and IHR2, but the time difference between the pair-produced electron and positron passing through each IH. Figure 3.3 (C), (D) and Fig. 3.4 (C), (D) are projections of each upper panel. They were fitted by single Gaussians with a range of $\mu \pm 1.5\sigma$, where μ and σ are mean and standard deviation of the Gaussian. The correction for time (dt), determined as a function of dE, was defined as,

$$dt = \frac{p_0}{|dE - p_1|}, \tag{3.3}$$

where p_i ($i = 0,\ 1$) are calibration parameters. Corrected time (t_c) was defined as $t_c = t - dt$ where t is time information of the hodoscope before PHC. t_c was used for further analysis of particle identification, etc.

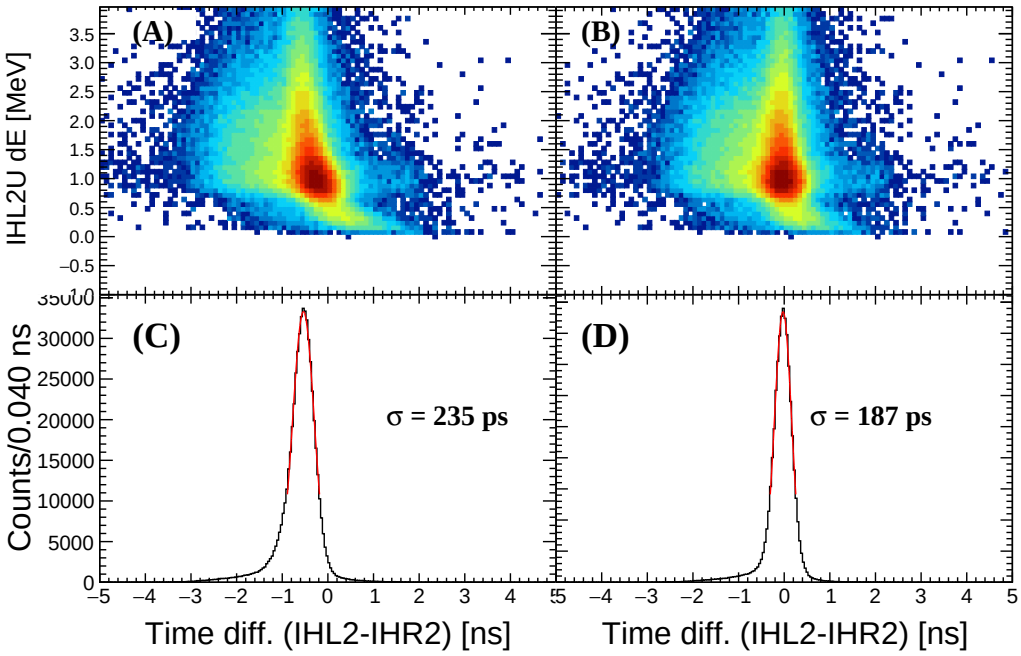

FIGURE 3.3: Time difference between IHL2 and IHR2 vs IHL2U *dE* before (A) and after (B) PHC. (C), (D) are projections of (A) and (B), respectively. They were fitted by Gaussians with a range of $\mu \pm 1.5\sigma$, where μ and σ are mean and standard deviation of the Gaussian. The fit range was obtained by iterating the fitting process.

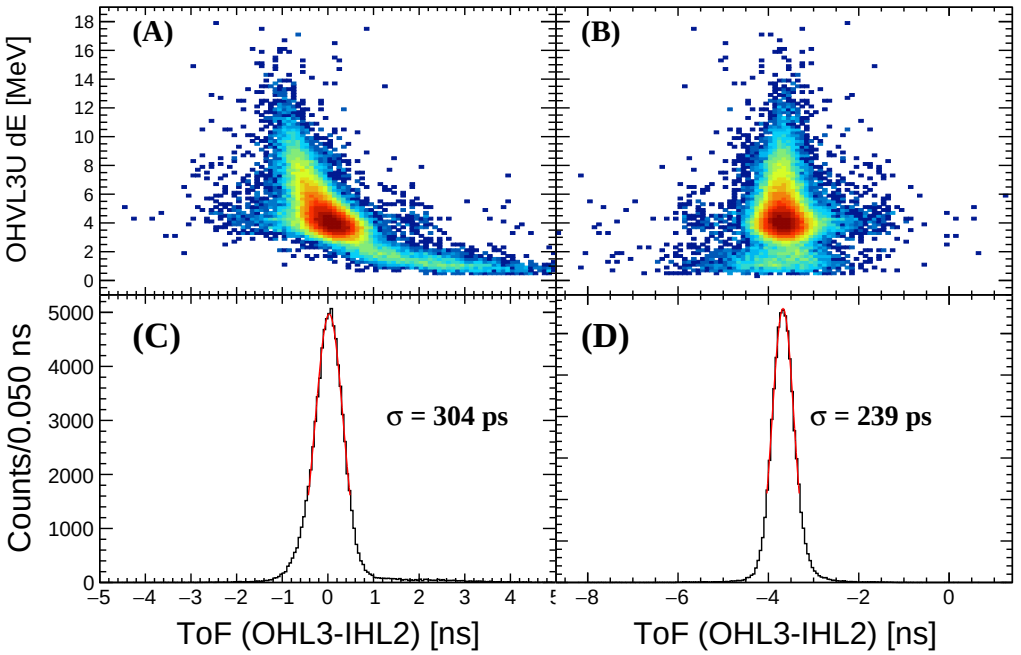

FIGURE 3.4: ToF between OHL3 and IHL2 vs OHL3U *dE* before (A) and after (B) PHC. (C), (D) are projection of (A) and (B), respectively. They were fitted by Gaussians with a range of $\mu \pm 1.5\sigma$, where μ and σ are mean and standard deviation of the Gaussian. The fit range was obtained by iterating the fitting process.

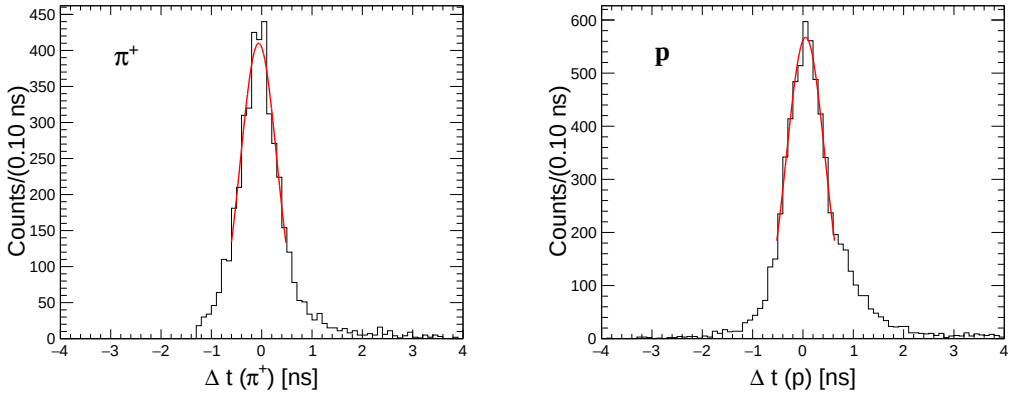

(A) π^+ (B) p

FIGURE 3.5: ΔToF distribution for π^+ (left) and p (right). Each distribution was fitted by a single Gaussian in a range of $\mu \pm 1.5\sigma$, where μ and σ are mean and standard deviation of the fitted Gaussian. The fit range was determined by iterating fitting process five times

Time Offset

First, adjust time offset parameters roughly so that $\beta = 1$ for $e^{\pm}$. The time offset parameters are then adjusted precisely after the particle identification. The time of flight, ToF, of a charged particle between IH and OH can be calculated not only from the time information of IH and OH ($\mathrm{ToF_{Hodo}}$), but also from the momentum obtained from the tracking information, as

$$\mathrm{ToF_{Mom}} = \frac{l_{IH-OH}}{\beta_{Mom} c}, \tag{3.4}$$

where l_{IH-OH} is a flight path length from IH to OH. β_{Mom} is calculated as,

$$\beta_{Mom} = \frac{p}{\sqrt{p^2 + m^2}}, \tag{3.5}$$

where p and m is momentum obtained from tracking information and mass of the charged particle, respectively. Since ToF was derived for the particle after passing through IH, the reconstructed momentum p was the value before the energy loss correction which is described in Sec. 3.3.5. Thus, by selecting specific particles, ΔToF is defined as,

$$\Delta\mathrm{ToF} = \mathrm{ToF_{Hodo}} - \mathrm{ToF_{Mom}}. \tag{3.6}$$

The time offset parameters were adjusted to minimize ΔToF for all IH and OH combination run by run.Typical ΔToF distributions of π^+ and p are shown in Fig. 3.5. Each distribution was fitted by a single Gaussian in a range of $\mu \pm 1.5\sigma$, where μ and σ are mean and standard deviation of the fitted Gaussian. The fit range was determined by iterating fitting process five times. Time dependence of the fit parameters of ΔToF is shown in Fig. 3.6. The typical resolution was $\sigma_{\Delta\mathrm{ToF}} \sim 350$ ps for $\pi^{\pm}$. The resolution of OH is the dominant component of the ToF resolution. Due to the effect of energy loss during flight, the mean values ($\mu_{\Delta\mathrm{ToF}}$) of $\pi^{\pm}$ and proton were slightly different.

After the time offset calibration, the correlation of momenta and velocities of charged particles was obtained and shown as Fig. 3.25(A).

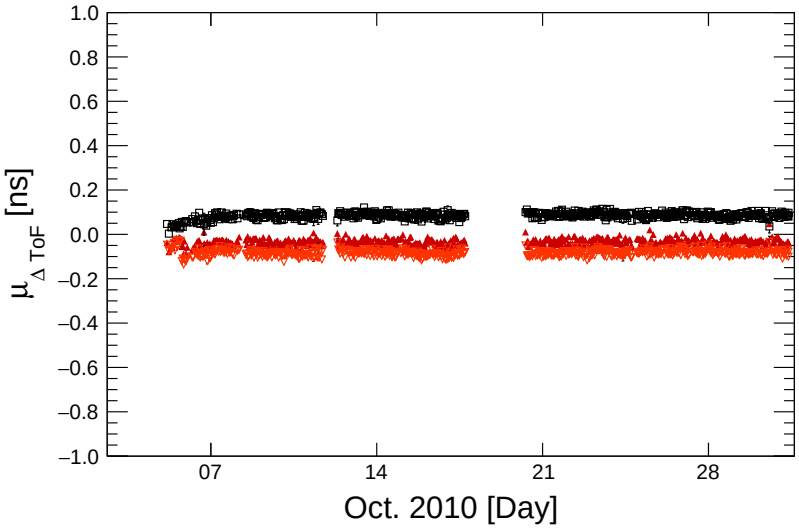

(A) $\mu_{\Delta\mathrm{ToF}}$

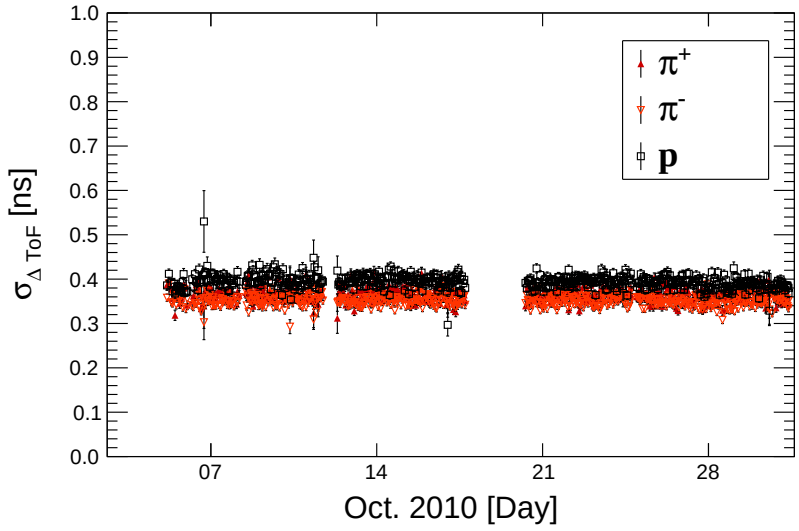

(B) $\sigma_{\Delta\mathrm{ToF}}$

FIGURE 3.6: Time dependence of fitting parameters of ΔToF distributions. Due to the effect of energy loss during flight, the mean values ($\mu_{\Delta\mathrm{ToF}}$) of $\pi^{\pm}$ and proton are different.

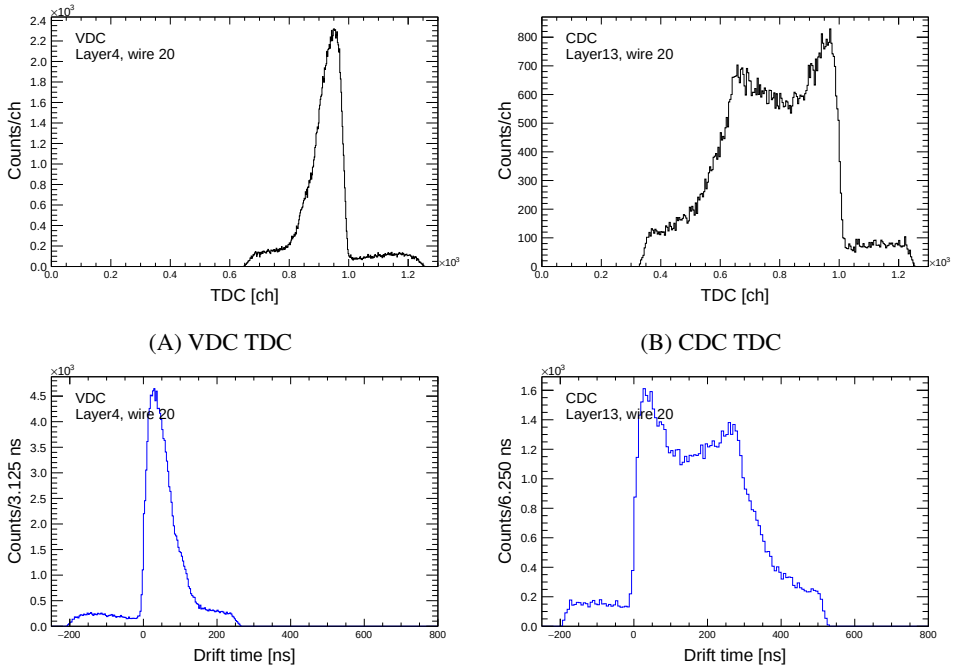

(A) VDC TDC

(B) CDC TDC

(C) VDC drift time

(D) CDC drift time

FIGURE 3.7: Typical TDC and t_0 corrected time distributions of DCs. TDC distributions of a wire of VDC (A), and CDC (B). Drift time distributions of a wire of VDC (C), and CDC (D). TDC was converted to the drift time by applying a time offset parameter (t_0) and a conversion parameter.

3.2.2 Drift Chambers (VDC, CDC)

VDC and CDC were the most important detectors for this experiment since they were used to reconstruct trajectories of charged particles and derive three-momentum vector of them. Drift chamber is a detector that can achieve a high positional resolution of several hundred μm by deriving the position of the passing charged particle from the drift time of ionized electrons. Thus, we needed to convert from time information (TDC) to position information (drift length) in a calibration process.

Drift Time

Digitized timing information (TDC) accumulated by the common stop mode had to be converted into physically meaningful time information. Figure 3.7(A) and 3.7(B) show typical TDC distributions of VDC and CDC, respectively, before the conversion. The trapezoidal signal distribution can be seen on top of the accidental uniform distribution. The offset parameter was set so that the rising point of the distribution was the origin of the drift time. Then, the drift time was converted to the drift time by multiplying by the TDC conversion parameter of -0.78 ns/ch. The drift time distribution after the conversion is shown in Fig. 3.7(C) and 3.7(D). The time offset parameters were calibrated run by run for each wire.

XT-curve calibration

A correlation of drift length (or distance from a wire to a track) and drift time is called XT-curve. XT-curve parameters were used to convert time information (T), drift time, to position information (X), drift length.

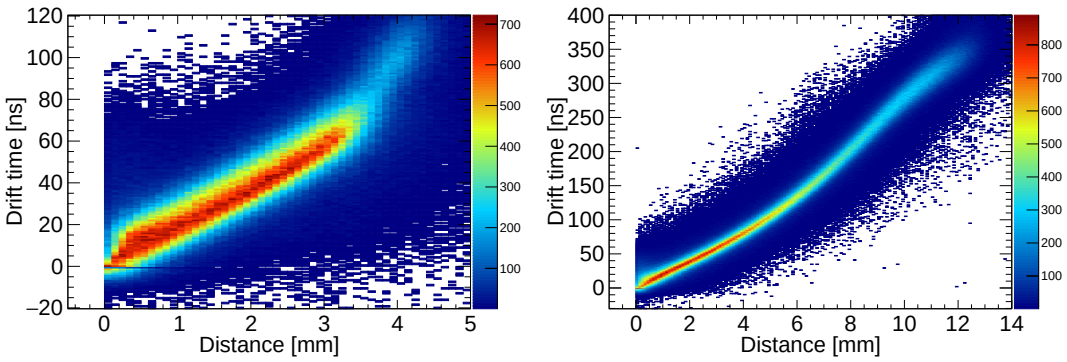

(A) XT curve of VDC (Layer1)

(B) XT curve of CDC (Layer14)

FIGURE 3.8: XT-curve of VDC (A) and CDC (B).

Figure 3.8 shows XT-curve distributions of a layer of VDC (Fig. 3.8(A)) and CDC (Fig. 3.8(B)). The closest distance from the wire to the track which was shown in the abscissa was derived by a tracking routine of NKS2 (Sec. 3.3) with optimized XT-curve parameters. The relation of the distance and the drift time was not linear due to a non uniform electric field around the wires. The calibration curve of the XT-curve was obtained by performing a linear approximation every 8 ns.

XT-curve parameters were optimized to minimize the residue of the drift length and the distance of the track and the sense wire as described follows. First, XT-curve parameters assuming a constant drift velocity independent of the position of the charged particle pass through were used to fit. Second, new XT distributions were derived by fitting with the XT-curve parameters. Thirdly, new XT-curve parameters were derived by fitting the sliced XT distributions. Then, tracks were reconstructed with the new XT-curve parameters. As tracking quality affected calibration precision of XT-curve parameters, these processes were iterated several times till the width of a residual distribution was no longer improved. The XT curve parameters were optimized run by run for each layer.

Position Resolution

Figure 3.9(A) shows the correlation of the distance from a track to a sense wire and the residual of VDC layer1. The one dimensional residual distribution of the drift length and distance of the track and the sense wire of VDC layer1 is shown with a fitted Gaussian function in Fig. 3.9(B). Figure 3.10(A) shows σ of a Gaussian function for each layers. However, the σ does not directly correspond to the intrinsic position resolutions of DCs since the σ depends on the other wires' hit information. To estimate the intrinsic position resolutions, a GEANT4 simulation was used. In the simulation, a finite resolution was assumed for each VDC and CDC, and the residue distribution was created using the same tracking routine as the real data. Fig. 3.10(B) shows comparison between real data and simulated result. The assumed resolution that best reproduced the data was obtained as σ = 500 μm, and 400 μm for VDC and CDC, respectively. Time dependence of fitting parameters of residual distributions is shown in Fig. 3.11. Each point in the graph shows the results of the fit for each day (24 hours) that the physics data was acquired. The performance of drift chambers were stable during the experiment.

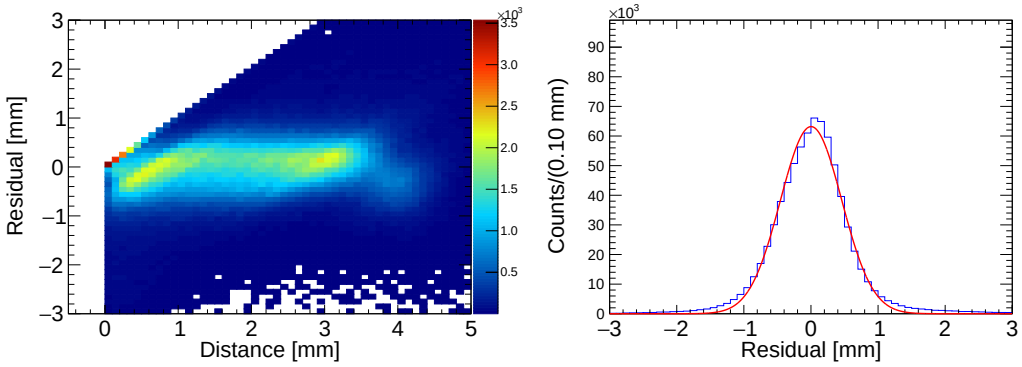

(A) Distance v.s. residual of VDC (Layer1)

(B) Residual of VDC (Layer1)

FIGURE 3.9: Residual of VDC layer1. (A) The correlation of the distance from a track to a sense wire and the residual. (B) The one dimensional residual distribution of the drift length and distance of the track and the sense wire of VDC layer1 is shown with a fitted Gaussian function

Wire Efficiency

The detection efficiency of each wire was estimated. When a track passed near a wire, the efficiency was calculated as the ratio of hits on the wire. Figure 3.12 shows wire efficiency of Layer1 (VDC, Fig. 3.12(A)) and Layer14 (CDC, Fig. 3.12(B)). The efficiencies of other layers are shown in Appendix **??**.

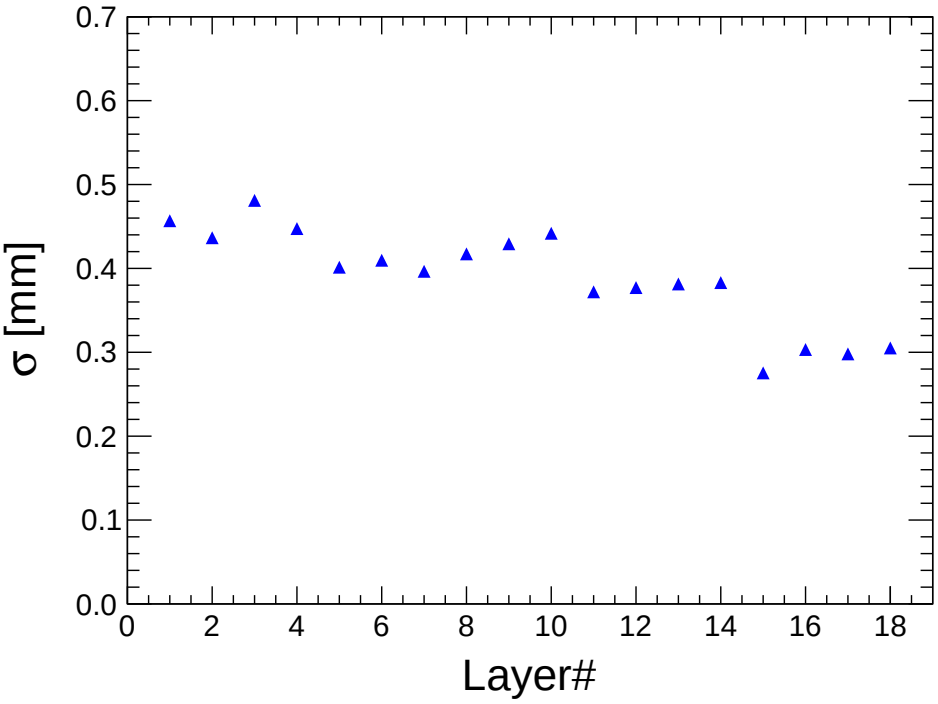

(A)

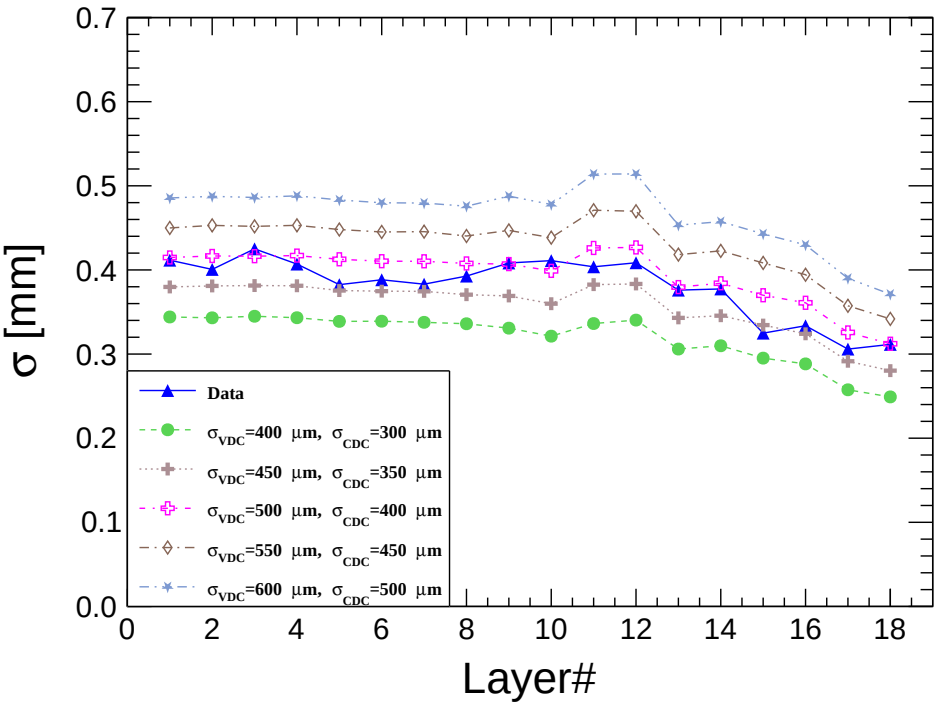

(B) Residual of

FIGURE 3.10: Width of residual distributions of DCs. (A) σ of the obtained by fitting of each layer. (B) Comparison with simulated σ assuming various position resolutions.

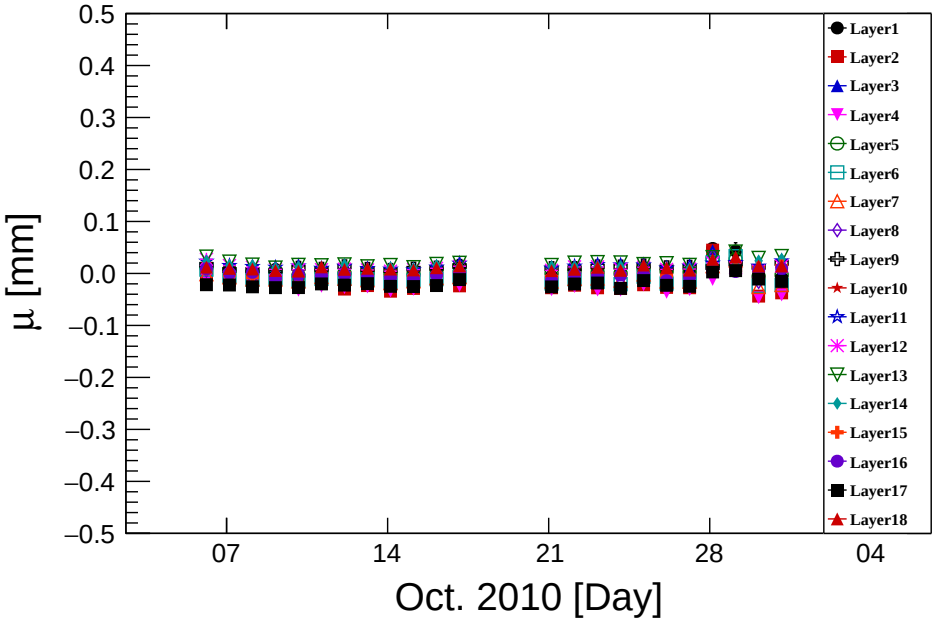

(A) μ

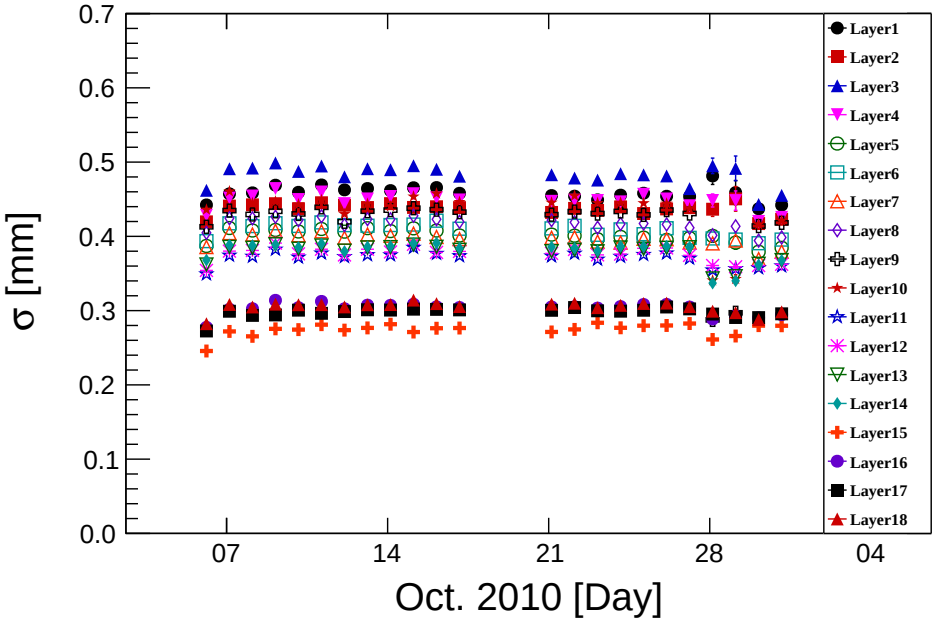

(B) σ

FIGURE 3.11: Time dependence of fitting parameters of residual distributions shown in Fig. 3.9. Mean (μ) (A) and width (σ) (B) are shown in upper and bottom panels, respectively.

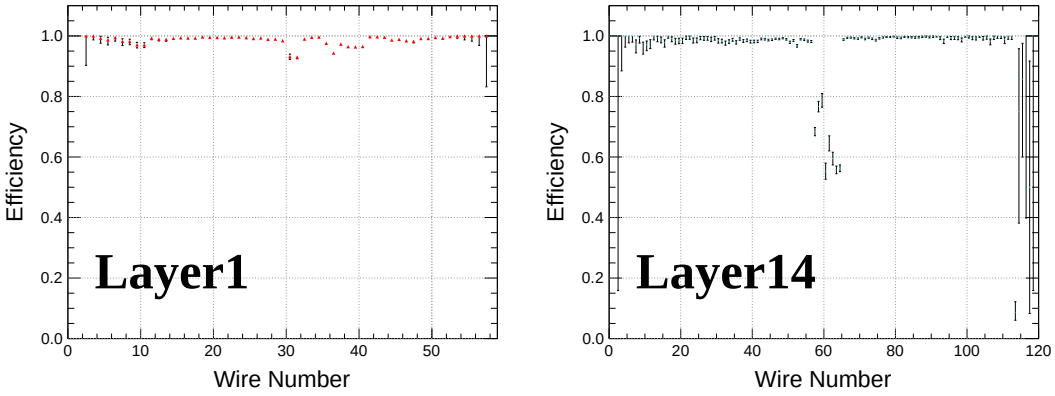

(A) Wire efficiency of VDC (Layer1)

(B) Wire efficiency of CDC (Layer14)

FIGURE 3.12: Wire efficiency of VDC Layer1 (A) and CDC Layer14 (B).

3.3 Tracking Algorithm

Two drift chambers (VDC and CDC) were used to reconstruct the trajectories of charged particles and obtain the three-dimensional momentum vectors of the particles. In this section, the algorithm of the track reconstruction is described. Figure 3.13 shows a flow chart of our tracking procedure. The tracking procedure consisted of following steps: clustering of neighboring hits of each wire, grouping of clusters into candidates of tracks, fitting to reconstruct the trajectory and momentum. The reconstructed trajectories were then associated with hits of hodoscopes for particle identification.

Figure 3.14 illustrates relations of wire hits, clusters, and groups. Neighboring wire hits formed clusters, and clusters on the same orbit formed a group. A group was used as a candidate track for trajectory optimization.

After searching and reconstructing tracks, the decay vertices were derived by calculating the closest distance approaches of the reconstructed tracks. After the particle identification, the energy loss of the charged particles during the flight was corrected by a function of the reconstructed momentum.

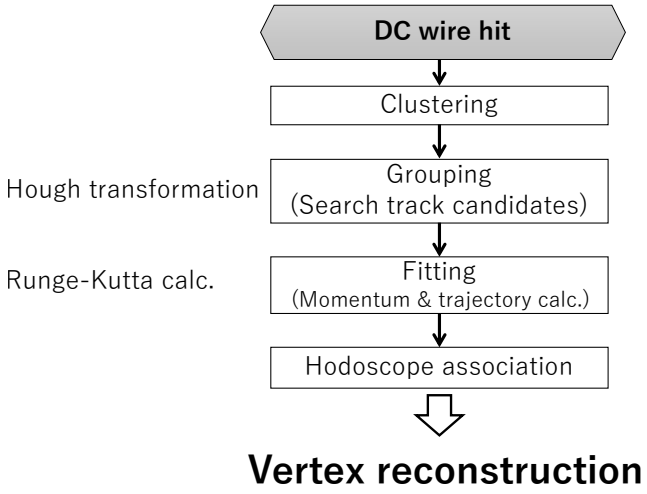

FIGURE 3.13: Flow chart of tracking procedure.

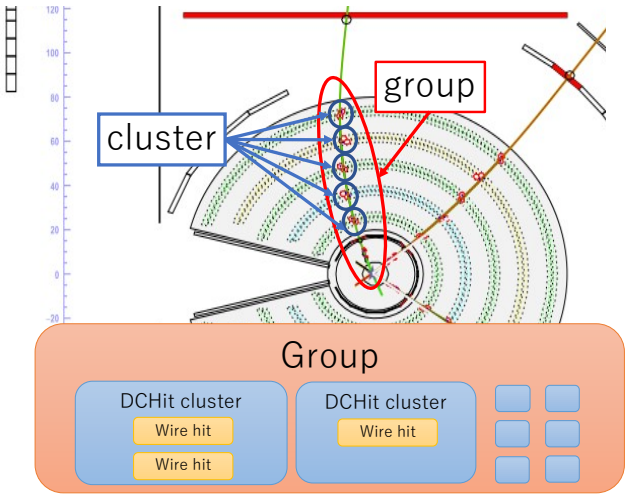

FIGURE 3.14: Illustration of relation of wire hits, DCHit clusters, and groups. Neighboring wire hits form clusters, and clusters on the same orbit form a group.

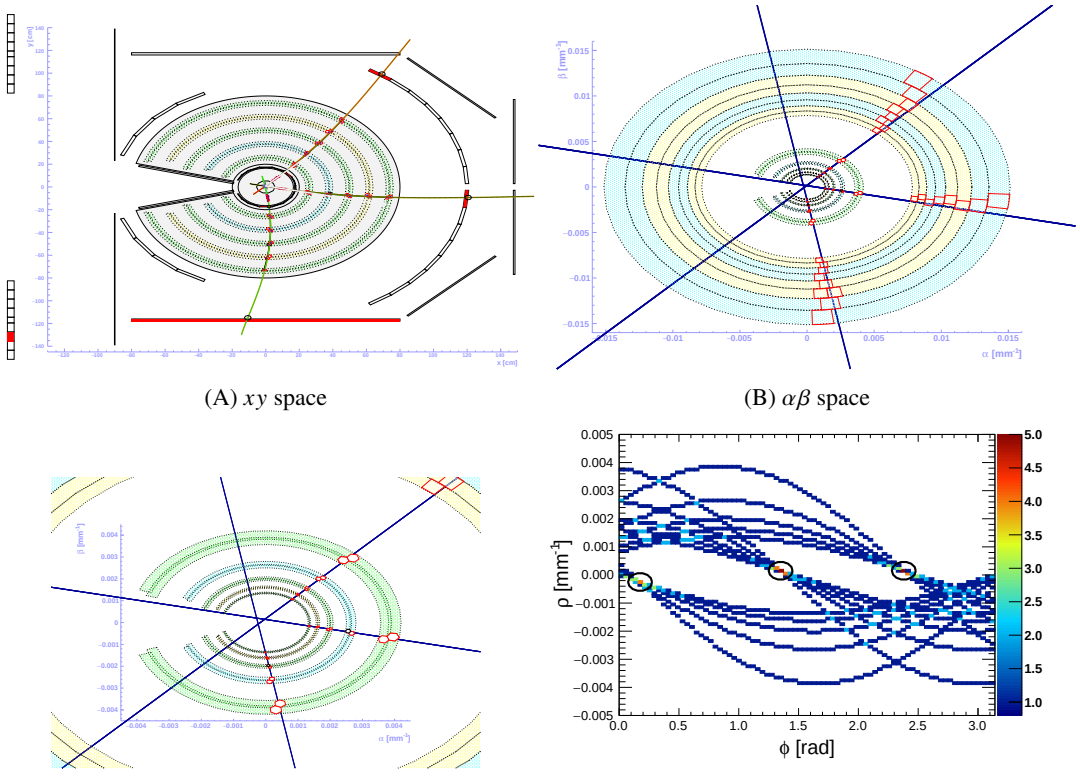

(A) xy space

(B) $\alpha\beta$ space

(C) $\alpha\beta$ space (CDC region only)

(D) Hough space ($\phi\rho$ space)

FIGURE 3.15: Event display of a typical 3 track event. (A) xy space. (B) $\alpha\beta$ space. Blue solid lines represent Hough lines. (C) same with (B) but different range. (D) Hough space. Each curve represents a hit cluster. Three intersection points are shown as black solid circles.

3.3.1 DCHit Clustering

CDC and VDC consisted 10 and 8 layers, respectively. Two adjacent layers had the same configuration and are treated as a single layer group. The even and odd layers were paired together (e.g., layer 1 and layer 2) to form a group of layers, i.e. the layer configuration of CDC was XX'UU'VV'XX'UU'VV'XX', where XX', UU', and VV' were the same layer groups. The hits of adjacent wires in the same layer group were bundled together to form a hit cluster (named DCHit cluster). DCHit clusters were used in following analysis. It should be noted that DCHit clusters with a single wire hit were also used in the following analysis.

3.3.2 Track Group Search

We used the Hough transformation to determine the combination of DCHit clusters to use for tracking. The position information of DCHit clusters of CDC in the beam plane (xy-plane at $z = 0$) was converted to the $\alpha\beta$-plane by the following equation,

$$\alpha = \frac{x}{r^2}, \tag{3.7}$$

$$\beta = \frac{y}{r^2}, \tag{3.8}$$

where, $r = \sqrt{x^2 + y^2}$. Figure 3.15(A) and 3.15(B) show typical event displays of 3-track event in the xy space and the $\alpha\beta$ space, respectively. Figure 3.15(C) shows an event display in the $\alpha\beta$ space with a region of CDC. The red rectangles represent cell region of hit wires of CDC.

In each DCHit cluster, α and β were obtained and then the curve was obtained in $\rho\phi$ space (Hough space) by,

$$\rho = \alpha \cos\phi + \beta \sin\phi. \tag{3.9}$$

Figure 3.15(D) shows Hough lines of DCHit clusters. Each curve represents a DCHit cluster. An intersection point of several curves represents a group of DCHit clusters. Three intersection points are shown as black solid circles in Fig. 3.15(D). Finding intersection points in Hough space equals to finding straight lines in $\alpha\beta$ space and circles through the origin in xy space. The values of $\rho\phi$ at the intersection points and DCHit clusters were used as initial parameters of a Hough line which is shown as a solid blue line in Fig. 3.15(B). The parameters of the Hough line, ρ and ϕ, were re-calculated by linear fitting of DCHit clusters in $\alpha\beta$ space. The hit clusters which were members of the intersecting curves were defined as one group to be used in the fitting process. CDC or VDC hit clusters which were not regarded as members of the group at this point but close to the Hough line were added as members of the group. The parameters of the straight line were updated after adding these DCHit clusters to the group. More than 3 clusters were required to form a track candidate.

3.3.3 Calculation of Momentum from Trajectory

The particle trajectory can be obtained by assuming a three-dimensional momentum vector of the particle at the starting point and solving the equation of motion of the charged particle in a magnetic field by successive approximation using the Runge-Kutta (RK) method [MB79]. The equation of motion was solved successively at each point for each step, assuming a certain step size. A straight line was used to interpolate between each calculation point (RK point) of the equation of motion in this analysis. The details of the equations of motion can be found in an appendix of [Kan+18].

The initial values of the momentum and the starting point of the trajectory were estimated from the hit patterns of the grouped hits of the wires. The starting point of the Runge-Kutta calculation was at $r = 20$ cm, which is the boundary between CDC and VDC. The step size of the Runge-Kutta calculation was taken as 0.2 cm only in the region near the target ($r < 10$ cm) and 0.5 cm in the other regions. Figure 3.16 shows a conceptual drawing of the RK calculation. The direction to the next RK point was determined by solving the equation of motion. The distance to the next RK point was defined as the step size artificially.

The momentum vector and initial position for the Runge-Kutta calculation were determined so that the residual between the calculated trajectory and the drift length at each wire was minimized. Minuit provided by the ROOT package [Ant+09] was used to optimize the parameters.

3.3.4 Hodoscope Hit Association

Particle identification is performed by combining flight distance from the track analysis and time information from the hodoscopes (IH, OH). The procedure of association of hit information between the track and the hits of hodoscopes is shown in Fig 3.17. "The sensitive region" of each scintillator in the beam plane (xy-plane) was defined as the inner surface of the scintillator (the side closer to the target) with margins included (a solid magenta line in Fig. 3.17). If the track passed through the sensitive region of a counter with a valid hit, the counter was associated with the track. When multiple counters of the same type (IH or OH) were associated, the information of the counter whose center of the scintillator was closest to the position where the track passes was used for analysis.

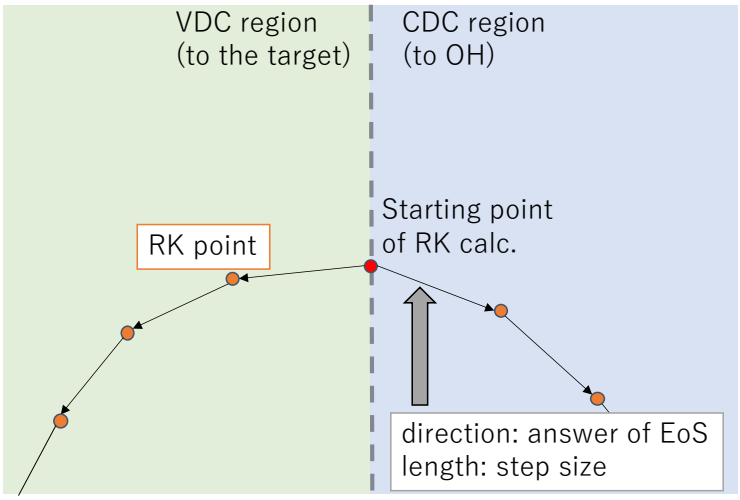

FIGURE 3.16: Conceptional illustration of the RK calculation. The boundary between CDC and VDC is used as the starting point for the RK calculation, and the trajectory calculation proceeds toward each VDC and CDC region. The direction to the next calculation point is determined by the solution of the equations of motion, and the distance is determined as the step size for each region.

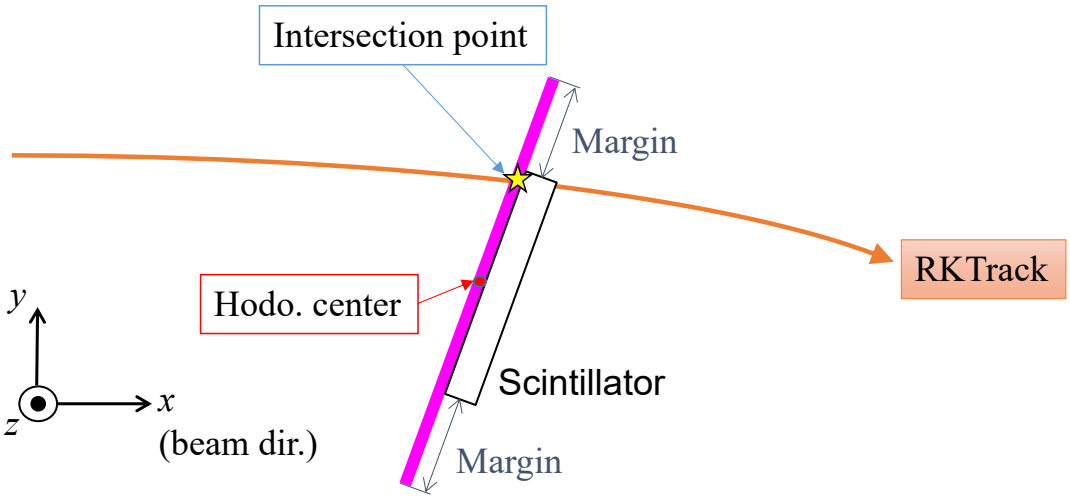

FIGURE 3.17: Schematic illustration of a track and a related hodoscope hit.

3.3.5 Energy Loss Correction

As our tracking routine did not take into account energy loss effect during the flight, there was a difference between reconstructed momentum and momentum at the production point which was obtained as a vertex point. Since the energy loss effect depended on mass of particle, it was necessary to identify the type of particles in order to correct the effect. In this study, correction functions were prepared for each particle (deuteron, proton, and pion) based on Monte Carlo simulations and the energy loss correction was applied to each particle. Correlation between reconstructed momentum and generated momentum are shown in Fig 3.18. Each panel shows a distribution for each particle, deuteron (Fig. 3.18(A)), proton (Fig. 3.18(B)), and pion (Fig. 3.18(C)). Dashed black lines are polynomial functions used for the energy loss correction. The correction function for deuteron was the following, which switches between linear and quadratic functions at momentum of 0.8 GeV/c,

$$\begin{aligned} f_d(x) &= p_0 + p_1 x + p_2 x^2, && (x \leq 0.8) \\ f_d(x) &= p_3 x + p_4, && (x > 0.8) \end{aligned} \tag{3.10}$$

where x represents momentum of deuteron, p_i is parameter of the function. 8th-degree polynomial functions were used for proton and pion. Parameters of these functions were tuned for each particles. Momentum distributions after the energy loss correction are shown in Fig. 3.19. Straight correlations were observed after applying the correction functions.

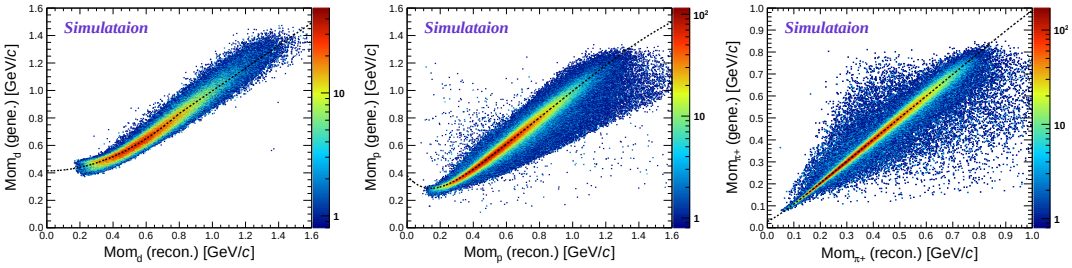

(A) deuteron (B) proton (C) π^+

FIGURE 3.18: Correlations of reconstructed momentum and generated momentum by the GEANT4 simulation for each particle. Dashed black lines are polynomial functions used for the momentum correction. A function presented by Eq. 3.10 was used for deuteron. 8th polynomial functions were used for proton and pion.

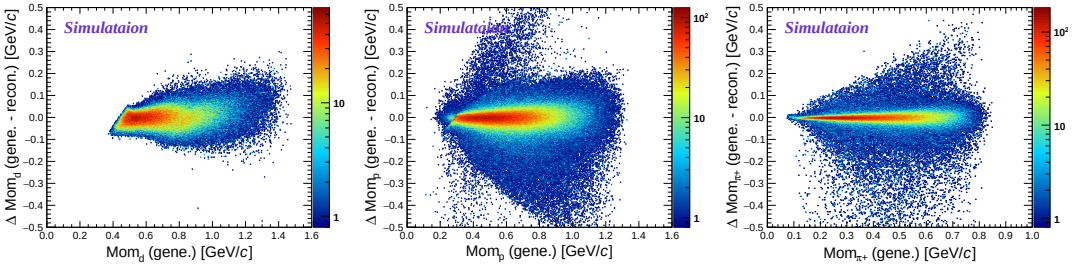

(A) deuteron (B) proton (C) π^+

FIGURE 3.19: Correlations between difference of reconstructed momentum and generated momentum by the GEANT4 simulation for each particle after applying the momentum correction. Straight correlations are obtained after the correction.

Accuracy of Mass of Λ and K^0

The reliability of the simulation-based energy loss correction functions was tested using real data too. The energy loss correction functions for pion and proton were tested by using known Λ and K^0 masses. Figure 3.20 shows invariant mass distributions of $p\pi^-$ and $\pi^+\pi^-$, before and after the energy loss correction. Bottom panels show distributions after applying the energy loss correction. In order to select weak-decayed events, we extracted events that decayed outside the target cell. Red dashed lines show PDG values of the Λ and K^0 masses ($M_\Lambda = 1115.683$ MeV/c^2 and $M_{K^0} = 497.611$ MeV/c^2) in Fig. 3.20(A) and 3.20(B), respectively. The invariant mass distributions were fitted by a sum of single Gaussian and a linear function. The fitted functions for before and after the correction were shown as blue dot-dashed lines and red solid lines, respectively. The discrepancies of the centroid values of the fitted Gaussians and PDG masses of Λ and K^0 before the correction were $\mu'_\Lambda - M_\Lambda = -1.97 \pm 0.09$ MeV/c^2 and $\mu'_{K^0} - M_{K^0} = -5.5 \pm 0.9$ MeV/c^2, respectively. The centroid values of the fitted Gaussians after applying the energy loss correction are in good agreement with the dashed line within the statistical error. The residuals of the centroid values and PDG masses were,

$$\mu_\Lambda - M_\Lambda = 0.05 \pm 0.09 \text{ MeV}/c^2, \tag{3.11}$$

$$\mu_{K^0} - M_{K^0} = -0.7 \pm 1.0 \text{ MeV}/c^2, \tag{3.12}$$

where μ_Λ and μ_{K^0} are the centroid values of fitted Gaussian. Since the know masses were consistently obtained by applying the energy loss correction, it was shown that the energy loss correction based on the simulation is reliable.

The FOREST experiment measured the mass and width of the $N\Delta$ resonance with a statistical and systematic error of $\sim$10 MeV/c^2 [Ish+19]. In this study, an accuracy of a few MeV/c^2 is required for comparison with previous studies and with the $N\Delta$ threshold (2.17 GeV/c^2), and the obtained invariant mass accuracy fully satisfied this requirement.

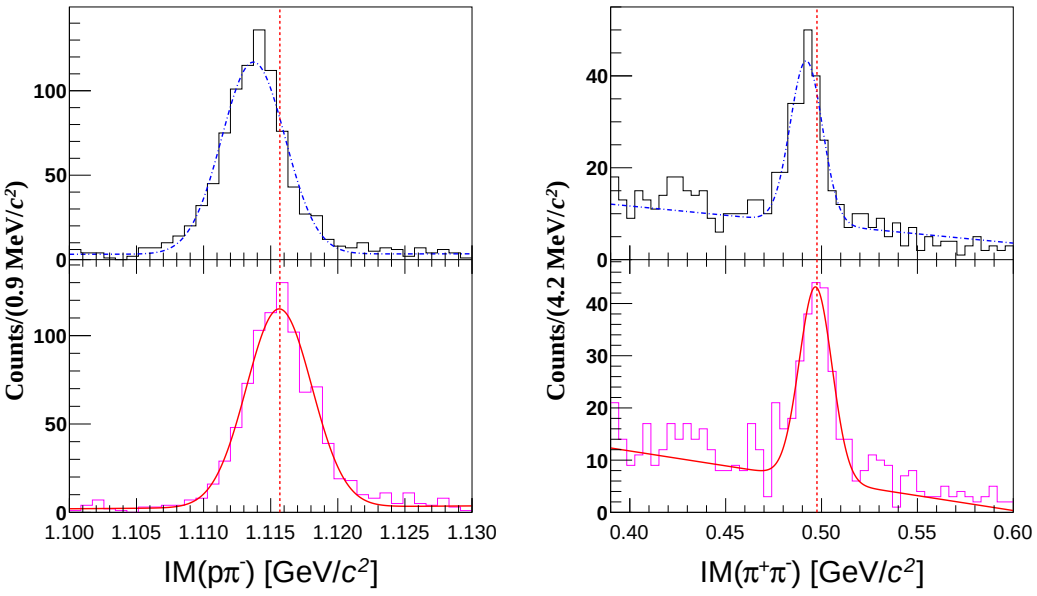

(A) invariant mass of $p\pi^-$

(B) invariant mass of $\pi^+\pi^-$

FIGURE 3.20: Invariant mass distributions of (A) $p\pi^-$ and (B) $\pi^+\pi^-$, before (top panels) and after (bottom panels) energy loss correction. Red dashed lines indicate PDG value of the Λ and K^0 masses. Red solid lines and blue dot-dashed lines show fitted functions, sum of Gaussian and linear function.

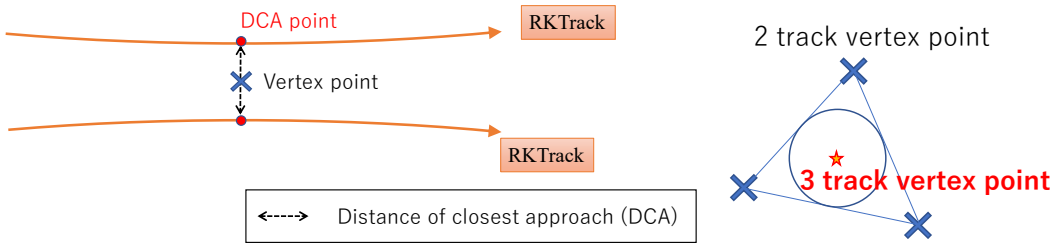

(A) 2-track (B) 3-track

FIGURE 3.21: Schematic illustration of DCA and vertex point for 2-track vertex (A) and 3-track vertex (B).

3.3.6 Vertex Reconstruction

The vertex points were reconstructed by calculating the distance of closest approach (DCA) of multiple tracks. The definition of DCA is illustrated as a dashed line in Fig. 3.21(A). As shown in Fig. 3.21(A), the DCA point was defined as the point on each track when the two tracks are closest to each other, and the vertex point of the two tracks (2-track vertex point) was defined as the midpoint of the two DCA points. The definition of the decay vertex for the 3-track case was as follows. First, three 2-track vertex points were obtained for each combination of the three tracks. The inner center of the triangle obtained by connecting the three 2-track vertex point was defined as the 3-track vertex point as shown in Fig. 3.21(B).

Vertex Resolution

Vertex position distributions of $\pi^+\pi^-$ events are shown in Fig. 3.22. Differential of x was fitted by lorentzian functions. FWHM values of the Lorentzian were 0.16 cm and 0.07 cm at $x = -3$ cm and 0.5 cm, respectively. Vertex resolutions for other combinations of the detected particles were evaluated. The result is summarized in Tab. 3.1.

TABLE 3.1: Vertex resolution.

Vertex type	FWHM (at $x = -3$)[mm]	FWHM (at $x = 0.5$)[mm]
$\pi^+\pi^-$	1.61	0.78
$p\pi^-$	1.77	1.17
$d\pi^\pm$	0.57	0.7

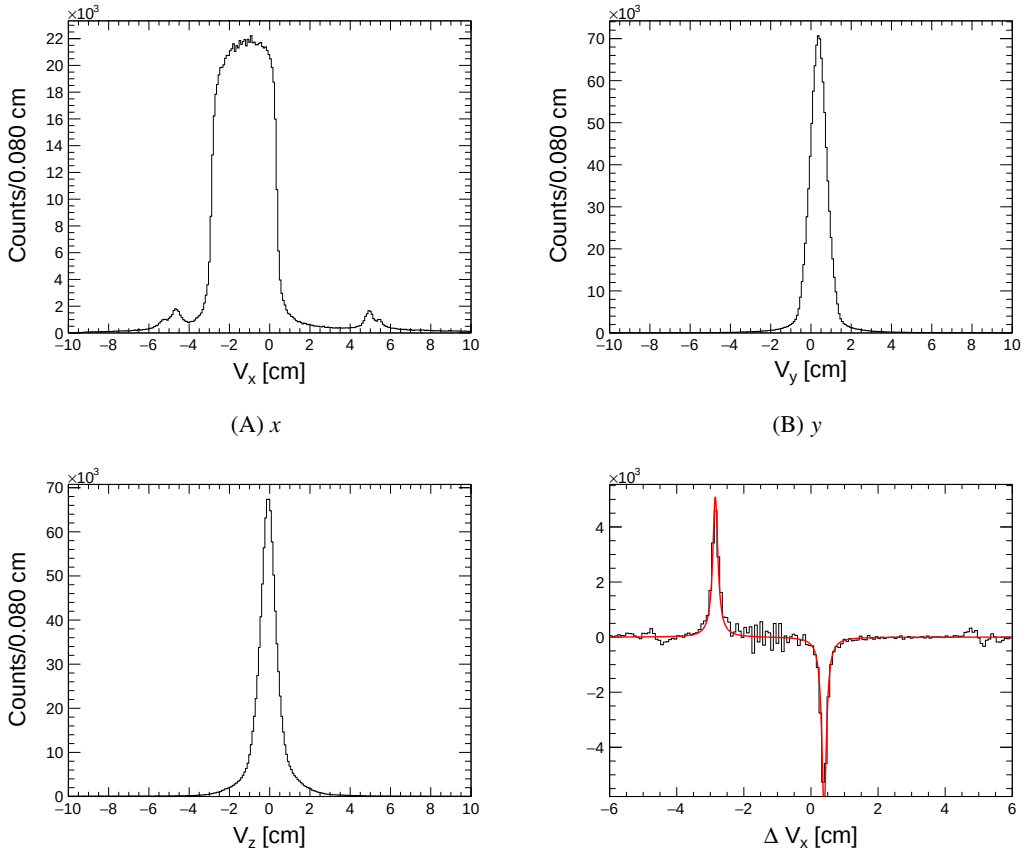

(A) x (B) y

(C) z (D) differential of x

FIGURE 3.22: Vertex distributions of $\pi^+\pi^-$ for each axis, x beam axis (A), y (B), z (C). (A) x axis is a beam axis in NKS2 coordinate. Peak which corresponds to target windows at $x \sim \pm 5$ cm is observed. (D) differential distribution of (A).

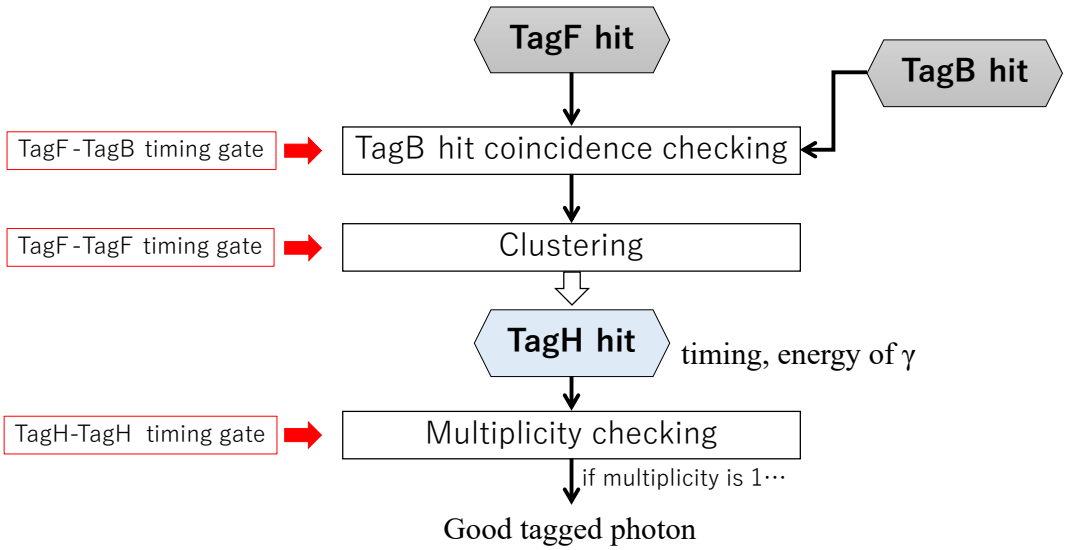

FIGURE 3.23: Flow chart of the tagger analysis procedure. Three time gates were used to select good tagged photons.

3.4 Event Selection Method

A method for selecting events to extract the $\gamma d \rightarrow d\pi^+\pi^-$ reaction is described in this section.

3.4.1 Tagged Photon Selection

As it is explained in Sec. 2.3.2, the tagger is composed of 2 type of detectors, TagF for energy measurement, TagB for taking coincidence with TagF. A proper trajectory of a scattered electron was selected by taking coincidence TagB and TagF.

The analysis algorithm of the tagger is illustrated in Fig. 3.23. First, for each TagF hit, we checked whether the corresponding TagB hit existed in the time gate ($|\Delta t\ (TagF - TagB)| <$ 2 ns). The distribution of the time difference between TagF and TagB is shown in Fig. 3.24(A).

When there were hits between adjacent segments of TagF and the time difference between the TagF hits was within the time gate ($|\Delta t\ (TagF - TagF)| <$ 3 ns), those hits were bundled as a cluster. The clustered hits of TagF and TagB were named TagH hits, and the produced time and energy of the incident photon were derived from the mean time of the hits in the cluster and the segment number of TagF, respectively. The time difference between the obtained TagH hits was examined, and the cases where multiple hit clusters existed in the time gate ($|\Delta t\ (TagH - TagH)| <$ 3 ns|) were excluded from the analysis because the energy of the incident photon could not be uniquely identified. The event with the multiplicity 1 of the TagH was identified as a good tagged photon and used for further analysis in combination with the NKS2 detector.

3.4.2 Particle Identification

The measured particles were identified from their momentum and velocity using the difference in the mass of the particles. The momentum was derived from the analysis of the drift chambers by reconstructing the trajectory of the charged particle in the magnetic field. $1/\beta$ which is an inverse of relative velocity against the velocity of light in vacuum was derived from timing information measured by IH (t_{IH}) and OH (t_{OH}) as,

$$\frac{1}{\beta} = \frac{t_{OH} - t_{IH}}{l_{IH-OH} \times c}, \tag{3.13}$$

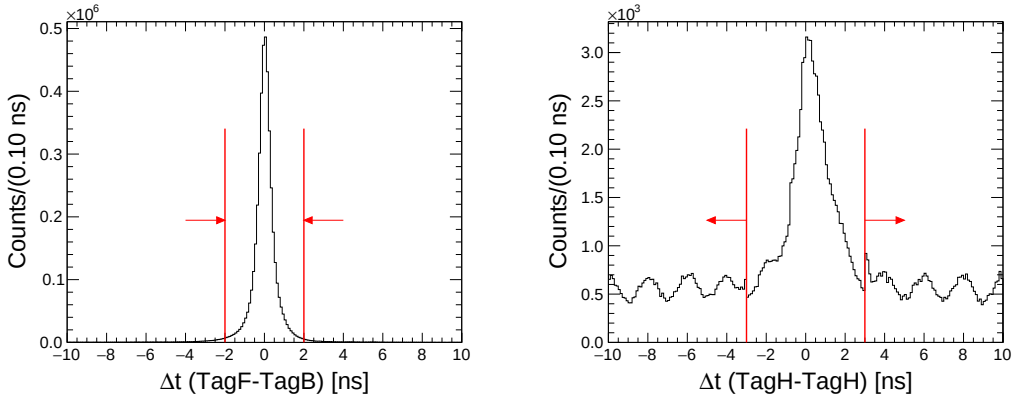

(A) Time difference of TagF and TagB.

(B) Time difference of TagH and TagH.

FIGURE 3.24: Tagger timing distributions. Red lines show event selection threshold. (A) Time difference of TagF and TagB. All TagF segments were merged. Events in ±2 ns region were selected as true events. (B) Time difference of two TagHs. Events in ±3 ns region were removed from $d\pi^+\pi^-$ analysis as photon energy could not be identified.

where l_{IH-OH} is the flight path length between IH and OH. Figure 3.25 shows a demonstration of particle identification of NKS2 with several event cuts of coincidence time (Sec. 3.4.2), tracking χ^2 (Sec. 3.4.4), vertex position (Sec. 3.4.5), opening angle of two tracks (Sec. 3.4.5), and DCA of two tracks (Sec. 3.4.5).

Figure 3.25(A) shows correlation between momentum and $1/\beta$ of the detected charged particles. The longitudinal axis of Fig. 3.25(A) is the momentum multiplied by the positive or negative charge of the particle, where more than 0 indicates positive charged particles and less than 0 indicates negative charged particles. Mass square which is shown in Fig. 3.25(B) is also useful to separate particles depending their mass. Mass square (m^2) can be derived as,

$$m^2 = \left(\frac{p}{c}\right)^2 \left(\frac{1}{\beta^2} - 1\right), \tag{3.14}$$

where p is a momentum of the charged particle.

Boundaries of particle identification in the analysis are shown as solid lines in Fig. 3.25(A). Red, black, and magenta lines show boundaries of π, p, and d, respectively. The above boundaries for deuteron and proton are mathematically expressed as,

$$2.56 < m^2 < 4.41 \qquad [(\mathrm{GeV}/c^2)^2] \text{ (for } d\text{)}, \tag{3.15}$$

$$0.5625 < m^2 < 2.25 \qquad [(\mathrm{GeV}/c^2)^2] \text{ (for } p\text{)}, \tag{3.16}$$

respectively. The boundary of pion is also expressed as,

$$m^2 < 0.16[(\mathrm{GeV}/c^2)^2] \cap 0.0144 < \left(\frac{p}{c}\right)^2 \left(\frac{1}{\beta^2} - 0.4\right) [(\mathrm{GeV}/c^2)^2]. \tag{3.17}$$

The boundary of pion was not as simple as that of proton or deuteron to eliminate low momentum electron and positron which were distributed around $1/\beta = 1$, $p \leq 0.1$ GeV/c in Fig. 3.25(A).

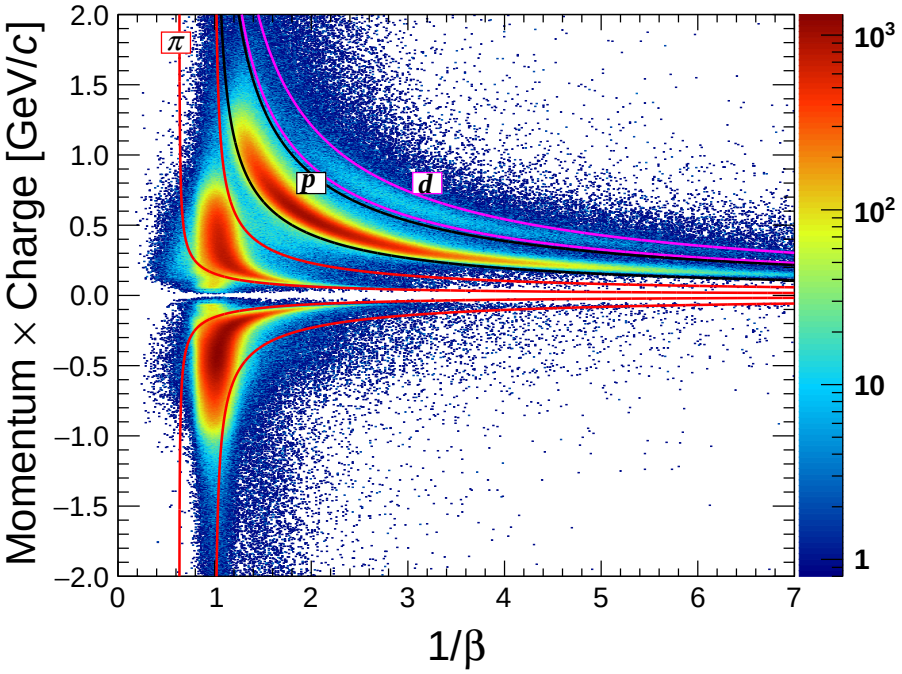

(A) $1/\beta$ v.s. Momentum $\times$ Charge

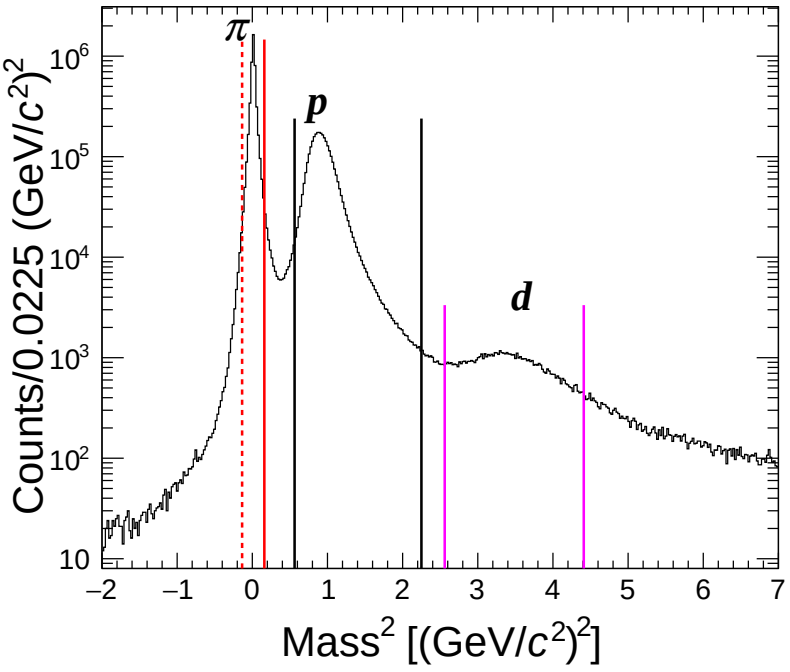

(B) Mass square distribution.

FIGURE 3.25: Particle identification demonstration of NKS2. Several cuts were applied for good signal to noise ratio. (A) Correlation of momentum $\times$ charge and $1/\beta$. Boundaries used in the analysis are shown as solid lines. Region between two-red, black, and magenta lines were selected as pion, proton, and deuteron events, respectively. (B) Mass square distribution. Boundaries of the particle identification are shown as solid lines. The red dashed line shows the lower boundary of pion mass square at $p = 0.5$ GeV$/c$ since the boundary is not a constant value of mass square but a function of momentum (p)

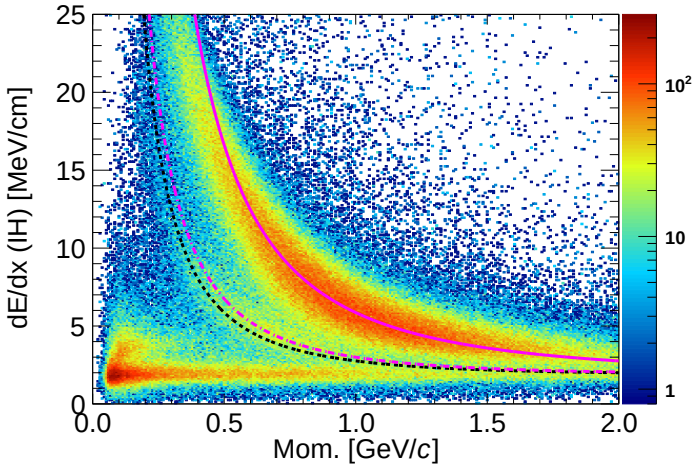

FIGURE 3.26: Correlation between dE/dx at IH and momentum with the deuteron mass region selection. The solid and dashed lines show the calculated values of dE/dx in a plastic scintillator for the deuteron and proton, respectively. The magenta dot-dashed line shows the boundary of deuteron selection by dE/dx at IH. Above the dot-dashed line region was selected as deuteron.

dE/dx cut for Deuteron Selection

The mean energy loss per distance, dE/dx [MeV/cm], in the scintillator of the charged particle was used for particle identification. Since the deuteron mass region contains a large amount of proton contamination, additional event selection using dE/dx measured by IH was carried out. Figure 3.26 shows the correlation between energy loss (dE/dx) at IH and momentum with the deuteron mass region selection. The solid and dashed lines show the calculated values of dE/dx in a plastic scintillator for the deuteron and proton, respectively. It can be seen that even after the deuteron mass region is selected, proton, pion, or positron events are still mixed in. In order to reduce the contamination, we accepted the deuteron events in the dE/dx region above the threshold indicated by the dot-dashed line in magenta in Fig. 3.26.

Figure 3.27(A) and Fig. 3.27(B) show the correlation between dE/dx and momentum in OH before and after the cut by dE/dx at IH, respectively. In Fig. 3.27(A), before the IH dE/dx cut, there are many events other than deuterons, especially positrons and pions, but after the IH dEdx cut, these events are eliminated. The linear correlation in the region below 0.5 GeV/c indicates that the total kinetic energy of the deuteron is lost and stopped inside of OH.

Coincidence Time of Tagger and IH

Time differences between Tagger and IH for each particles are shown in Fig. 3.28. Beam bunch structures were observed which was consistent with the radio frequency of the accelerator ~500 MHz. Due to the difference of velocity, the distributions of each particles are slightly different. Event selection boundaries for each particle are shown as red solid lines. The distributions of $\pi^{\pm}$ were fitted by Gaussians. The events inside the solid lines were accepted as true coincidence events. The number of accidental background contamination was estimated in Sec. 3.5.2.

Figure 3.29 shows time dependence of fitting parameters of $\pi^{\pm}$ coincidence time. Figure 3.29(A) and 3.29(B) show mean (μ) and (σ), respectively. Each point in the graph shows

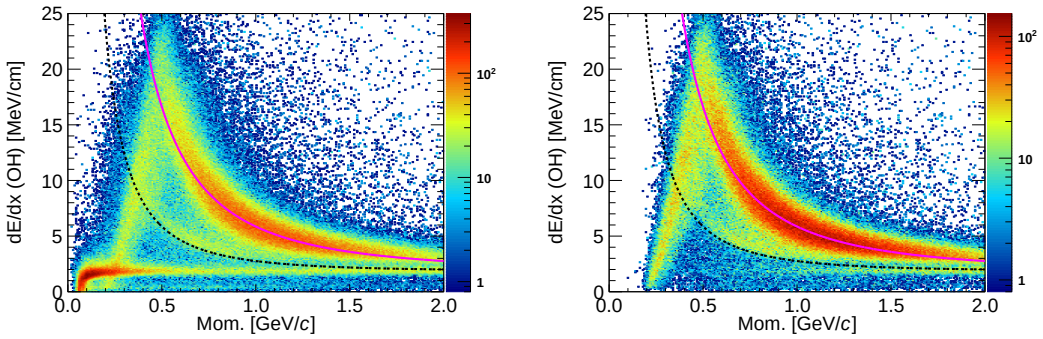

(A) dE/dx at OH before IH dE/dx cut

(B) dE/dx at OH after IH dE/dx cut

FIGURE 3.27: the correlation between dE/dx and momentum at OH. The solid and dashed lines show the calculated values of dE/dx in a plastic scintillator for the deuteron and proton, respectively. (A) Before the cut by dE/dx at IH. There are many events other than deuterons. (B) After the cut by dE/dx at IH.

the results of the fit for each physics run (~1 hour). The resolution (σ) of the coincidence time was distributed in a range of $350 \lesssim \sigma \lesssim 600$ ps.

3.4.3 Drift Chamber Multiplicity Selection

The multiplicity of drift chambers (DC multiplicity). Figure 3.30(A) and Fig. 3.30(B) shows multiplicity of a layer of VDC and CDC, respectively. Larger multiplicity makes too many track candidates and needs longer CPU time. Therefore, less than 20 hits per layer was required for efficient analysis. The efficiency of this selection was about 85% in average. The efficiency was estimated run by run.

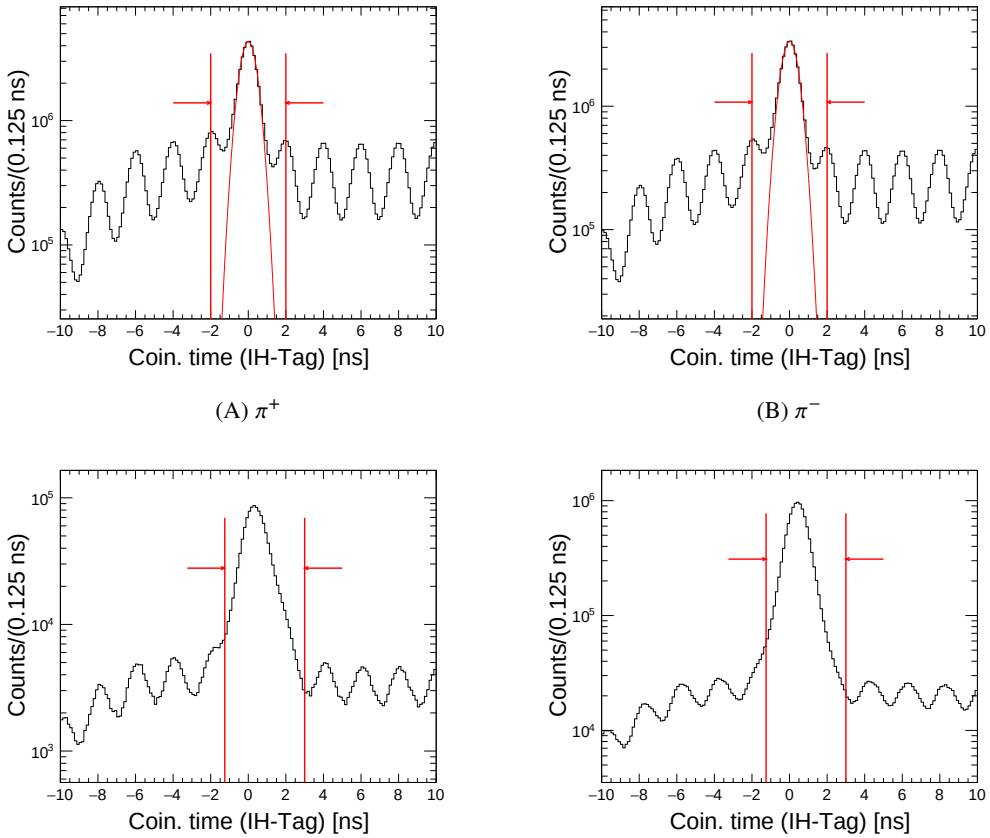

(A) π^+ (B) π^-

(C) deuteron (D) proton

FIGURE 3.28: Tagger and IH coincidence time of each particle for π^+ (A), π^- (B), deuteron (C), and proton (D). The distributions of $\pi^\pm$ were fitted by Gaussians.

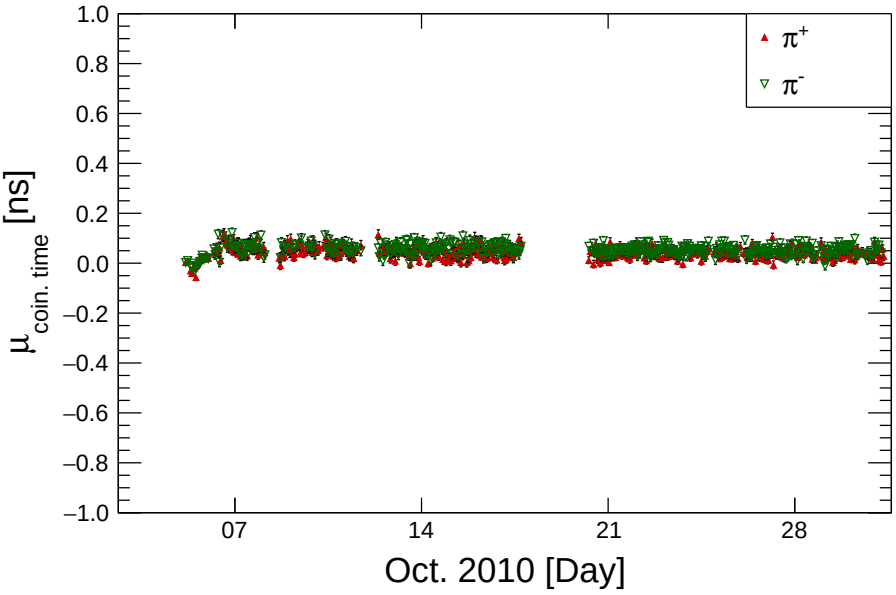

(A) $\mu_{\Delta\text{coin. time}}$

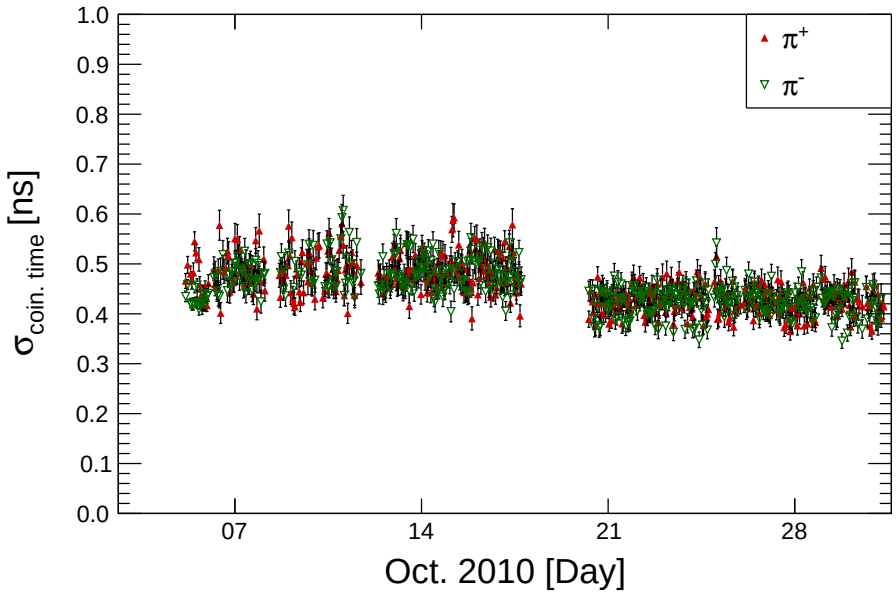

(B) $\sigma_{\text{coin. time}}$

FIGURE 3.29: Time dependence of IH-Tag coincidence time distribution. Each point in the graph shows the results of the fit for each physics run.

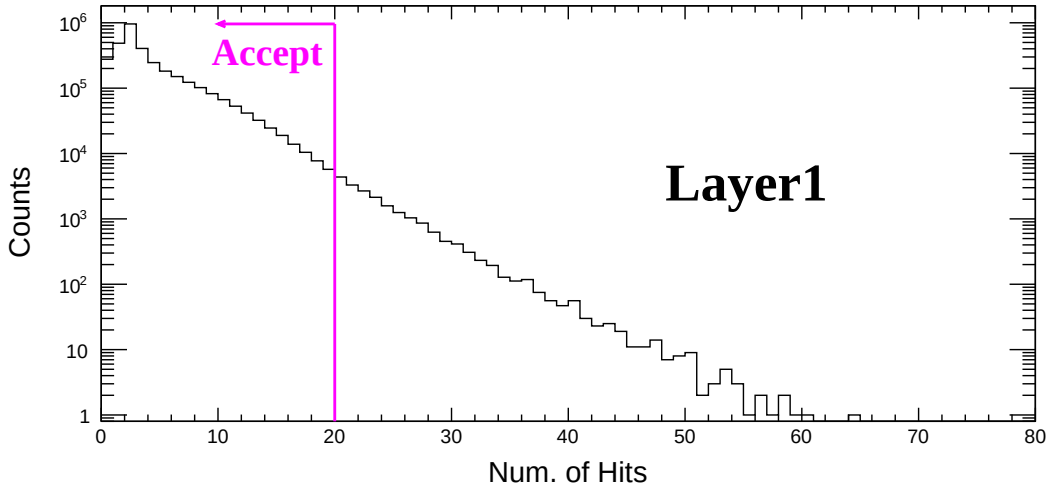

(A) Multiplicity of the most inner layer of VDC (Layer1).

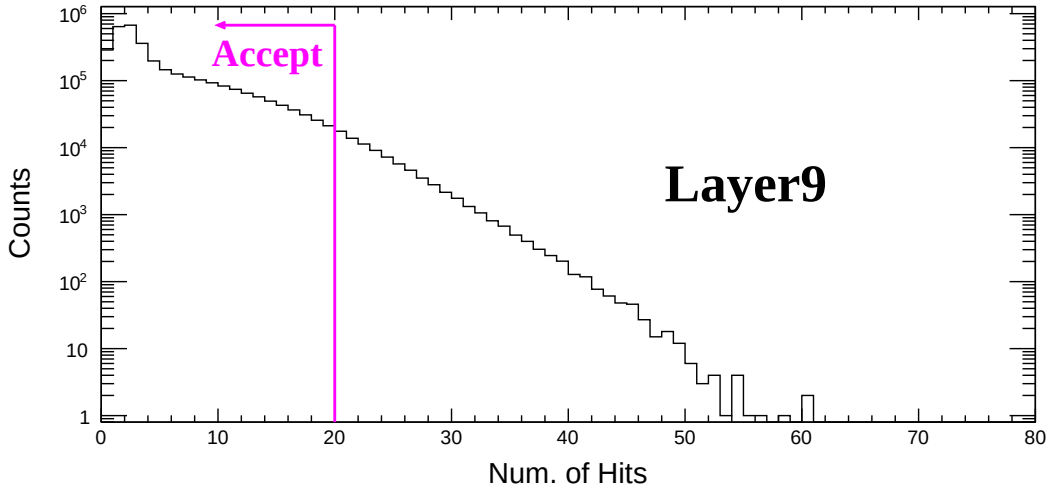

(B) Multiplicity of the most inner layer of CDC (Layer9).

FIGURE 3.30: Drift chamber multiplicity.

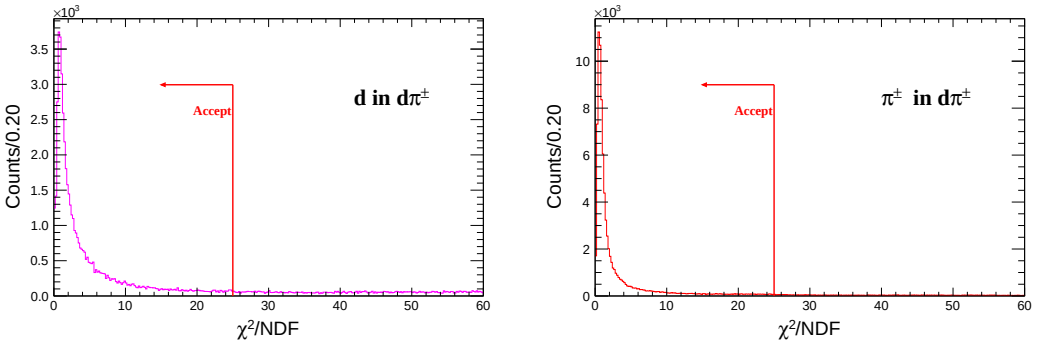

(A) χ^2/NDF of deuteron track

(B) χ^2/NDF of $\pi^{\pm}$ track

FIGURE 3.31: χ^2 distribution normalized by NDF in d$\pi^{\pm}$ vertex. Tracks with $\chi^2/\text{NDF} < 25$ were accepted as good tracks.

3.4.4 Track Selection

χ^2/NDF selection

Tracking χ^2 is defined as,

$$\chi^2 = \sum \left(\frac{dist. - dl}{\sigma_{DC}} \right)^2, \tag{3.18}$$

where $dist.$, dl, and σ_{DC} represent distance between a track and a wire with hit, drift length of the hit, and resolution of drift chambers. Number of degree of freedom (NDF) was defined as,

$$\text{NDF} = (\text{Num. of hit points}) - (\text{Num. of free parameters of the fit function}). \tag{3.19}$$

χ^2/NDF distributions for $d\pi$ vertex events are shown in Fig 3.31. Figure 3.31(A), 3.31(B) show normalized χ^2 distribution of deuteron tracks and π tracks, respectively. Tracks with $\chi^2/\text{NDF} < 25$ were chosen as good tracks and used in further analysis.

Hodoscope Hit Position Selection

As described in Sec. 3.3.4, we used the information on the intersection of the track and scintillator to link the track to the hit information of the hodoscope. The intersection point was determined by defining the sensitive area of the scintillator with a margin from the actual size of the scintillator according to the position resolution of the track. Figure 3.32 shows the distance from the intersection point to the edge of the scintillator. Negative values indicate that the intersection is located on the scintillator surface, while positive values indicate that the intersection is located off the scintillator. It can be seen that the number of events decreases from the origin to the positive value. For the distributions shown in the figure, cuts were made to select events in the regions of <2.0 cm, <5.0 cm, <5.0 cm, and <10.0 cm for IH, OHV forward (segment 1–8), OHV backward (segment 9–12), and OHH, respectively.

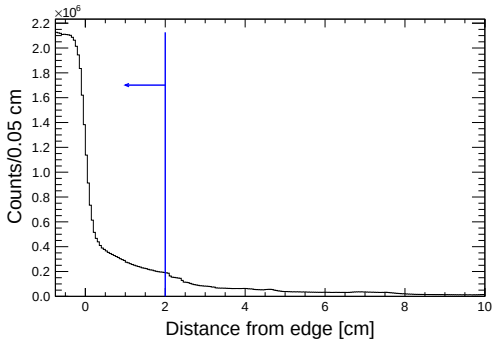

(A) IH

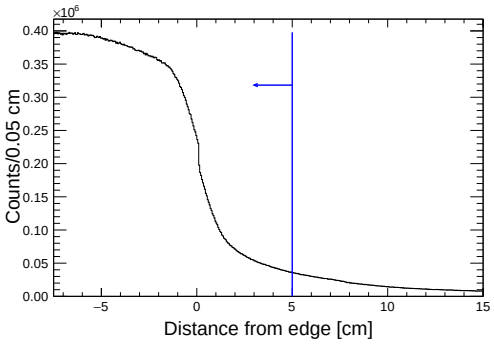

(B) OHV1–8

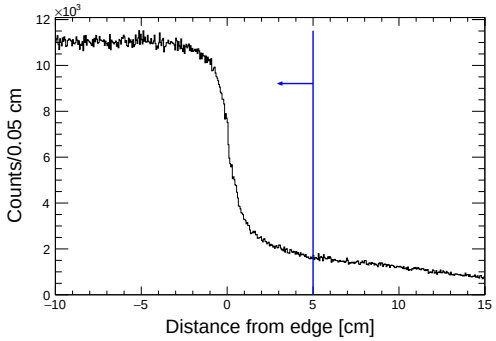

(C) OHV9–12

FIGURE 3.32: Hodoscope hit position residual distributions. The origin of the abscissa represents the edge of scintillators. Negative (positive) values indicate that the intersection is inside (outside) of the scintillator.

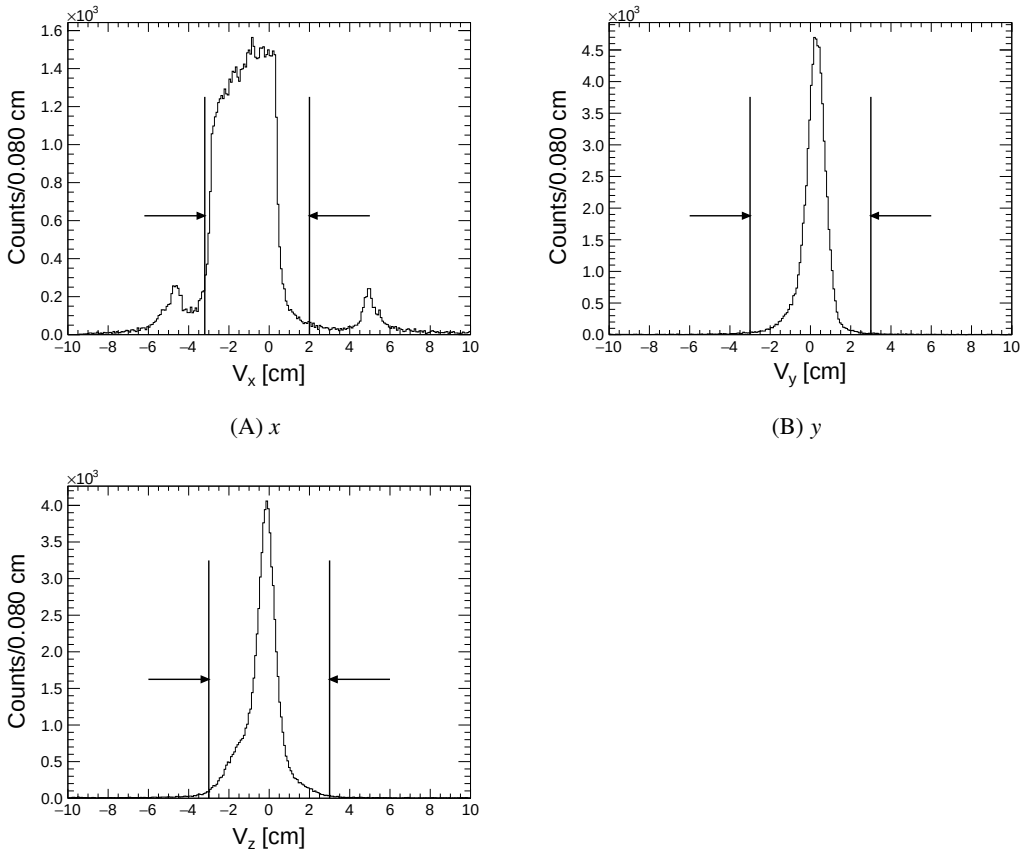

(A) x (B) y

(C) z

FIGURE 3.33: Vertex distributions of $d\pi^{\pm}$ for each axis. Event selection boundaries are shown as solid lines. (A) The x-axis is beam direction. Peaks at $x$pm5 cm correspond to the target windows. (B), (C) y and z axises are horizontal and vertical (gravitational direction) axises, respectively.

3.4.5 Vertex Selection

Event selections were applied on the vertex related variables, vertex positions, DCA, and opening angle of two tracks, to improve the signal to noise ratio.

Vertex Position Selection

Reconstructed vertex position distributions of $d\pi^{\pm}$ are shown in Fig. 3.33. Peaks at $x \sim \pm 5$ cm in Fig. 3.33(A) correspond to the target windows. The events inside the solid lines were accepted as the reaction was occurred inside the target cell. The numerical expression of the vertex position selection is $-3 < v_x < 2 \cap -3 < v_y, v_z < 3$ [cm].

DCA Selection

As it was defined in Sec. 3.3.6, DCA is the distance of closest approach of 2-tracks. DCA selection was used to extract the tracks produced by the same reaction.

Figure 3.34 shows DCA distributions of each vertex type, e^+e^-, $\pi^+\pi^-$, $p\pi^-$, and $d\pi^{\pm}$. The event in DCA < 2 cm region was accepted as true vertex event.

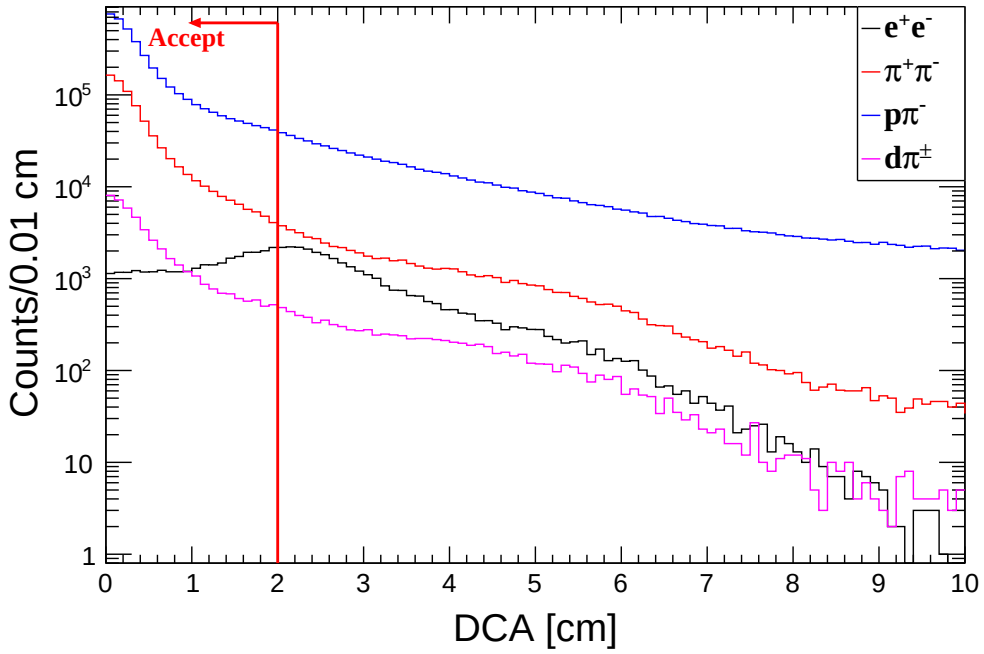

FIGURE 3.34: DCA distribution of each vertex type. Black, red, blue, and magenta lines show opening angle distributions of e^+e^-, $\pi^+\pi^-$, $p\pi^-$, and $d\pi^\pm$, respectively.

Opening Angle Selection

Opening angle cut was also applied as another event selection. It is shown in Fig. 3.35 that an opening angle distribution of each vertex type, e^+e^-, $\pi^+\pi^-$, $p\pi^-$, and $d\pi^\pm$ in the laboratory frame. The distribution of e^+e^- vertex is concentrated in $\cos\theta_{OA} > 0.9$ region. The region in $\cos\theta_{OA} < 0.92$, shown as a red solid arrow, was accepted as $d\pi^\pm$ (or $\pi^+\pi^-$, $p\pi^-$) vertex event. This event selection worked to reduce the large amount of e^+e^- pairs produced in the very forward direction.

3.4.6 Kinematical Event Selection for 3 Track Analysis

Since all final state particles were detected in the 3-track analysis, background can be suppressed by selecting events with satisfying conservation laws of energy and momentum. From the energy of the tagged photon, momenta of the charged particles (d, π^+, and π^-) detected by NKS2, and the total energy, the equations of the conservation laws for the four kinematic variables were available. Since the γ beam axis was taken as the x axis, the four equations of the conservation laws are expressed as,

$$\Delta p_x = p_x^\gamma - p_x^d - p_x^{\pi+} - p_x^{\pi-} = 0, \tag{3.20}$$

$$\Delta p_i = -p_i^d - p_i^{\pi+} - p_i^{\pi-} = 0 \qquad (i = y, z), \tag{3.21}$$

$$\Delta E = E_\gamma + M_d - E_d - E_{\pi+} - E_{\pi-} = 0, \tag{3.22}$$

where ΔX represents a residual of the initial state and final state of a variable X. The distributions of four kinematical variables are shown as Fig. 3.37. Each distribution of ΔX was fitted by a Gaussian with a range of $\mu \pm 1.5\sigma$, where μ and σ were a mean and a standard deviation of the Gaussian. The fit range was obtained by iterating the fitting procedure 6 times.

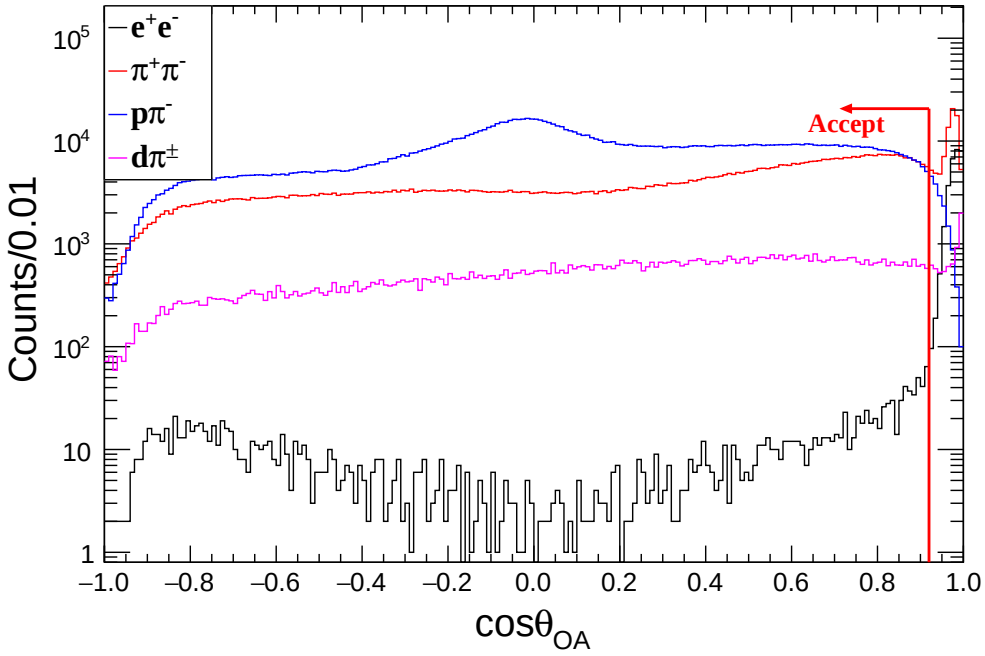

FIGURE 3.35: Opening angle distribution of each vertex type. Black, red, blue, and magenta lines show opening angle distributions of e^+e^-, $\pi^+\pi^-$, $p\pi^-$, and $d\pi^\pm$, respectively. The distribution of e^+e^- vertex is concentrated in $\cos\theta_{OA} > 0.9$ region. The rise at $\cos\theta_{OA} = 0.9$ in the distribution of $\pi^+\pi^-$ vertex is thought to be due to the inclusion of e^+e^- vertex. The region in $\cos\theta_{OA} < 0.92$, shown as a red solid arrow, was accepted as $d\pi^\pm$ vertex event.

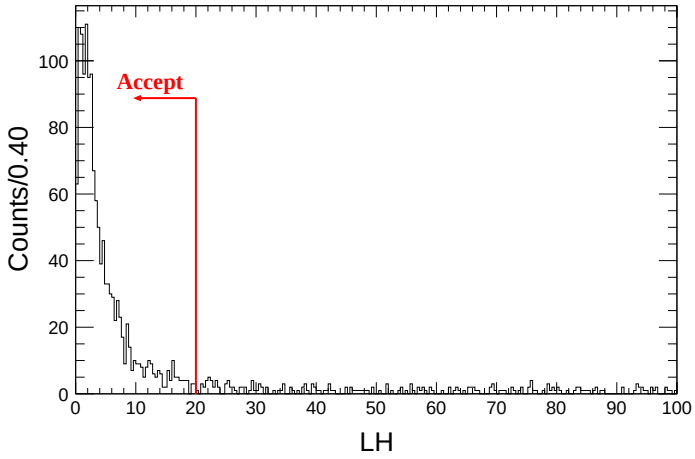

FIGURE 3.36: Distribution of LH. Definition of LH is shown as Eq. 3.23.

Using the respective standard deviations (σ) obtained from the fitted Gaussians, the variable LH is defined as,

$$LH = \left(\frac{\Delta p_x}{\sigma_{px}}\right)^2 + \left(\frac{\Delta p_y}{\sigma_{py}}\right)^2 + \left(\frac{\Delta p_z}{\sigma_{pz}}\right)^2 + \left(\frac{\Delta E}{\sigma_E}\right)^2. \tag{3.23}$$

The distribution of LH is shown as Fig. 3.36. The events in $LH < 20$ region was selected as $\gamma d \to d\pi^+\pi^-$ events.

3.4.7 Kinematical Event Selection for 2 Track Analysis

As the number of over constraint of the $\gamma d \to d\pi^+\pi^-$ reaction by measuring d and single π was only one, a one dimensional cut of missing mass was applied. In addition, deuteron momentum selection was applied to reduce proton misidentified as deuteron.

Missing Mass Selection

In the 2 track analysis, π^+ or π^- are identified by a missing mass method. The missing mass (M_X) is described as,

$$M_X = \sqrt{(E_\gamma + M_{targ} - E_d - E_\pi)^2 - (\boldsymbol{p_\gamma} - \boldsymbol{p_d} - \boldsymbol{p_\pi})^2}, \tag{3.24}$$

where M_{targ} represents the mass of a target particle, deuteron in this analysis. Figure 3.38 shows a distribution of M_X. When M_X is an imaginary value, it is plotted as a negative real number. The region of $0.05 < M_X < 0.25$ [GeV/c^2] was selected as the $\gamma + d \to d\pi^+\pi^-$ reaction event.

Deuteron Momentum Cut

Figure 3.39 shows a momentum distribution of deuteron in the $\gamma d \to d\pi^+\pi^-$ reaction. The region of $mom_d < 1.2$ GeV/c was selected because proton contamination in $mom_d > 1.2$ GeV/c was serious (see Sec. 3.5.1 for detail).

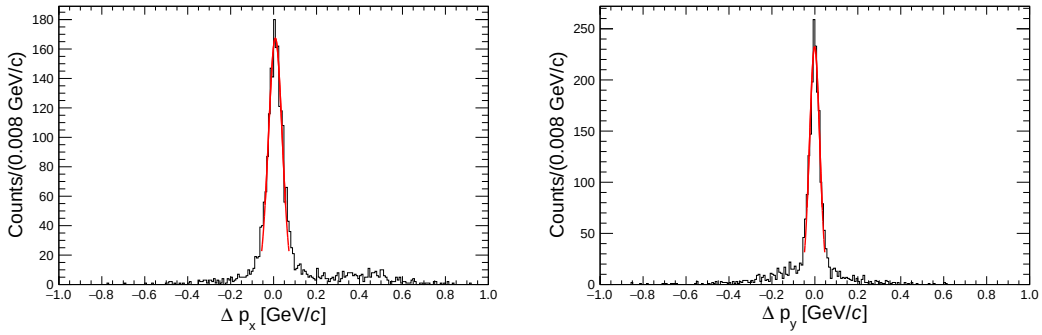

(A) Δp_x (B) Δp_y

(C) Δp_z (D) ΔE

FIGURE 3.37: The distributions of four kinematical variables. (A)-(C)p_x, p_y, p_z. (D) Total energy E. Red solid lines show fitted Gaussians.

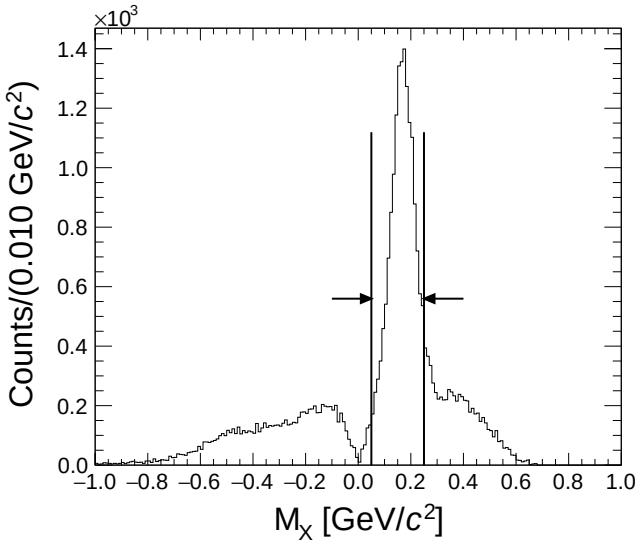

FIGURE 3.38: Missing mass distribution of the $\gamma d \rightarrow d\pi^{\pm}X$. Boundaries of the $\gamma d \rightarrow d\pi^{+}\pi^{-}$ reaction are shown as black solid lines. Imaginary numbers of M_X were projected on the negative value regions.

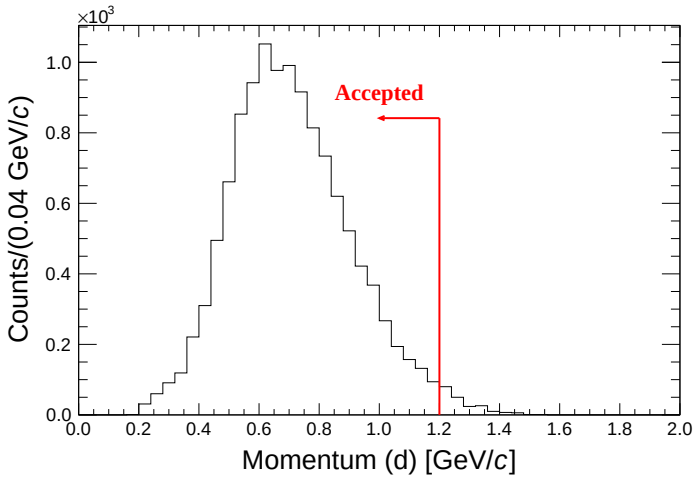

FIGURE 3.39: Deuteron momentum distribution in the $\gamma d \to d\pi^+\pi^-$ reaction.

TABLE 3.2: Summary of $d\pi^+\pi^-$ event selection

Cut	condition	efficiency	stat. error	syst. error
DC Multiplicity	$\mathrm{nHit}_{\mathrm{Layer}} < 20$	0.85	<0.001	-
Mass of d	$1.6 < m_d < 2.1$ [GeV/c^2]	0.89	0.002	0.01
Mass of π	$m_\pi < 0.14$	0.95	0.002	0.005
dE/dx of d	See Sec. 3.4.2	0.97	0.001	<0.01
Coin time of d	$-1.25 < t < 3.0$ [ns]	0.99	0.001	-
Coin time of pi	$-2.0 < t < 2.0$ [ns]	0.99	0.001	-
Tracking χ^2	$\chi^2/ndf < 25$	0.85	0.003	0.01
Hodoscpe hit poisition	< 2 cm (IH), < 4 cm (OH)	0.99	0.003	-
Vertex position	$-3 < v_x < 2 \cap -3 < v_y, v_z < 3$ [cm]	0.96	0.002	0.01
DCA	< 2 cm	0.99	0.001	0.01
Opening angle	$\cos\theta_{OA} < 0.92$	0.99	0.001	0.01
Missig mass of π	$0.05 < M_X < 0.25$ [GeV/c^2]	0.65	0.003	0.02
Momentum of d	< 1.2 GeV/c	>0.99	<0.001	<0.01
Total		0.41	0.01	0.03

3.4.8 Summary of Event Selection

The analysis efficiency for each cut is shown in Tab. 3.2. The efficiencies were estimated by relaxing each cut one by one. The uncertainties of total event selection were estimated by quadratic sum of all event selection efficiencies.

3.5 Background Estimation

Due to finite detector resolutions, contaminations of backgrounds were inevitable. Major background distributions are estimated in this section. The backgrounds are subtracted in the final invariant mass and angular distribution spectra shown in Chapter4.

3.5.1 $p\pi X$ Contamination

Even after $d\pi^+\pi^-$ selection as described in Sec. 3.4, $p\pi X$ contamination was inevitable especially in the higher deuteron momentum region ($p > 0.8$ GeV/c), although kinematic constraints (energy and momentum conservation) served to reject most of these contamination. Contamination of the $p\pi X$ events was estimated by using the number of protons in the deuteron mass region after applying kinematical cuts. The background consisted of $p\pi^+\pi^-$, $p\pi^\pm\pi^0$ events and so on. The $p\pi^+\pi^-$ background was dominant in the 3-track analysis. Proton contamination in π^+ mass region, thus the event of $\pi^+\pi^+\pi^-$ or $pp\pi^-$ misidentified as $d\pi^+\pi^-$, was also estimated and found negligible (<0.1%).

Response Function of the Proton Mass Square Distribution

Deuteron and proton were discriminated by using the mass square as described in Sec. 3.4.2. In order to estimate the number of protons in the deuteron mass region, the response function of the proton mass square distribution was estimated. The mass square distribution of the proton was obtained by selecting the proton tracks with the correlation between the momentum and dE/dx at IH and OH. Figure 3.40 shows the correlation between the momentum and dE/dx at IH (Fig. 3.40(A)) and OH (Fig, 3.40(B)). The events in the region between 2 black solid lines of each distribution were selected as proton tracks. The mass square distribution for proton obtained after the selection by dE/dx at IH and OH is shown in Fig. 3.41. The several functions were tested to fit the tail component of the proton mass square: 2nd order polynomial, exponential, and $\exp(1/x)$. The fitted results of the functions are shown as a red dotted line, a blue dashed line, and a magenta solid line in Fig 3.41. It is clear that the 2nd order polynomial function and the exponential function do not fit the shape of the tail component, and the $\exp(1/x)$ function reproduces the tail component reasonably well. Therefore, $f_p(m^2) = p_0 \exp(p_1/m^2)$ was chosen to estimate the contamination of proton in the deuteron mass region, where the parameters, p_0, p_1, were determined by the fit.

Estimation of the Quantity of $p\pi X$ Contamination

Figure 3.42 shows the correlation between mass square in proton and deuteron region and momentum after applying cuts for the $d\pi^+\pi^-$ selection described in Sec. 3.4, except for the deuteron mass and momentum cuts. Figure 3.42(B) shows the projection of Fig. 3.42(A) to the axis of mass squared for the momentum below 1.2 GeV/c. Solid lines show the results of the fit by summing the proton tail component function $f_p(m^2)$ determined in the previous section and the deuteron response function defined by the convoluted function of the Landau and Gaussian functions. The results of separating the proton and deuteron components by using the parameters obtained from the fit are shown as dashed and single-dotted lines, respectively. The response function of the deuteron was determined based on the simulation. From this result, the proton contamination ratio in the deuteron mass region which was indicated by the magenta arrows in Fig 3.42(B) was estimated as 4% (695 events). The proton contamination ratio for each deuteron momentum region was estimated, and the result is summarized in Tab. 3.3. The boundaries of deuteron momentum regions are indicated by red dashed lines in Fig. 3.42. The mass square distribution for each momentum region is shown in Appendix B.2.

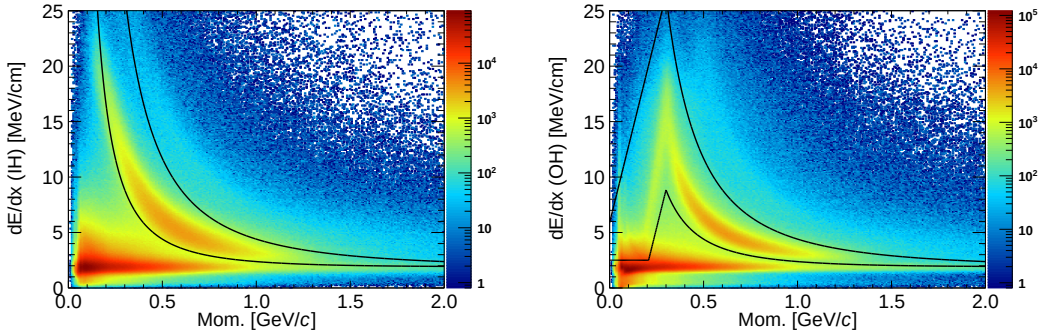

(A) dE/dx at IH vs momentum.

(B) dE/dx at OH vs momentum.

FIGURE 3.40: The correlations between the momentum and dE/dx at (A) IH and (B) OH. Black solid lines indicate boundaries of proton selection by dE/dx. The curves of the black solid lines were computed by Bethe-Bloch formula with assuming mass of the particle 0.75, 1.50 GeV/c^2. The straight lines in the right figure in < 0.3 GeV/c were defined to select the tracks which was stopped inside of OH.

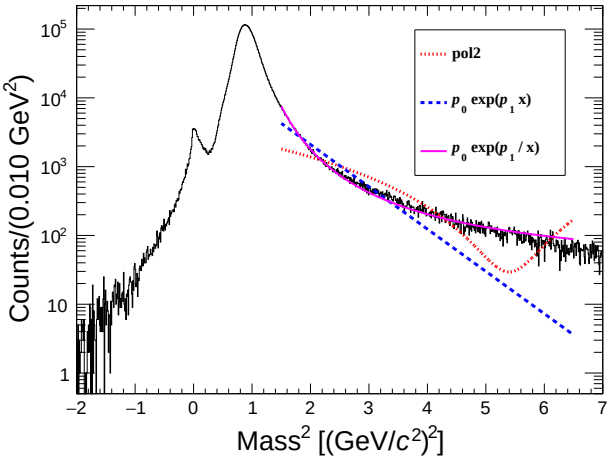

FIGURE 3.41: Mass square distribution of proton with fitted functions.

TABLE 3.3: $p\pi X$ contamination ratio for each momentum region.

Momentum range [GeV/c]	deuteron [%]	proton tail [%]
<0.4	98	2
0.40–0.50	97	3
0.50–0.60	97	3
0.60–0.70	97	3
0.70–0.80	96	4
0.80–0.90	95	5
0.90–1.00	89	11
1.00–1.10	83	17
1.10–1.20	79	21
>1.20[1]	15	85
Total (<1.20 GeV/c)	96	4

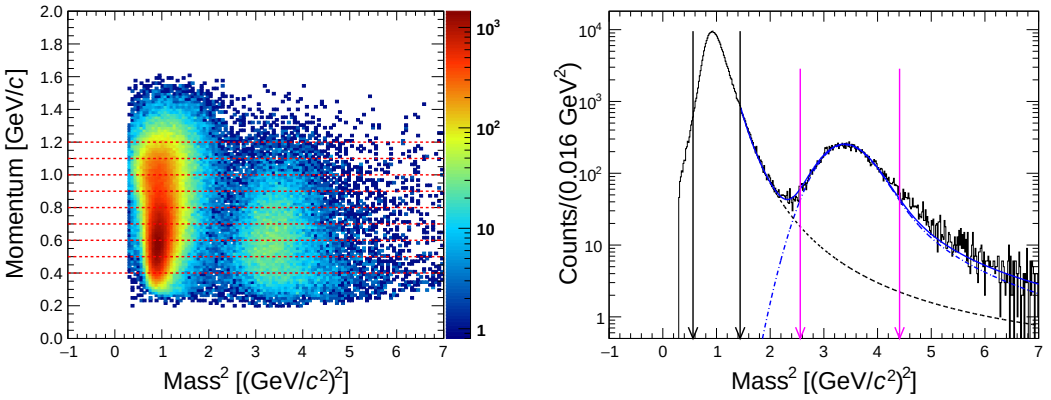

(A) Mass square v.s. momentum

(B) Mass square distribution of $Mom. < 1.2$ GeV$/c$.

FIGURE 3.42: $p\pi X$ in momentum of deuteron and proton in the 2-track analysis with the $d\pi^+\pi^-$ selection. (A) Correlation between the mass square and the momentum of proton and deuteron after applying kinematical event cut in 2 track analysis. Dashed lines show . (B) The mass square distributions sliced by the momentum. Magenta and black arrows show the nominal mass selection region of deuteron and proton, respectively.

Contamination in Invariant Mass Spectra and Angular Distribution

Proton contaminations in the invariant mass spectra and angular distributions of deuteron were estimated by gating proton mass region instead of deuteron mass region in mass square distribution (fake proton selection). Mass gates for nominal deuteron selection and fake proton selection are shown as magenta arrows and black arrows in Fig. 3.42(B), respectively. Figure 3.43 shows three invariant mass spectra and an angular distribution of deuteron for all incident photon energy region.

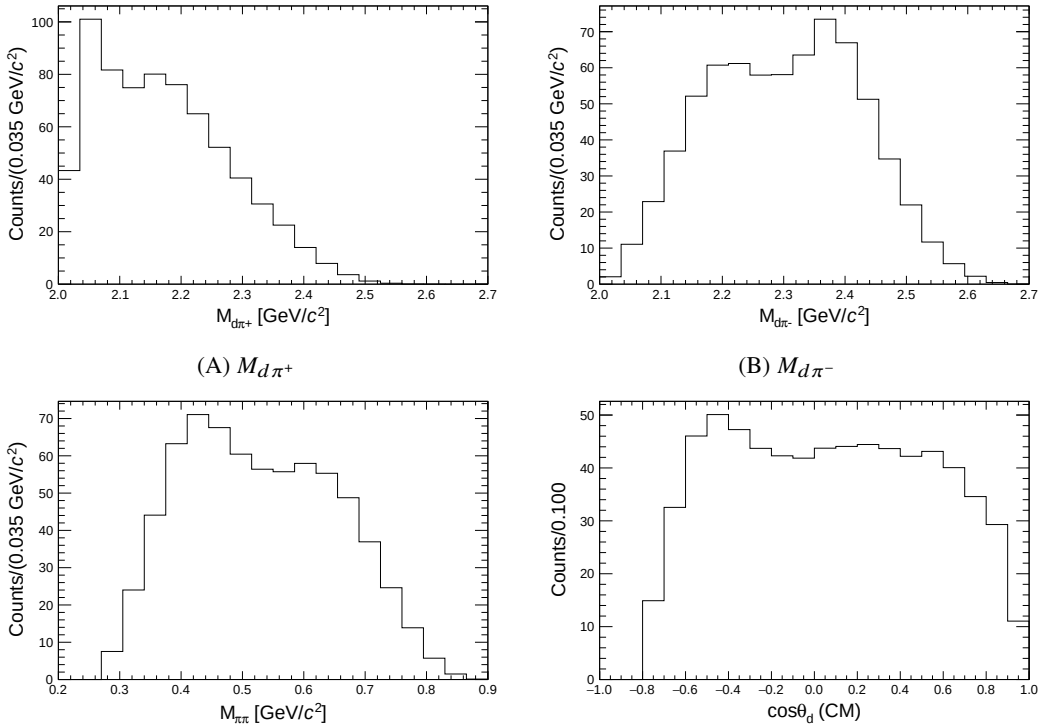

(A) $M_{d\pi^+}$ (B) $M_{d\pi^-}$

(C) $M_{\pi\pi}$ (D) $\cos\theta_d$ (γd CM frame)

FIGURE 3.43: Three invariant mass spectra and an angular distribution of deuteron for all incident photon energy regions. The spectra were scaled to make the total number of the each histogram was scaled to 695.

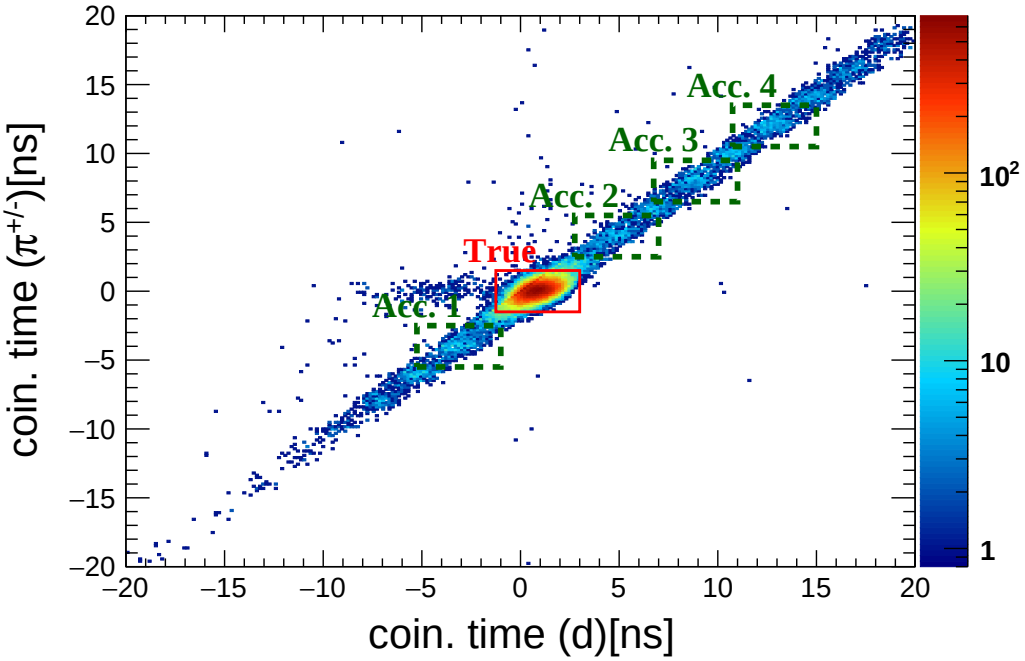

FIGURE 3.44: Coincidence time ($d\pi\pi$)

3.5.2 Accidental Background

In the spectra of IH and Tagger coincidence time, bunch structure which corresponds to RF frequency (~500 MHz) can be seen. That suggested that untagged photon events were contaminated in true coincidence time window region. To estimate the distribution and amount of accidental background, off-time gate analysis was performed. Figure 3.44 shows correlation of coincidence time of deuteron and coincidence time of pion in the 2-track analysis. The region surrounded by red solid lines was selected as true coincidence events and the regions surrounded by green dashed lines were chosen as accidental coincidence events. The amount of accidental coincidence events were estimated approximately 1% in true coincidence region (<150 events) by averaging of the number of events in the four accidental coincidence regions.

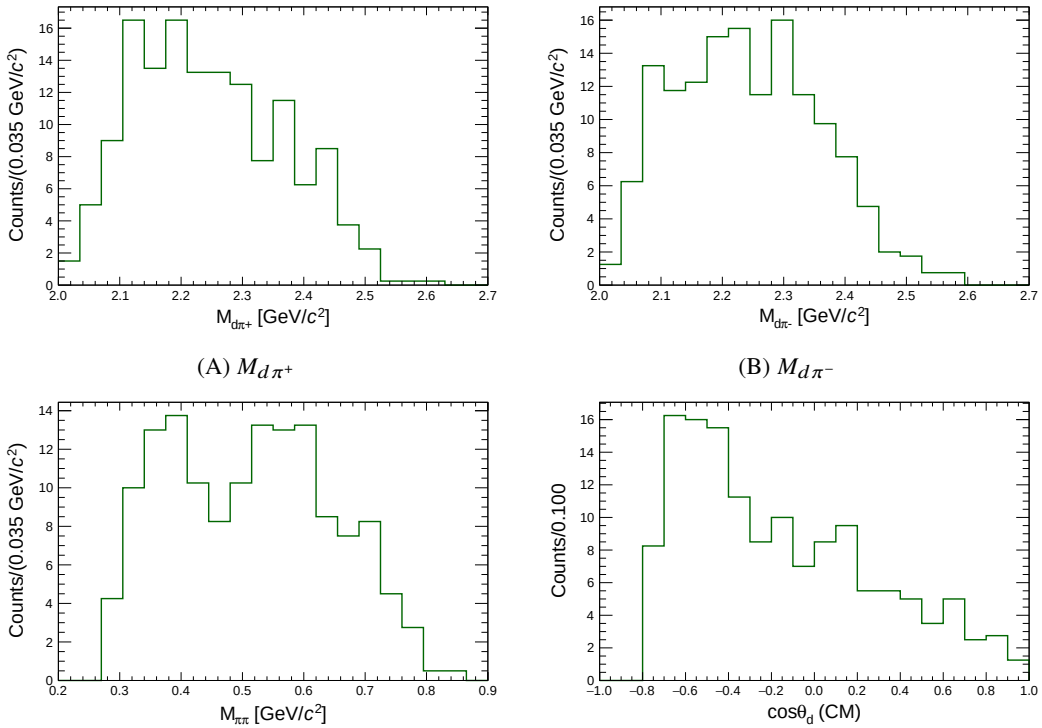

(A) $M_{d\pi^+}$ (B) $M_{d\pi^-}$

(C) $M_{\pi\pi}$ (D) $\cos\theta_d$ (γd CM frame)

FIGURE 3.45: Three invariant mass spectra and angular distribution of deuteron for all incident photon energy regions.

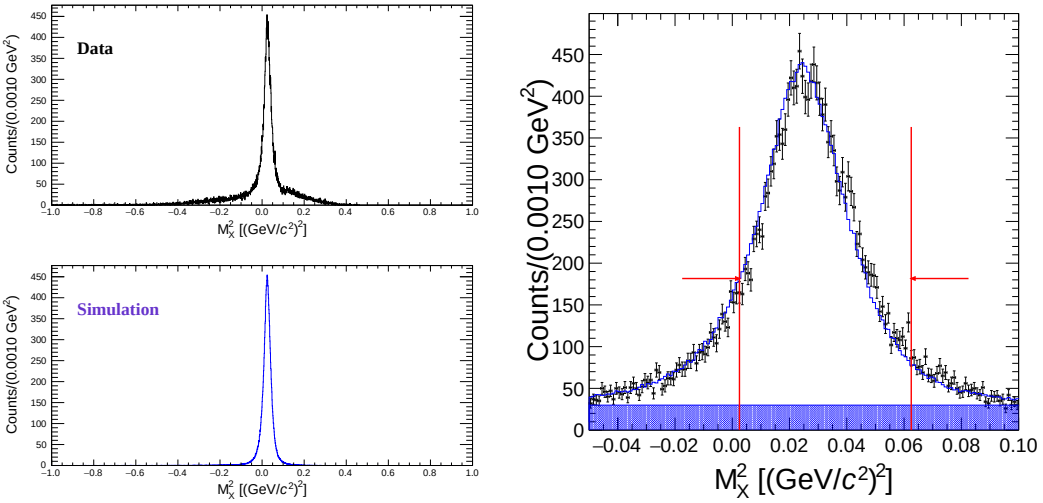

(A) M_X^2 (B) M_X^2

FIGURE 3.46: Square of missing mass of the $\gamma d \rightarrow d\pi^2 X$ (M_X^2). (a) Upper and lower panels show M_X^2 distributions of real data and simulated data, respectively. (b) The real data M_X^2 distribution (black crossed points) was fitted by the simulated distribution (blue solid line) and constant background (hatched histogram). Red solid lines show the boundary of the event selection corresponding to $0.05 < M_X < 0.25$ GeV/c^2.

3.5.3 Background Estimation by Using the Missing Mass Distribution

We also estimated the signal-to-noise ratio from the missing mass distribution. The upper panel of Fig. 3.46(A) shows square of missing mass expressed as,

$$M_X^2 = (E_\gamma + M_{targ} - E_d - E_\pi)^2 - (\boldsymbol{p_\gamma} - \boldsymbol{p_d} - \boldsymbol{p_\pi})^2, \tag{3.25}$$

where M_{targ} represents the mass of deuteron. The lower panel shows a M_X^2 distribution produced by the simulation of the $\gamma d \rightarrow d\pi^+\pi^-$ reaction. The event generator of the simulation was tuned to reproduce the kinematics of the read data (See Sec. 3.6.1 for detail). The M_X^2 distribution of the real data was fitted by that of the simulated data and constant background in the region of $-0.05 < M_X^2 < 0.10$ (GeV/c^2)^2. Figure 3.46(B) shows the fitting result. The black crossed points represent the real data. The blue solid line shows the simulated distribution with scaling and offset. The offset is shown as a blue hatched histogram. Red solid lines show the boundary of the event selection corresponding to $0.05 < M_X < 0.25$ GeV/c^2 as explained in Sec. 3.4.7.

The number of background events in the accepted region was estimated to 1830 ± 40. About 850 of these events can be explained by the $p\pi X$ contamination and the accidental background as shown in the previous section. Thus, about 1000 background events have not been identified. This background contribution is removed by scaling, such as the invariant mass spectra since there is a risk of a strong bias when estimating the contribution to the invariant mass spectra from sidebands of the missing mass spectrum. In addition, since the source of the background event is not clear, the contribution of this background event is treated with a systematic error of 100% as 500 ± 500 ($syst.$).

3.6 Acceptance Estimation

Geant4 simulation was performed to estimate the acceptance of NKS2. The simulator was adjusted to reproduce the various kinematic distributions obtained from the real data, and the acceptance were estimated using the simulator. The same analysis procedure for the real data were applied to the simulation data including detectors' efficiencies and resolutions. The acceptance (η_{acpt}) was estimated as the fraction of events generated by the simulation that were identified as being the $\gamma d \rightarrow d\pi^+\pi^-$ reaction by the analyzer as,

$$\eta_{acpt} = \frac{\text{Number of } d\pi^+\pi^- \text{ identified event.}}{\text{Number of generated event}}. \tag{3.26}$$

3.6.1 Event Generation

In the $\gamma d \rightarrow d\pi^+\pi^-$ reaction, there are nine degrees of freedom for the momentum components of the three particles in the final state, and four constraints from the energy and momentum conservation laws. In addition, symmetry in the direction of rotation about the beam axis reduces the number of degrees of freedom by one. Thus, the kinetics of the reaction can be specified by using the distribution of the four kinetic variables for a fixed incident photon energy. For each photon incident energy region, the event generator was tuned to reproduce the three invariant mass distributions ($M_{d\pi^+}$, $M_{d\pi^-}$, $M_{\pi\pi}$) and the angular distribution of the deuteron in the γd-center-of-mass system ($\cos\theta_d$ (CM)) which were obtained from real data. In the simulation, the weighted event generation against uniform distributions in a phase space was performed using enhancement factors $f_X(M_X,\ E_\gamma)$ that were functions of the incident photon energy (E_γ) and each kinematic variables (X). The probability density distribution used for event generation, $F(E_\gamma,\ M_{d\pi^+},\ M_{d\pi^-},\ M_{\pi\pi},\ \cos\theta_d\ (\text{CM}))$, is described as,

$$\begin{aligned} &F(E_\gamma,\ M_{d\pi^+},\ M_{d\pi^-},\ M_{\pi\pi},\ \cos\theta_d\ (\text{CM})) = \\ &V_{PS}(E_\gamma)\cdot f_{d\pi^+}(M_{d\pi^+},\ E_\gamma)\cdot f_{d\pi^-}(M_{d\pi^-},\ E_\gamma)\cdot f_{\pi\pi}(M_{\pi\pi},\ E_\gamma)\cdot f_{\cos\theta_d}(\cos\theta_d\ (\text{CM}),\ E_\gamma), \end{aligned} \tag{3.27}$$

where $V_{PS}(E_\gamma)$ is a flat distribution in phase space. The acceptances of NKS2 were evaluated based on the simulation with the tuned event generator.

Tuning Process

As explained in Sec. 3.6.1, the enhancement factors were applied to the three invariant mass and angular distributions for each incident photon energy to reproduce the real data with respect to the uniform distribution in three-body phase space. Figure 3.47 shows the comparison of the invariant mass and angle distributions in each TagB region for the simulation of uniform event generation in a three-body phase space (red points), the tuned simulation (blue points), and real data (black lines). Though only the distributions of TagB1 and TagB12 were shown in Fig. 3.47, distributions of other TagB segment region are shown in Appendix **??**. Each histogram was normalized so that the total number of entries was 1. The abscissas of the invariant mass distributions were also normalized so that the upper limit in the phase space was 1 and the lower limit was 0, making it a dimensionless quantity. For the invariant mass spectra of $d\pi^\pm$ and $\pi\pi$, the normalized invariant masses $\overline{M^{norm}_{d\pi^\pm}}$ and $\overline{M^{norm}_{\pi\pi}}$

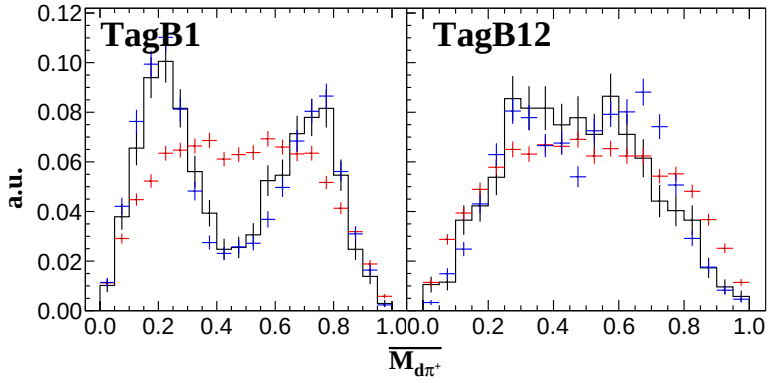

(A) $d\pi^+$ normalized invariant mass.

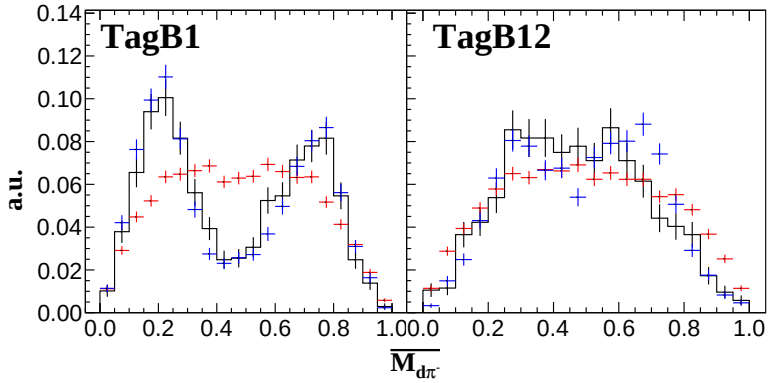

(B) $d\pi^-$ normalized invariant mass.

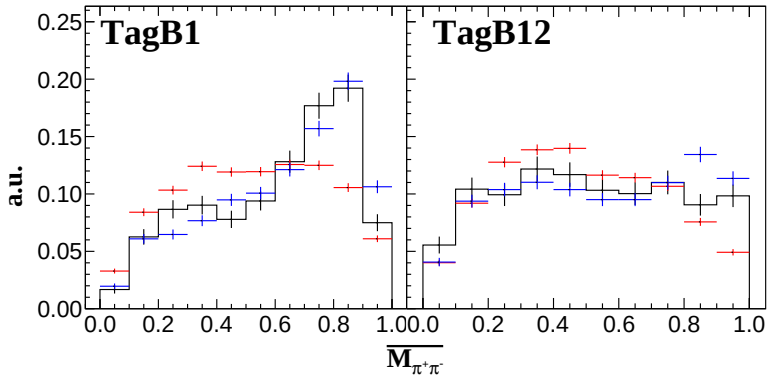

(C) $\pi^-\pi^+$ normalized invariant mass.

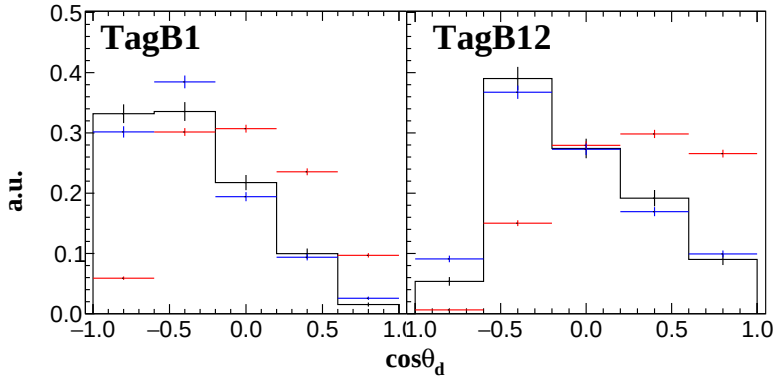

(D) $\cos\theta_d$ in γd-CM frame.

FIGURE 3.47: Normalized invariant mass spectra and angular distribution of deuterons. Black lines, red points, and blue points show the distributions of real data, the three-body phase space simulation, and the tuned simulation, respectively. (A)$d\pi^+$ (B) $d\pi^-$ (C) $\pi^-\pi^+$ (D) $\cos\theta_d$ in γd-CM frame.

were defined as,

$$\overline{M^{norm}_{d\pi^{\pm}}} = \frac{M_{d\pi^{\pm}} - (M_\pi + M_d)}{W - (M_d + 2M_\pi)}, \tag{3.28}$$

$$\overline{M^{norm}_{\pi\pi}} = \frac{M_{\pi\pi} - 2M_\pi}{W - (M_d + 2M_\pi)}, \tag{3.29}$$

where M_d and M_π represent mass of deuteron and charged pion, respectively. W is total energy of γd system. To determine the parameters of the enhancement factor functions, the ratio of the distribution of simulated data to that of real data was calculated for each distribution and fitted by each function.The fit functions for each distribution were defined as,

$$f(\overline{M^{norm}_{d\pi}}) = \frac{p_0}{(\overline{M^{norm}_{d\pi}} - \overline{\mu})^2 + \overline{\Gamma}^2} + \frac{p_1}{(\overline{M^{norm}_{d\pi}} - \overline{\mu})^2 + \overline{\Gamma}^2}, \tag{3.30}$$

$$f(\overline{M^{norm}_{\pi\pi}}) = p_0(\overline{M^{norm}_{\pi\pi}} - p_1)^2 + p_2, \tag{3.31}$$

$$f(\cos\theta_d\ (\mathrm{CM})) = \exp(p_1(\cos\theta_d\ (\mathrm{CM}) + 1)), \tag{3.32}$$

where $\overline{\mu}$ and $\overline{\Gamma}$ represent mean value and width of resonance like distribution in $d\pi^{\pm}$ invariant mass distributions, respectively. They were fixed at $\mu = 2.13\,\mathrm{GeV}/c^2$, and $\Gamma = 0.085\,\mathrm{GeV}/c^2$. These values were set manually to reproduce the invariant mass distributions. These values were converted to $\overline{\mu}$ and $\overline{\Gamma}$ by using Eq. 3.28 as,

$$\overline{\mu} = \frac{\mu - (M_d + M_\pi)}{W - 2M_\pi - M_d}, \tag{3.33}$$

$$\overline{\Gamma} = \frac{\Gamma}{W - 2M_\pi - M_d}. \tag{3.34}$$

Each parameter was defined to be smooth with respect to incident photon energy, E_γ, as,

$$p_i = \alpha_i E_\gamma + \beta_i. \tag{3.35}$$

By fitting the distributions for each E_γ region with the functions of Eq. 3.30, 3.31, and 3.32, tentative p_i for each E_γ was obtained. E_γ was classified 12 regions correspond to the region covered by a single TagB segment. Then, parameters α_i and β_i were derived by fitting tentative p_is with a linear function of E_γ, and p_is were redefined as a function of E_γ.

Since the each enhancement factor couples to each other, the parameters were determined by iterating the event generation and fitting process through a phase space uniform simulation as a starting point. At this iteration process, when fitting to determine the enhancement factor for each distribution, an event generator was used with the enhancement factor for the target distribution to be set to 1. The enhancement factors for the other distributions were obtained from the previous fitting process. For example, when tuning the enhancement factor for the invariant mass distribution of $d\pi^+$, an event generator with $f_{d\pi^+}(M_{d\pi^+},\ E_\gamma) = 1$ was used. Figure 3.48 shows the results of the fit of each distribution after the fifth iteration. χ^2 was introduced as a measure of agreement between the data and the simulation, and its correlation with the number of fitting iterations was examined. χ^2 was defied as,

$$\chi^2 = \sum_X \sum_{TagB_i} \sum_{bin=0}^{nbin} \frac{(N_{Data} - N_{Sim.})^2}{\sigma^2_{Data} + \sigma^2_{Sim.}}, \tag{3.36}$$

where X express each kinematic variables, $M_{d\pi+}$, $M_{d\pi-}$, $M_{\pi\pi}$, and $\cos\theta_d$. N_{Data} and $N_{Sim.}$ are the number of normalized counts for each bin of the real data histograms and that of the simulated histograms in Fig. 3.47, respectively. σ_{Data}. and$\sigma_{Sim.}$ are their statistical errors.

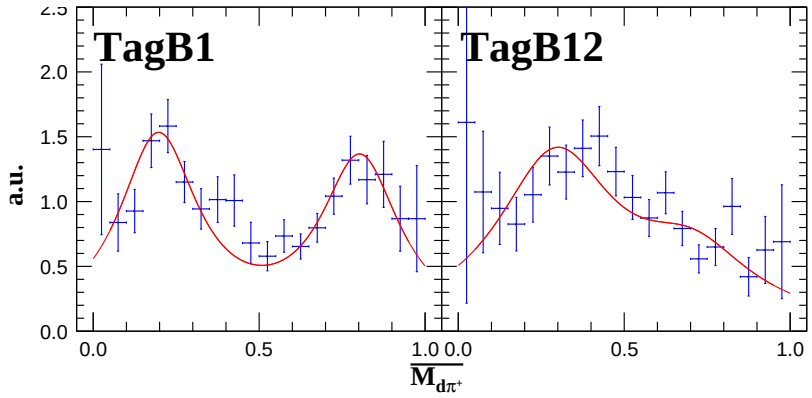

(A) $d\pi^+$ normalized invariant mass.

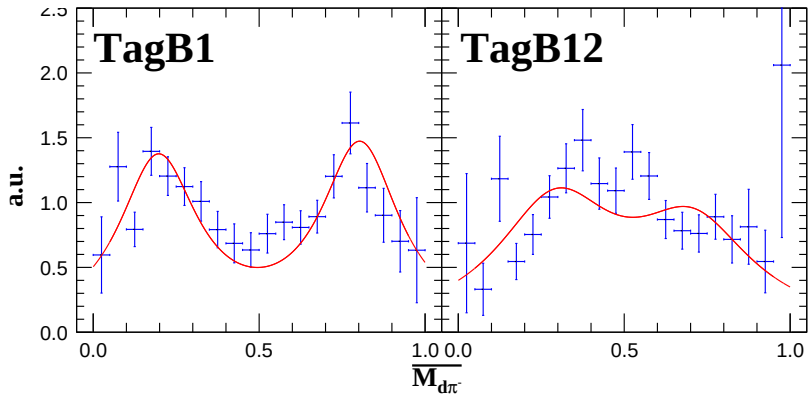

(B) $d\pi^-$ normalized invariant mass.

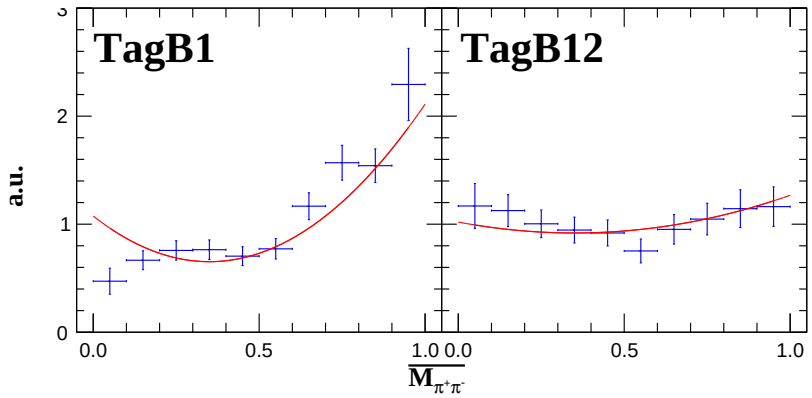

(C) $\pi^-\pi^+$ normalized invariant mass.

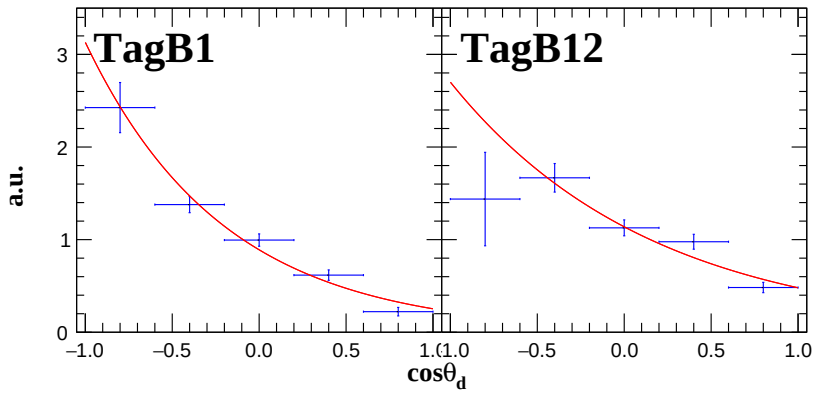

(D) $\cos\theta_d$ in γd-CM frame.

FIGURE 3.48: Normalized invariant mass spectra and angular distribution of deuterons. Fit results are shown as red solid lines. (A)$d\pi^+$ (B) $d\pi^-$ (C) $\pi^-\pi^+$ (D) $\cos\theta_d$ in γd-CM frame.

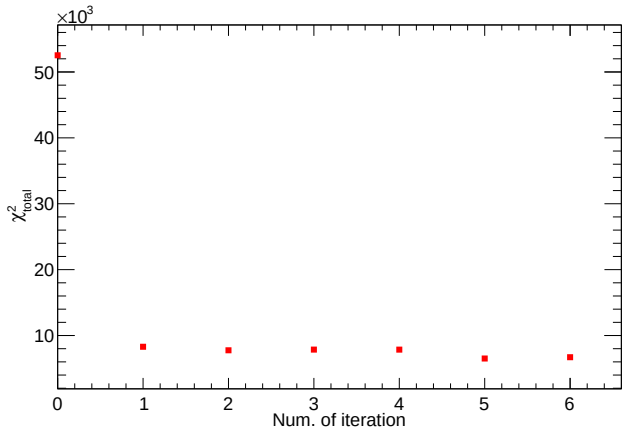

FIGURE 3.49: χ^2 distribution of normalized invariant mass and deuteron angular distribution spectra. The number of degree of freedom was 680.

$TagB_i$ is a segment of each TagB, from 1 to 12. $nbin$ is the number of bins for each distribution, 20, 20, 20, and 5 for $M_{d\pi+}$, $M_{d\pi-}$, $M_{\pi\pi}$, and $\cos\theta_d$, respectively. Figure 3.49 shows correlation of χ^2 and the number of iteration. After the first tuning, it have already reached an almost plateau region. The event generator after performing 6 times tuning iteration was used as a nominal event generator for the acceptance estimation. Figure 3.50 shows a comparison between the simulations and the real data of momentum distributions reconstructed by the analyzer without before energy loss correction (Sec. 3.3.5). Though the deuteron momentum was not explicitly incorporated in the tuning of the simulation, the tuned simulation reproduces well the real data. The angular distributions are shown in Fig B.4. That confirmed that our generator reproduced the real data well.

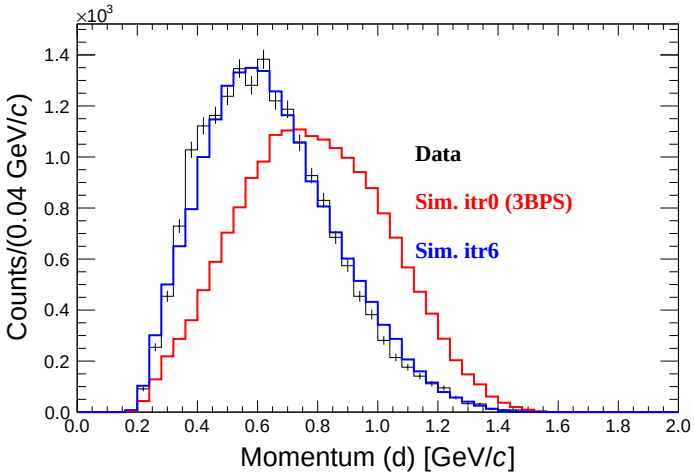

(A) Deuteron

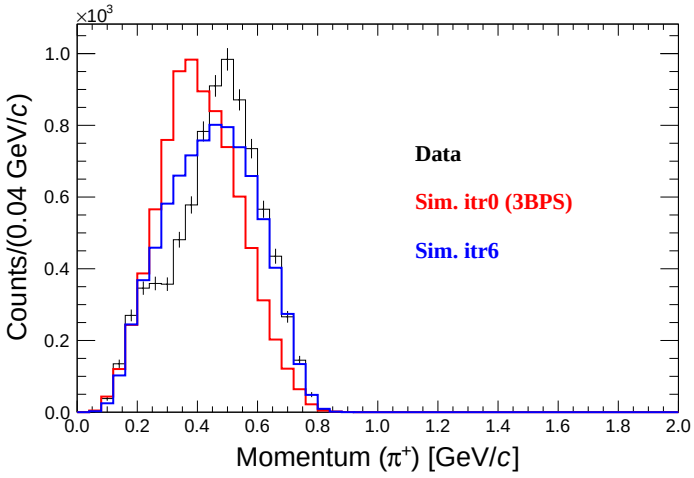

(B) π^+

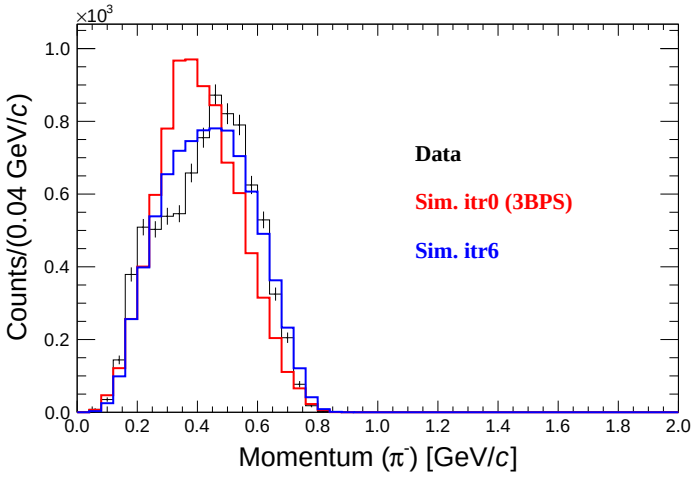

(C) π^-

FIGURE 3.50: Momentum distributions reconstructed by the analyzer for deuteron (A), π^+ (B), and π^- (C) in the $\gamma d \to d\pi^+\pi^-$ reaction. Black line distribution was obtained from real data. Red line distribution was obtained from a simulation before tuning (3-body phase space decay). Blue line distribution was obtained from a simulation after tuning (6 times iteration).

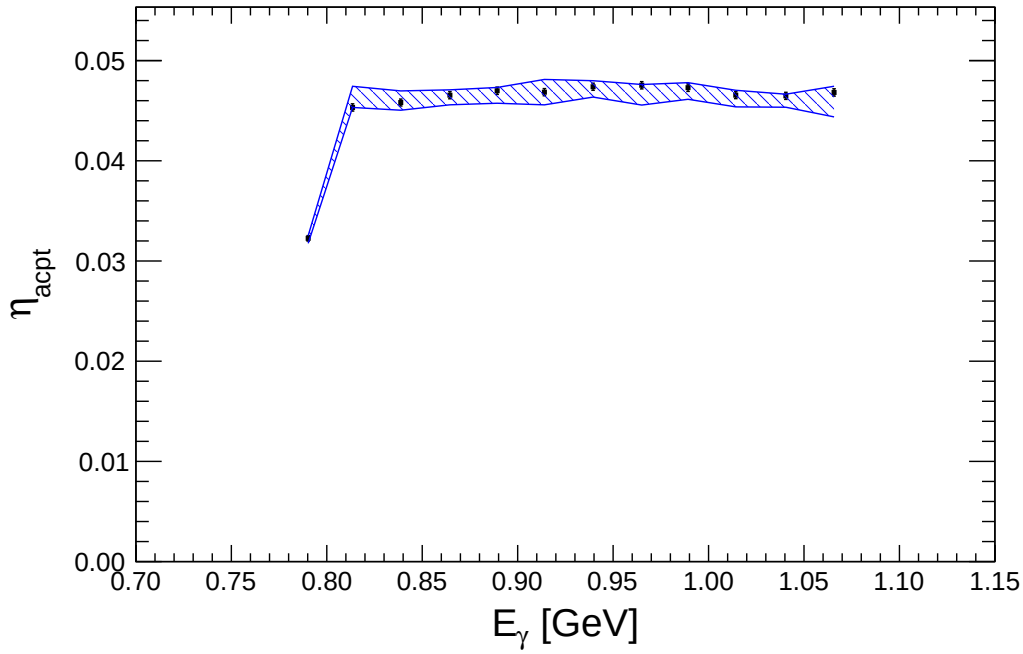

FIGURE 3.51: η_{acpt}^{Total} for each TagB segment. Blue shaded region indicates systemetic uncertainty of η_{acpt}^{Total}. The typical uncertainty is ±5%.

3.6.2 η_{acpt} estimation

We were able to create a simulator that reproduces the real data, this simulator was used to estimate the acceptance. The simulator was used to estimate η_{acpt}^{Total}, which was used to evaluate the total cross section, and η_{acpt}^{Diff}, which was used to evaluate the differential cross section. It should be noted that η_{acpt}^{Total} and η_{acpt}^{Diff} were evaluate in a limited kinematic region with $|t| > 0.15$ GeV^2, where t is the Mandelstam variable expressed as $t = P_\gamma - P_{\pi\pi}$ with four vectors of incident photon (P_γ) and 2-pion system ($P_{\pi\pi}$). This was because deuteron with < 400 MeV/c that corresponds to about $|t| < 0.15$GeV^2 does not reach OH due to energy loss during flight and is not included obtained data. The extrapolation to the $|t| < 0.15$ GeV^2 region is discussed in Sec. 5.3.1.

To evaluate the total cross section, η_{acpt}^{Total} were determined for each TagB segment. Figure 3.51 shows energy dependence of η_{acpt}^{Total}. In order to evaluate the differential cross section, the acceptances of the invariant mass distributions and the angular distribution of deuterons were evaluated for each bin of the distribution and each TagB segment as shown in Fig. 3.52.

3.6.3 Systematic Uncertainty of the Acceptance of NKS2

Systematic uncertainty of η_{acpt}^{Total} for each incident photon energy region was evaluated by changing the tuned event generator. For the invariant mass distributions, the cross section values do not change significantly with or without the enhancement factor. The systematic uncertainty due to the deuteron angular distributions generated by the simulation were estimated by deliberately generating events that were more forward or backward peaked than the real data since by the flat distribution of $\cos\theta_d$ ($f_{\cos\theta_d} = 1$). Specifically, the systematic error was estimated from the change in χ^2 when the offset parameter β_1 in $f_{\cos\theta_d}$ was varied. Figure 3.53 shows the offset parameter of β_1 in $f_{\cos\theta_d}$ dependence of χ^2. The point at $\Delta\beta_1 = 0$ means the default value obtained as a result of tuning; the region where $\Delta\beta_1 < 0$ is the more

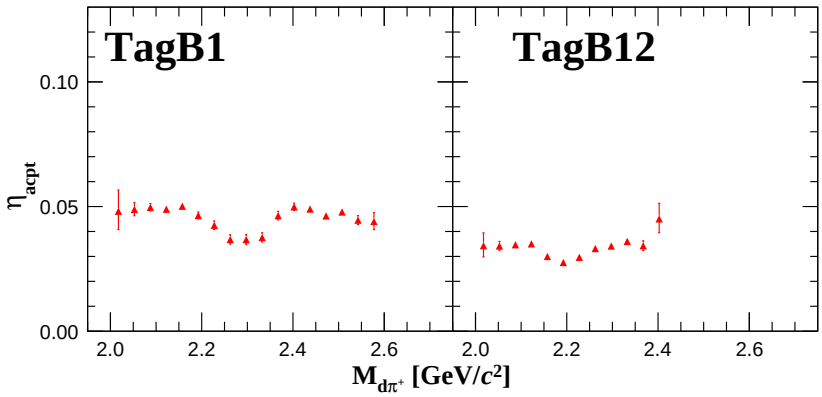

(A) $d\pi^+$ invariant mass.

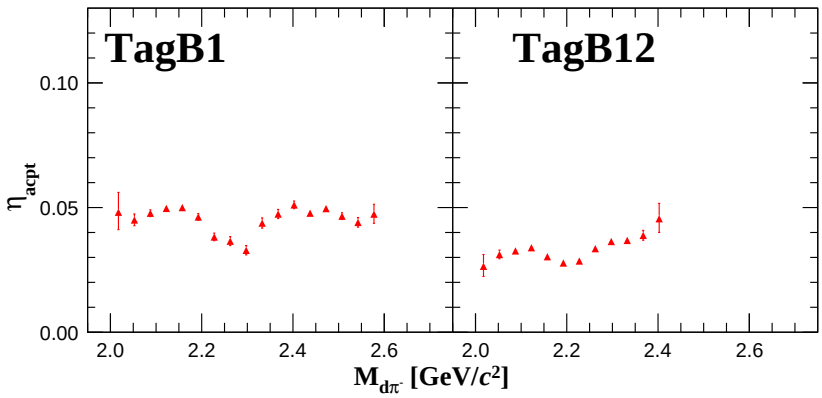

(B) $d\pi^-$ invariant mass.

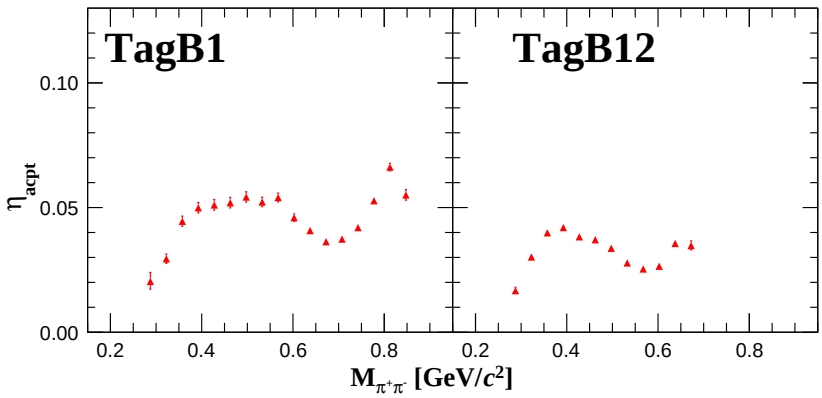

(C) $\pi^-\pi^+$ invariant mass.

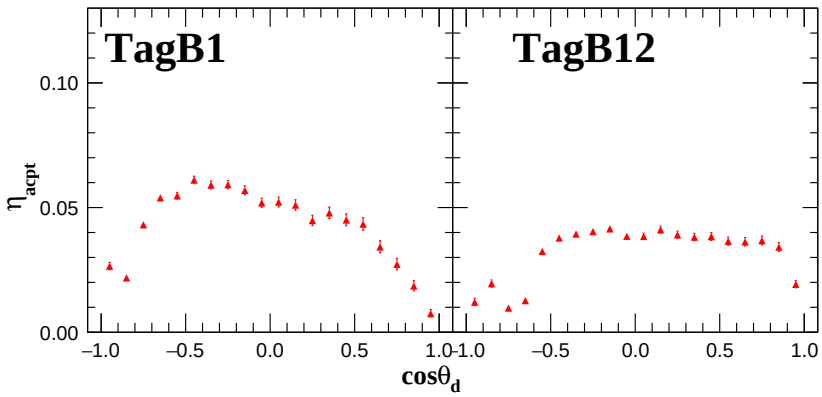

(D) $\cos\theta_d$ in γd-CM frame.

FIGURE 3.52: η_{acpt} for each invariant mass and angular distribution of deuteron. (A)$d\pi^+$ (B) $d\pi^-$ (C) $\pi^-\pi^+$ (D) $\cos\theta_d$ in the γd-CM frame.

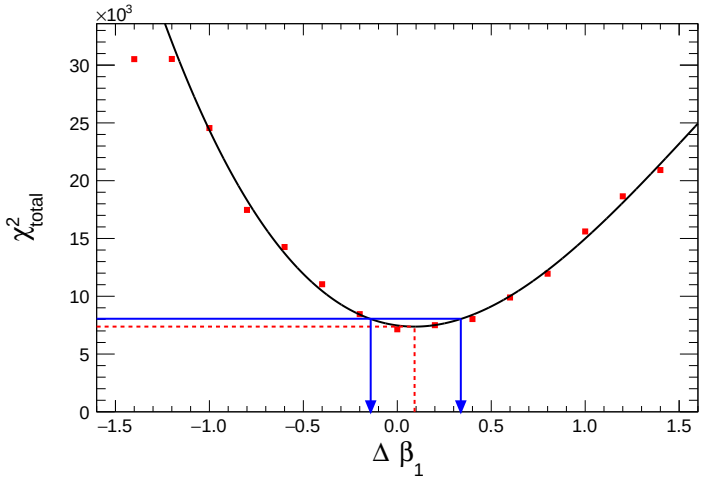

FIGURE 3.53: Offset parameter dependence of χ^2.

backward peaked deuteron emission. The solid black line shows the result of fitting with a cubic function. From the fitted function, the minimum value of χ^2 and the value of the offset when χ^2 increases by the number of degrees of freedom (ndf=680) were obtained. The red dashed line shows the minimum value of χ^2, and the blue arrow shows the value of the offset when χ^2 increases by 1 ndf. Generally, the forward (backward) peaked distribution of deuteron give the larger (smaller) η_{acpt}^{Total}.

The systematic uncertainty was estimated for each incident photon energy as the maximum and minimum values of η_{acpt}^{Total} obtained when the invariant mass distribution and the angular distribution of deuterons were changed as described above. The systematic uncertainty was shown as a blue shaded region in Fig. 3.51. The typical uncertainties were 5%.

3.7 Invariant Mass Resolution of the $d\pi^{\pm}$ and $\pi^{+}\pi^{-}$ in the 2-track analysis

The invariant mass resolutions were evaluated by the simulation. The reasonability of the simulation was studied by confirming that the simulated resolution of each component of the momentum in the $d\pi^{+}\pi^{-}$ 3-track analysis agreed with the real data. The residual of the generated value of the invariant mass and that reconstructed by the analyzer was used to evaluate the resolution.

3.7.1 Momentum Resolution in the 3-track Analysis

In the $\gamma d \rightarrow d\pi^{+}\pi^{-}$ reaction, the 3-track analysis that detects all three particles in the final state can produce the residual distributions of the initial and final states in the four kinematic variables, momentum among each axis (p_x, p_y, , p_z), and total energy E, based on the conservation laws of momentum and total energy. The residual of the initial and final states of each kinematic variables are expressed as Δp_i ($i = x,\ y,\ z$), ΔE. The width of the distributions of the simulation was compared with that of the real data. The distributions of each kinematic variable obtained from the simulation is shown in Fig. 3.54 along with the fitted Gaussians. The fitted distributions for the real data are shown in Fig. 3.37. The fitting by the Gaussian was iterated to adjust the fit range to the region of central value $\pm 1.5\sigma$. The width of the distributions of real and simulated data are listed as σ of fitted Gaussian in Tab. 3.4. The values in the rightmost column of Tab. 3.4 were obtained when the effect of the additional resolution factor was incorporated into the simulation as follows. Since the statistical errors of the simulated data were more than one order of magnitude smaller than that of the real data, the description is omitted in Tab. 3.4. To the momentum component p_i^{def} of each particle which was reconstructed by the analyzer, randomly generated δ_{pi} was added and $p_i = p_i^{def} + \delta_{pi}$ was used to reconstruct the invariant mass where i shows x, y, or z. The probability density function of δ_{pi} was a Gaussian with a mean of p_i^{def} and a standard deviation of $0.02 \times p_i^{def}$. This smearing by δ_{pi} was independent of the particle type (d, π) and was performed for each particle and each component. Figure 3.55 shows comparison of distributions of four kinematic variables between simulation and real data.

As a result, the smeared simulation reproduced real data better than the original simulation but showed slightly broader distribution than the real data, especially in Δp_x. Considering the fact that background events other than the $\gamma d \rightarrow d\pi^{+}\pi^{-}$ reaction are included in the real data, this smeared simulation is considered to be a rather over estimation of the resolution. Therefore, the smeared simulation was used to determine the upper limit of the systematic error of the detector resolution.

TABLE 3.4: Width of the residual distributions of four kinematic valuables in σ.

	Data	Simulation (original)	Simulation (smeared)
$\sigma_{\Delta px}$ [GeV/c]	0.032 (1)	0.032	0.034
$\sigma_{\Delta py}$ [GeV/c]	0.024 (1)	0.021	0.024
$\sigma_{\Delta pz}$ [GeV/c]	0.035 (1)	0.033	0.033
$\sigma_{\Delta E}$ [GeV]	0.024 (1)	0.021	0.024

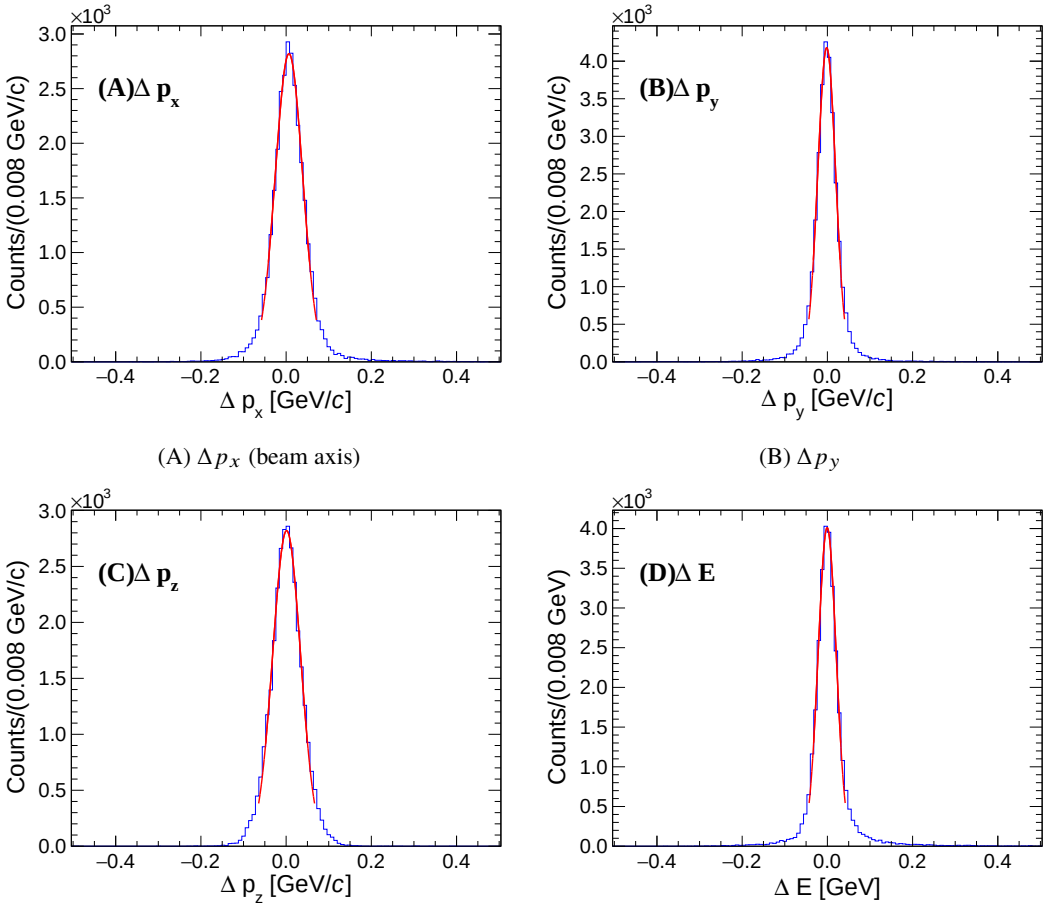

(A) Δp_x (beam axis)

(B) Δp_y

(C) Δp_z

(D) ΔE

FIGURE 3.54: The simulated distributions of four kinematic variables. (A)-(C)p_x, p_y, p_z. (D) Total energy E. Red solid lines show fitted Gaussians.

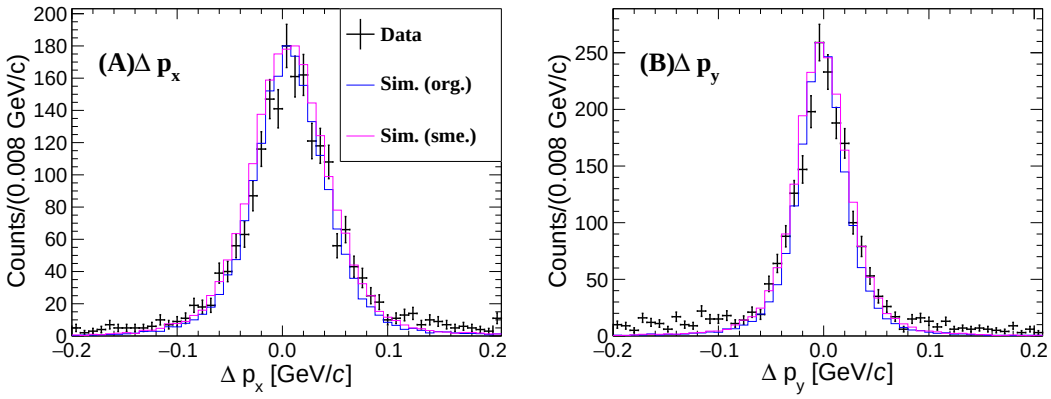

(A) Δp_x (beam axis) (B) Δp_y

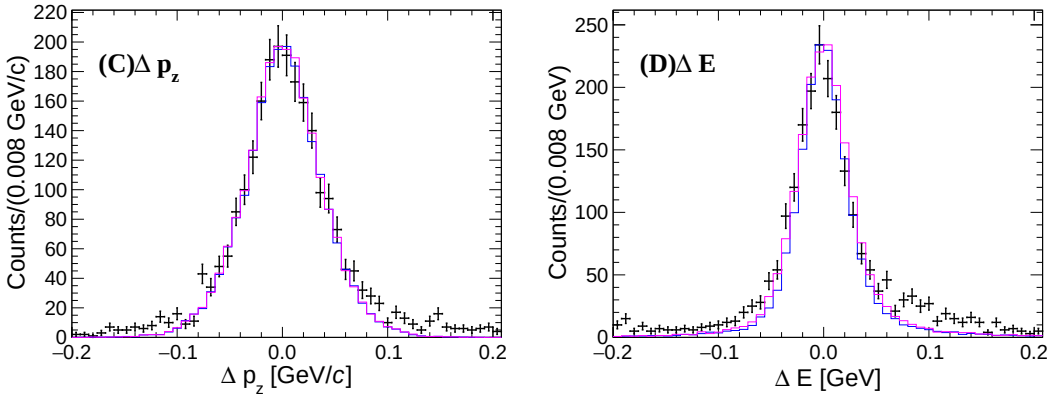

(C) Δp_z (D) ΔE

FIGURE 3.55: Comparison of distributions of four kinematic variables between simulation and real data. Black crossed lines show real data. Blue and magenta solid lines show simulated histograms with and without momentum smearing, respectively. (A)-(C) The residual of each momentum component, p_x, p_y, p_z. (D) The residual of the total energy E.

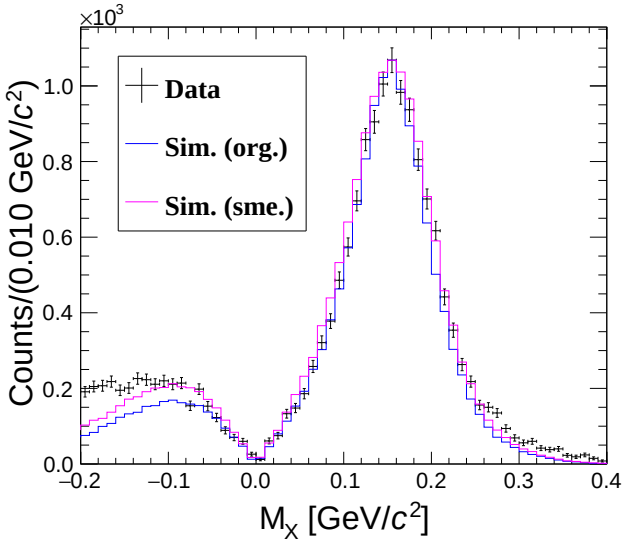

FIGURE 3.56: Missing mass of the $\gamma d \to d\pi^{\pm}X$ reaction. Black crossed lines show real data. The region of $M'_X < 0$ in a missing mass distribution of the $\gamma p \to p\pi^{\pm}X'$ was selected. Blue and magenta solid lines show simulated histograms with and without momentum smearing, respectively.

3.7.2 Missing Mass Resolution in the 2-track Analysis

The distribution of the missing mass of $\pi^{\pm}$ in the 2-track analysis was compared with the simulation. Figure 3.56 shows a comparison of the missing mass distributions for real and simulated data. In these distributions, the region of $M'_X < 0$ in a missing mass distribution of the $\gamma p \to p\pi^{\pm}X'$ was selected to improve signal to noise ratio as described in Sec. 3.4.7. The distribution of the real data is shown as black crossed lines. The simulated distributions with and without momentum smearing, which are shown as blue and magenta solid lines, were normalized at $M_X = 0.125$ GeV/c^2 so that the maximum values match the real data. Both distributions reproduce the width of the real data well. The discrepancies in $M_X < -0.1$ and $M_X > 0.3$ were due to contamination of the $\gamma p \to p\pi X$ reaction in the real data.

3.7.3 Invariant Mass Resolution in the 2-track Analysis

Since it was found that the simulation reproduced the resolution of the real data reasonably well, we used the simulation to estimate the resolution of the invariant mass distribution. Figure 3.57 shows the distribution of the difference between the error-free invariant mass value generated by the simulation and the invariant mass value reconstructed by the analyzer.

The obtained distributions were fitted with a phenomenological function expressed as a product of Lorentzian and Gaussian with asymmetric width parameters,

$$f_{\mathrm{IM}}(x) = p_0 \exp\left(-\frac{(x-\mu)^2}{2\sigma^2}\right) \cdot \frac{\Gamma^2}{(x-\mu)^2 + (\Gamma/2)^2}, \tag{3.37}$$

where p_0, μ, σ, and Γ are parameters represent amplitude, central value of the peak, standard deviation of the Gaussian, and width (full width of half maximum, FWHM) of the Lorentzian, respectively. Different values for σ and Γ were used in the $x > \mu$ and $x < \mu$ regions. Obtained FWHM of $f_{\mathrm{IM}}(x)$ are listed in Tab. 3.5. The obtained functions were regarded as the response functions of the invariant mass spectra and used when $d\sigma/dM_X$ ($X = d\pi^{+}$, $d\pi^{-}$, $\pi\pi$) was fitted.

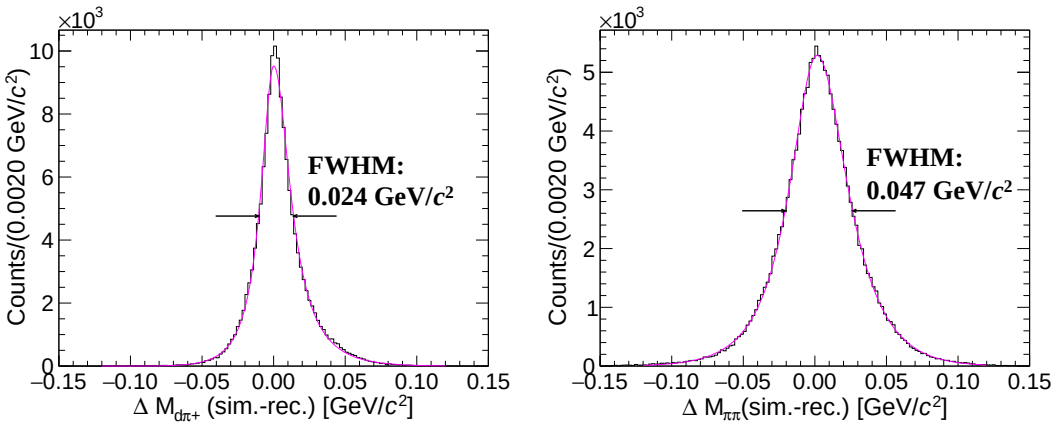

(A) $\Delta M_{d\pi^+}$ (B) $\Delta M_{\pi\pi}$

FIGURE 3.57: The residual of the invariant mass which was generated by the simulation and that reconstructed by the analyzer. Each distribution was fitted by the function expressed as Eq. 3.37.

TABLE 3.5: Invariant mass resolutions.

	Simulation (original)	Simulation (smeared)
Width $\Delta M_{d\pi+}$ (FWHM) [GeV/c^2]	0.24	0.28
Width $\Delta M_{d\pi-}$ (FWHM) [GeV/c^2]	0.24	0.28
Width $\Delta M_{\pi\pi}$ (FWHM) [GeV/c^2]	0.47	0.50

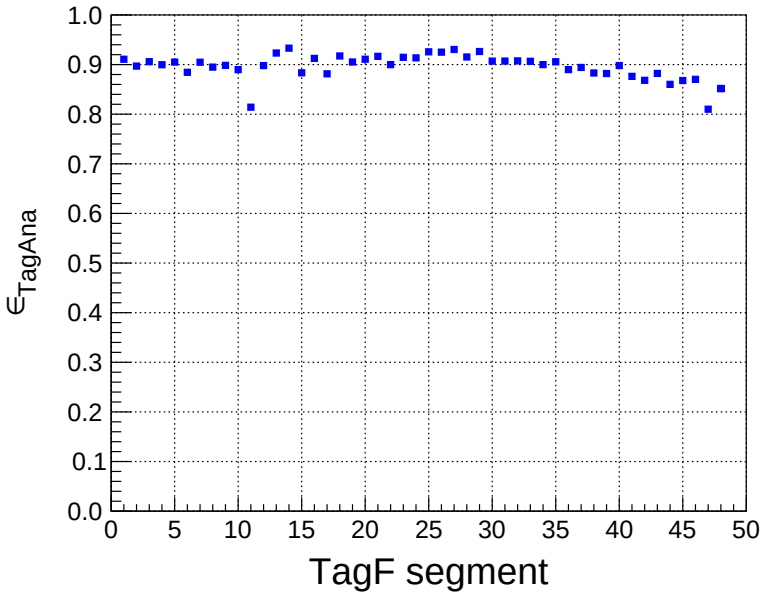

FIGURE 3.58: Tagger analysis efficiency obtained for each TagF segment.

3.8 Number of Incident Photons N_γ

The number of incident photons can be described as

$$N_\gamma = \epsilon_{\mathrm{TagAna}} \cdot \epsilon_{\mathrm{TagEff}} \cdot N_{\mathrm{scaler}}$$

, where $\epsilon_{\mathrm{TagAna}}$, $\epsilon_{\mathrm{TagEff}}$, N_{scaler}, mean analysis effiency of the tagger, photon tagging efficiency, and scaler output value, respectively.

3.8.1 Analysis Efficiency of the Tagger $\epsilon_{\mathrm{TagAna}}$

As mentioned in Sec. 3.4.1, several time gates were applied for tagged photon selection. Therefore, the effective number of available photons is the number of events counted by the scaler multiplied by the analysis efficiency.

Analysis efficiency of the tagger is defined as,

$$\epsilon_{\mathrm{TagAna}} = \frac{\text{All Tagger hit events in the time gates}}{\text{All TagF TagB coincidence hit events}}. \tag{3.38}$$

$\epsilon_{\mathrm{TagAna}}$ was evaluated for each segment of TagF and for each production run. Typical $\epsilon_{\mathrm{TagAna}}$ of each TagF segment for a given run is shown in Fig. 3.58. The statistical errors of the efficiency is much smaller ~0.1% than makers in the figure.

3.8.2 Tagging Efficiency $\epsilon_{\mathrm{TagEff}}$

Tagging efficiency is defined as following equation.

$$\epsilon_{\mathrm{TagEff}} = \frac{\text{Number of photons at the target}}{\text{Number of tagged photons}}.$$

Tagging efficiency cannot be 100% due to following reasons.

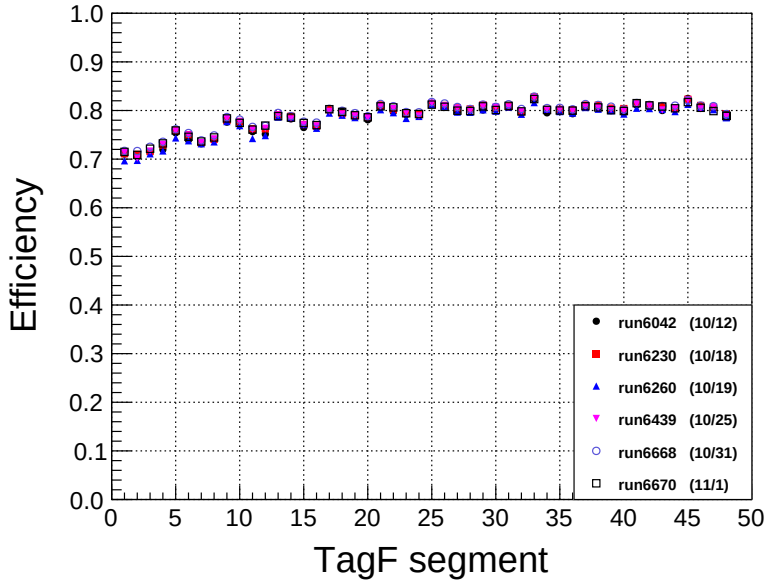

FIGURE 3.59: Tagging efficiency.

- The photon collimator placed in front of the pair magnet
- Materials from the radiator to the target
- Electrons not from the radiator directory
- Accidental coincidence of TagF and TagB

Tagging efficiency was measured with a lead glass counter (LG) put on the most downstream of the photon beam line. We used faint beam (a few kHz) in tagging efficiency study as LG has low rate tolerance.

Tagging efficiency is technically expressed as

$$\epsilon_{\text{TagEff}} = \frac{1}{\eta_{\text{attenate}}} \frac{N_{\text{LG hit}}}{N_{\text{TagHit}}}, \tag{3.39}$$

where η_{attenate} is attenuation ratio. η_{attenate} was used to correct the number of photon at LG to that at the target because actual position of the target was placed about 3 m downstream from the position of LG. The amount of materials between the target positions and LG are estimated to be $0.03X_0$ (X_0 is radiation length) [Bec13]. That corresponds to $\eta_{attenate} = 1.02$.

Tagging efficiency were measured at the beginning, end, and middle of the experiment. Fig. 3.59 shows obtained tagging efficiencies of each TagF segment. Systematic errors of the tagging efficiency were estimated <2% from the deviation of the values per measurement.

3.8.3 Scaler Count of the Tagger N_{scaler}

The number of coincidence signals of a TagB and corresponding TagFs, named TagSum, was countered by CAMAC scalers. In addition, more than 12 photon energy segmentation was not necessary for this analysis. Thus, only TagSum scaler information was used to estimate the number of incident photons.

TABLE 3.6: Summary of N_γ.

TagB	Energy [GeV]	TagSum Scaler	$\epsilon_{\mathrm{TagAna}}$	$\epsilon_{\mathrm{TagEff}}$	N_γ
1	1.0535–1.0780	2.67×10^{11}	0.9	0.7	1.7×10^{11}
2	1.0275–1.0535	2.62×10^{11}	0.9	0.7	1.6×10^{11}
3	1.0010–1.0275	2.50×10^{11}	0.9	0.7	1.6×10^{11}
4	0.9775–1.0010	2.50×10^{11}	0.9	0.7	1.6×10^{11}
5	0.9525–0.9775	2.51×10^{11}	0.9	0.7	1.6×10^{11}
6	0.9265–0.9525	2.53×10^{11}	0.9	0.7	1.6×10^{11}
7	0.9015–0.9265	2.55×10^{11}	0.9	0.8	1.8×10^{11}
8	0.8770–0.9015	2.71×10^{11}	0.9	0.8	2.0×10^{11}
9	0.8520–0.8770	2.63×10^{11}	0.9	0.8	1.9×10^{11}
10	0.8255–0.8520	2.96×10^{11}	0.9	0.8	2.1×10^{11}
11	0.8015–0.8255	2.45×10^{11}	0.9	0.8	1.8×10^{11}
12	0.7790–0.8015	1.80×10^{11}	0.9	0.8	1.3×10^{11}
Total	0.7790–1.078	3.04×10^{12}	0.9	0.75	2.1×10^{12}

TABLE 3.7: DAQ efficiency.

	Scaler count
Request	1.71×10^9
Accepted	2.42×10^9
DAQ efficiency	0.706

Summary of N_γ is shown in Tab. 3.6. Though efficiency values shown in the table were not directly used to derive cross sections since efficiencies were evaluated for each production run or for each segment of TagF, it would be helpful to describe averaged values here.

3.9 DAQ Efficiency ϵ_{DAQ}

DAQ efficiency is defined as an efficiency of data taking. It is obtained from scaler information of a trigger request singal and a trigger accepted signal. Total number of counts of the scalers during the experimental term are shown in Tab. 3.7. In the cross section analysis, DAQ efficiency were calculated run by run. Statistical errors of DAQ efficiency for each runs were negligibly small (~0.02%).

3.10 Number of Target Nuclei N_{Target}

Number of deuterons was estimated from measured thickness of the target cell, and monitored temperature and pressure. Figure 3.60 shows the flowchart of the target number estimation procedure.

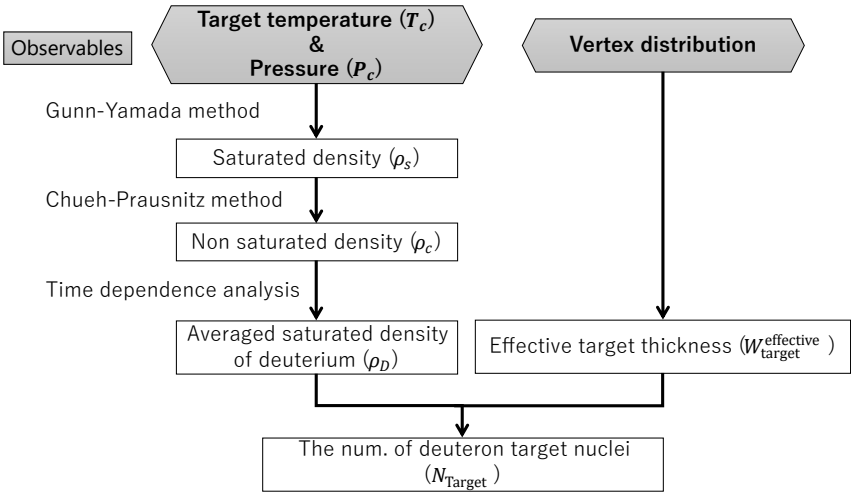

FIGURE 3.60: Flow chart of the estimation of the number of target nuclei.

3.10.1 Effective Thickness of Target

Effective thickness of the target was estimated from reconstructed $\pi^+\pi^-$ vertex distribution shown in Fig. 3.22(B). The difference of the peaks of two Lorentzians was 3.251 ± 0.002 cm , and it corresponds to the length of the target cell. The same analysis procedure was carried out for $p\pi^-$ and $d\pi^\pm$ vertex events to estimate systematic errors. A systematic error originated from fitting function was estimated by changing Lorentzians to Gaussians. As a result, a systematic error of the target thickness was estimated as 0.1 cm. The obtained target thickness was larger than the designed value of the target cell 3 cm (shown in Sec. 2.4.2). That was because the film expand by the differential pressure between the inside and outside of the film.

3.10.2 Target Density Calculation

Figure 3.61 shows time dependence of temperature (Fig. 3.61(A)) and pressure (Fig. 3.61(B)) of the target cell. The red shaded region means the period when calibration data was acquired,

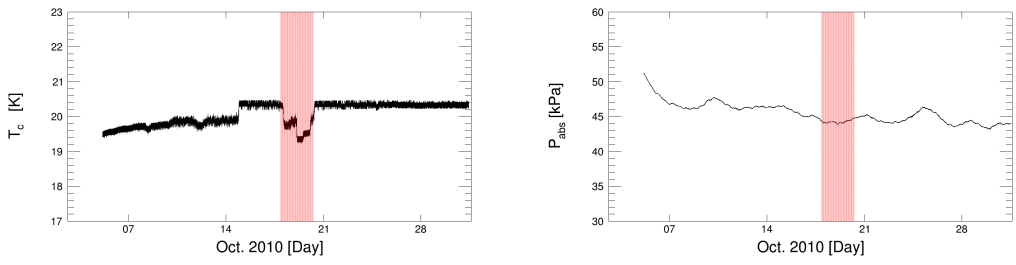

(A) Temperature (B) Pressure

FIGURE 3.61: Time dependence of the target temperature and pressure on temperature. (A) Target temperature. (B) Target pressure.

TABLE 3.8: Variables and constants for target density calculation.

Variable	Meaning	Values
T_b	Boiling temperature [K]	19.0
T_c	Critical temperature [K]	45.9
T_r	Reduced temperature	
T^R	Reference temperature [K]	19.0
P_c	Critical pressure [atm]	7.4
V_c	Critical molecular volume [$cm^3/g \cdot mol$]	60.3
V_s	Saturated molecular volume [$cm^3/g \cdot mol$]	
Z_c	Compressibity factor at critical point	0.314
ω	Pitzer's eccentric factor	-0.13
ρ^R	Density at reference temperature T^R [g/cm^3]	0.17328
ρ_s	Saturation density [g/cm^3]	
M	Molecular weight [g/mol]	4.032
P_{vp}	Vapor pressure	

and no physical data was acquired.

To calculate the density, we used the method which is a combination of the Gunn-Yamada method [GY71] for estimating the saturated liquid density and the Chueh-Prausnitz method [Pol+87] for estimating the density change of the liquid due to pressure change. Variables and constants used for the target density calculation are listed in Tab. 3.8. Reduced temperature was obtained as:

$$T_r = \frac{T}{T_c}. \tag{3.40}$$

The saturated volume V_s is expressed a function of the reduced temperature as,

$$V_s = V_{sc} V_r(T_r)(1 - \omega\Gamma(T_r)), \tag{3.41}$$

where V_{sc} is a scaling factor at $T_r = 0.6$, V_r and Γ are parametrized with T_r at the range of $0.2 < T_r < 0.8$. Explicit functions are given as,

$$V_r(T_r) = 0.33593 - 0.33953T_r + 1.51941T_r^2 - 2.02512T_r^3 + 1.11422T_r^4, \tag{3.42}$$

$$\Gamma(T_r) = 0.29607 - 0.09045T_r - 0.04842T_r^2. \tag{3.43}$$

The volume at reference temperature is expressed as,

$$V^R = V_{sc} V_r(T^R/T_c)(1 - \omega\Gamma(T^R/T_c)). \tag{3.44}$$

Scaling factor V_{sc} in Eq. 3.41 is eliminated with Eq. 3.44 as,

$$V_s = \frac{V_r(T_r)(1 - \omega\Gamma(T_r))}{V_r(T^R/T_c)(1 - \omega\Gamma(T^R/T_c))} V^R. \tag{3.45}$$

The reference volume V^R is numerically obtained by using the known density at reference temperature ρ^R and molecular weight M as,

$$V^R = \frac{M}{\rho^R}. \tag{3.46}$$

Then, saturated density ρ_s is obtained as,

$$\rho_s = \frac{M}{V_s}. \tag{3.47}$$

Finally, non-saturated density of the deuterium ρ_c is calculated as,

$$\rho_c = \rho_s \left[1 + \frac{9 Z_c N \left(P - P_{vp}(T) \right)}{P_c} \right]^{1/9}. \tag{3.48}$$

The vapor pressure $P_{vp}(T)$ is calculated by the Antoine equation [Pol+87],

$$P_{vp}(T) = \exp\left(A - \frac{B}{T + C} \right). \tag{3.49}$$

The constants A, B, and C for deuterium are 13.2954, 157.89, and 0.0, respectively. They were tuned to reproduce the measured values. The index N is expressed as,

$$\begin{aligned} N =& (1.0 - 0.89\omega) \\ & \times \exp\left(6.9547 - 76.2853 T_r + 191.3060 T_r^2 - 203.5472 T_r^3 + 82.7631 T_r^4 \right). \end{aligned} \tag{3.50}$$

The reference temperature $T^R = 19.0$ K which was different from the previously used value in [Bec13] was chosen to achieve more accurate estimation. As a result of this change, the error in density estimation of each measured point was reduced to much less than 1%.

Figure 3.62(A) shows time dependence of the calculated target density. In fact, within the measurement range, the change in target density depends only on temperature, and the effect of pressure change is minimal. Figure 3.62 is a projection of Fig. 3.62(A) except the red shaded region. The behavior of density was changed after around 10/15 6:30 as shown in Fig. 3.62(A), and is shown as two peaks in the projected distribution, Fig. 3.62(A). The two peaks were fitted by 2 Gaussians.

The higher density peak at $\rho_c \sim 0.1717$ g/cm^3 and the lower density peak at $\rho_c \sim 0.1705$ g/cm^3 correspond to before and after 10/15 6:30, respectively. The density of the target was calculated as the weighted average of the central values of the two peaks with the number of incident photons in each time period as,

$$\rho_D = 0.1710 \pm 0.0007\ (syst.)\ [\mathrm{g/cm^3}]. \tag{3.51}$$

A statistical error of fitted Gaussians was negligibly small (2×10^{-7} g/cm^3.) A systematic error was estimated from difference between the weighted mean density and the densities of each time region.

3.10.3 Calculation of the Number of Deuteron Target Nuclei

The number of target deuterons (N_{Target}) was estimated from the target density (ρ_D), Avogadro constant ($N_A = 6.02214076 \times 10^{23}$ mol^{-1}), the effective thickness of the target ($W_{\mathrm{target}}^{\mathrm{effective}}$) which was estimated from vertex distributions in Sec. 3.10.1, and atomic mass of deuterium $M_D = 2.01410178$ g/mol as,

$$N_{\mathrm{Target}} = \frac{\rho_D \cdot N_A \cdot W_{\mathrm{target}}^{\mathrm{effective}}}{M_D} = 0.166 \pm 0.005\ [\mathrm{b^{-1}}]. \tag{3.52}$$

Target parameters used in the above calculation were summarized in Tab. 3.9. The errors are systematic errors since statistical errors are negligibly small. The error of the number

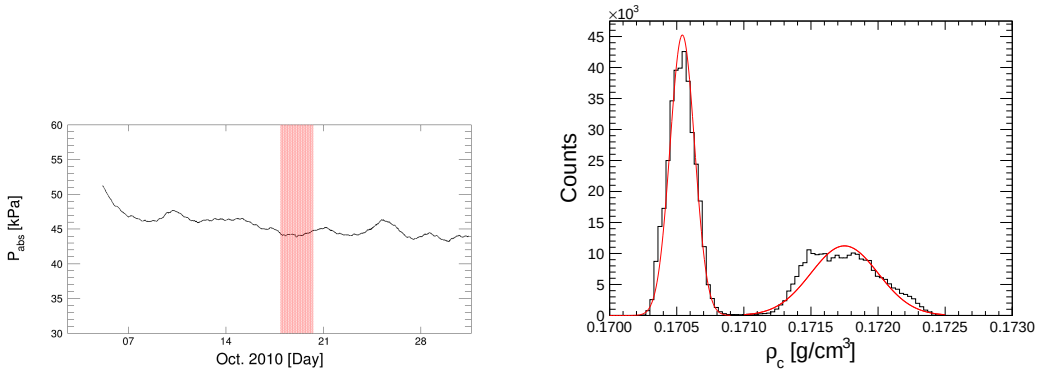

(A) Target density time structure

(B) Target density distribution.

FIGURE 3.62: Target density distributions calculated from monitored pressure and temperature. (A) Time dependence of the target density. (B) Target density distribution fitted by 2 gaussians.

of the target was dominated by uncertainty of the target thickness deduced from the vertex information.

TABLE 3.9: Target parameters.

Thickness $W_{\mathrm{target}}^{\mathrm{effective}}$ [cm]	Density ρ_D [g/cm^3]	Deuteron target N_{Target} [b^{-1}]
3.24 ± 0.10	0.1710 ± 0.0007	0.166 ± 0.005

TABLE 3.10: Source of systematic errors

Source	accronym	Relative error (%)
$d\pi^+\pi^-$ selection	$\epsilon_{d\pi}$	3
The number of target	N_{Target}	3
The number of photon	N_γ	2
Back ground subtraction	N_{BG}	3
NKS2 acceptance	η_{acpt}	~5
Total		~8

3.11 Summary and Systematic Errors

$\gamma d \rightarrow d\pi^+\pi^-$ events were extracted using various information of NKS2 detectors and Tagger. The number of identified events were ~15000 and ~2000 for 2 track vertex analysis and 3 track vertex analysis, respectively. Quantities and distributions of various backgrounds were estimated. To convert obtained $d\pi\pi$ distributions to cross sections, the acceptance of NKS2 and its systematic error were estimated by Monte-Carlo simulation based on Geant4 framework. Also, other systematic errors were estimated and found that the acceptance correction part dominates the systematic errors of the cross section. The sources of the systematic error for the cross section estimation are summarized in Tab. 3.10. The systematic error was asymmetry due to acceptance uncertainty as describe in Sec. 3.6. Invariant mass spectra and angular distributions before and after acceptance correction will be shown in next chapter.

4 Experimental Results

The obtained invariant mass spectra and the cross sections of the $\gamma d \to d\pi^+\pi^-$ reaction will be shown in this chapter.

4.1 Invariant Mass and Angular Distribution Spectra

After the event selection which was described in Sec. 3.4, we obtained the three invariant mass spectra ($M_{d\pi^+}$, $M_{d\pi^-}$, $M_{\pi^+\pi^-}$) and the angular distribution of deuteron in the γd-CM frame. In distributions shown in this section, The contaminations of $p\pi X$ and accidental background estimated in Sec. 3.5 were subtracted. Figure 4.1 shows 2-dimensional plots of invariant mass spectra and Fig. 4.2 shows correlations between E_γ and the invariant masses obtained by 2-track analysis. Threshold of the $N\Delta$ was shown as red solid lines. In the $M_{d\pi^+}$ vs $M_{d\pi^-}$ spectrum (Fig. 4.1(A)), enhancements below the $N\Delta$ threshold was observed in both axises. Owing to the limited phase space in E_γ = 0.78–1.08 GeV, no events were observed in the upper right and lower left regions in Fig. 4.1(A). Figure 4.2(A) shows that the enhancement of $M_{d\pi^+}$ is independent of E_γ. In Fig. 4.1(A), an enhancement of around $M_{\pi\pi}$ = 0.7 GeV/c^2 was observed in addition to the enhancement in the $M_{d\pi^+}$ distribution. This enhancement of $M_{\pi\pi}$ was due to ρ^0 production. Since the phase space did not cover the central mass region of ρ^0 (= 0.77 GeV/c^2), the enhancement was located around edge of the phase space limit as shown in Fig. 4.2(B).

1-dimensional spectra of the invariant masses and angular distribution of deuteron in the γd-CM frame are shown as black solid lines in Fig. 4.3 (2-track analysis) and Fig. 4.4 (3-track analysis), classified into four categories according to the incident photon energy range. Upper panels show higher energy regions. The phase space distributions distorted by the acceptance of NKS2 are also shown as blue solid lines in Fig 4.3. There are clear resonance like peaks slightly below the threshold of $N\Delta$ at $M_{d\pi} \sim 2.14$ GeV/c^2 and the reflections of them at $M_{d\pi} \sim 2.3$ GeV/c^2 in all total energy regions in the $d\pi$ invariant mass spectra (second and third columns from the left), and they are beyond the phase space distribution. The enhancement due to ρ^0 production was observed in the left most column. The angular distribution of the deuteron (right most column in Fig. 4.3) shows a slight backward peak, but there is also a certain intensity in the forward region.

The 2-dimensional invariant mass spectra for each incident photon energy region are shown in Appendix B.4.

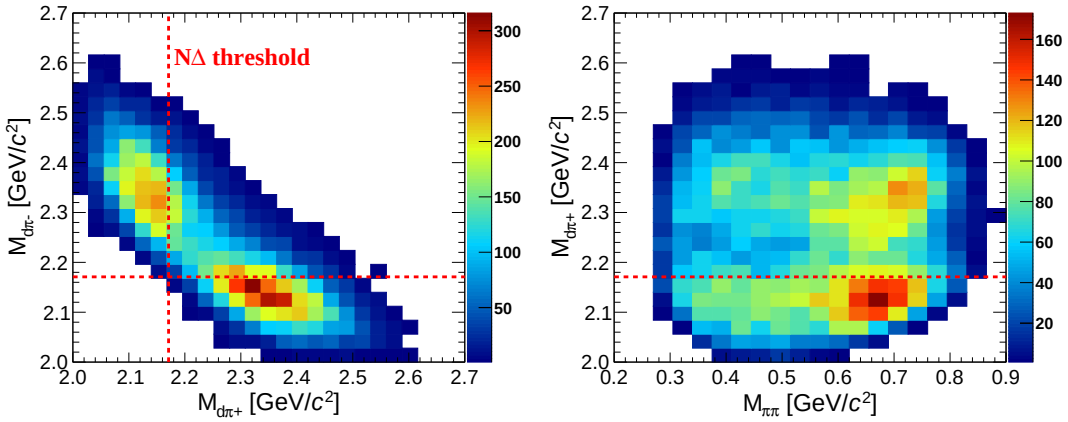

(A) $M_{d\pi+}$ vs $M_{d\pi-}$ (B) $M_{\pi\pi}$ vs $M_{d\pi+}$

FIGURE 4.1: 2D plots of the invariant mass spectra. Red dashed line indicates threshold of $N\Delta$. (A) a correlation of $M_{d\pi^+}$ and $M_{d\pi^-}$. Enhancements below the $N\Delta$ threshold was observed in both axises. Owing to the limited phase space in E_γ = 0.78–1.08 GeV, no events were observed in the upper right and lower left regions. (B) a correlation of $M_{\pi\pi}$ and $M_{d\pi^+}$.

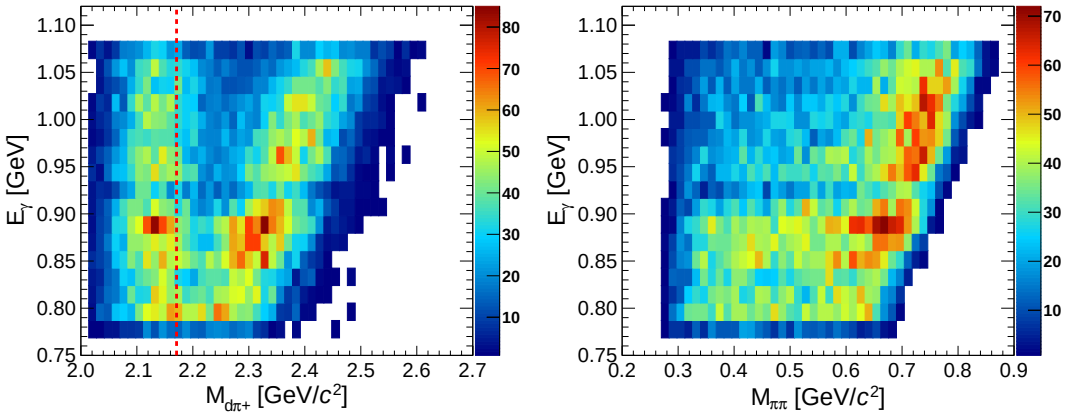

(A) $M_{d\pi+}$ vs E_γ (B) $M_{\pi\pi}$ vs E_γ

FIGURE 4.2: 2D plots of the invariant mass and E_γ. Red dashed line indicates threshold of $N\Delta$. (A) a correlation of $M_{d\pi^+}$ and E_γ. An enhancement of $M_{d\pi^+}$ at 2.14 GeV is independent of E_γ. An diagonal enhancement around $M_{d\pi^+} \sim 2.4$ GeV is a reflection of an enhancement of $M_{d\pi^-}$ at 2.14 GeV. (B) a correlation of $M_{\pi\pi}$ and E_γ. An enhancement at phase space limit of $M_{\pi\pi}$ is due to ρ^0 production.

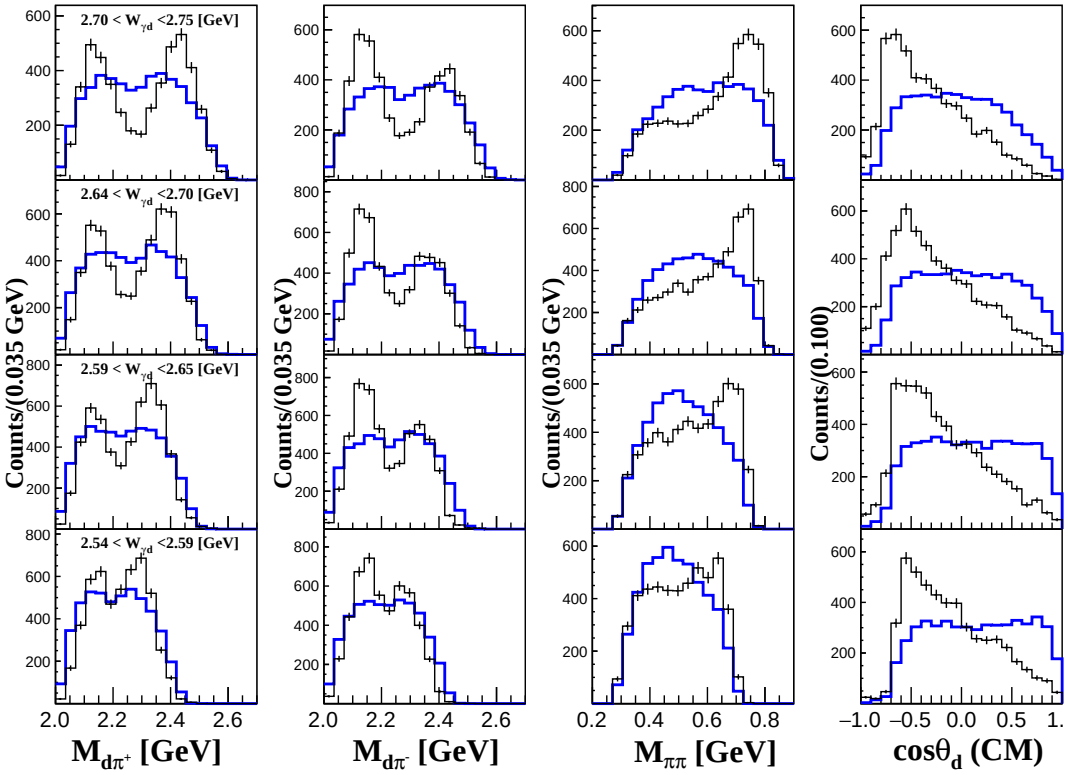

FIGURE 4.3: Invariant mass spectra and deuteron angular distributions obtained by 2-track analysis for four incident photon energy regions. The panels are arranged in order of incident energy from the top to the bottom. Blue histograms shows shape of pure phase space decay events by the simulation. There are clear peak structures at ~2.14 GeV/c^2 in $M_{d\pi^+}$ and $M_{d\pi^-}$ distributions. The enhancement around 0.7 GeV/c^2 in $M_{\pi\pi}$ is due to ρ^0 production. The angular distribution of deuteron in γd-CM frame shows backward peaking structure rather than flat distribution in the phase space.

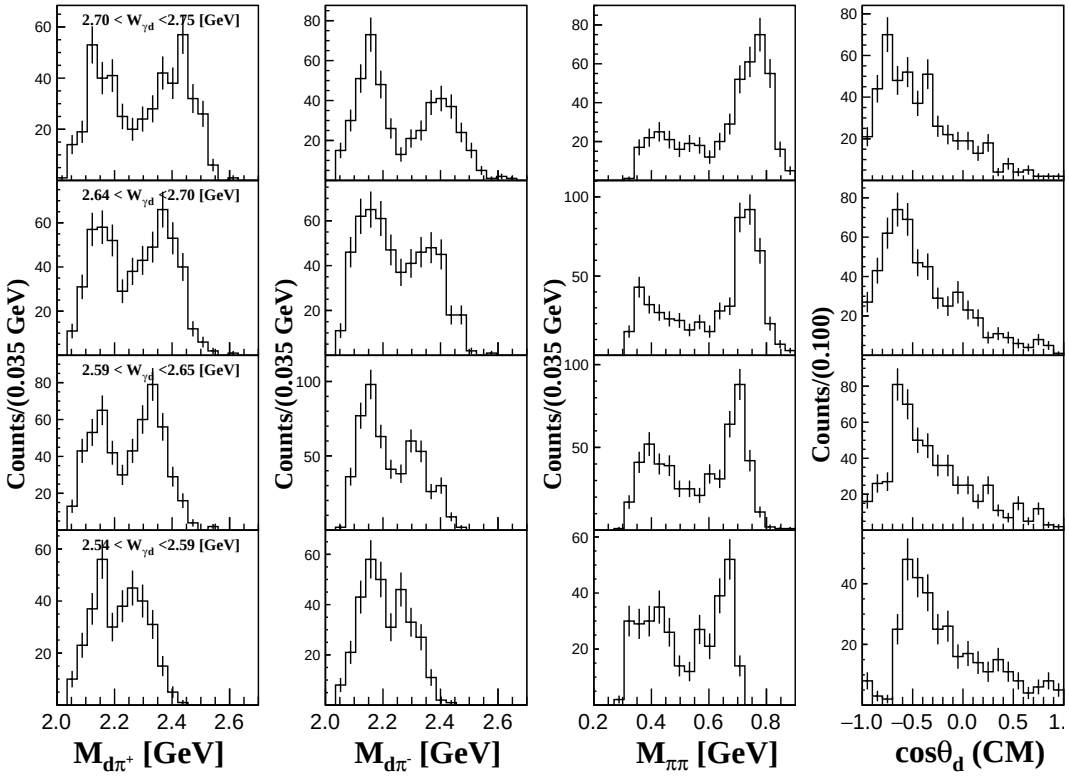

FIGURE 4.4: Invariant mass spectra and deuteron angular distributions obtained by 3-track analysis for four incident photon energy regions. The panels are arranged in order of incident energy from the top to the bottom. Similar structures with Fig. 4.3 are observed.

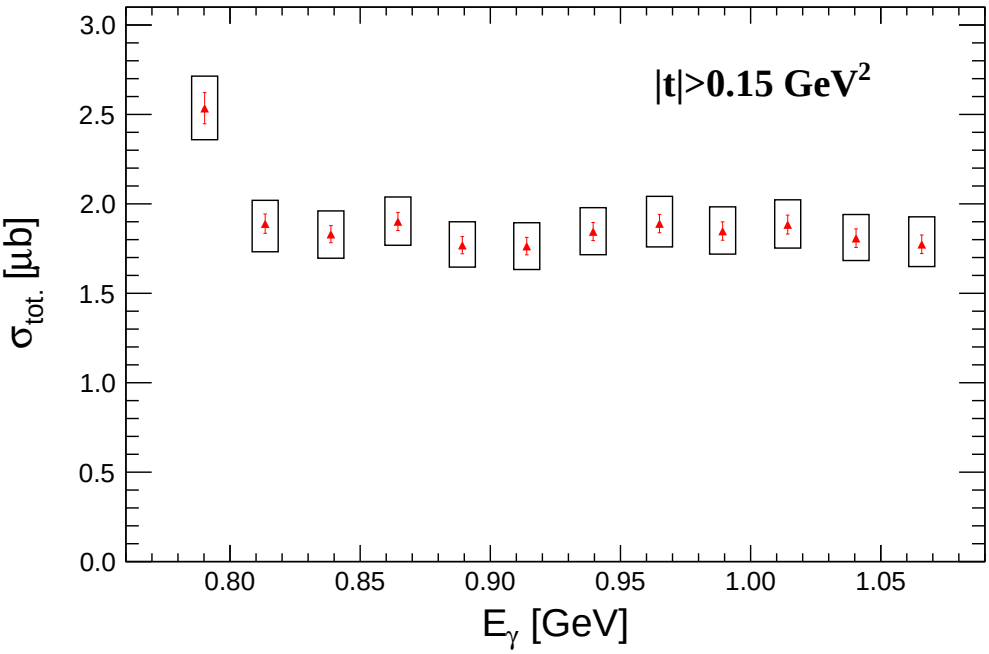

FIGURE 4.5: Total cross section of the $\gamma d \rightarrow d\pi^+\pi^-$ reaction. Error bars show statistical error and black rectangles show systematic uncertainties.

4.2 Cross Section

Total cross section of the $\gamma d \rightarrow d\pi^+\pi^-$ reaction and differential cross sections, $d\sigma/dM_{d\pi+}$, $d\sigma/dM_{d\pi-}$, $d\sigma/dM_{\pi\pi}$, and $d\sigma/d\cos\theta_d$, are shown in this section. As explained in Sec. 3.6.2, the cross sections are derived in the limited kinematic region of $|t| > 0.15$ GeV^2.

4.2.1 Total Cross Section

The total cross section σ_{CS} is described as,

$$\sigma_{CS} = \frac{N_{ev}}{N_{\text{Target}} \cdot N_\gamma \cdot \eta_{acpt} \cdot \epsilon_{DAQ} \cdot \epsilon_{Ana}},$$

as shown in Eq. 3.1. η_{acpt}^{Total} estimated in Sec. 3.6.2 was used as η_{acpt}. Though some components of ϵ_{Ana} was included in the η_{acpt} estimation, these of the real data and simulated data were not perfectly reproduced. Thus, a correction factor of ϵ_{Ana} was introduced. The obtained total cross section of the $\gamma d \rightarrow d\pi^+\pi^-$ reaction is shown in Fig. 4.5. Error bars show statistical error and black rectangles show systematic uncertainties. Almost flat distribution was obtained except for the lowest energy bin.

4.2.2 Differential Cross Section

In the differential cross section estimation, η_{acpt}^{Diff} estimated in Sec. 3.6.2 was used as η_{acpt}. The contribution of resolution to the reconstructed invariant mass distribution was corrected by estimating the probability density distribution of the generated invariant mass by the simulation. Figure 4.6 shows the differential cross sections $d\sigma/dM_{d\pi^+}$ (left most column), $d\sigma/dM_{d\pi^-}$ (center column), $d\sigma/dM_{\pi\pi}$ (right column) for four photon energies. The fitted functions and components of the functions are shown as solid, dashed, and dotted lines. The procedure of the fitting is described in the following section. The differential cross section

$d\sigma/d\Omega_d$ for four photon energies is shown in Fig. 4.7. Since the events in $|t| < 0.15$ GeV^2 were excluded in the acceptance estimation, the differential cross section in $\cos\theta_d < -0.6$ was strongly distorted. The further discussion of the angular distribution is described in Sec. 5.2.

Fitting of Differential Cross Section of the Invariant Mass

The obtained differential cross sections $d\sigma/dM_{d\pi^+}$, $d\sigma/dM_{d\pi^-}$, and $d\sigma/dM_{\pi\pi}$ were fitted by functions with amplitudes of $d\pi^\pm$ isovector resonances (R^{++}_{IV} from $d\pi^+$, R^0_{IV} from $d\pi^-$), an amplitude of ρ^0 mesons, and a background proportional to the phase space. The fitting function of $d\sigma/dM_{d\pi^+}$ is given by the convolution of the experimental response function Eq. 3.37 with parameters estimated in Sec. 3.7.3, and

$$N\left(m_{d\pi^+}\right) = \int_{m_{\pi\pi}} \int_{m_{d\pi^-}} \left(\left| \alpha A^{R^{++}_{IV}}_{M_{++},\Gamma_{++}}\left(m_{d\pi^+}\right) + \beta A^{R^0_{IV}}_{M_0,\Gamma_0}\left(m_{d\pi^-}\right) + \gamma A^{\rho}_{M_\rho,\Gamma_\rho}\left(m_{\pi\pi}\right) \right|^2 + C \right) \cdot V_{\mathrm{PS}}\left(m_{d\pi^+}, m_{d\pi^-}, m_{\pi\pi}\right) dm_{d\pi^-} dm_{\pi\pi}, \quad (4.1)$$

where V_{PS} is the phase space distribution, C is a constant background proportional to phase space, $A_{M,\Gamma}(m) = \left(M^2 - m^2 + iM\Gamma\right)^{-1}$ is the Breit-Wigner (BW) amplitudes with parameters M and Γ. R^{++}_{IV} and R^0_{IV} express the assumed isovector resonances of the $d\pi^+$ and $d\pi^-$, respectively. The fitting functions of $d\sigma/dM_{d\pi^-}$ and $d\sigma/dM_{\pi\pi}$ are given by swapping the integral variables of Eq. 4.1 and changing parameters of the response function to corresponding values.

The χ^2 fitting was performed independently for four energy region but simultaneously for the three invariant mass spectra using MIGRAD in the MINUIT package. The χ^2 was defined as,

$$\chi^2 = \sum_{m_X} \sum_{i=0}^{nbin} \frac{\left(\frac{d\sigma}{dm_X}\left(m_i\right) - f_{m_X}\left(m_i\right) \right)^2}{\delta_{d\sigma/dm_X}\left(m_i\right)^2} \quad (4.2)$$

where m_X is three invariant masses ($m_X = M_{d\pi^+},\ M_{d\pi^-}, M_{\pi\pi}$), m_i is a central value of each bin of the differential cross section histograms in Fig. 4.6, $f_{m_X}\left(m_i\right)$ is the convoluted fitting function of m_X, $\frac{d\sigma}{dm_X}$ is a differential cross section value, and $\delta_{d\sigma/dm_X}$ is a statistical error of the differential cross section value. The χ^2 was calculated only in the $d\sigma/dm_X\left(m_i\right) > 0$ region.

Free parameters of the fitting are amplitudes (α, β, γ), parameters of BW (M_{++}, M_0, Γ_{++}, Γ_0), and constant value for the phase space background (C). Therefore, the number of the free parameters was 8. The fixed values for M_ρ and Γ_ρ were 0.770 GeV/c^2 and 0.150 GeV/c^2, respectively. The fit result with free ρ^0 parameters are also shown in Appendix. B.5. The numbers of data points used in the fitting for four energy region are listed in Tab. 4.1. Figure 4.8 shows obtained parameters of R_{IV}, mass, width, and amplitude. The weighted averages of M_{++}, M_0, Γ_{++}, Γ_0 for four energy region are,

$$M^{4W}_{++} = 2.1316 \pm 0.0012 \text{ GeV}, \quad (4.3)$$
$$M^{4W}_{0} = 2.1340 \pm 0.0011 \text{ GeV}, \quad (4.4)$$
$$\Gamma^{4W}_{++} = 0.0992 \pm 0.0030 \text{ GeV}, \quad (4.5)$$
$$\Gamma^{4W}_{0} = 0.1072 \pm 0.0030 \text{ GeV}. \quad (4.6)$$

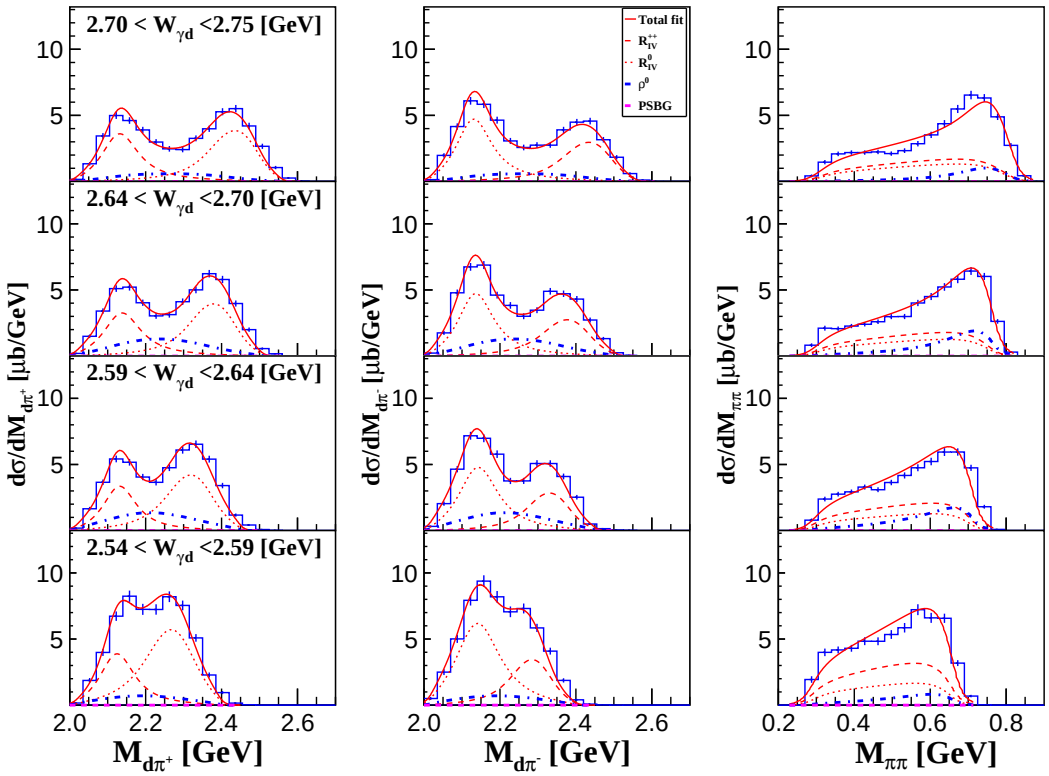

FIGURE 4.6: Differential cross sections ($d\sigma/dM$) for four W region. Upper panels show higher energy regions. The red solid lines show total fit results. The red dashed (dotted) lines show the BW contribution of R^{++}_{IV} (R^{0}_{IV}). The blue dot-dashed lines and magenta dashed lines show contributions of ρ^0 and phase space background, respectively. It should be noticed that the sum of all dashed, dotted, and dot-dashed lines in a panel does not equal to the solid line because the each contribution is summed up at amplitude level as shown in Eq. 4.1.

TABLE 4.1: Number of data points used in the fit

	Row of Fig. 4.6	1	2	3	4
	W [GeV]	2.70–2.75	2.64–2.70	2.59–2.65	2.54–2.59
Num.	$d\sigma/dM_{d\pi^+}$	18	16	14	13
of	$d\sigma/dM_{d\pi^-}$	18	16	15	13
data points	$d\sigma/dM_{\pi\pi}$	17	16	15	13
	Total	53	48	44	39

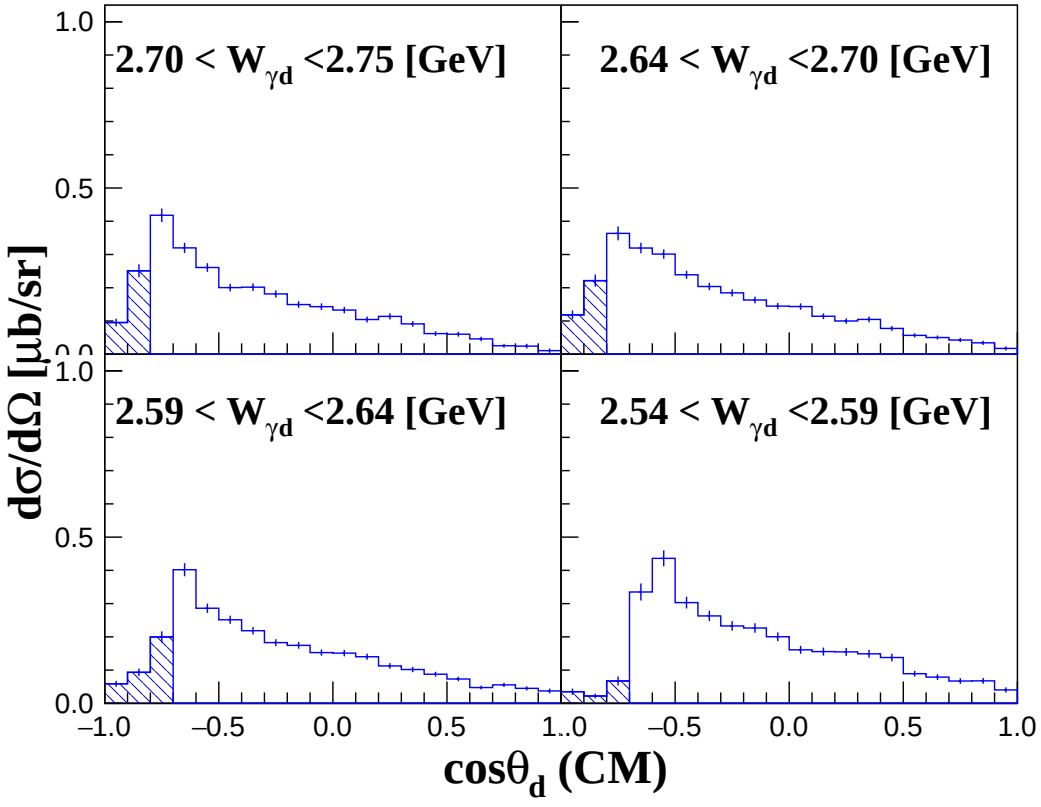

FIGURE 4.7: Differential cross section $d\sigma/d\Omega$ for four incident photon energy regions. The differential cross sections shown as shaded area were strongly distorted because of the limited t acceptance.

The weighted averages of the mass and width for the two charge states are,

$$M^{4W}_{R_{IV}} = 2.1329 \pm 0.0008 \text{ GeV}, \tag{4.7}$$
$$\Gamma^{4W}_{R_{IV}} = 0.1033 \pm 0.0021 \text{ GeV}. \tag{4.8}$$

The systematic uncertainty of the fit was estimated by calculating weighted deviation of the parameters.

$$\delta_M = 0.0044 \text{ GeV}, \tag{4.9}$$
$$\delta_\Gamma = 0.0092 \text{ GeV}. \tag{4.10}$$

The deviation due to uncertainty of ρ^0 shape was estimated by fitting of the differential cross sections with free mass and width parameters of ρ^0. The mass and width obtained by fit with free mass and width parameters of ρ^0 are,

$$M^{4W}_{R_{IV}}(\text{free } \rho^0) = 2.1244 \pm 0.0010(stat.) \pm 0.0045(syst.) \text{ GeV}, \tag{4.11}$$
$$\Gamma^{4W}_{R_{IV}}(\text{free } \rho^0) = 0.1011 \pm 0.0020(stat.) \pm 0.0094(syst.) \text{ GeV}. \tag{4.12}$$

The width is consistent with the fixed parameter fit. Thus, δ_Γ was adopted as the systematic error of Γ. However, the mass is different by 0.0085 GeV which is larger than $\delta_M = 0.0044$ GeV. Since the treatment of the shape of ρ^0 is not so trivial, we adopt this discrepancy as the systematic error. Figure B.9 shows the fitting result with free ρ^0 parameters.

As a result, the obtained mass and width of R_{IV} in this study were,

$$M_{R_{IV}} = 2.1329 \pm 0.0008\ (stat.) \pm 0.0085\ (syst.) \text{ GeV}, \tag{4.13}$$
$$\Gamma_{R_{IV}} = 0.1033 \pm 0.0021\ (stat.) \pm 0.0092\ (syst.) \text{ GeV}. \tag{4.14}$$

The mass and width of R^{++}_{IV} and R^0_{IV} are consistent with these of D_{12} reported by the FOREST group, $(M,\ \Gamma) = (2.140 \pm 0.011 \text{ GeV},\ 0.091 \pm 0.011 \text{ GeV})$ [Ish+19].

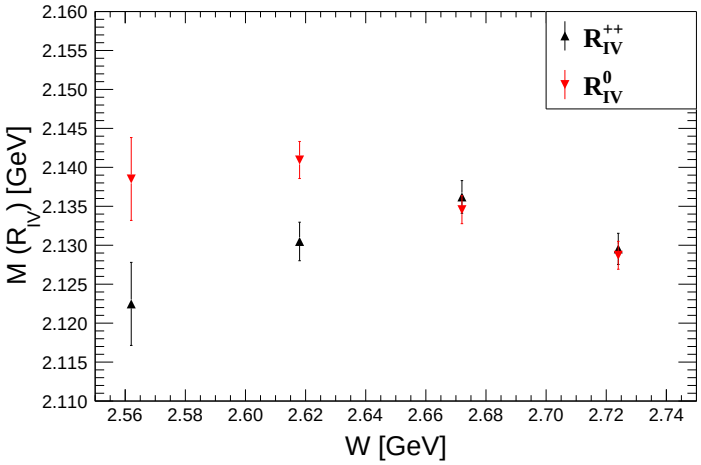

(A) Mass of R_{IV}

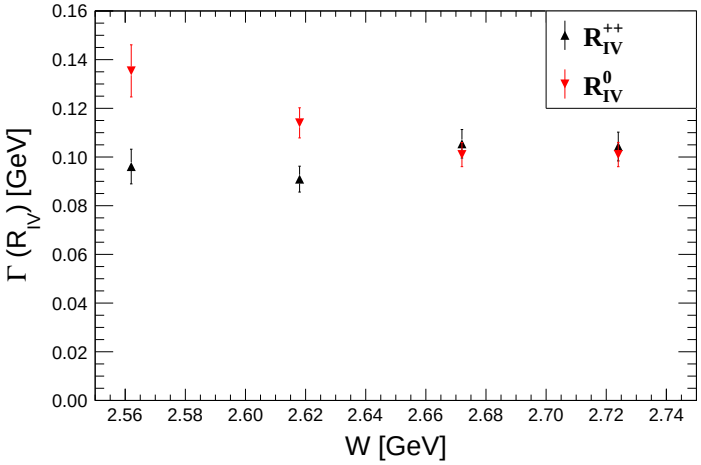

(B) Width (Γ) of R_{IV}

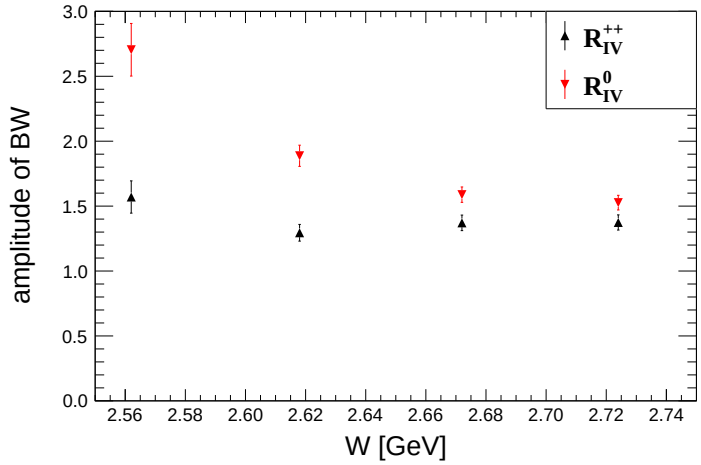

(C) Amplitude of R_{IV}

FIGURE 4.8: Fitting results of the differential cross sections. Mass (A), width (B), and amplitude (C) of the assumed resonances R_{IV} are shown.

5 Discussions

We have observed possible isovector resonance structures in the invariant mass distributions of $d\pi^{\pm}$ as shown in Chapter 4. In this chapter, we will discuss the properties of the possible resonance structures based on the fit parameters and the production process of the structures based on the angular distribution of deuteron emission. In addition, the present result was compared with the $\gamma d \to d\pi^{+}\pi^{-}$ reaction measured in the past using a bubble chamber. Finally, future prospects of experiments and analyses are discussed.

5.1 Proprieties of R_{IV}

The mass and width of the resonance structures obtained by fit are 2.13 GeV and 0.10 GeV as described in Sec. 4.2.2, respectively. The obtained mass is lower than the $N\Delta$ threshold (~2.17 GeV) and the width is narrower than the width of a single Δ particle (~0.12 GeV). The results are consistent with the mass and width of D_{12} obtained by FOREST [Ish+19]. The energy dependence of the strength of the cross sections is shown in Fig. 4.8(C). The amplitudes of R_{IV} decrease with increasing the incident photon energy. The energy dependence of the total cross section is almost flat, indicating that the ρ^0 cross section increases in the high energy region, while the R_{IV} cross section decreases. The cross section of R^0_{IV} is larger than that of R^{++}_{IV} in all energy regions. Neither qualitative nor quantitative interpretation of this result is yet available.

5.2 Deuteron Emission Angle and Production Process

From the angular distribution of deuterons, we discuss possible production processes of the peak structure at $M_{d\pi} = 2.13$ GeV/c^2. Figure 5.1 shows reaction diagrams considered in this section. As it is discussed in the $\gamma d \to d\pi^0\pi^0$ reaction [Ish+19], there are two possible scenarios for the formation process of isovector dibaryon resonances.

Scenario 1: γd emits two π via the dibaryon state, forming d in the final state (Fig. 5.1(A)).

Scenario 2: $\gamma d \to \pi R_{IV}$ reaction forms π and isovector dibaryon R_{IV}, and R_{IV} decays to π and d (Fig. 5.1(B)).

These scenarios can be distinguished by examining the angular distribution of the deuteron emission in the γd center-of-mass system. In scenario 1, deuteron is isotropically emitted. This is the result of the $\gamma d \to d\pi^0\pi^0$ reaction measurement, in which isovector dibaryons are observed in a continuous decay process from isoscalar dibaryons [Ish+19]. Scenario 2 shows an angular distribution of deuteron emission with a sideway peak. The position of the peak depends on the incident photon energy.

In addition to these scenarios, it is known that the process of quasi-free 2π production without going through the dibaryon state also produces a peak structure near the threshold of $N\Delta$.

Scenario 3: Quasi-free 2π production (Fig. 5.1(C)).

However, due to the kinematic constraint that the quasi-free produced Δ resonance and the spectator nucleon N_{spec} form a deuteron in the final state, the relative momenta of N_{spec} and Δ resonance must be small, resulting in deuteron being ejected ultra-backward in the γd center-of-mass system. Figure 5.2 shows a simple cartoon of the reaction mechanism of quasi-free 2π production with a Δ resonance. A nucleon and γ are reacted and produce Δ resonance with emitting the first π (labeled as π_1) forward in Step 2. Δ decays to $N\pi_2$ with emitting the second π (labeled π_2) forward, too. Then two nucleons in the final state can form a deuteron since relative momentum of them are small. If two π are not produced in the forward angle (which equals to that deuteron in the final state has backward momentum), the formation probability of deuteron in the final state will be extremely small. And in this quasi-free scenario, relative momentum of $N\Delta$ in an intermediate state is also small. Therefore, it is expected that a peak structure with a mass of $N\Delta$ and a width of Δ appears in th invariant mass spectrum of $d\pi_2$.

The deuteron angular distribution of each scenario is shown in Fig. 5.3. Red solid line, green dashed line, and magenta dotted line correspond to the scenario 1, 2, and 3, respectively. However, a certain cross section > 0.1 μb is observed in the region where $\cos\theta_d > 0$, suggesting that the spectator nucleon N and the quasi-free-generated Δ are not only close to each other with small relative momenta, but are also in a process via the dibaryon state. This suggests that the spectator nucleon and the quasi-free-generated Δ are not just close to each other with low relative momenta, but that the process is via a dibaryon state. In addition, the forward cross section is consistent with the interpretation that the process is via dibaryon production, since the deuteron emission angle at ρ^0 production is expected to be a strong backward peak.

In addition to these scenarios, there is a theoretical calculation which has suggested that a pion exchange process between spectator nucleons and quasi-free nucleon resonances increases the forward deuteron emission cross section [Ego20]. Figure. 5.1(D) shows an example of the diagrams which were taken into account in [Ego20]. Although this theoretical calculation still underestimates the forward cross section of the $\gamma d \to d\pi^0\pi^0$ reaction, it will be interesting to see how well this model reproduces the deuteron angular distribution of the $\gamma d \to d\pi^+\pi^-$ reaction obtained in this thesis.

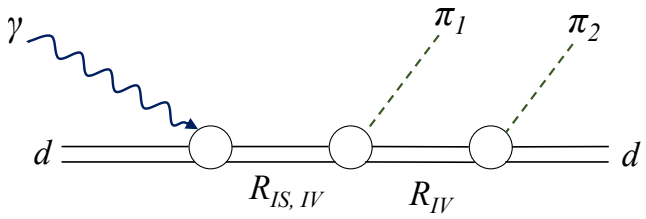

(A) Sequential decay from a dibaryon

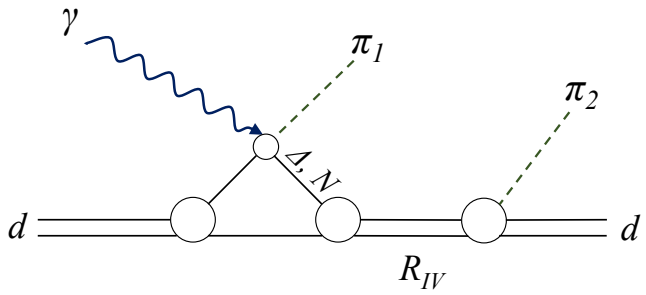

(B) Direct production of an isovector dibaryon

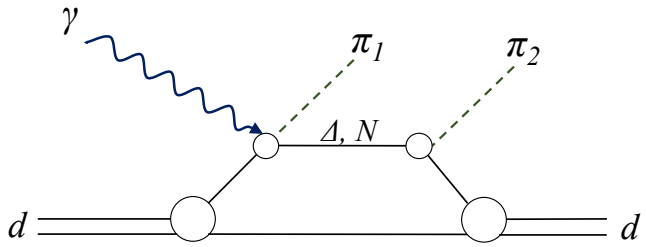

(C) Quasi-free 2-pion production

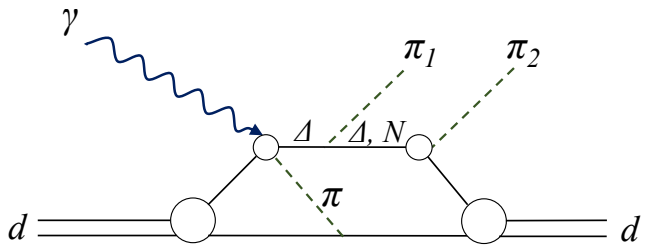

(D) Quasi-free 2-pion production with π exchange between spectator nucleon and quasi-free produced nuclear resonance

FIGURE 5.1: Possible diagrams of $\gamma d \rightarrow d\pi^+\pi^-$ with peak structures in $M_{d\pi}$. R_{IS} and R_{IV} represent isoscaler and isovector dibaryon, respectively. (A) R_{IV} is produced as a decay product of another dibaryon. (B) R_{IV} is directly produced. (C) Quasi-free 2-pion production without any dibaryon. (D) Quasi-free 2-pion production with π exchange between spectator nucleon and quasi-free produced nuclear resonance. It is an example of proposed mechanism in [Ego20].

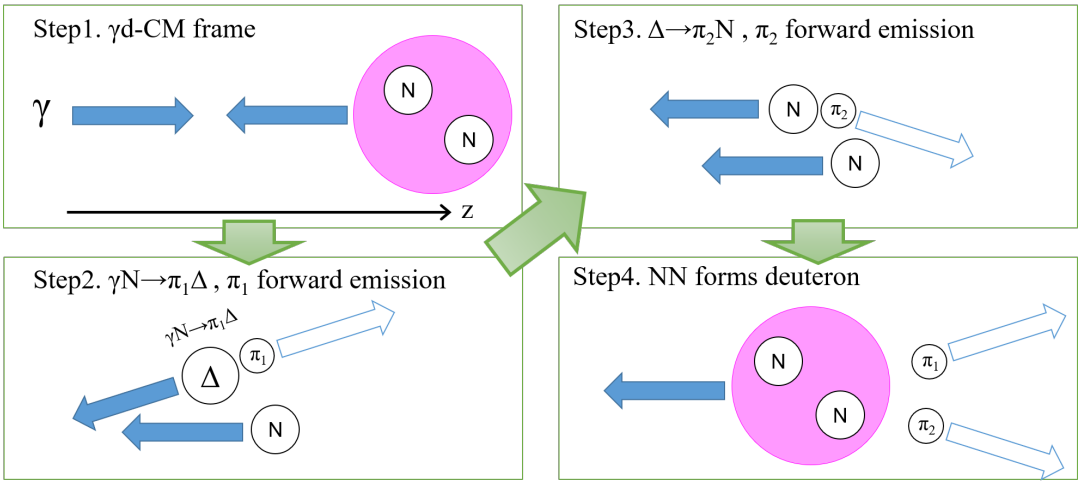

FIGURE 5.2: Animation of quasi-free 2-pion production in the γd−CM frame. (1) "Forward" direction is defined as direction of γ in the γd−CM frame. (2) A nucleon and γ are reacted and produce Δ resonance with emitting π_1 forward. (3) Δ decays to $N\pi_2$ with emitting π_2 forward. (4) Two nucleons forms deuteron.

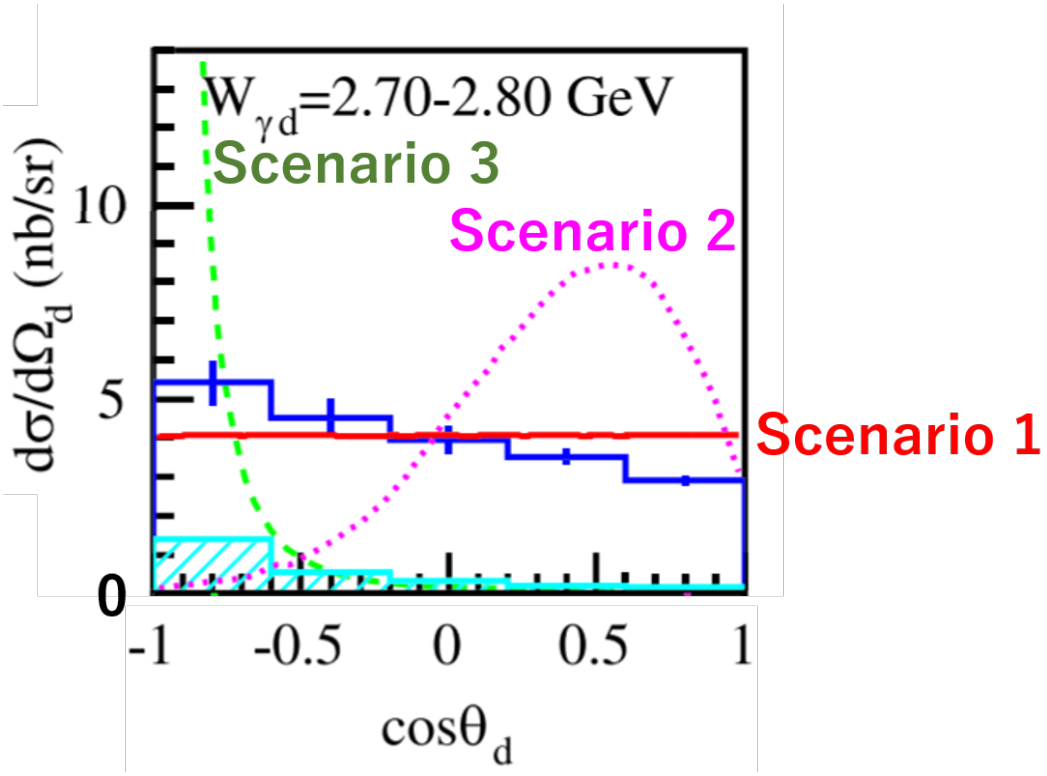

FIGURE 5.3: An angular distribution of deuteron in the $\gamma d \to d\pi^0\pi^0$ reaction [Ish+19]. Red solid line, green dashed line, and magenta dotted line correspond to the spherically uniform decay process (phase space decay), the quasi-free 2-pion production process based on [FA05], and the direct production of an isovector dibaryon process, respectively.

5.3 Comparison with the Previous Measurement

There is only one measurement of the $\gamma d \to d\pi^+\pi^-$ reaction around this energy region which was done by P. Benz *et al.* using a bubble chamber in 1970's [Ben+74]. In this paper, the analysis mainly focused on the production cross section of vector mesons, ρ and ω. However, a total cross section and invariant mass spectra were given. They can be compared with the result of this study. The total cross section and ρ^0 production cross section of the $\gamma d \to d\pi^+\pi^-$ with limited t region at E_γ = 1.4–5.0 GeV are shown in Fig. 5.4. The variable of t is a Mandelstam variable which is defined as,

$$t = (P_\gamma - P_{\pi\pi})^2, \tag{5.1}$$

where P_γ and $P_{\pi\pi}$ represent four vector of an incident photon and 2-pion system, respectively.

Invariant mass spectra of $M_{d\pi^+}$ for five incident photon energy regions are shown in Fig. 5.5. The invariant mass spectra were fitted by a sum of the phase space background (dashed lines) and ρ^0 production process. No peak structure was observed at $M_{d\pi}$ = 2.14 GeV.

The difference in the structure of the invariant mass distribution from the present study can be attributed to the fact that the kinematics measured by P. Benz *et al.* were limited in $0.04 < |t| < 0.20$ GeV^2. In the small $|t|$ region, the deuteron emission angle is restricted to the backward direction ($\cos\theta_d(\mathrm{CM}) \lesssim -0.8$), and a diffluctive vector meson production process dominated by ρ^0 is main component. If the dibaryon production is mainly produced by the process of deuteron forward emission, as discussed in the previous section, then it is understandable that the dibaryon signal cannot be observed in such a kinematic range, $0.04 < |t| < 0.20$ GeV^2.

Although the overlap region of the photon energy is small, the bubble chamber experiment shows a predominantly larger cross section than the measurement in the present study. In the incident photon energy range of the present experiment ($0.77 < E_\gamma < 1.08$ GeV), deuteron momentum in the laboratory system in the $|t| < 0.2$ GeV^2 region corresponds $\lesssim 0.4$ GeV/c, and this momentum deuteron is not measurable in this analysis scheme. The deuteron with momentum $\lesssim 0.4$ GeV/c cannot reach OH, the trigger counter of NKS2, due to the energy loss in the material during flight. Therefore, it is difficult to make a direct comparison with the experimental data. With the improvement of the analysis software, direct comparison between this experimental data and the bubble chamber experiment might be possible. The future prospects will be discussed in Sec. 5.4.

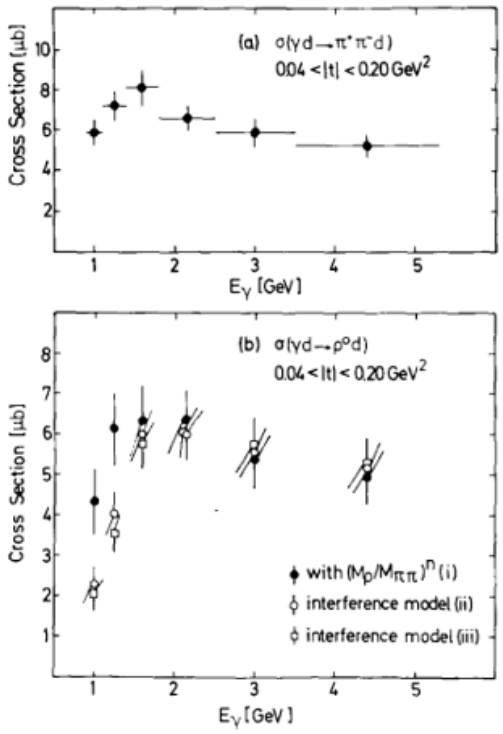

FIGURE 5.4: Total cross section of the (a) $\gamma d \to d\pi^+\pi^-$ and (b) $\gamma d \to d\rho^0$ reaction measured in 1974 [Ben+74]. The kinematics was limited in $0.04 < |t| < 0.20$ GeV^2. The filled circles, open circles, and open squares show the cross sections of the $\gamma d \to d\rho^0$ reaction with different ρ^0 resonance shape assumptions.

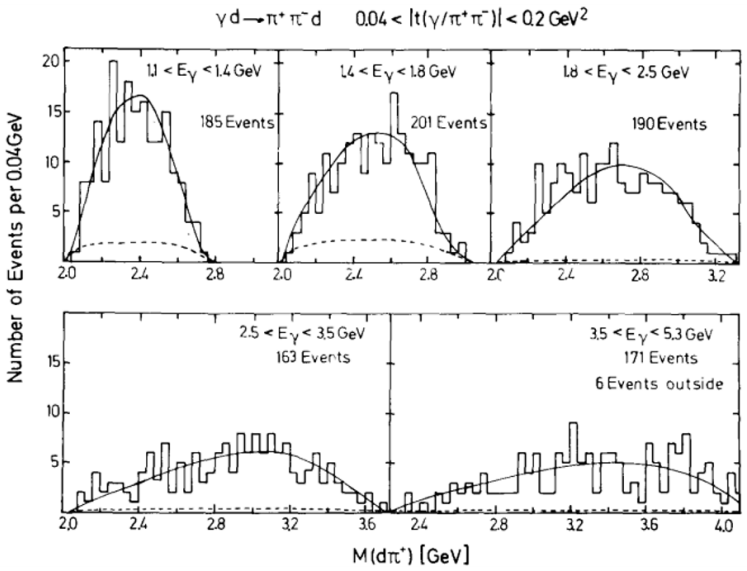

FIGURE 5.5: The invariant mass spectra of $M_{d\pi^+}$ for five photon energy region [Ben+74]. The solid lines and dashed lines show the total distribution and phase space background distribution obtained by fit, respectively. The total distribution is described as an incoherent sum of ρ^0 resonance term and the phase space background term.

5.3.1 Extrapolation of NKS2 data to $|t| < 0.15$ GeV^2 region

As mentioned in the previous section, the region of $|t| < 0.20$ GeV^2 was outside the acceptor in this measurement, however we extrapolated the obtained results and compared the total cross section with that of P. Benz *et al.*[Ben+74]. As described in Sec. 3.6, we evaluated the acceptance of NKS2 using the simulator whose production distribution was tuned to reproduce the invariant mass and angular distributions of the real data. The blue shaded histogram in Fig. 5.6 shows the t-distribution generated by the tuned simulator in the $1.054 < E_\gamma < 1.078$ GeV which corresponding to the energy region covered by TagB1. The slope parameter $b_{NKS} = 2.3$ GeV^{-2} of a function of $\exp(-b|t|)$ was estimated by fitting the distribution in $0.60 < |t| < 1.20$ [GeV] region. In the $0.04 < |t| < 0.15$ GeV^2 region of Fig. 5.6, the solid lined histogram shows the distribution when the cross section of $0.04 < |t| < 0.20$ GeV^2 is ~6 b and the distribution follows $\exp(-b|t|)$. Another constraint was that distributions must be smoothly connected at $|t| = 0.15$ GeV^2. As a result, $b \sim 40$ GeV^{-2} was obtained. P. Benz *et al.* obtained $b \sim 24$ GeV^{-2} in the region of $1.8 < E_\gamma < 2.5$ GeV. The b value of P. Benz *et al.* differed by a factor of 2. Note that the value of b in the region $E_\gamma < 1.8$ GeV is not shown in [Ben+74]. Although there is a slight deviation from these values, considering that the dependence of b on the cross section is $\propto \exp(b|t_{max}|)$ where $|t_{max}| = 0.20$ GeV^2 is a maximum $|t|$ for an integration, we can say that the slope is about the same. However, in the measurement of P. Benz *et al.*, the production of ρ^0 accounts for the majority of the cross section, as can be seen from the fit of the invariant mass distribution. This energy region, $1.054 < E_\gamma < 1.078$ GeV, is below the ρ^0 production threshold, so the ρ^0 t-channel production is suppressed and the b value is smaller than it for $1.8 < E_\gamma < 2.5$ GeV. It is natural to assume that the value of b is smaller than it for $1.8 < E_\gamma < 2.5$ GeV. Therefore, it is a bit premature to conclude that the results of NKS2 and P. Benz *et al.* are consistent. At the very least, the cross section obtained in this study and that measured by P. Benz *et al.* cannot be explained consistently as can be easily seen from Fig. 5.6 unless there is a structure in which the shape of the distribution changes dramatically depending on the region of t.

Figure 5.7 is another demonstration of the comparison between the result of NKS2 and that of P. Benz *et al.*. This is the distribution of $\cos\theta_d$ expected when the total cross section of 6 μb is in the region of $0.04 < |t| < 0.20$ GeV^2 in $2.70 < W < 2.75$ GeV region. The assumed cross sections in the region of $0.04 < |t| < 0.20$ GeV^2 are shown as a green shaded histogram, the differential cross section obtained in this study is shown as a blue solid line (same with the top left distribution in Fig. 4.7), and their summation is shown as a black solid line. In this W region, the events in $0.04 < |t| < 0.20$ GeV^2 distribute in $\cos\theta_d < -0.8$. The distribution of t should have a certain distribution in the region of $\cos\theta_d < -0.8$, but we assume that the distribution is flat in the corresponding two bins.

A more quantitative comparison needs by performing measurements in the $|t| < 0.15$ GeV^2 region with NKS2 in future as described in the next section.

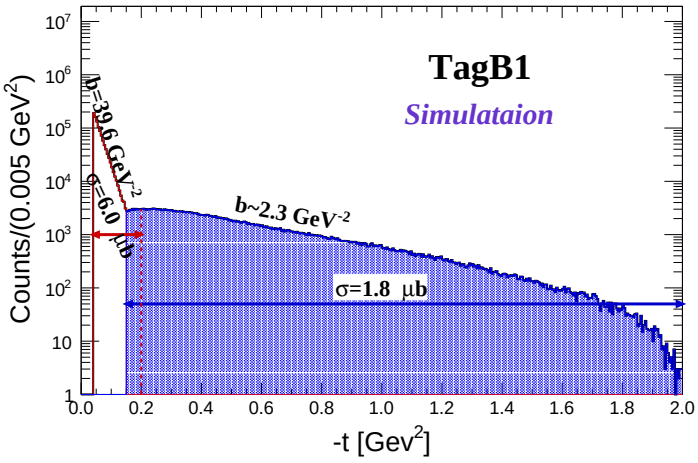

FIGURE 5.6: Simulated t distribution in $1.054 < E_\gamma < 1.078$ GeV. The blue shaded histogram shows the t-distribution which reproduces the experimental result of this study. The black solid line shows the simulated distribution to reproduce the total cross section obtained by P. Benz *et al*. [Ben+74]. The both distributions are fitted by a function of $\exp(-b|t|)$. The obtained b parameters for the blue and black histograms are 2.3 and 39.6 GeV^{-2}, respectively.

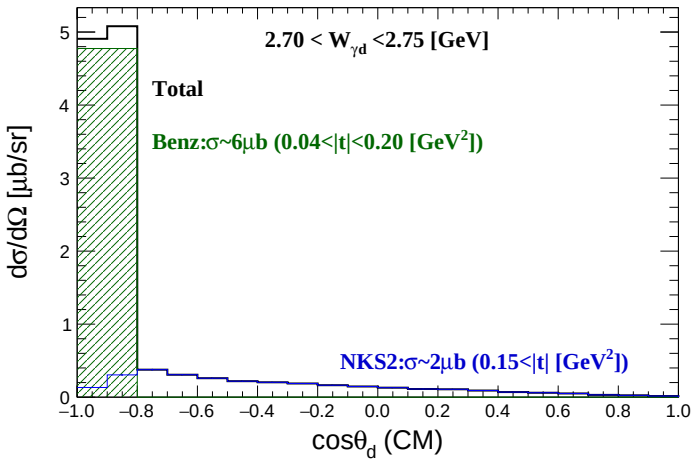

FIGURE 5.7: Demonstration of the comparison of differential cross section obtained in this study and P. Benz *et al*.. This is the distribution of $\cos\theta_d$ expected when the total cross section of 6 μb is in the region of $0.04 < |t| < 0.20$ GeV^2 in $2.70 < W < 2.75$ GeV region. The assumed cross sections in the region of $0.04 < |t| < 0.20$ GeV^2 are shown as a green shaded histogram, the differential cross section obtained in this study is shown as a blue solid line (same with the top left distribution in Fig. 4.7), and their summation is shown as a black solid line.

5.4 Future Prospects

Future prospects of the further analysis of the present data and possible measurements of dibaryon by NKS2 will be discussed in this section.

5.4.1 Spin and Parity of R_{IV}

For the isovector resonance structure R_{IV} in the $d\pi^{\pm}$ invariant mass spectra, we obtained mass and width in the reaction that are consistent with the D_{12} found in the $\gamma d \to d\pi^0\pi^0$ reaction. On the other hand, the behavior of the total cross section and the angular distribution of deuteron show different trends in the $\gamma d \to d\pi^+\pi^-$ and $\gamma d \to d\pi^0\pi^0$ reactions. It is necessary to analyze the decay angle distribution of $d\pi^{\pm}$ to determine the spin parity in order to compare the observed R_{IV} with D_{12}.

5.4.2 Measurement of Deuteron with Lower Momentum

In this study, we analyze the event where the deuteron reaches the OH, the downstream detector of the NKS2 system. Due to the energy loss between the target and the OH, deuterons below about 0.4 GeV/c cannot be measured. This resulted in a low sensitivity to events where deuterons were ejected backward. In order to measure low-momentum charged particles, we are developing an algorithm to reconstruct the trajectory using only VDC for particles that do not reach the OH. By improving the deuteron backward sensitivity, we will be able to make measurements in the region of $|t| < 0.2$ GeV, which will allow us to make a direct comparison with the bubble chamber experiment, where no resonance signal was observed, and provide a more quantitative discussion of the process of creating the resonance state obtained in this measurement.

5.4.3 Measurement of $\gamma d \to d\pi^+\pi^-$ and $\gamma d \to d\pi^+\pi^-\pi^0$ with Higher Incident Photon Energy

In this measurement, we observed an isovector resonant structure which is consistent with D_{12} in the $M_{d\pi}$ distributions. D_{12} could also be measured as a decay product from D_{03} which was observed by WASA-at-COSY or as a decay of the isoscalar dibaryon observed by FOREST. In order to observe D_{03} in NKS2, it is necessary to measure the total cross section of the $\gamma d \to d\pi^+\pi^-$ reaction at low energies or to observe the peak structure of the $d\pi\pi$ invariant mass in the $\gamma d \to d\pi\pi\pi$ reaction. Since it is difficult to operate the accelerator at ELPH with reduced energy of the orbiting electrons, it is practical to measure the $\gamma d \to d\pi^+\pi^-$ reaction. In addition, the accelerator upgrade in 2011 increased the maximum photon beam energy to 1.2 GeV. By measuring the $\gamma d \to d\pi^+\pi^-$ reaction again in the current energy range, it will be easier to separate the ρ^0 and D_{12} signals. The $\gamma d \to d\pi^+\pi^- X$ reaction measurement experiment is currently underway at NKS2 to search for a bound state of $\eta' d$. The data obtained from this experiment is expected to provide new insights into the above study.

6 Summary and Conclusion

In hadron physics, exotic hadrons, which are not classified as conventional baryons or mesons, are interesting objects of study because their internal structures and quantum states provide probes for further understanding of hadronic interactions and QCD. The dibaryon state with a baryon number of two has been studied for a long time as one of the exotic hadrons.

In this study, we measured the $\gamma d \to d\pi^+\pi^-$ reaction using NKS2, a magnetic spectrometer with a large acceptance. The experiment was carried out in October 2010 in the second experimental hall of ELPH at Tohoku University. In the $0.78 < E_\gamma < 1.08$ GeV region, a 166 mb^{-1} liquid deuterium target was irradiated with $\sim 10^{12}$ real photons, and the charged particles after the reaction were analyzed for momentum by NKS2. In an analysis in which two particles of $d\pi^+\pi^-$ were detected by NKS2 and the undetected π was measured with missing mass, ~15000 events were identified as the $\gamma d \to d\pi^+\pi^-$ reaction events. In an analysis where all three particles in the final state were detected by NKS2, ~2000 events were identified as the $\gamma d \to d\pi^+\pi^-$ reaction events.

In this thesis, we have shown the total cross section, the differential cross sections of the $\gamma d \to d\pi^+\pi^-$ reaction in the region of $|t| > 0.15$ GeV^2. This is the world's first measurement of this reaction in this energy region. The total cross section showed flat distribution within the measured energy range. Dibaryon resonance structures were observed below the $N\Delta$ threshold in the differential cross section of the invariant mass of $d\pi^\pm$. A function taking into account ρ^0, backgrounds proportional to phase space, and detector resolution, the peak structure was fitted with a Breit-Wigner function, yielding a mass and width of $2.1329 \pm 0.0008\ (stat.) \pm 0.0085\ (syst.)$ GeV and $0.1033 \pm 0.0021\ (stat.) \pm 0.0092\ (syst.)$ GeV, respectively. The obtained mass and width are consistent with these of D_{12} measured by the $\gamma d \to d\pi^0\pi^0$ reaction [Ish+19]. There is certain cross section > 0.1 μb/sr is observed in the deuteron forward emitted region where $\cos\theta_d > 0$, though the deuteron emission angular distribution shows a slightly backward enhanced structure, unlike the $\gamma d \to d\pi^0\pi^0$ reaction. The conventional quasi-free pion photoproduction processes cannot explain the cross section in $\cos\theta_d > 0$. In addition, the fact obtained width of the resonance was narrower than that of free Δ by ~20 MeV. From these results, the observed structures can be regarded as $N\Delta$ dibaryons, especially neutral and $z = 2$ charge states of theoretically predicted and experimentally studied D_{12}. This is the first measurement of D_{12} in the $\gamma d \to d\pi^+\pi^-$ reaction.

A Cross Section of Λ

The cross section of inclusive Λ production on the deuteron target was studied to verify the cross section analysis of the $\gamma d \to d\pi^+\pi^-$ reaction.

A.1 Cross Section

The obtained cross section is shown in Fig. A.1. The acceptance for Λ measurement was estimated by a function of initial momentum of Λ based on the Monte-Carlo simulation. The rectangles show systematic uncertainties which are dominated by the background subtraction though further investigation for the uncertainties would be necessary. Consistent with previous study of NKS2 [Bec13] within the systematic uncertainties.

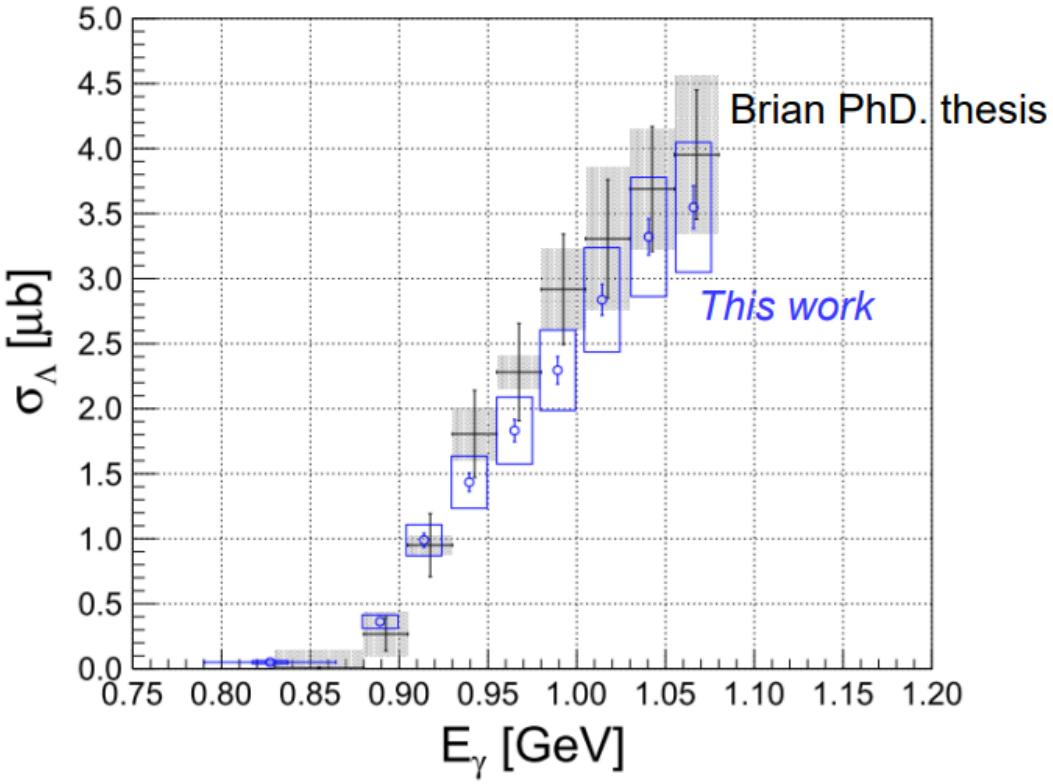

FIGURE A.1: Total cross section of Λ

B Supplemental Figures

Supplemental figures referred in the thesis will be shown in this appendix.

B.1 Wire Efficiency

The wire efficiencies of Layer1 and Layer14 was shown in Sec. 3.2.2. The wire efficiencies of all layers are shown in Fig. B.1.

Figure B.2 shows comparison of the wire efficiency of the real data and that of the simulated data. The embedded efficiencies were reasonably reproduced by the simulation.

B.2 Proton Contamination for Each Momentum Region

$p\pi X$ contamination was estimated in Sec. 3.5.1. The fitting results of mass square distribution for all momentum region are shown in Fig. B.3.

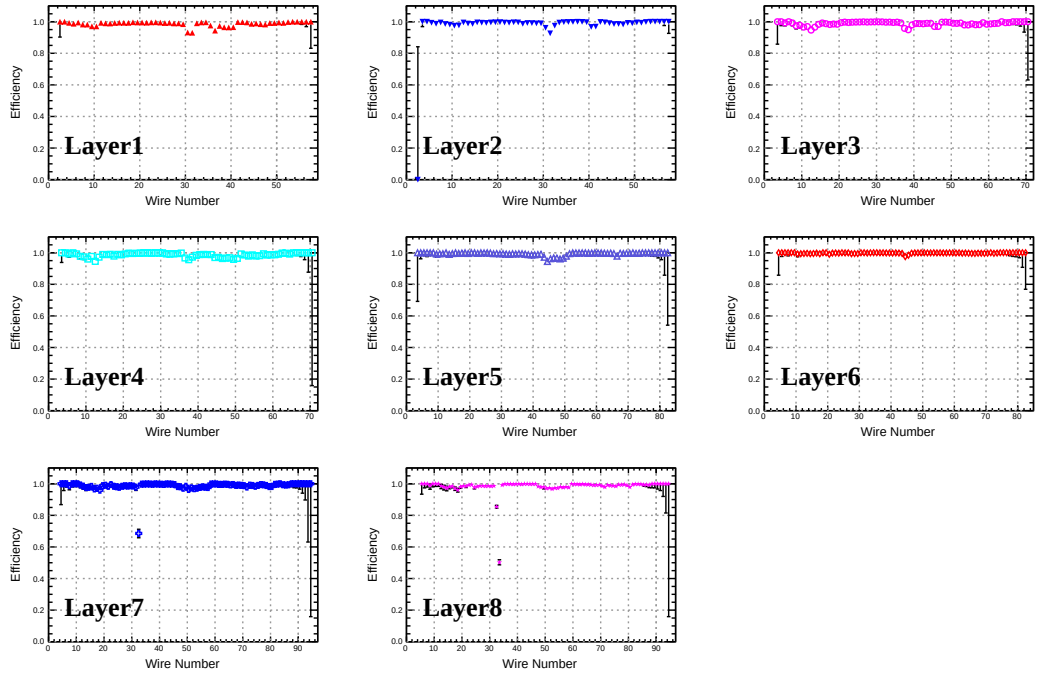

(A) VDC wire efficiency

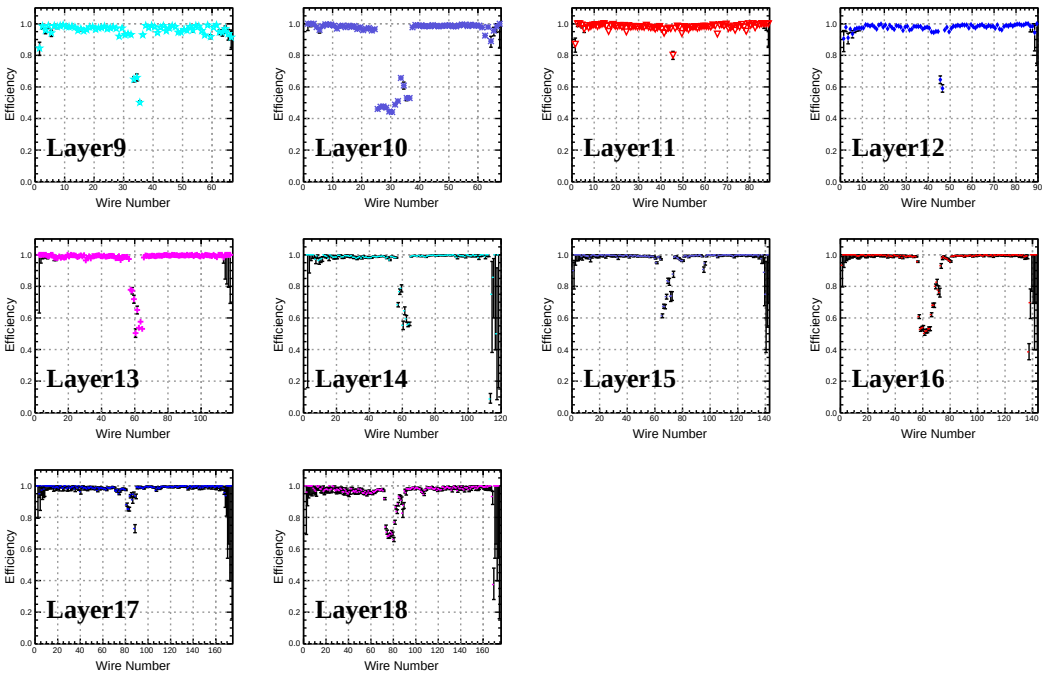

(B) CDC wire efficiency

FIGURE B.1: Wire efficiency.

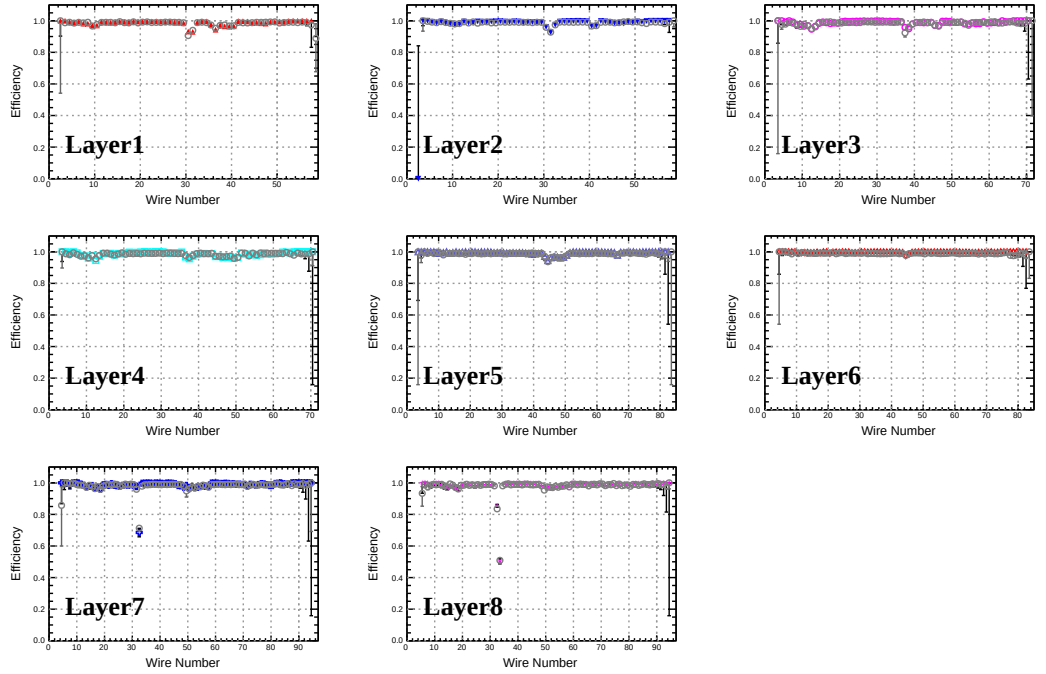

(A) VDC wire efficiency

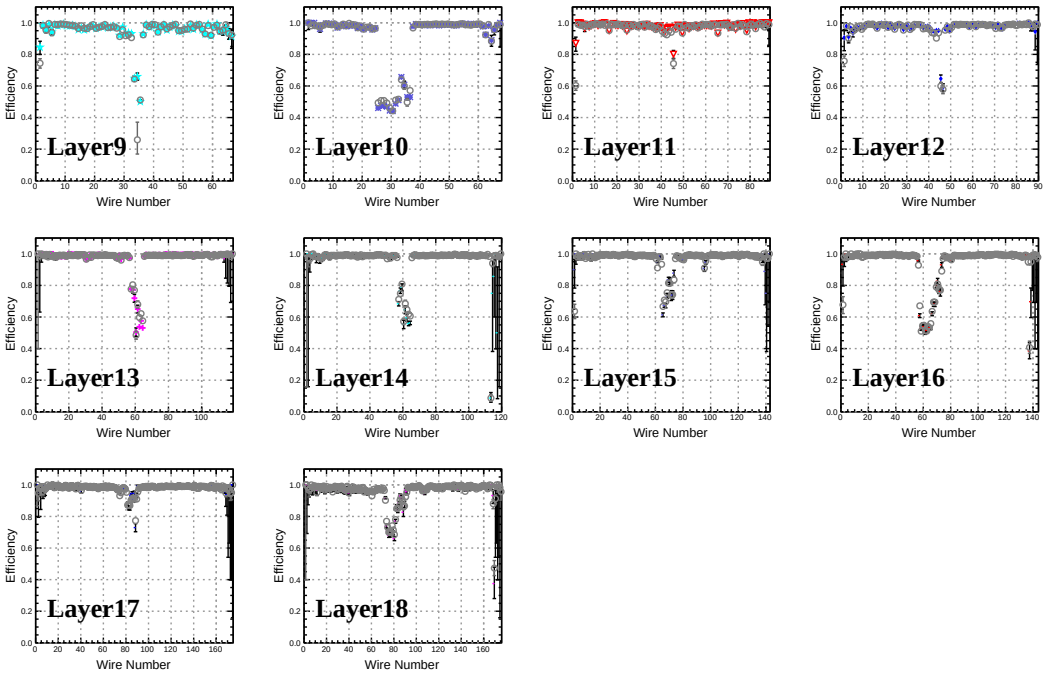

(B) CDC wire efficiency

FIGURE B.2: Wire efficiency with simulation. Gray points show the efficiency derived from simulated data.

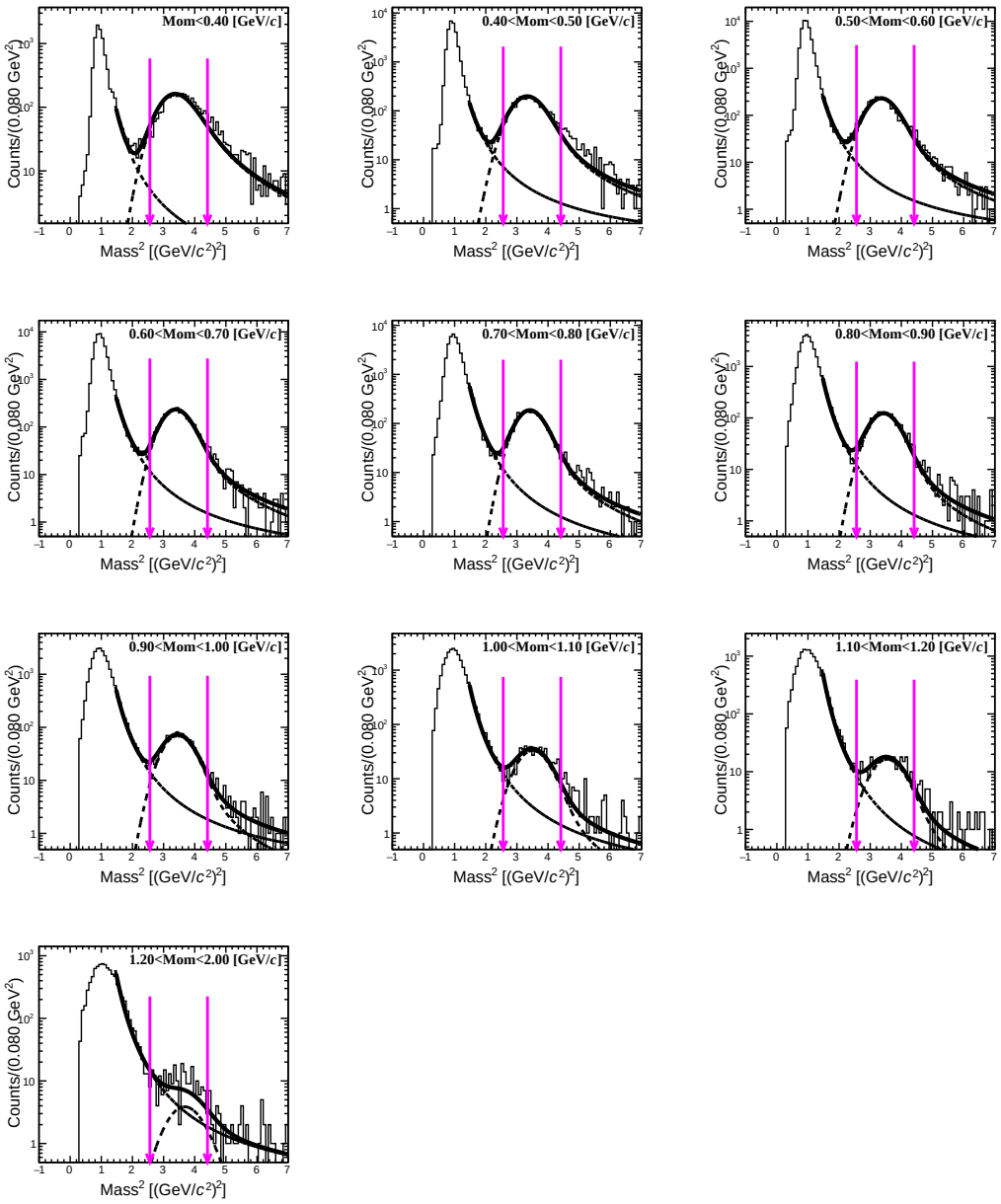

FIGURE B.3: proton contamination fit of all momentum regions

B.3 MC tuning

The tuned simulator which was used to estimate η_{acpt} was introduced in Sec. 3.6.1. The comparison of the invariant mass and angle distributions for each TagB segment for the simulation of uniform event generation in a three-body phase space (red points), the tuned simulation (blue points), and real data (black lines) are shown in Fig. B.4. The results of the fit of each distribution for each TagB segment after the fifth iteration to determine each enhancement function are shown in Fig. B.5. The obtained η_{acpt} for each TagB segment is shown in Fig. B.6.

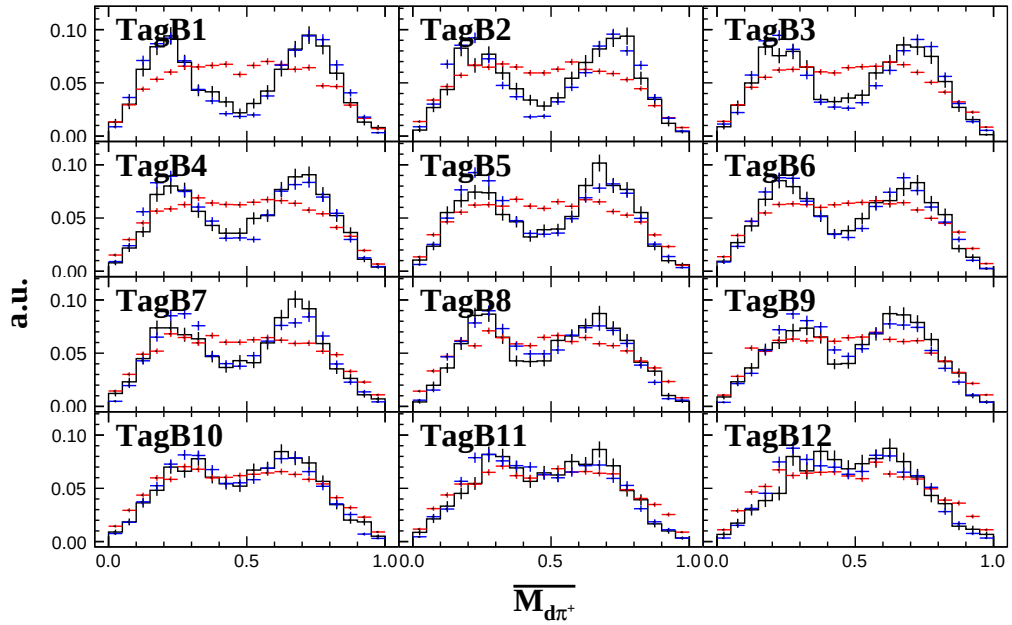

(A) $d\pi^+$ normalized invariant mass.

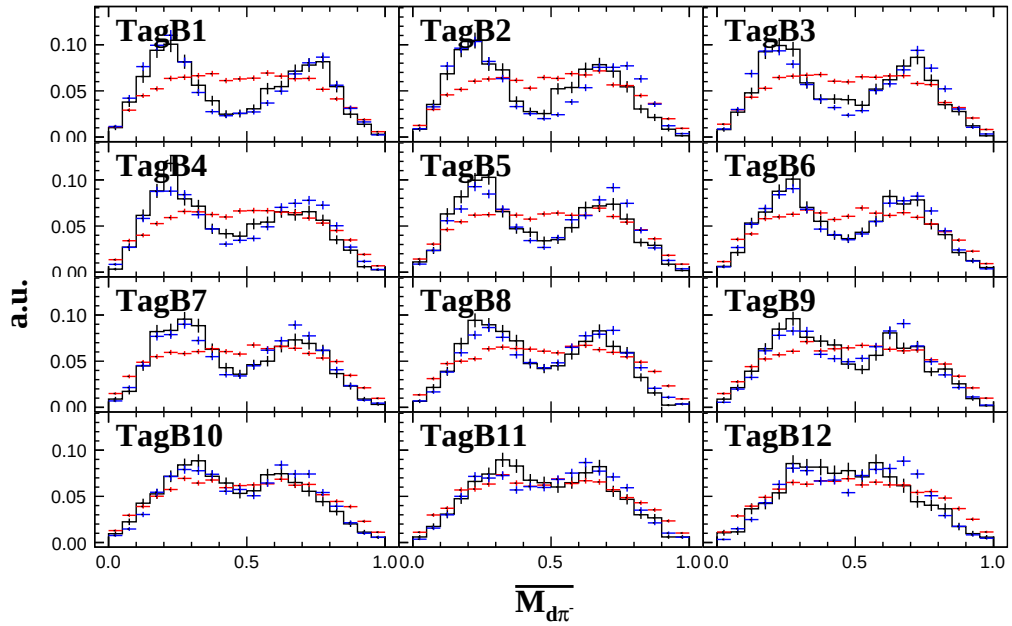

(B) $d\pi^-$ normalized invariant mass.

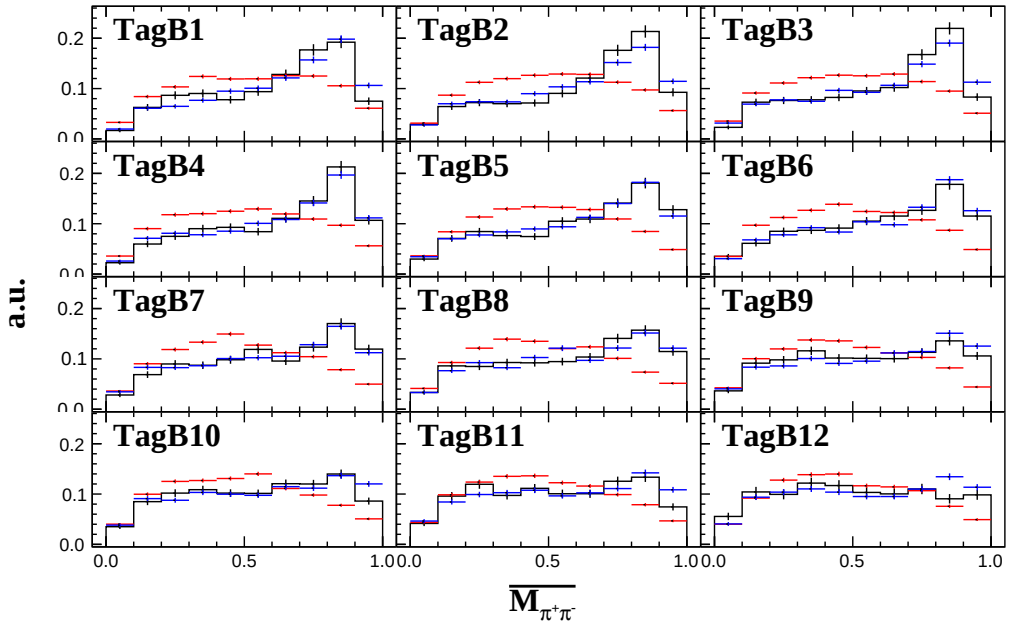

(C) $\pi^-\pi^+$ normalized invariant mass.

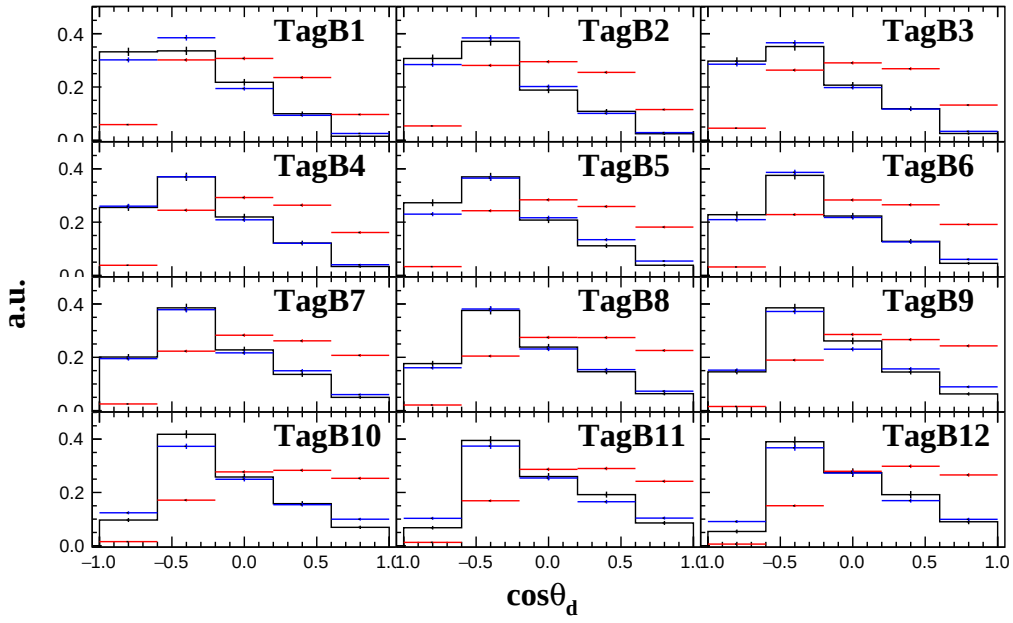

(D) $\cos\theta_d$ in γd-CM frame.

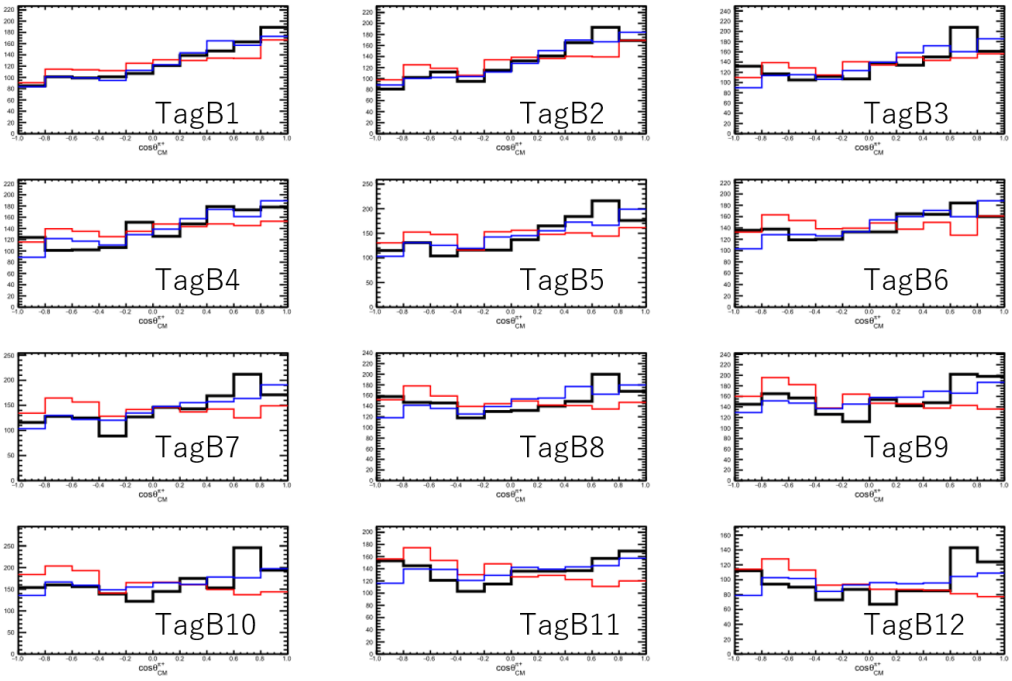

(A) $\cos\theta_{\pi+}$ in γd-CM frame

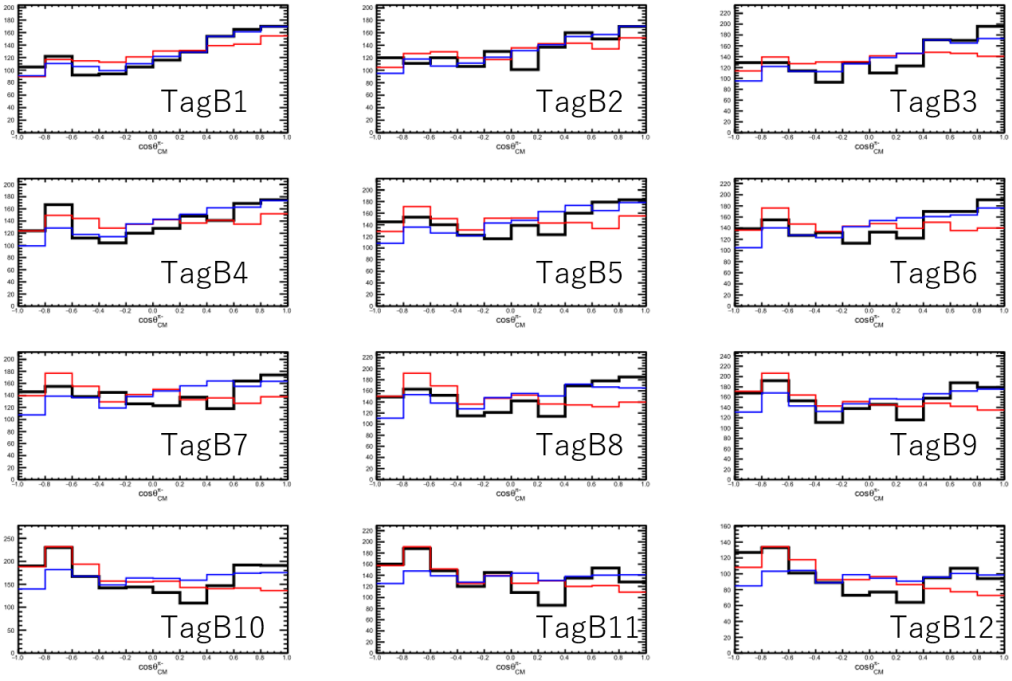

(D) $\cos\theta_{\pi-}$ in γd-CM frame.

FIGURE B.4: Normalized invariant mass spectra and angular distribution of deuterons. Black lines show the real data. Red points show the three-body phase space simulation. Blue lines show the tuned simulation. (A)$d\pi^+$ (B) $d\pi^-$ (C) $\pi^-\pi^+$ (D) $\cos\theta_d$ in γd-CM frame. (E) $\cos\theta_{\pi+}$ in γd-CM frame. (F) $\cos\theta_{\pi-}$ in γd-CM frame.

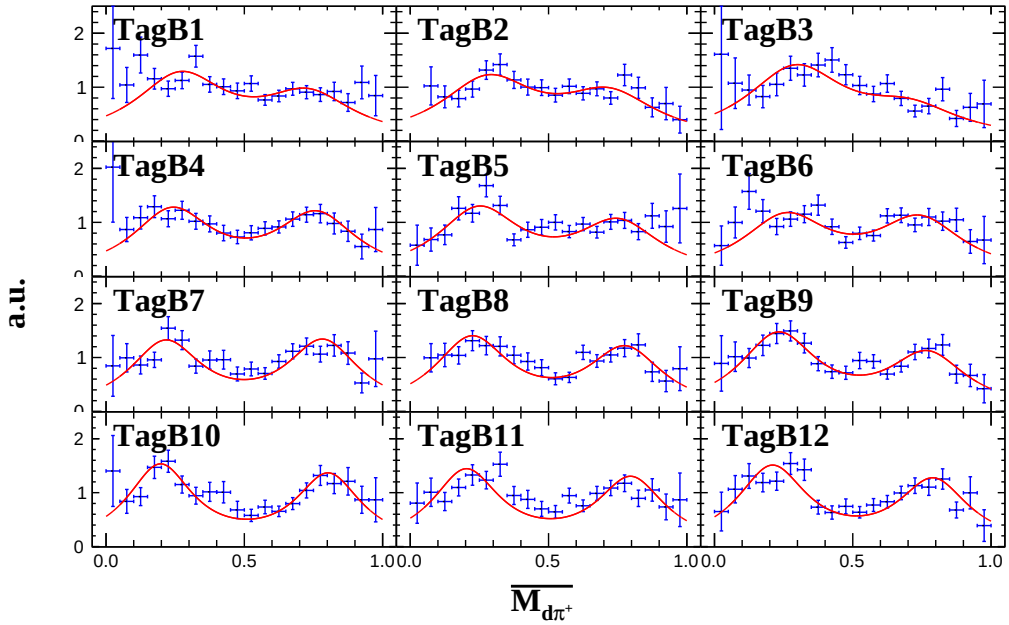

(A) $d\pi^+$ normalized invariant mass.

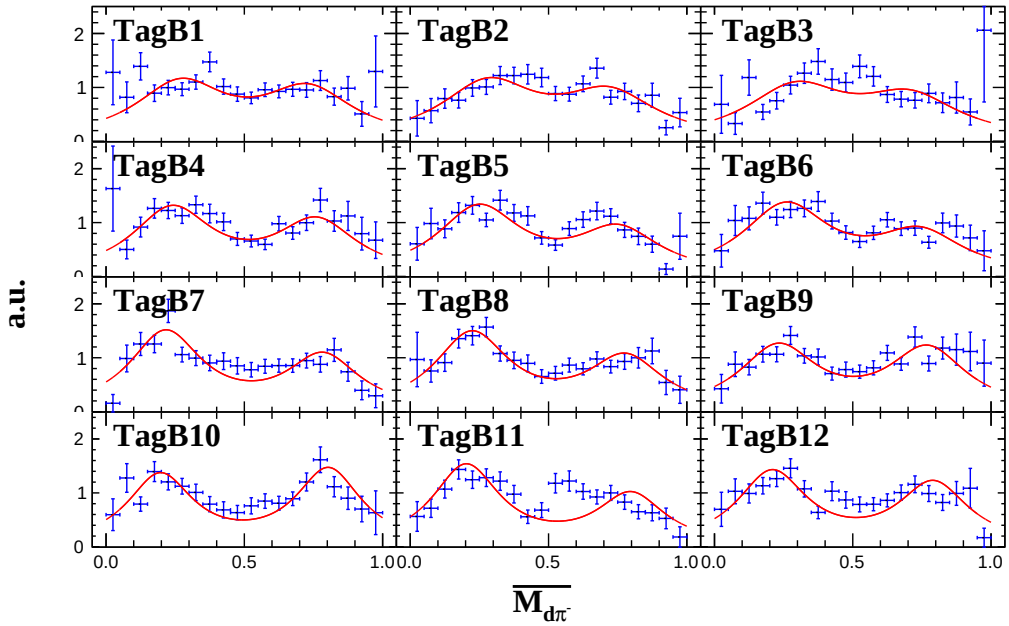

(B) $d\pi^-$ normalized invariant mass.

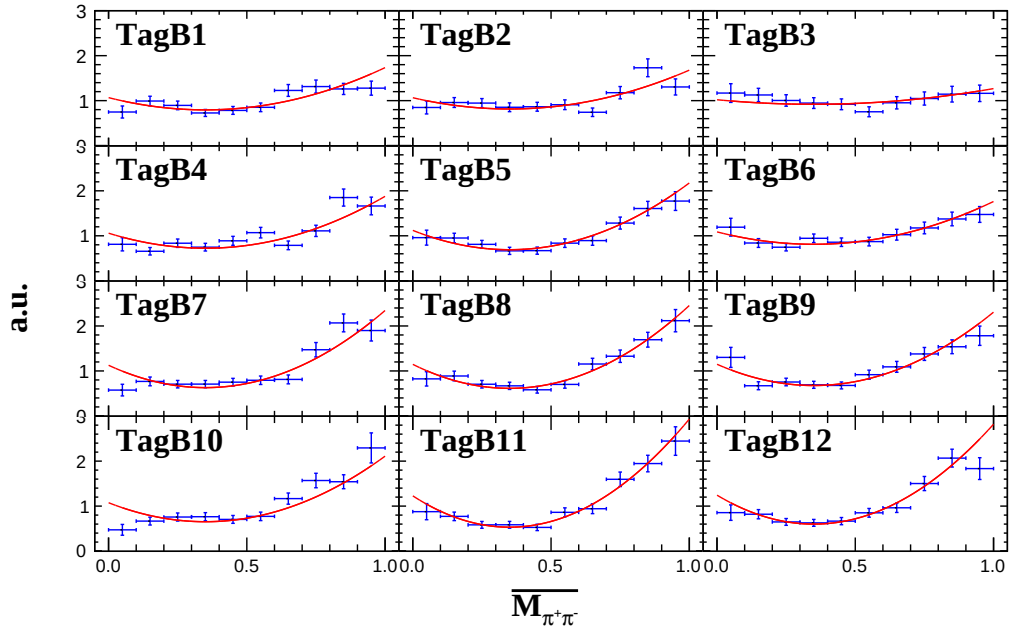

(C) $\pi^-\pi^+$ normalized invariant mass.

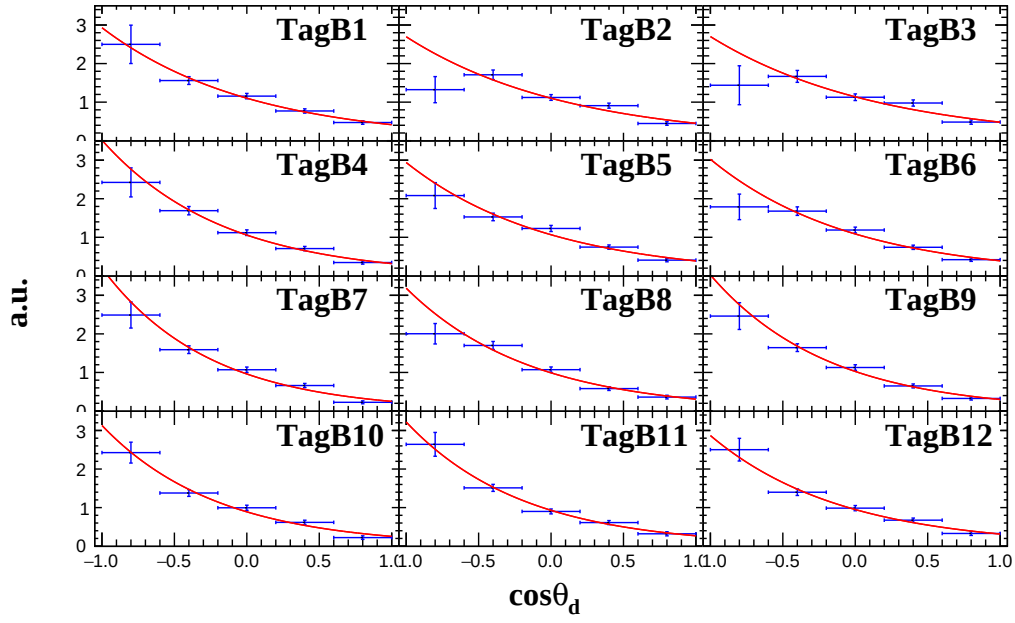

(D) $\cos\theta_d$ in γd-CM frame.

FIGURE B.5: Normalized invariant mass spectra and angular distribution of deuterons. (A)$d\pi^+$ (B) $d\pi^-$ (C) $\pi^-\pi^+$ (D) $\cos\theta_d$ in γd-CM frame.

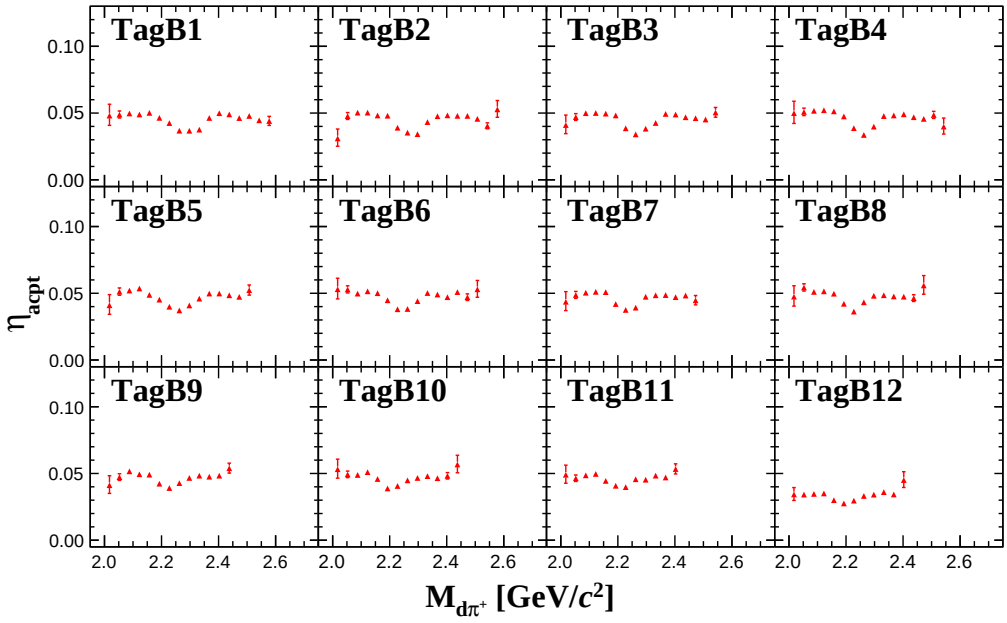

(A) $d\pi^+$ invariant mass.

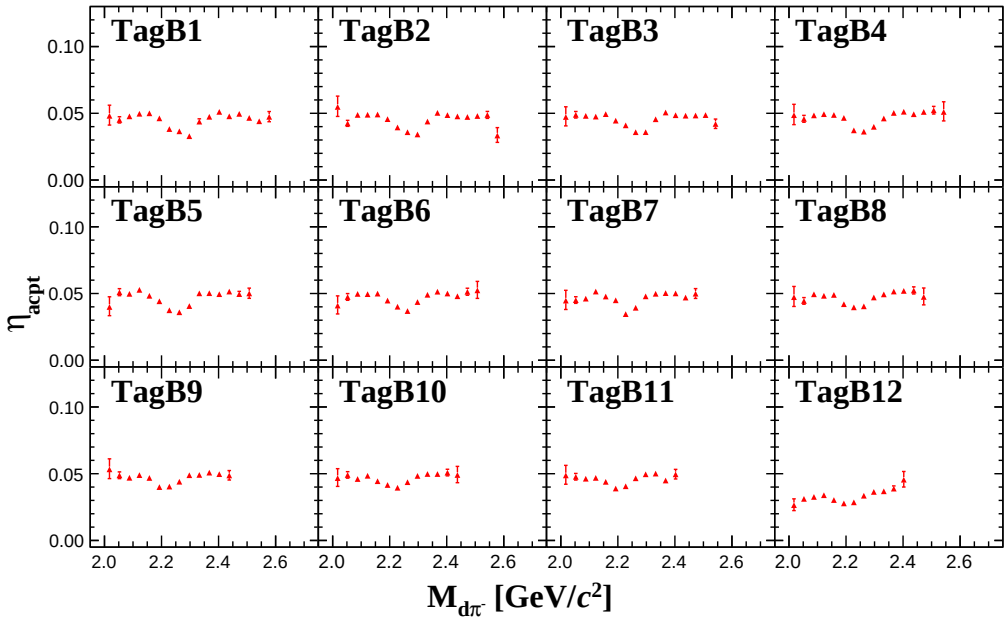

(B) $d\pi^-$ invariant mass.

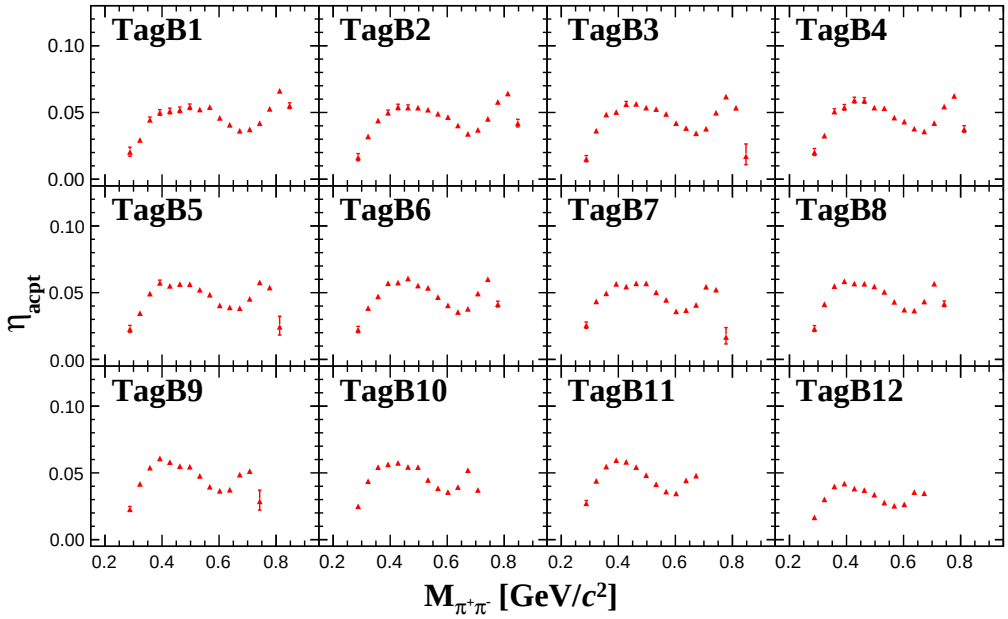

(C) $\pi^-\pi^+$ invariant mass.

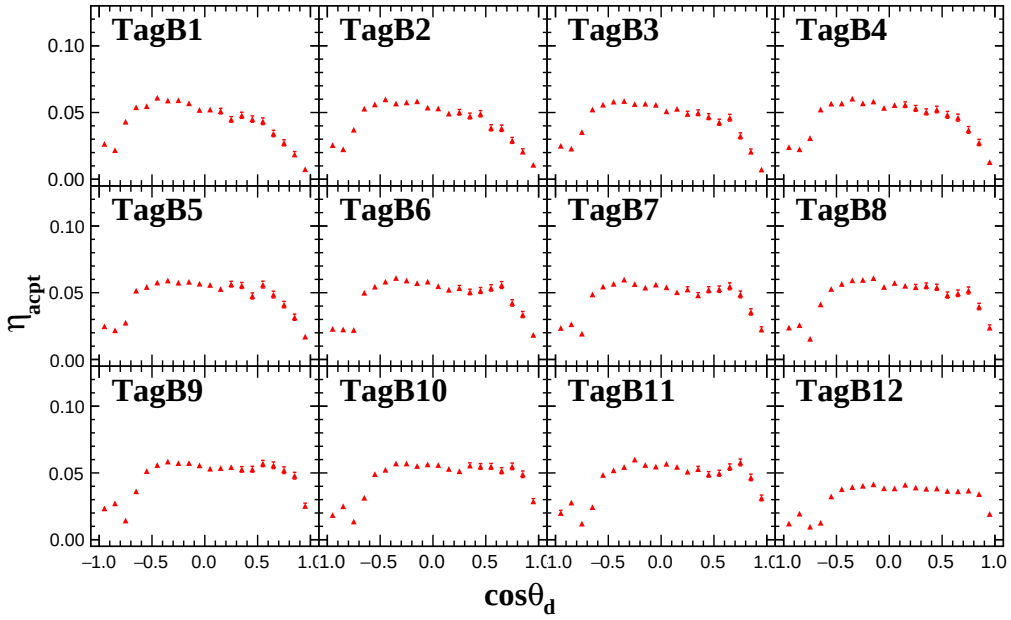

(D) $\cos\theta_d$ in γd-CM frame.

FIGURE B.6: η_{acpt} for each invariant mass and angular distribution of deuterons. (A)$d\pi^+$ (B) $d\pi^-$ (C) $\pi^-\pi^+$ (D) $\cos\theta_d$ in γd-CM frame.

B.4 Invariant Mass Spectra for Each Incident Photon Energy Region

2-dimensional plots of invariant mass spectra for hole measured energy region were shown in Fig. 4.2. The 2-dimensional invariant mass spectra for each incident photon energy region are shown in Fig. B.7.

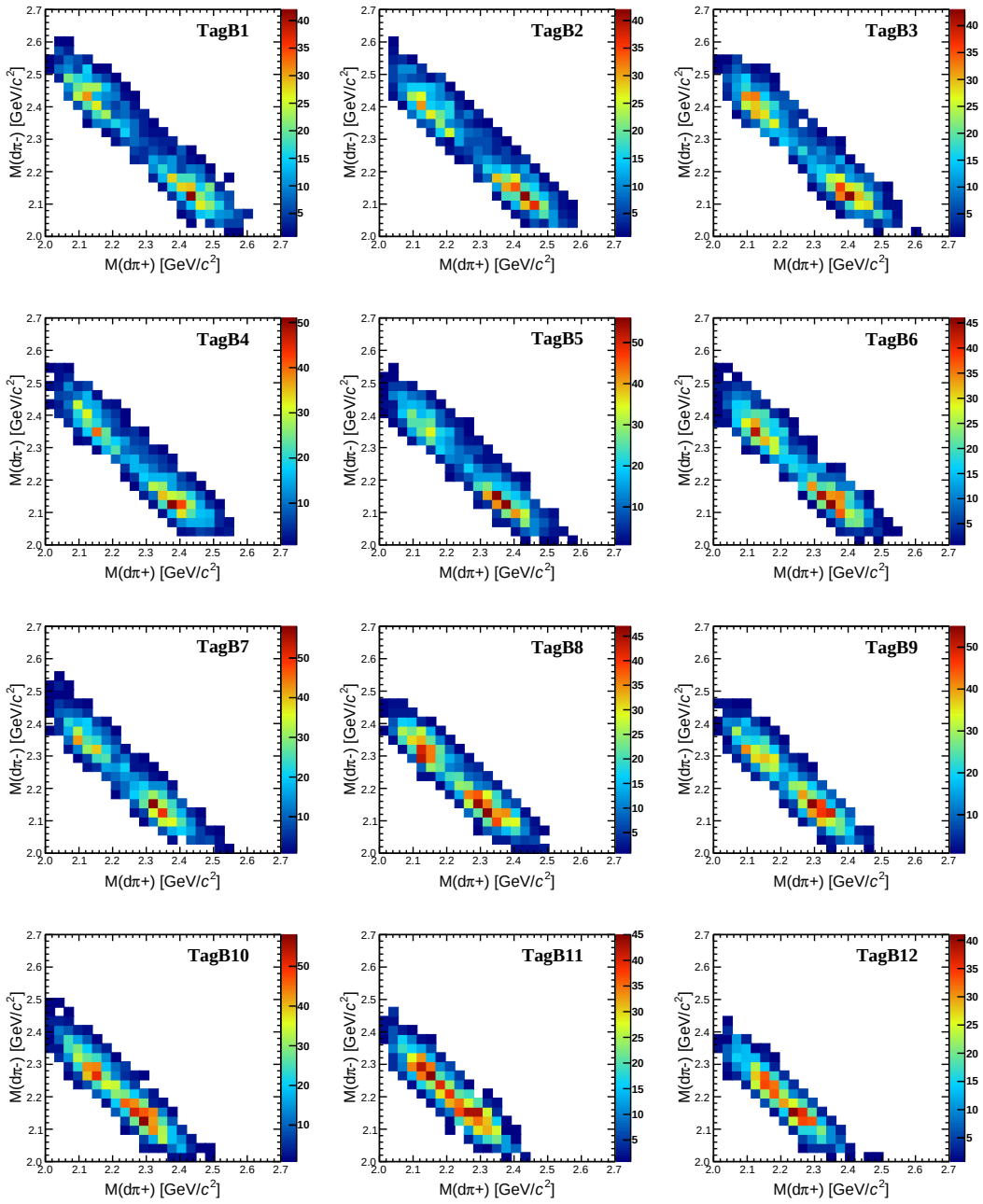

(A) $M_{d\pi^+}$ vs $M_{d\pi^-}$

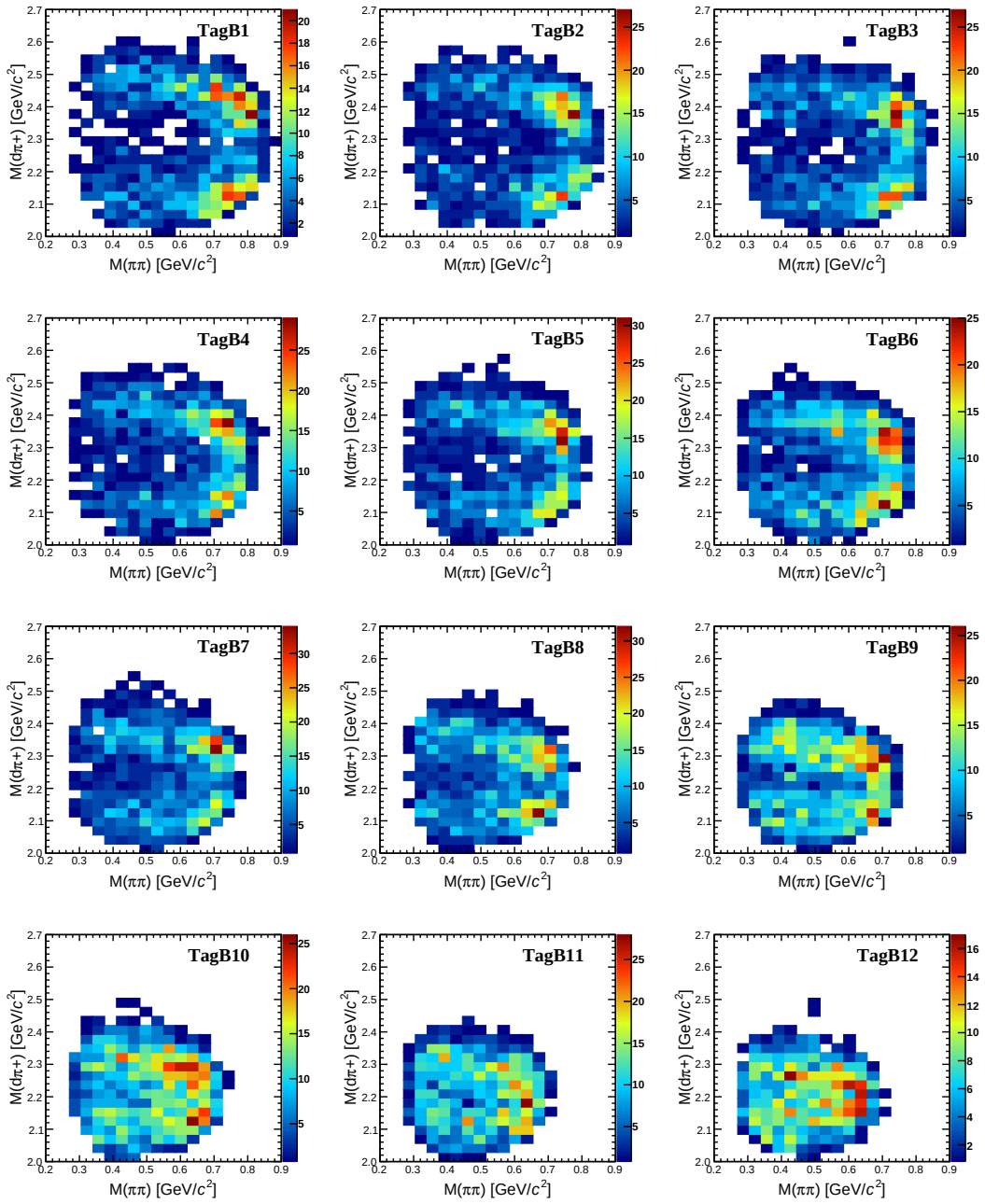

(B) $M_{\pi\pi}$ vs $M_{d\pi^+}$

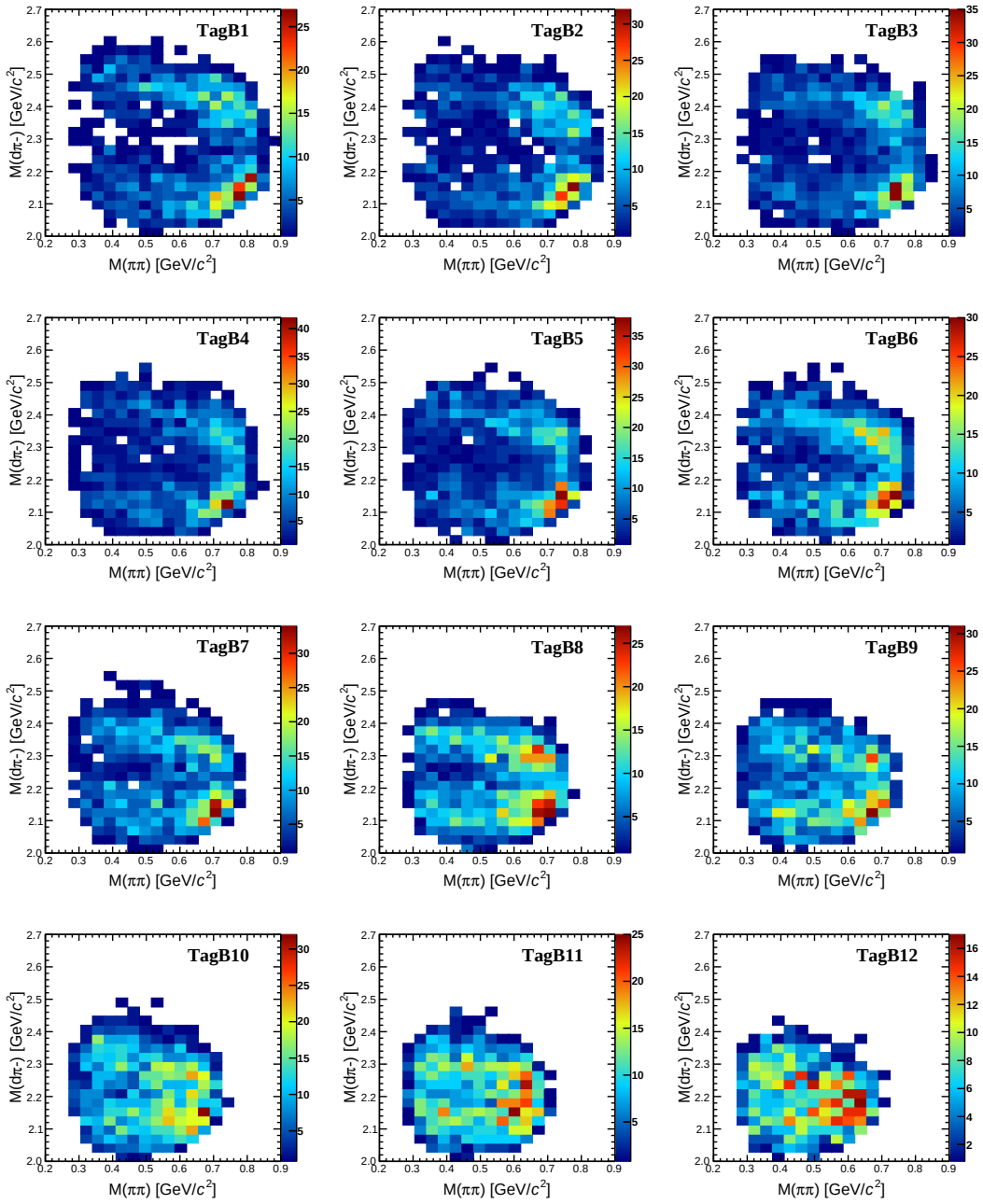

(C) $M_{\pi\pi}$ vs $M_{d\pi^-}$

FIGURE B.7: The 2-dimensional invariant mass spectra for each TagB segment

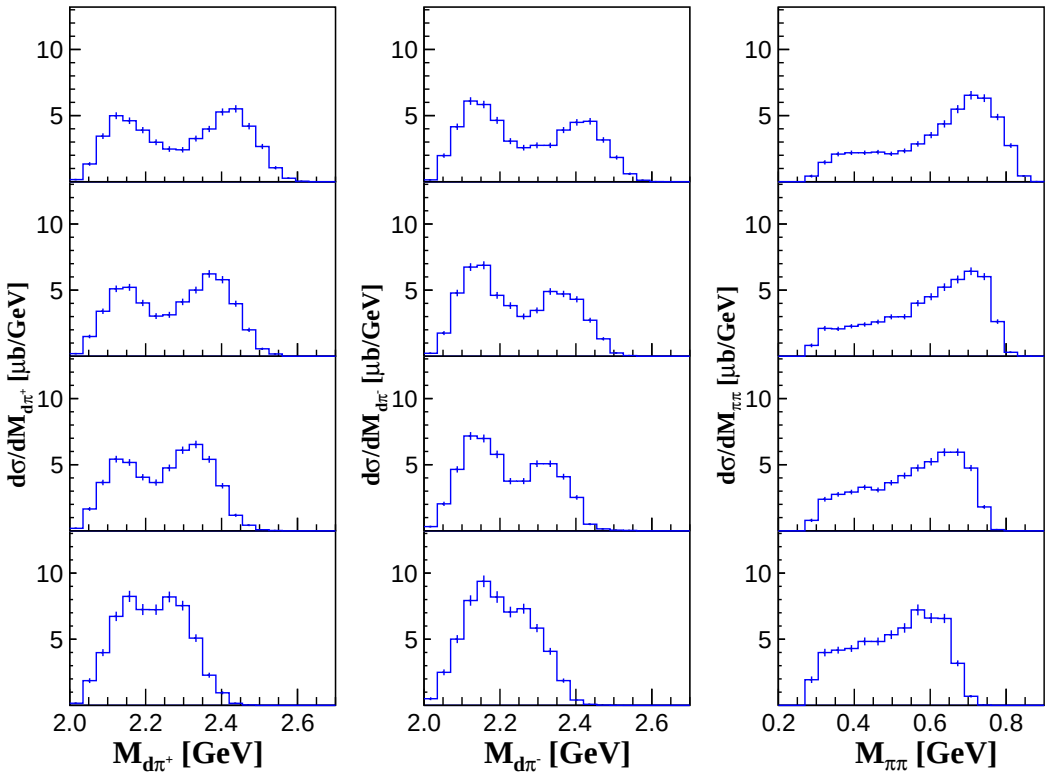

FIGURE B.8: Differential cross sections ($d\sigma/dM$) for four W region without fitting functions.

B.5 Cross Sections of the $d\pi^+\pi^-$ reaction

The differential cross sections ($d\sigma/dM$) for four W region without fitting functions are shown in Fig. B.8. The cross sections are same with Fig. 4.6.

The fit result with free ρ^0 parameters are shown in Fig. B.9. Free parameters of the fitting were amplitudes (α, β, γ), parameters of BW (M_{++}, M_0, M_ρ, Γ_{++}, Γ_0, Γ_ρ), and constant value for the phase space background (C). Therefore, the number of the free parameters was 10. It is known that the shape of ρ^0 around the threshold region is distorted due to interference between ρ^0 production and Drell-mechanism which is not included our fitting function [Sö66].

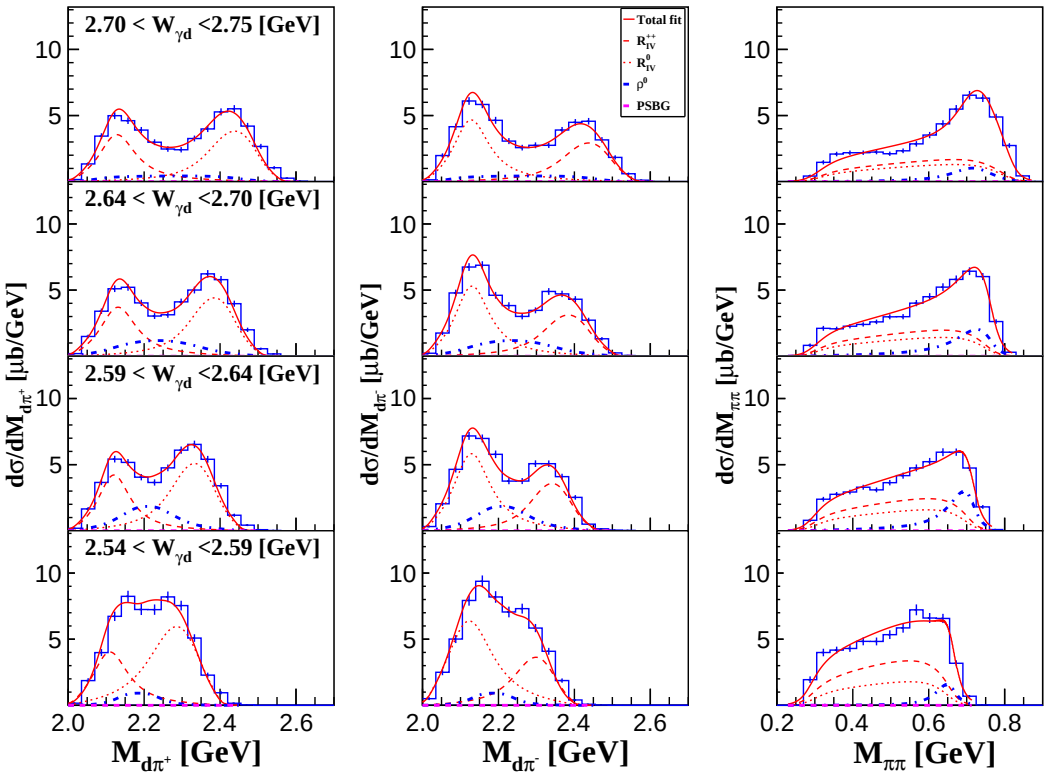

FIGURE B.9: Differential cross sections ($d\sigma/dM$) for four W region fitted by free ρ^0 parameters.

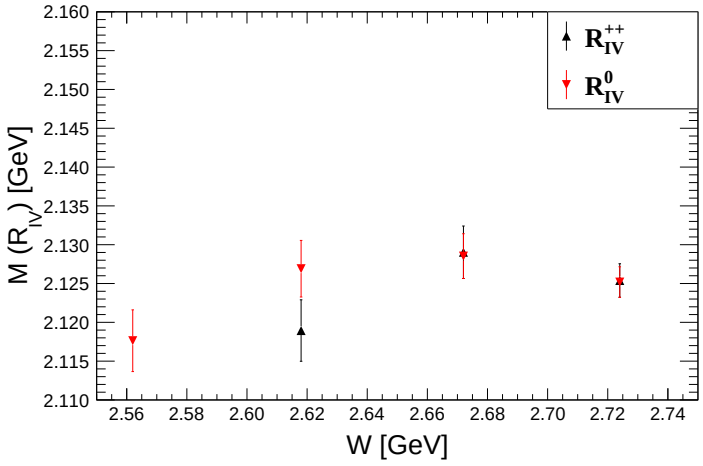

(A) Mass of R_{IV}

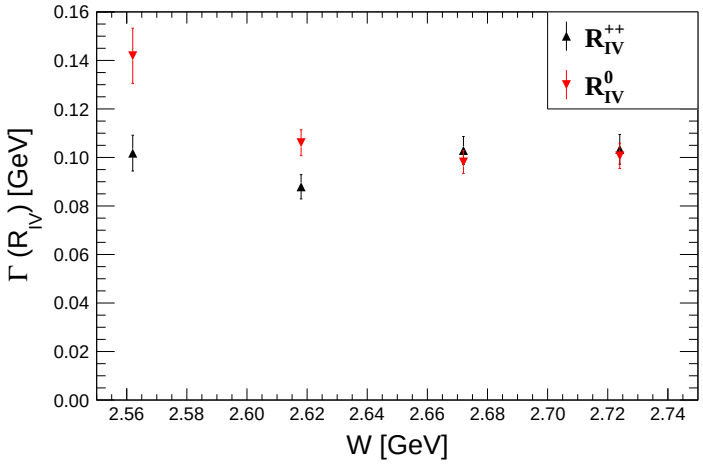

(B) Width (Γ) of R_{IV}

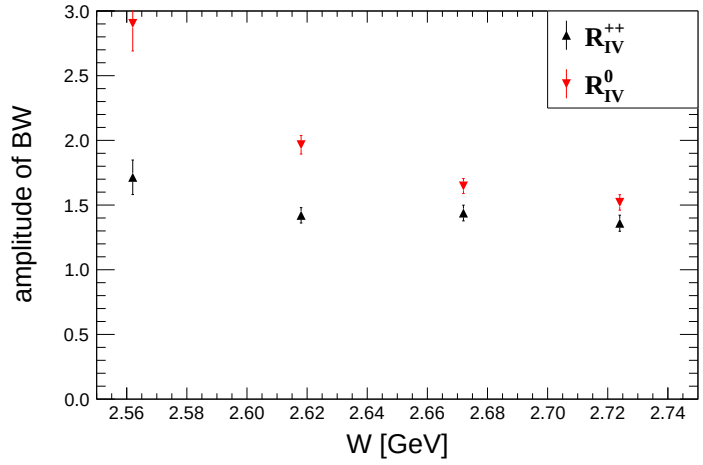

(C) Amplitude of R_{IV}

FIGURE B.10: Fitting results of the differential cross sections. Mass (A), width (B), and amplitude (C) of the assumed resonances R_{IV} are shown.

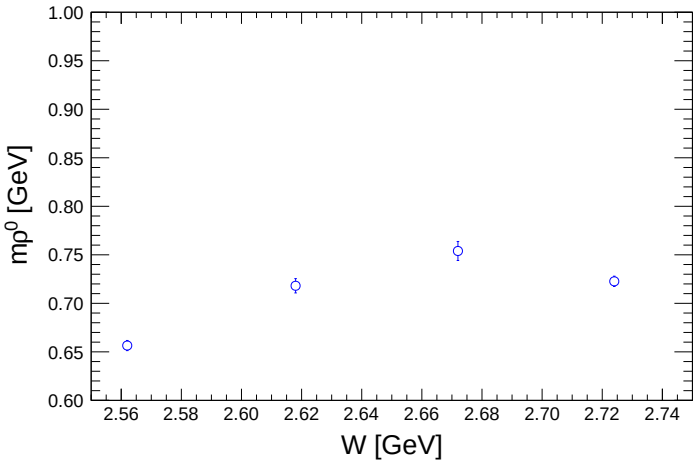

(A) Mass of ρ^0

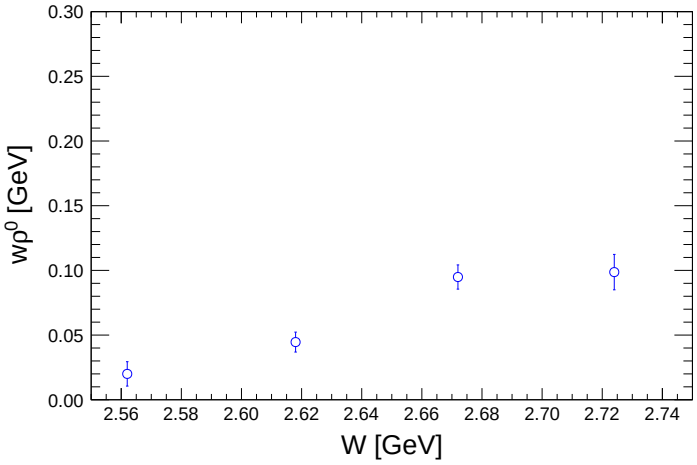

(B) Width (Γ) of ρ^0

C Estimation of Acceptance η_{acpt} and Cross Section with 3 Body Phase Space Decay Simulation

To estimate the systematic error due to the generator in the simulation used for acceptance correction, we used a simulation with an unbiased generator. The difference we obtained here clearly overestimates the systematic error, but it did not change the results significantly.

A event generator with

$$f_{d\pi^+}(M_{d\pi^+},\ E_\gamma) = f_{d\pi^-}(M_{d\pi^-},\ E_\gamma) = f_{\pi\pi}(M_{\pi\pi},\ E_\gamma) = f_{\cos\theta_d}(\cos\theta_d\ (\mathrm{CM}),\ E_\gamma) = 0, \tag{C.1}$$

in Eq. 3.27 was tested to estimate the acceptance. The obtained η^{3BPS}_{acpt} was compared with the η_{acpt} which was estimated by the tuned event generator in Fig. C.1.

The differential cross sections derived by using η^{3BPS}_{acpt} are compared with the cross sections shown in Chapter 4 in Fig. C.2, C.3, C.4. The total cross section is shown in Fig. C.4.

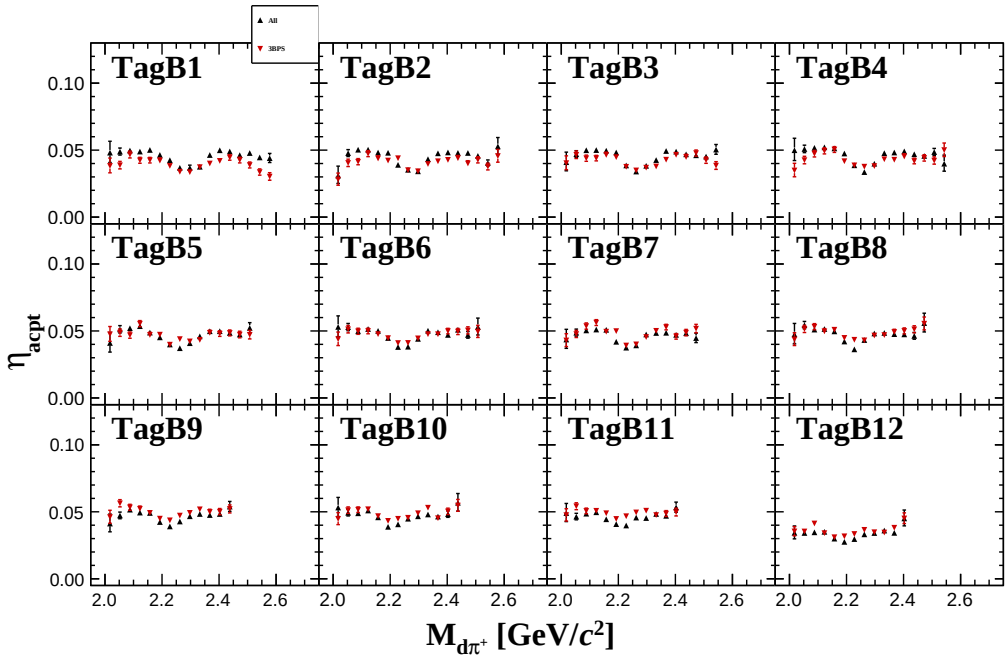

(A) $d\pi^+$ invariant mass.

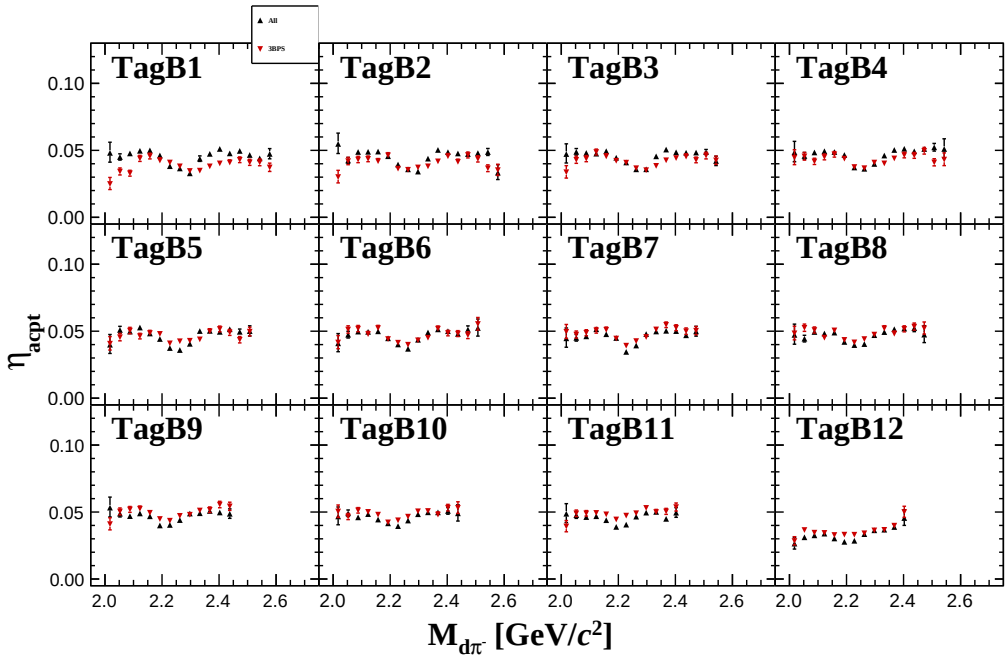

(B) $d\pi^-$ invariant mass.

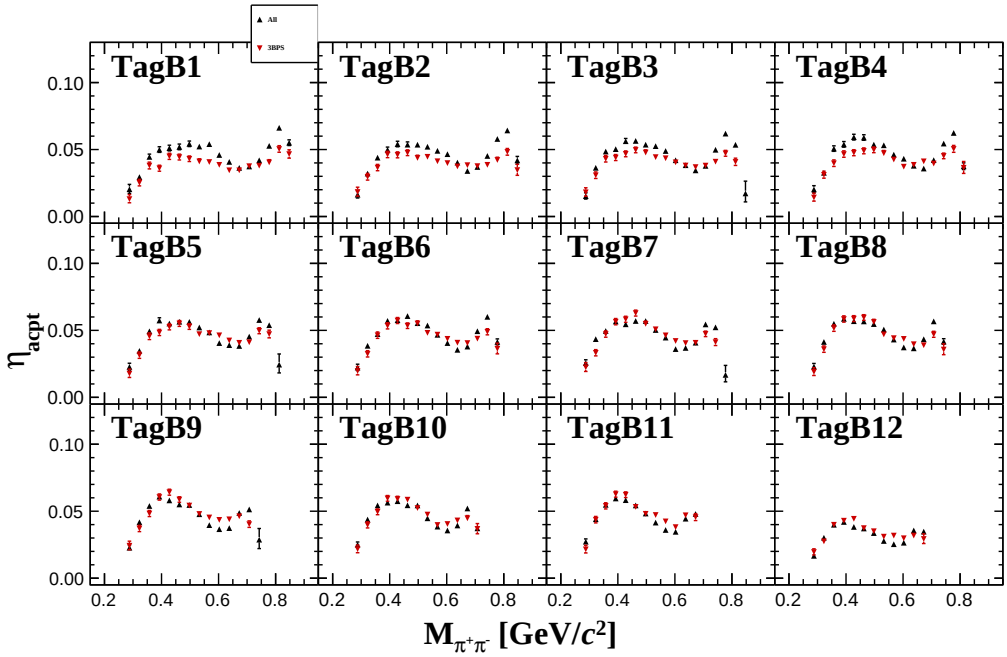

(C) $\pi^-\pi^+$ invariant mass.

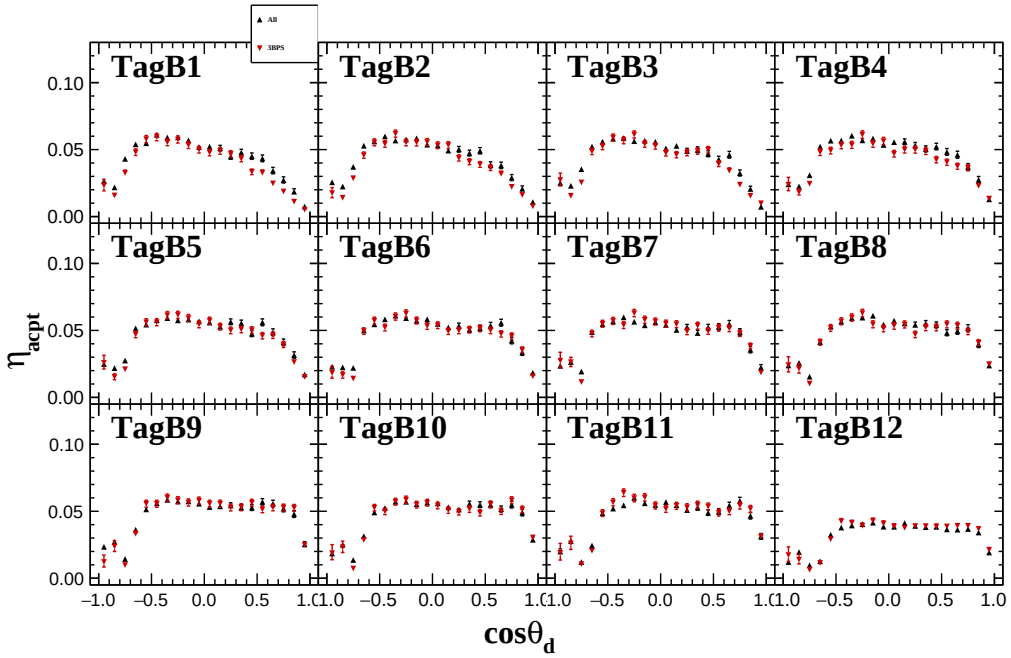

(D) $\cos\theta_d$ in γd-CM frame.

FIGURE C.1: η_{acpt} for each invariant mass and angular distribution of deuterons. (A)$d\pi^+$ (B) $d\pi^-$ (C) $\pi^-\pi^+$ (D) $\cos\theta_d$ in γd-CM frame.

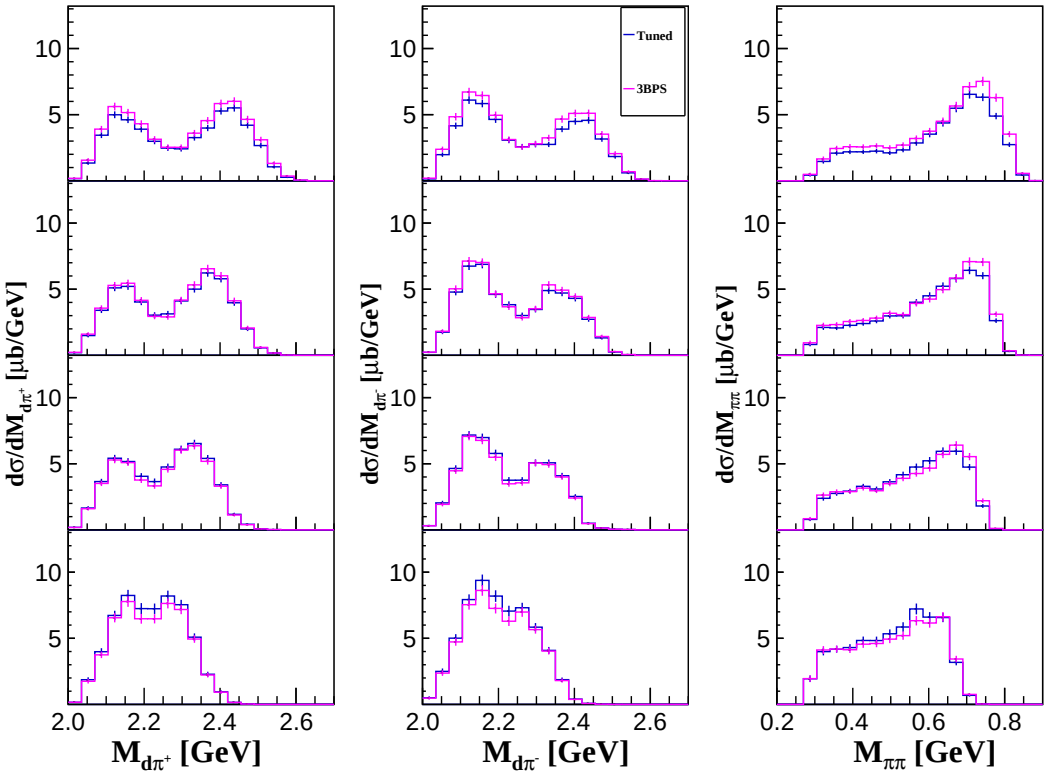

FIGURE C.2: Differential cross sections ($d\sigma/dM$) for four W region. Upper panels show higher energy regions. Blue lines show the cross section derived by using tuned event generator simulation. Magenta lines show that derived by using 3 body phase space decay simulation.

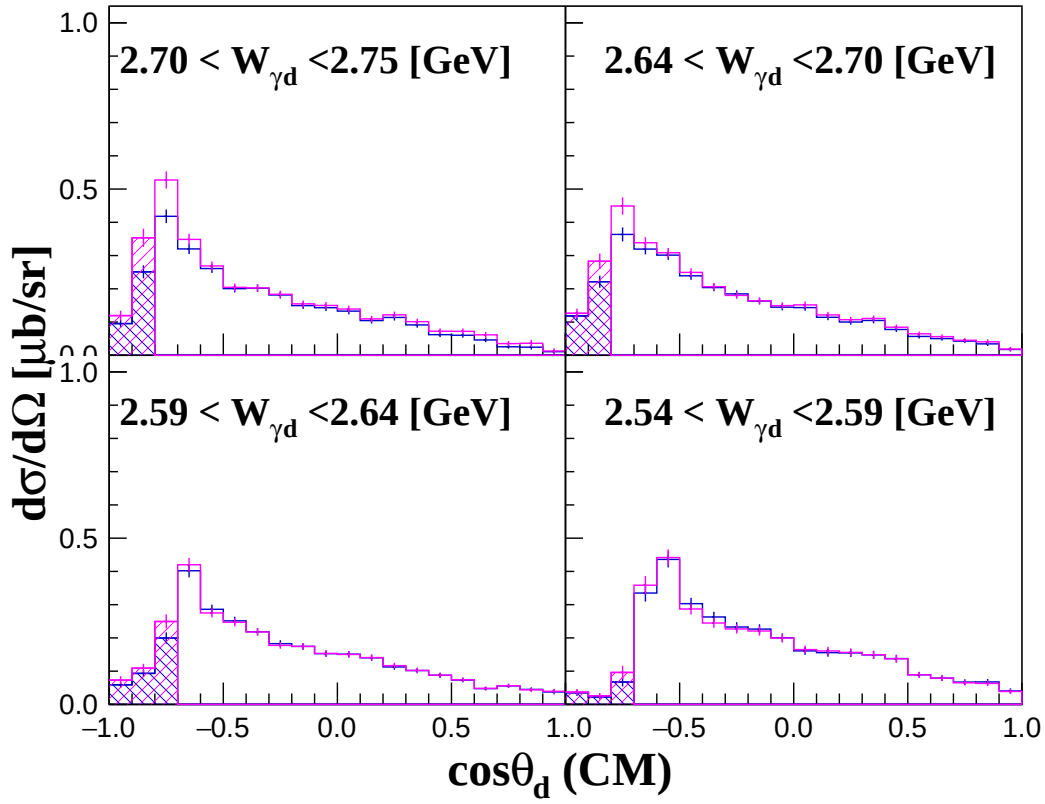

FIGURE C.3: Differential cross sections ($d\sigma/dM$) for four W region. Blue lines show the cross section derived by using tuned event generator simulation. Magenta lines show that derived by using 3 body phase space decay simulation.

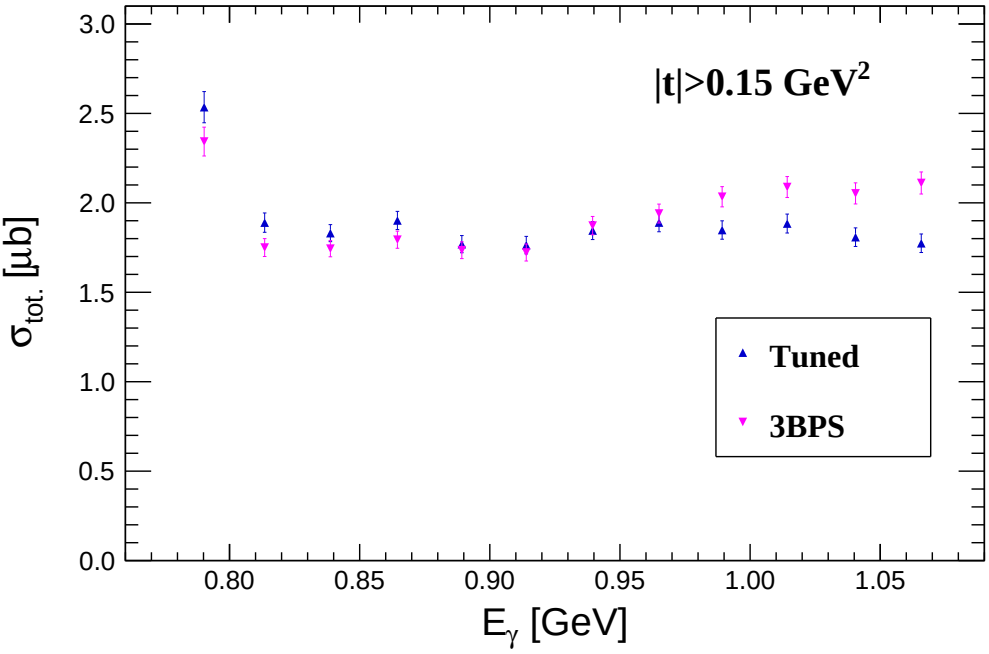

FIGURE C.4: Total cross section of the $\gamma d \rightarrow d\pi^+\pi^-$ reaction. Error bars show statistical error and black rectangles show systematic uncertainties. Blue lines show the cross section derived by using tuned event generator simulation. Magenta lines show that derived by using 3 body phase space decay simulation.

Bibliography

[ABC60] Alexander Abashian et al. *Phys. Rev. Lett.* 5 (6 1960), pp. 258–260.

[Adl+11] P. Adlarson et al. *Phys. Rev. Lett.* 106 (24 2011), p. 242302.

[Adl+13a] P. Adlarson et al. *Phys. Lett. B* 721.4 (2013), pp. 229 –236.

[Adl+13b] P. Adlarson et al. *Phys. Rev. C* 88 (5 2013), p. 055208.

[Adl+14] P. Adlarson et al. *Phys. Rev. C* 90 (3 2014), p. 035204.

[Adl+15] P. Adlarson et al. *Phys. Lett. B* 743 (2015), pp. 325–332.

[Aga+15] G. Agakishiev et al. *Phys. Lett. B* 750 (2015), pp. 184–193.

[Ant+09] I. Antcheva et al. *Comput. Phys. Commun.* 180.12 (2009), pp. 2499–2512.

[Arn+00] J. Arnold et al. *Euro. Phys. J. C - Particles and Fields* 17.1 (2000), pp. 67–81.

[Arn+93] Richard A. Arndt et al. *Phys. Rev. C* 48 (4 1993), pp. 1926–1938.

[ASW94] Richard A. Arndt et al. *Phys. Rev. C* 50 (4 1994), pp. 1796–1806.

[BAC61] Norman E. Booth et al. *Phys. Rev. Lett.* 7 (1 1961), pp. 35–39.

[Bal+87] J. Ball et al. *Nucl. Phys. B* 286 (1987), pp. 635–642.

[Bal+93] J. Ball et al. *Nucl. Phys. A* 559.4 (1993), pp. 489–510.

[Bas+09] M. Bashkanov et al. *Phys. Rev. Lett.* 102 (5 2009), p. 052301.

[Bec13] B.O. Beckford. *PhD thesis, Tohoku University* (2013).

[Ben+74] P. Benz et al. *Nucl. Phys. B* 79.1 (1974), pp. 10–37.

[Bro+02] W Brodowski et al. *Phys. Lett. B* 550.3 (2002), pp. 147–153.

[CBS15] H Clement et al. *Physica Scripta* T166 (2015), p. 014016.

[Cho+03] S.-K. Choi et al. *Phys. Rev. Lett.* 91 (26 2003), p. 262001.

[Cle17] H. Clement. *Prog. Part. Nucl. Phys.* 93 (2017), pp. 195 –242.

[Dra+00] J. Draeger et al. *Phys. Rev. C* 62 (6 2000), p. 064615.

[DX64] Freeman J. Dyson and Nguyen-Huu Xuong. *Phys. Rev. Lett.* 13 (26 1964), pp. 815–817.

[DX65] Freeman J. Dyson and Nguyen-huu Xuong. *Phys. Rev. Lett.* 14 (9 1965), pp. 339–339.

[Ego20] Mikhail Egorov. *Phys. Rev. C* 101 (6 2020), p. 065205.

[FA05] A. Fix and H. Arenhövel. *Euro. Phys. J. A* 25.1 (2005), pp. 115–135.

[FW07] V. V. Flambaum and R. B. Wiringa. *Phys. Rev. C* 76 (5 2007), p. 054002.

[Gab+84] B. Gabioud et al. *Nucl. Phys. A* 420.3 (1984), pp. 496–524.

[GG14] Avraham Gal and Humberto Garcilazo. *Nucl. Phys. A* 928 (2014), pp. 73–88.

[Gla+93] G. Glass et al. *Phys. Rev. C* 47 (4 1993), pp. 1369–1375.

[Gro+20] Particle Data Group et al. *Progress of Theoretical and Experimental Physics* 2020.8 (2020).

[GY71] R. D. Gunn and Tomoyoshi Yamada. *AIChE Journal* 17.6 (1971), pp. 1341–1345.

[Hos93] Norio Hoshizaki. *Progress of Theoretical Physics* 89.2 (1993), pp. 569–574.

[Hua+15] Fei Huang et al. *Chin. Phys. C* 39.7 (2015), p. 071001.

[Ish+10] T. Ishikawa et al. *Nucl. Instrum. Methods Phys. Res., Sect. A* 622.1 (2010), pp. 1 –10.

[Ish+19] T. Ishikawa et al. *Phys. Lett. B* 789 (2019), pp. 413 –418.

[Ish+20] T. Ishikawa et al. *Proposal to J-PARC* P79 Experiment (2020).

[Jaf77] R. L. Jaffe. *Phys. Rev. Lett.* 38 (5 1977), pp. 195–198.

[Kan+18] M. Kaneta et al. *Nucl. Instrum. Methods Phys. Res., Sect. A* 886 (2018), pp. 88 –103.

[Les+99] A. de Lesquen et al. *Euro. Phys. J. C* 11.1 (1999), pp. 69–78.

[Mac01] R. Machleidt. *Phys. Rev. C* 63 (2 2001), p. 024001.

[Mak+80] Y. Makdisi et al. *Phys. Rev. Lett.* 45 (19 1980), pp. 1529–1533.

[MAS80] P. J. Mulders et al. *Phys. Rev. D* 21 (9 1980), pp. 2653–2671.

[MB79] Jan Myrheim and Lars Bugge. *Nucl. Instrum. Methods* 160.1 (1979), pp. 43–48.

[McG+08] J. C. McGeorge et al. *Euro. Phys. J. A* 37.1 (2008), pp. 129–137.

[McK+06] B. McKinnon et al. *Phys. Rev. Lett.* 96 (21 2006), p. 212001.

[McN+93] M. W. McNaughton et al. *Phys. Rev. C* 48 (1 1993), pp. 256–265.

[MT83] P J Mulders and A W Thomas. *J. Phys. G: Nucl. Phys.* 9.10 (1983), pp. 1159–1167.

[Mur+14] N. Muramatsu et al. *Nucl. Instrum. Methods Phys. Res., Sect. A* 737 (2014), pp. 184 –194.

[Nak+03] T. Nakano et al. *Phys. Rev. Lett.* 91 (1 2003), p. 012002.

[New+89] C. R. Newsom et al. *Phys. Rev. C* 39 (3 1989), pp. 965–974.

[Nis82] J.A. Niskanen. *Phys. Lett. B* 112.1 (1982), pp. 17–21.

[Nom+94] M Nomachi et al. Tech. rep. 1994.

[Noy72] H P Noyes. *Annu. Rev. Nucl. Sci.* 22.1 (1972), pp. 465–484.

[NP19] B.S. Neganov and L.B. Parfenov. *SOVIET PHYSICS JETP* 7 (0019), pp. 528 –529.

[OY80] M. Oka and K. Yazaki. *Phys. Lett. B* 90.1 (1980), pp. 41–44.

[PK13] M. N. Platonova and V. I. Kukulin. *Phys. Rev. C* 87 (2 2013), p. 025202.

[PK16] M.N. Platonova and V.I. Kukulin. *Nucl. Phys. A* 946 (2016), pp. 117–157.

[Pol+87] R.E. Poling et al. McGraw-Hill chemical engineering series 10. McGraw-Hill, 1987. ISBN: 9780070517998.

[Sch+87] O. Schori et al. *Phys. Rev. C* 35 (6 1987), pp. 2252–2257.

[Set88] KK Seth. *Bad Honnef* 1988 (1988), p. 41.

[Sob+00] D.I. Sober et al. *Nucl. Instrum. Methods Phys. Res., Sect. A* 440.2 (2000), pp. 263 –284.

[ST80] J. Simkin and C.W. Trowbridge. English. *IEE Proceedings B (Electric Power Applications)* 127 (6 1980), 368–374(6).

[Sö66] P. Söding. *Physics Letters* 19.8 (1966), pp. 702–704.

[UBM32] Harold C. Urey et al. *Phys. Rev.* 39 (1 1932), pp. 164–165.

[Yam+05] H. Yamazaki et al. *Nucl. Instrum. Methods Phys. Res., Sect. A* 536.1 (2005), pp. 70 –78.

[YC+10] HAN Yun-Cheng et al. *Chin. Phys. C* 34.2009-0022 (2010), p. 35.